DOT/FAA/RD-81/65

Project Report
ATC-107

Experimental Measurements of Low Angle Ground Reflection Characteristics at L- and C-Bands for Irregular Terrain

D.F. Sun

1 November 1982

Lincoln Laboratory
MASSACHUSETTS INSTITUTE OF TECHNOLOGY
LEXINGTON, MASSACHUSETTS

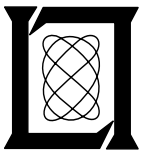

Prepared for the Federal Aviation Administration,
Washington, D.C. 20591

This document is available to the public through
the National Technical Information Service,
Springfield, VA 22161

TECHNICAL REPORT STANDARD TITLE PAGE

1. Report No.	2. Government Accession No.	3. Recipient's Catalog No.
DOT/FAA/RD-81/65		

4. Title and Subtitle

Experimental Measurements of Low Angle Ground Reflection Characteristics at L- and C-Bands for Irregular Terrain

5. Report Date
1 November 1982

6. Performing Organization Code

7. Author(s)
D.F. Sun

8. Performing Organization Report No.
ATC-107

9. Performing Organization Name and Address
Massachusetts Institute of Technology
Lincoln Laboratory
P.O. Box 73
Lexington, MA 02173-0073

10. Work Unit No.

11. Contract or Grant No.
DOT-FA74-WAI-461

12. Sponsoring Agency Name and Address
Department of Transportation
Federal Aviation Administration
Systems Research and Development Service
Washington, DC 20591

13. Type of Report and Period Covered
Project Report

14. Sponsoring Agency Code

15. Supplementary Notes

The work reported in this document was performed at Lincoln Laboratory, a center for research operated by Massachusetts Institute of Technology, under Air Force Contract F19628-80-C-0002.

16. Abstract

Field measurements of terrain reflection data at L band and C band have been taken during 1980 at several test sites at Hanscom airport, Fort Devens, and Camp Edwards, Massachusetts. These field data are used for (1) characterization of the L band and C band multipath environments, (2) validation of terrain multipath propagation models, and (3) assessment of TRSB elevation angle estimation performance with various aperture sizes.

Conventional beamsum, maximum likelihood, and maximum entropy angular power spectral estimates have been employed as a means to characterize the multipath environment. The maximum entropy angular power spectral estimate offered highest resolution of the various multipath signals.

The L-band field measurement results indicated that the terrain multipath were specular reflections with a high multipath levels. L-band M/D ratios ranging from -5 dB to 1 dB were observed in a variety of terrain conditions. At C band, diffuse ground reflections were evident at some measurement sites, especially at Camp Edwards J2 range site, where small scale terrain roughness was fairly visible. However, these C-band diffuse reflections appeared to be at fairly low levels, e.g., -15 dB to -20 dB relative to the direct signal. The C-band peak specular multipath levels of -10 dB to -2 dB were slightly lower than those of the L-band for the same terrain geometry.

The phenomenon of the "focusing" ground reflections, i.e., more than one specular ground reflection present at the same time, was observed at both L-band and C-band. For the L-band, this generally occurred in the rolling type of terrain. However, for the C-band, this also happened in the fairly flat terrain at Hanscom airport site.

17. Key Words	18. Distribution Statement
field measurements low angle ground reflection data L-band C-band irregular terrain	Document is available to the public through the National Technical Information Service, Springfield, VA 22161.

19. Security Classif. (of this report)	20. Security Classif. (of this page)	21. No. of Pages	22. Price
Unclassified	Unclassified	228	

Form DOT F 1700.7 (8-69)

16. Abstract (Continued)

The L-band azimuth field measurement results showed that the observed ground reflections and the direct signal appeared to arrive from the same azimuth angle. So, apparently, the terrain cross-range tilts observed at various measurement sites were not large enough to make the azimuth arrival angle of the ground reflection deviate significantly from the direct signal azimuth angle.

The validation of the MLS terrain propagation models was accomplished by comparison of the field measured results and the MLS multipath simulation predicted results for the angular power spectrum. The agreement between these two sets of results depended strongly on the terrain conditions. For the terrain which had minimal cross-range tilts and was electrically fairly smooth, the field measurements could be well explained with the simulation prediction results. This good agreement was obtained in terms of the number of multipath arrivals, their arrival angles, and M/D ratios. However, for the more complicated terrain, the agreement was often poor, especially for those cases where the diffuse ground reflections appeared to exist in the field measured results. This more complicated terrain was generally characterized by lower multipath levels.

For the assessment of the elevation angle estimation performance with various array aperture sizes in various terrain conditions, approximations to the MLS (TRSB) "dwell gate" angle processor and the "single edge" flare processor were used to process C-band field data for array beamwidths of 1°, 2°, 3°, and 4° respectively. A significant reduction (on the order of 0.1° to 0.3°) in the angular error was observed when the array beamwidth was decreased from 4° to 3°, especially for the single edge processor. However, in general, the angle estimation performance with either angle estimator was not significantly degraded by increasing the array beamwidth from 1° to 3°.

ABSTRACT

Field measurements of terrain reflection data at L band and C band have been taken during 1980 at several test sites at Hanscom airport, Fort Devens, and Camp Edwards, Massachusetts. These field data are used for (1) characterization of the L-band and C-band multipath environments, (2) validation of terrain multipath propagation models, and (3) assessment of TRSB elevation angle estimation performance with various array aperture sizes.

Conventional beamsum, maximum likelihood, and maximum entropy angular power spectral estimates have been employed as a means to characterize the multipath environement. The maximum entropy angular power spectral estimate offered highest resolution of the various multipath signals.

The L-band field measurement results indicated that the terrain multipath were specular reflections with high multipath levels. L-band M/D ratios ranging from -5 dB to 1 dB were observed in a variety of terrain conditions. At C band, diffuse ground reflections were evident at some measurement sites, especially at Camp Edwards J2 range site, where small scale terrain roughness was fairly visible. However, these C-band diffuse reflections appeared to be at fairly low levels, e.g., -15 dB to -20 dB relative to the direct signal. The C-band peak specular multipath levels of -10 dB to -2 dB were slightly lower than those of the L band for the same terrain geometry.

The phenomenon of the "focusing" ground reflections, i.e., more than one specular ground reflection present at the same time, was observed at both L band and C band. For the L band, this generally occurred in the rolling type of terrain. However, for the C band, this also happened in the fairly flat terrain at the Hanscom airport site.

The L-band azimuth field measurement results showed that the observed ground reflections and the direct signal appeared to arrive from the same azimuth angle. So, apparently, the terrain cross-range tilts observed at various measurement sites were not large enough to make the azimuth arrival angle of the ground reflection deviate significantly from the direct signal azimuth angle.

The validation of the MLS terrain propagation models was accomplished by comparison of the field measured results and the MLS multipath simulation predicted results for the angular power spectrum. The agreement between these two sets of results depended strongly on the terrain conditions. For the terrain which had minimal cross-range tilts and was electrically fairly smooth, the field measurements could be well explained with the simulation predictions results. This good agreement was obtained in terms of the number of multipath arrivals, their arrival angles, and M/D ratios. However, for the more complicated terrain, the agreement was often poor, especially for those cases where the diffuse ground reflections appeared to exist in the field measured results. This more complicated terrain was generally characterized by lower multipath levels.

For the assessment of the elevation angle estimation performance with various array aperture sizes in various terrain conditions, approximations to the MLS (TRSB) "dwell gate" angle processor and the "single edge" flare processor were used to process C-band field data for array beamwidths of 1°, 2°, 3°, and 4° respectively. A significant reduction (on the order of 0.1° to 0.3°) in the angular error was observed when the array beamwidth was decreased from 4° to 3° , especially for the single edge processor. However, in general, the angle estimation performance with either angle estimator was not significantly degraded by increasing the array beamwidth from 1° to 3°.

CONTENTS

ACKNOWLEDGMENTS

The hardware modifications on the existing PALM equipment that resulted in the experimental facility for the 1980 field measurements reported here involved direct efforts from many people including J. Evans, F. Irons, R. Parr, P. Swett, A. Vierstra, J. Bertram, R. Catalan, and A. Gregory.

The field measurements in 1980 were carried out with great assistance from B. Devine, A. Gregory, D. Hamilton, J. Kalil and J. Yaeger-Charriere. A. Gregory handled most of the details involved in the transportation of the measurement facility to various test sites and in the coordination for the deployment of the antenna arrays. The actual transportation was mostly provided by the Hanscom AFB motor pool personnel.

The helicopter used in the field measurements was arranged and handled by the Lincoln Flight Facility personnel including E. Becotte, T. Magnan, D. Cassalia, D. Davis, and J. Eisenhower.

Terrain surveys for various test sites were made by D. Stuart and J. Sullivan.

C. Catalano was responsible for the implementation and maintenance of the software on the Eclipse computer used in the field measurements. J. Yaeger-Charriere processed most of the field data and MLS multipath simulation data. N. Whitaker did the preliminary data comparison between the field measurements and the MLS multipath simulations, and contributed the Appendices A and B in this report. N. Campbell, D. Young, K. Eastburn, C. Carter Likas and D. DiClemente were responsible for the typing work on this report.

Finally, I would particularly like to express my sincere gratitude to J. Evans for his numerous helpful comments and suggestions for the work presented in this report.

I. INTRODUCTION

This report presents the results of an ongoing terrain multipath measurement program to obtain ground reflection field data in various terrain conditions for the following purposes:

(1) characterization of the terrain multipath environment which is of concern to the microwave landing system (MLS),

(2) validation of terrain multipath propagation models which are used in the MLS simulation program developed by Lincoln Laboratory [1], and

(3) assessment of the angle estimation accuracy obtainable with various array aperture sizes using the angle estimators which are used in the MLS angle receivers.

The initial results presented in our earlier report [2] indicated that the reflections observed in the field data appeared to be specular in nature and could be explained by the flat plate models utilized in the MLS propagation model. High reflection levels (e.g., >-3 dB) were observed. "Focusing" ground reflections, i.e., more than one specular reflection present at a given time, arose in several sites where terrain had various upsloping and downsloping features. These results were obtained from the field data taken at a carrier frequency of 1090 MHz (L band) and might not be applicable to 5 GHz (C band) which is the MLS angle data frequency. Thus, the need for the C-band field data was quite obvious.

During 1979, our experimental facility was modified and expanded to include a C-band measurement capability. The major components in the C-band measurement facility include: (1) a 57 λ elevation receiving antenna array consisting of 29 C-band horns and (2) a 5-channel C-band RF receiver. The C-band measurements were made at 5.1618 GHz with the CW signal transmitted from a 20-watt TWT on board an aircraft. In addition to the new C-band equipment, an L-band azimuth array was added on to the existing L-band elevation system. This L-band azimuth array consists of 6 original PALM antennas [3]. Measurement with the L-band azimuth array was motivated by the DAS concept for the MLS 360° azimuth coverage. Figure 1-1 shows a photo of our current experimental facility as set up for a typical field measurement.

Fig. 1-1. Experimental system for L/C band ground reflection data collection.

Results reported here were obtained from the field measurements which were taken in 1980 at L.G. Hanscom airport (Bedford, MA), Fort Devens, MA and Camp Edwards, MA. L-band measurements had been made at Hanscom airport and Fort Devens two years ago. Revisiting these two old sites for more measurements not only produced the new C-band data to be compared with the corresponding L-band data but also gave us the opportunity to determine the data repeatability at L band. The three sites at Camp Edwards offered us three fairly different terrain conditions as compared to those at Hanscom airport and Fort Devens. One site was fairly flat but rough and the other two sites were fairly smooth but rolling with large scale variation at one site and small scale variation at the other. Also, the vegetation cover on the ground at Camp Edwards was less uniform than that at Hanscom airport or Fort Devens. So, the results presented here cover wide varieties of terrain conditions.

To more accurately model the terrain at a given measurement site for the MLS multipath simulation run, a more detailed terrain survey was made this time than last time. The terrain survey at a measurement site considered both the ground height profile along a given radial direction and the ground tilt in the cross range direction, as opposed to just the height profile alone in the past. Thus, the ground model to be input to the MLS simulation run could be made to agree better with the actual ground. The actual ground was modeled as a series of rectangular plates with their "along-range" slopes and "cross-range" tilts properly accounted for.

For the propagation model validation, the comparison between the field measured data and the MLS multipath simulation predicted data was made in terms of angular power spectrum, as in [2]. The basic processing algorithms to estimate the angular power spectrum are the same as before, namely, the beamsum (BS), the maximum likelihood (ML) and the maximum entropy (ME). However, the ML and ME algorithms have been refined to yield better resolution of various signal arrivals (direct and multipath) and better estimates of the multipath levels (M/D). For the angle estimation of various signal arrivals, the ML and ME angular power spectrum were calculated using the modified covariance method [4]. The M/D's (also the multipath relative RF phases) were

then obtained by an alternative scheme due to S. Lang [5] which is based on the least-squares fitting, using the estimated signal arrival angles.

The MLS multipath simulation program [1] has an option, named "focusing ground" option, whereby specular ground reflections can be computed for a number of arbitrarily oriented rectangular or triangular ground plates. In this option, the formula used for computing the scattered field from an individual plate involves the use of an effective reflection coefficient, R_{eq}, which is a function only of the angle of incidence. This approximation is valid at the specular point where the reflection angle is equal to the incidence angel. However, the numerical integration used to determine the received field will include points on the plate where the reflection angle is not equal to the incidence angle. To examine the validity of the R_{eq} approximation for the non-specular points, a theoretical study was made of the scattered field from a tilted dielectric facet. Appendices A and B summarize the results of that study.

In addition to the multipath environment characterization and the propagation model validation, the field measured data were also used in a trade-off study on the elevation angle estimation accuracy versus the antenna array aperture size. The objective here is to see to what extent the absolute angle error (i.e., in degrees as opposed to array beamwidths) depends on the antenna aperture size in various natural terrain conditions. Two angle estimators, the beamsum (BS) and the single edge processor (SEP), were chosen for the study. The BS estimator corresponds to the conventional MLS (TRSB) angle processing and the SEP estimator is the MLS angle processor suggested for use in the flare region.

The remainder of this report proceeds as follows. Chapter II will describe the measurement facility which produced the field data reported here. Only the equipment which differ from those described in our previous reports [2] will be discussed in detail, e.g., the new C-band receiving antenna system. The methods involved in the propagation model validation, such as the spectral estimation algorithms, and in the elevation angle estimation will be briefly discussed in Chapter III. Chapter IV will describe the terrain

conditions for the measurement sites we visited and shows the ground models, constructed from the terrain surveyed data, used in the MLS multipath simulation runs. Chapter V will present the experimental results for the terrain multipath. These results will be discussed in connection to the propagation model validation and the L-band/C-band multipath environment characterization. The results on the elevation angle estimation with antenna arrays of four different aperture sizes, (1°, 2°, 3°, and 4° beamwidths) will be presented in Chapter VI. In the last Chapter, we will summarize the results reported here and say a few words about the modelling of specific terrain types for the MLS simulation, and the nature of the observed terrain multipath and its implication for the MLS performance.

II. MEASUREMENT FACILITY

The experimental system used in the field measurement is described in this Chapter. The current experimental system was basically built around the existing L-band measurement facility used in the previous terrain reflection measurement program during the 1977-1979 period [2]. Figure 2-1 shows a simple block diagram of our current measurement system. It consists of six major parts: (1) the C-band subsystem, (2) the L-band subsystem, (3) the IF subsystem, (4) the transmitter subsystem, (5) the calibration subsystem and (6) the computer subsystem.

The C-band subsystem contains one elevation receiving array consisting of 29 horn antennas and one 5-channel receiver RF front end. The L-band subsystem consists of two receiving arrays (one elevation array of 11 dipoles and one azimuth array of 6 PALM antennas [3]) and one 5-channel receiver RF front end. The IF subsystem covers the common 5-channel receiver IF and downstream shared by both the C-band and the L-band subsystems. The transmitter subsystem is made up of a ground based L-band ATC transponder interrogator and two airborne transmitters (L-band ATC radar beacon transponder and C-band TWT). The computer subsystem consists of an Eclipse computer and a disk drive together with a CRT terminal, a tape drive and a copier.

The IF subsystem, the L-band transmitter and receiver subsystems, and the computer subsystem essentially are the original hardware in our previously existing L-band equipment [2,3]. However, some modifications were made in the procedures of signal recording and equipment calibration; and some hardware components were physically relocated and rearranged. Hence, the discussion of the current experimental hardware will be focused on those modifications and on the new additions (e.g., the C-band subsystem) to the existing equipment.

A. Equipment Set-Up

The experimental configuration for the measurements is shown in Fig. 2-2. The RF signal needed for the ground reflection measurements was transmitted from either the L-band ATC transponder or the C-band TWT CW source onboard the helicopter. The L-band frequency was at 1090 MHz and the C-band

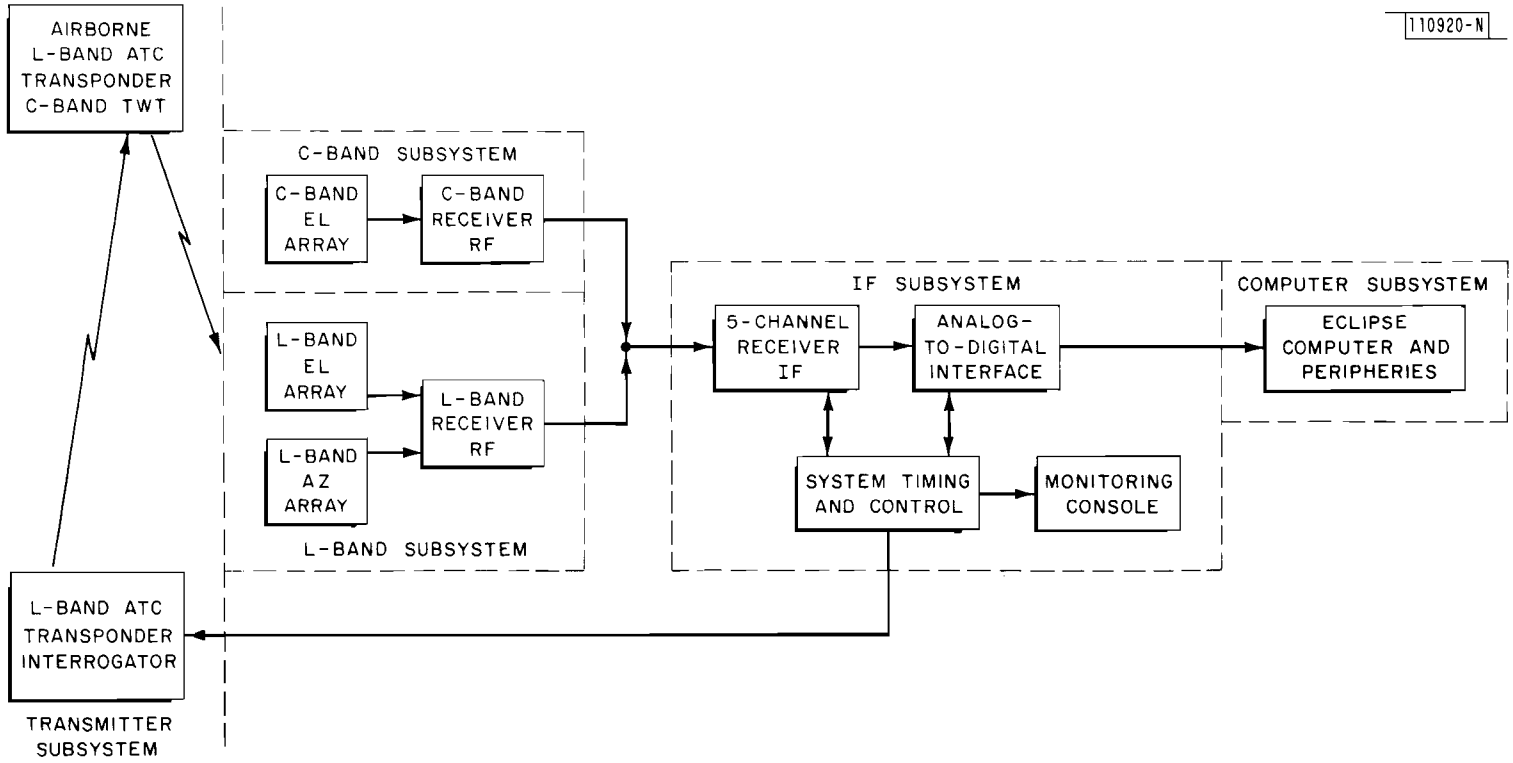

Fig. 2-1. Simple block diagram of our current measurement system.

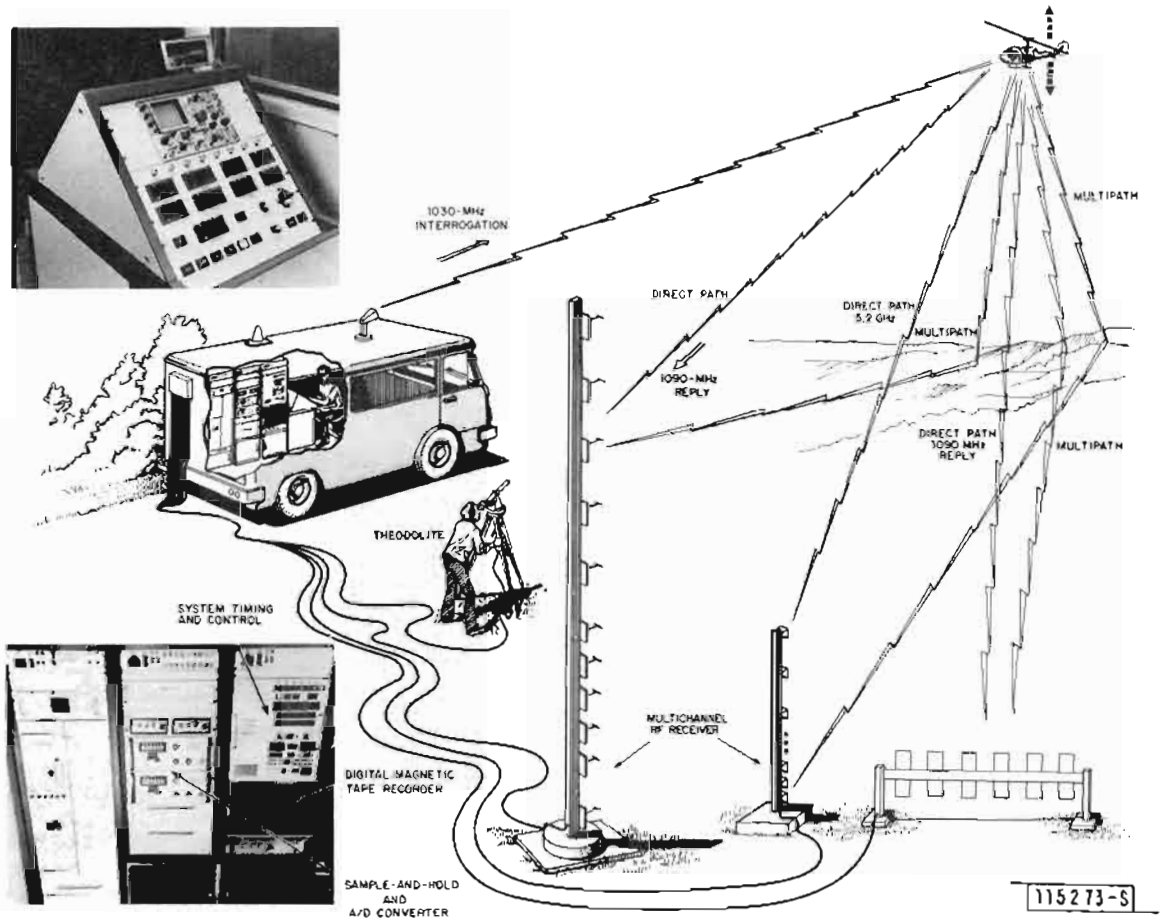

Fig. 2-2. The experimental configuration for the terrain reflection measurement.

was at 5.1618 GHz. The L-band transponder would only reply with the pre-selected pulse signal to the interrogation from our ground interrogator, while the C-band TWT would be transmitting at all times during a given measurement mission. Since the C-band and the L-band subsystems shared the same IF receiver, the measurements for the L-band and the C-band were done in the time-sharing fashion. That is, at a given measurement location, our measurement system was completely dedicated to the L band for an entire flight path, then was switched to the C band for another identical flight path. Figure 2-3 shows a more detailed block diagram of the L-band, C-band and IF subsystems.

1. L-band Subsystem

Referring to Fig. 2-3 (a,c), the L-band subsystem covers the system path from the L-band antenna element down to the L-band IF bandpass (BP) filter. The elevation (EL) receiving array consists of eleven L-band vertical dipole antennas with reflectors, mounted on a 30-foot vertical mast. This EL antenna array is the one which we used in the previous measurement program [2]. These eleven dipoles gave us two uniformly spaced arrays, as can be seen in Fig. 1-1, one with 9 elements spacing at 3.24 wavelengths (λ) apart and the other with 5 elements at 1.62 λ spacing. The results reported here were obtained with the 9 element array (26 λ aperture and 2° beamwidth). The azimuth (AZ) receiving array is a 6-element equally spaced array, with 14 λ aperture (about 4° beamwidth). The antennas of the AZ array are the original PALM antennas [3], mounted on a 15-foot horizontal mast at 4-foot height with vertical polarization. For the detailed characteristics of the EL and AZ array elements, please see references [2] and [3], respectively.

The RF front ends of the 5-channel receiver are the original components in the existing L-band equipment [2,3]. However, some modifications were made to reduce channel drifts and to use the additional arrays. The RF front ends were moved outside the van and installed right behind the antenna elements. This meant the long cable connection (about 50 feet) needed between the antenna outputs and the van input ports could be operated at 60 MHz IF frequency, as opposed to the original arrangement where the RF front ends were inside the van and the signal received at each antenna was fed back to the van

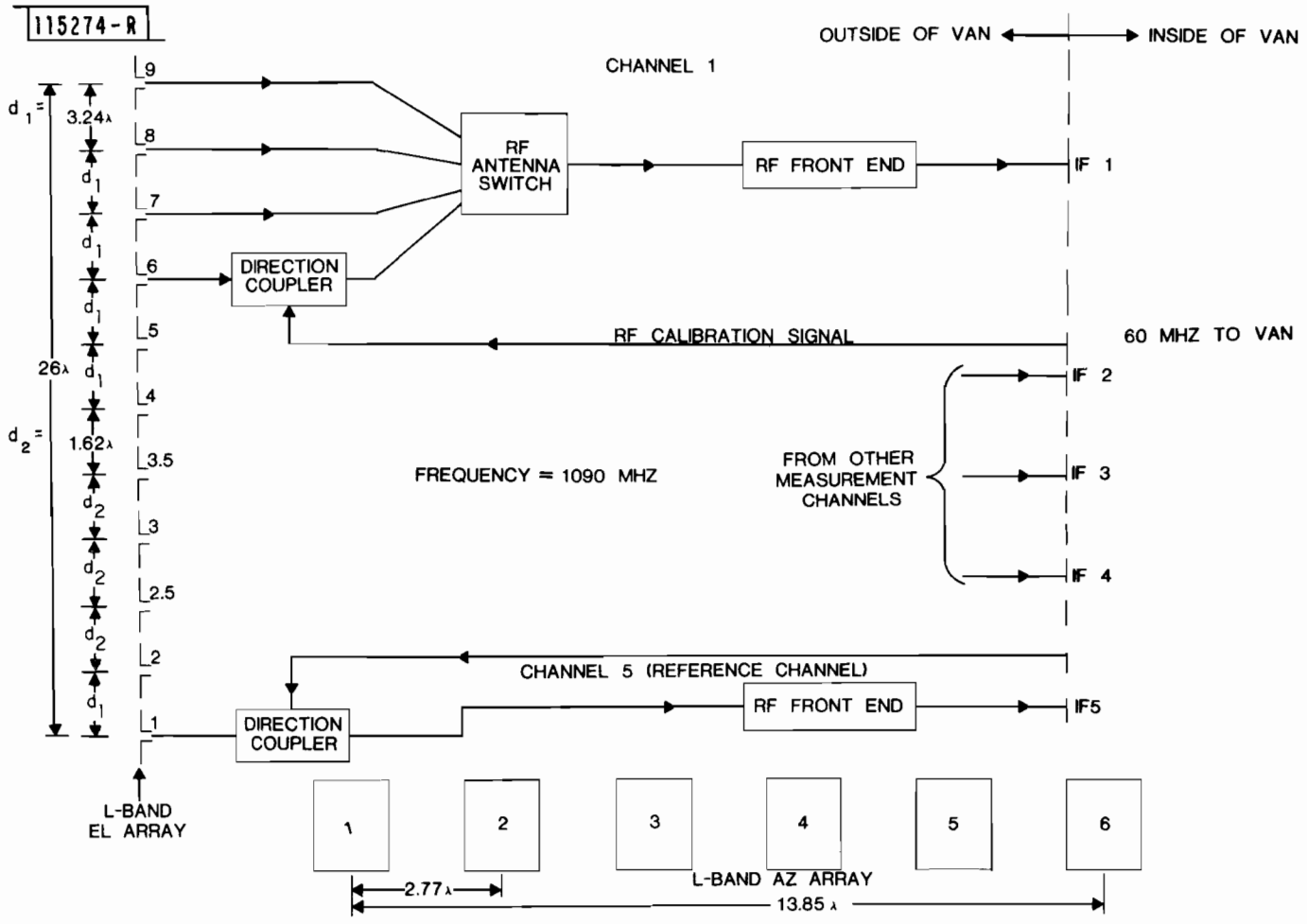

Fig. 2-3a. Block diagram of the L-band subsystem.

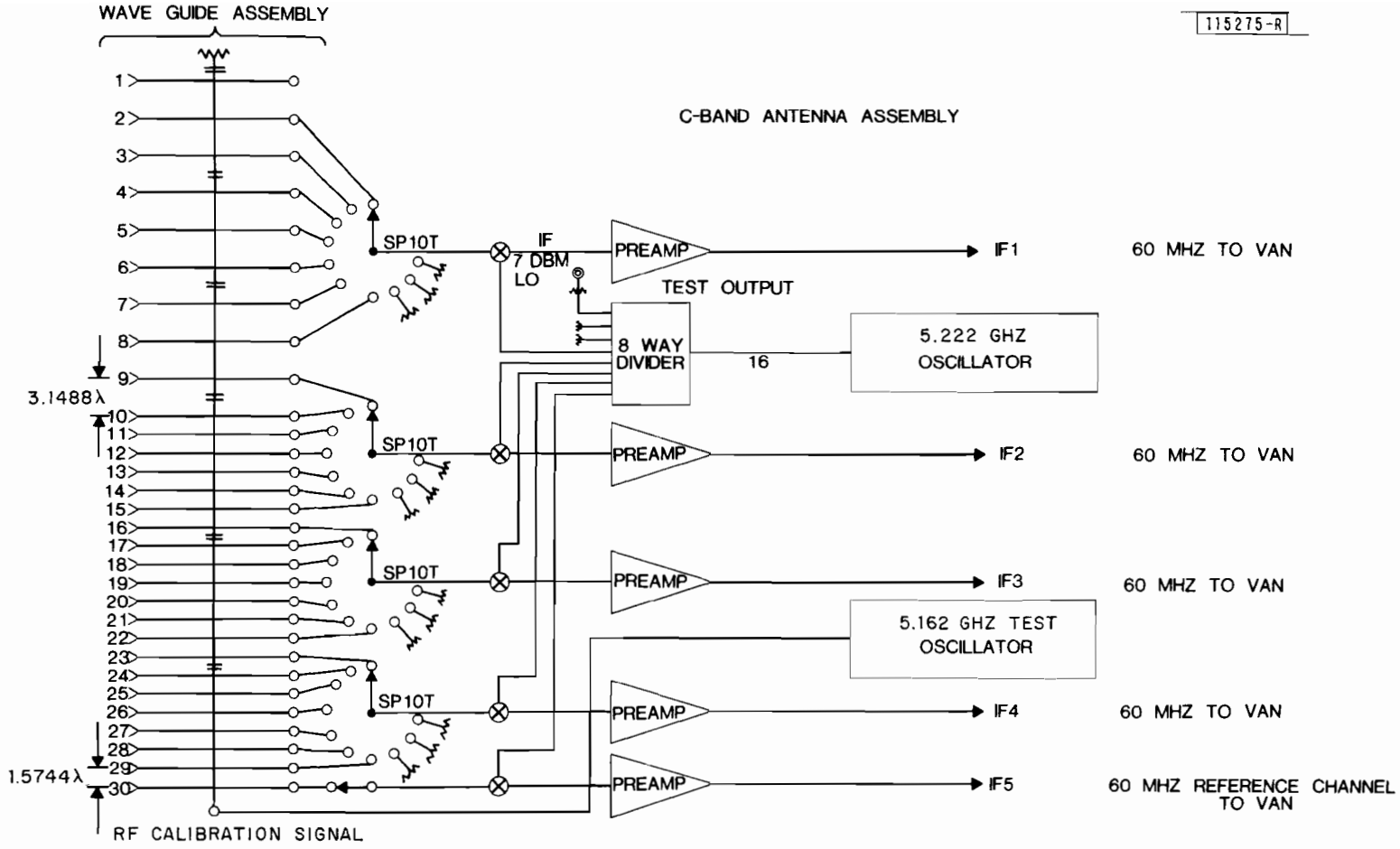

Fig. 2-3b. Block diagram of the C-band subsystem.

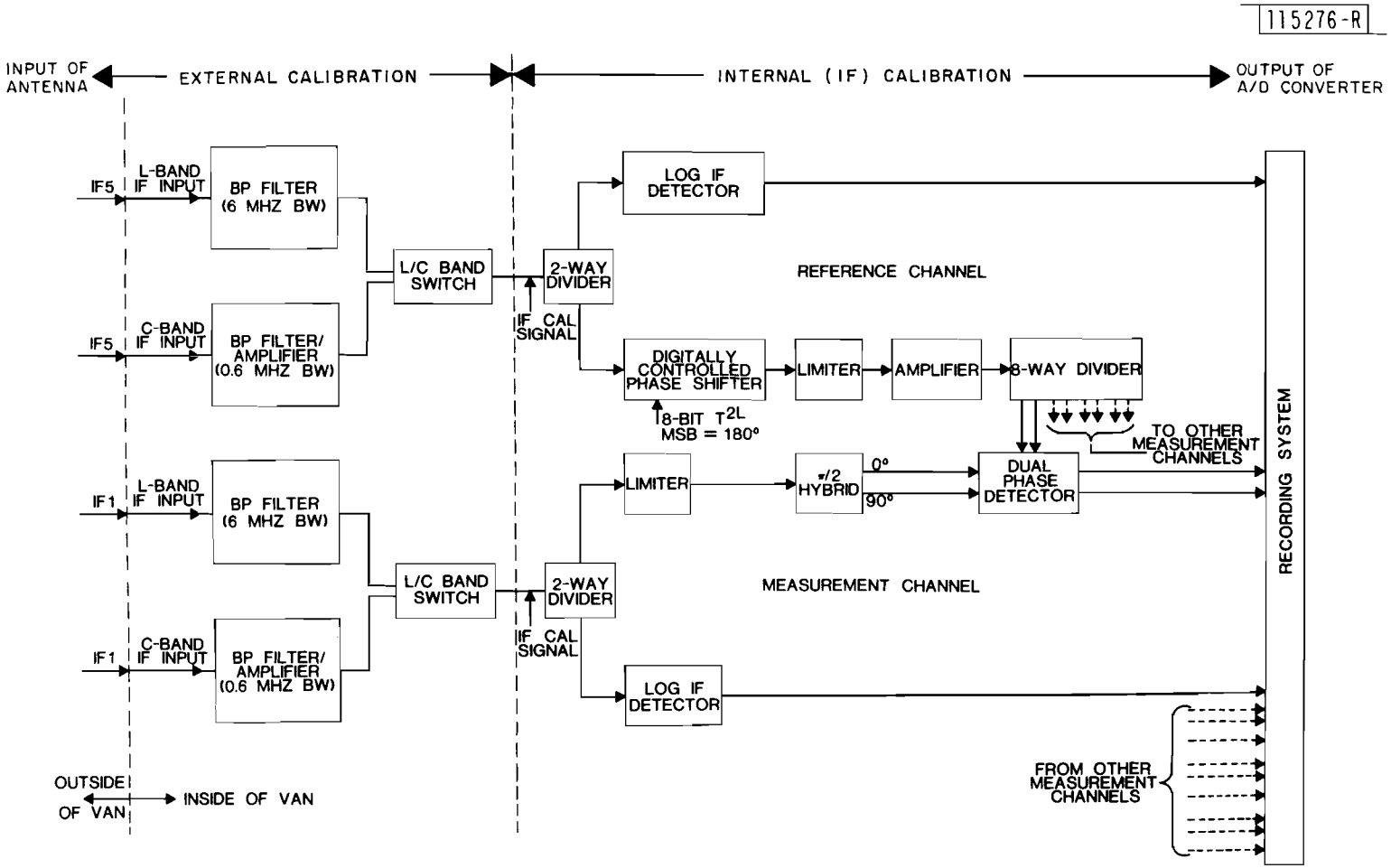

Fig. 2-3c. Block diagram of the IF subsystem.

at 1090 MHz RF frequency. This relocation of the RF front ends was made to improve the channel differential stability among five receiver channels, as was discussed in [6]. Also, now the 5-channel RF receiver had to serve a total of 17 antenna elements (11 EL and 6 AZ antennas), as opposed to 11 EL antennas in the past.

Since 17 antenna elements have to time-share five receiver channels, the recording of the incoming replies at these antenna elements are grouped into four modes: A, B, C and D, as shown in Fig. 2-4. The EL antenna #1 (Fig. 2-3a) is used as the phase reference antenna and is connected to the reference receiver channel #5 all the time. Thus the remaining 16 antenna elements are time multiplexed into the receiver channels #1 to #4, as indicated in Fig. 2-4. This time multiplexing was accomplished with a single pole four throw (SP4T) RF switch in each receiver channel, as indicated in Fig. 2-4. In the normal measurement mode, measurements of the incoming signal are made on successive ATC transponder replies in the order ABCD ABCD AB. Since the ATC transponder replies are normally 0.1 second apart (10 Hz interrogation rate), the time required to measure on all four modes to yield the received signal at all antenna elements is 0.4 second. To ensure that the change in the terrain multipath could be ignored during this 0.4 second interval, the measurements were made with the helicopter either doing vertical descent/ascent at a very slow rate (typically 2-3 feet per second) or hovering at desired waypoints along a given vertical flight path.

2. C-band Subsystem

Referring to Fig. 2-3 (b,c), the C-band subsystem covers the system path from the C-band antenna element down to the C-band IF BP filter. This subsystem was built for these measurements using some new components as well as some used components from the 12 foot ITT Gilfillan C-band elevation array developed for the FAA MLS Phase II field tests.

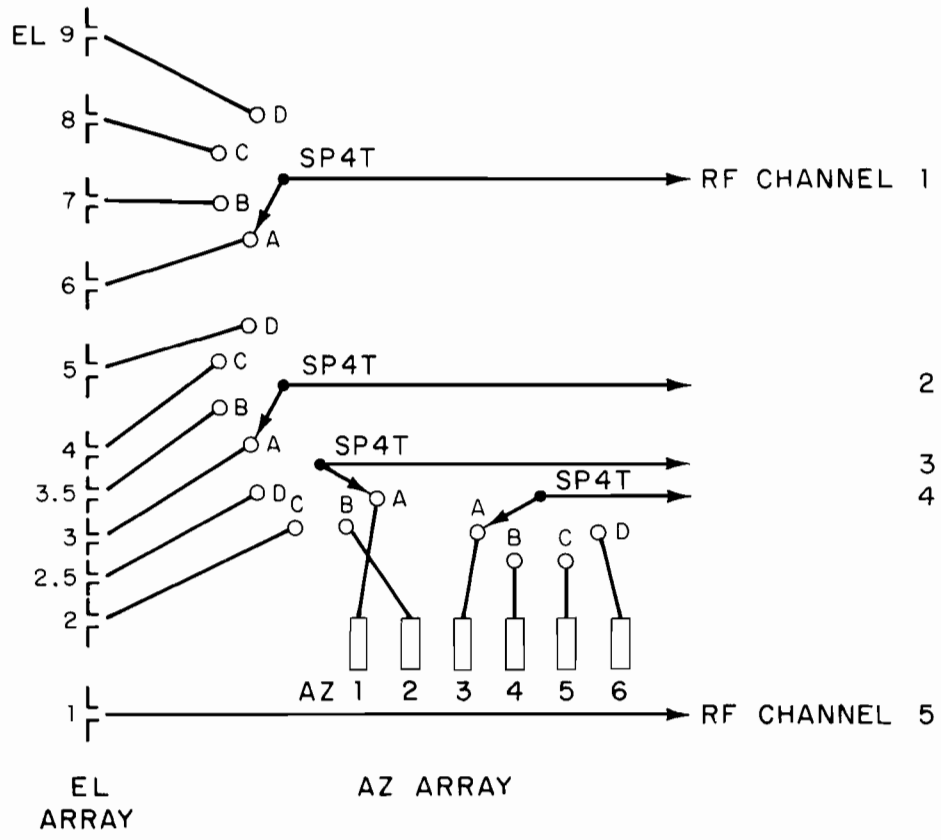

110921-N

ANTENNA SWITCHING MATRIX

b \ a / c	A	B	C	D
1	EL 6	EL 7	EL 8	EL 9
2	EL 3	EL 3.5	EL 4	EL 5
3	AZ 1	AZ 2	EL 2	EL 2.5
4	AZ 3	AZ 4	AZ 5	AZ 6
5	EL 1	EL 1	EL 1	EL 1

a : RECORDING MODE
b : ANTENNA NUMBER
c : RF CHANNEL NUMBER

Fig. 2-4. Relation of antenna elements to the RF receiving channels: L-band elevation and azimuth arrays.

The elevation receiving array, as shown in Fig. 2-5*, consists of 30 antenna elements with two different element spacings. The elements in the upper half of the array have 3.15 λ spacing (distance between the centers of two adjacaent elements) and those in the lower half of the array have 1.57 λ spacing. In the actual C-band measurement, only the lower 29 elements are used.** This yields the usable array aperture of 56.7 λ. The results reported here were obtained from four different array configurations consisting of 19, 21, 14 and 10 equally spaced elements, respectively, as indicated in Fig. 2-6. The 19-element array (56.7 λ aperture and 1° beamwidth) was used in angular power spectral estimation for multipath environment characterization. The 21-element array (2° beamwidth), 14-element array (3° beamwidth), and 10-element array (4° beamwidth), together with the 19-element array, were used in the helicopter elevation angle estimation performance comparison among various array aperture sizes.

The individual antenna element consists of an E-plane sectoral horn and a twisted waveguide section with the coaxial feed at the far end of the waveguide section, as sketched in Fig. 2-7. This twisted waveguide section was necessitated by the desired broad-wall to broad-wall waveguide coupling for the RF test signal injection for the RF calibration as will be discussed in the next section. This E-plane sectoral horn has the following radiation characteristics: 12 dB directivity, 32° E-plane 3-dB beamwidth and 72° H-plane 3-dB beamwidth. The VSWR (with respect to the 50-Ω line) for the individual horn assembly is less than 1.2:1.

As in the L-band subsystem, the 5-channel receiver RF front ends were installed together with the C-band antenna array outside of the electronic van. However, as can be seen in the photos (Figs. 1-1 and 2-5), the antenna

---

*In this picture, the array radome was removed to show the actual antenna elements.

**The use of only 29 elements (instead of available 30) is to make each of the four RF front ends shared by the same number (7) of antenna elements, with the bottom element (designated as antenna #30 in Fig. 2-3b) used as phase reference antenna which is connected to the reference receiver channel.

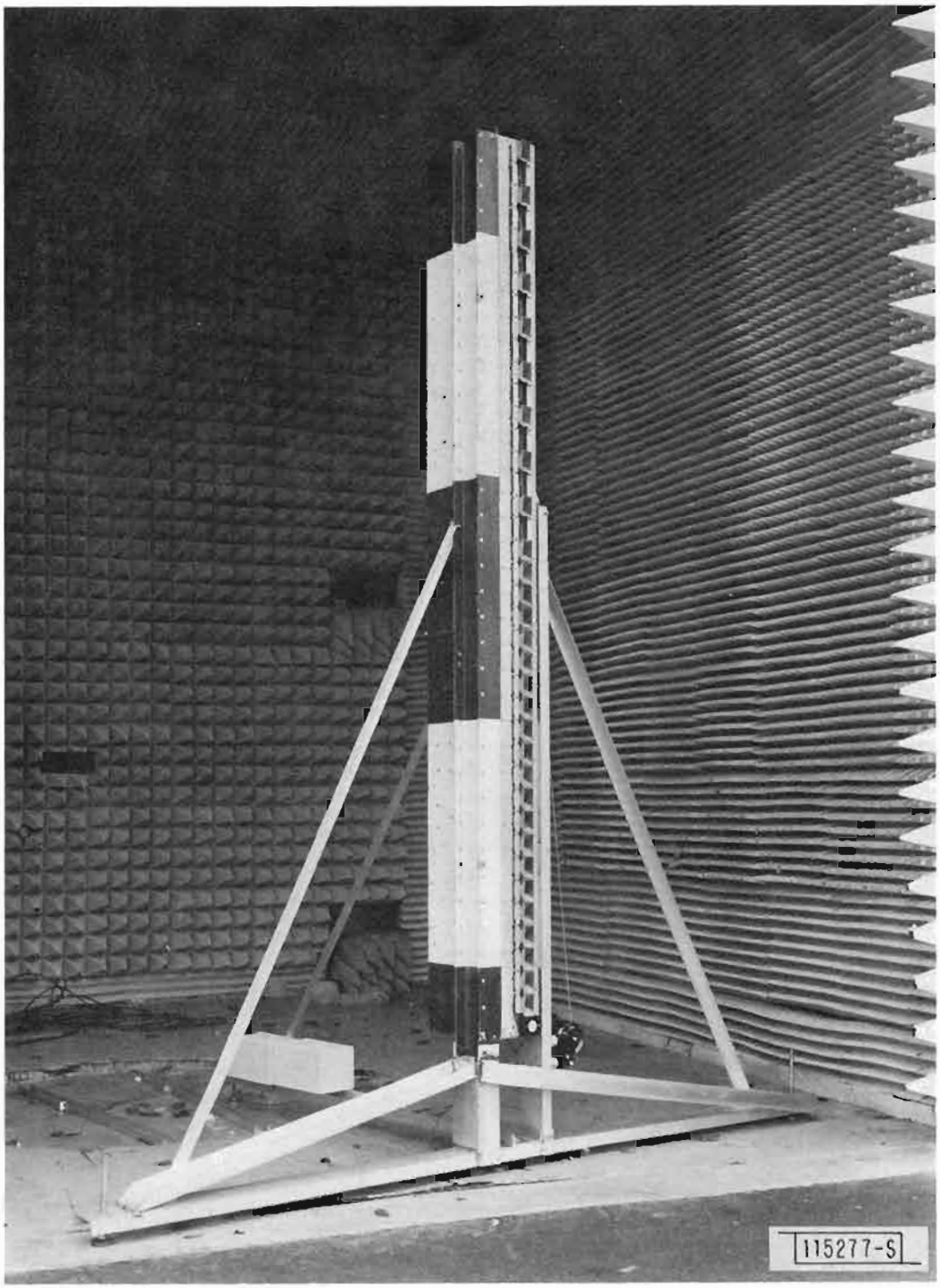

Fig. 2-5. The C-band elevation receiving array.

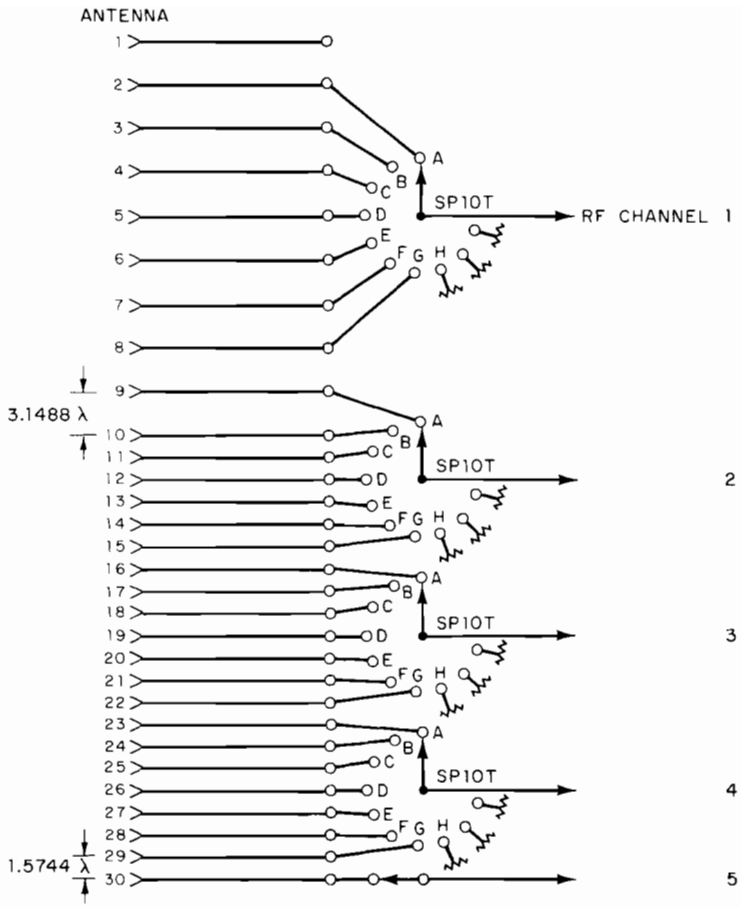

ANTENNA SWITCHING MATRIX

b / a / c	A	B	C	D	E	F	G	H
1	2	3	4	5	6	7	8	*
2	9	10	11	12	13	14	15	*
3	16	17	18	19	20	21	22	*
4	23	24	25	26	27	28	29	*
5	30	30	30	30	30	30	30	30

a : RECORDING MODE
b : ANTENNA NUMBER
c : RF CHANNEL NUMBER

ARRAY CONFIGURATIONS USED :

(1) 19-ELEMENT ARRAY : ANTENNAS 2-10, 12, 14, 16, 18, 20, 22, 24, 26, 28, 30
(2) 21-ELEMENT ARRAY : ANTENNAS 10-30
(3) 14-ELEMENT ARRAY : ANTENNAS 17-30
(4) 10-ELEMENT ARRAY : ANTENNAS 21-30

Fig. 2-6. Relation of antenna elements to the RF receiving channels: C-band elevation array.

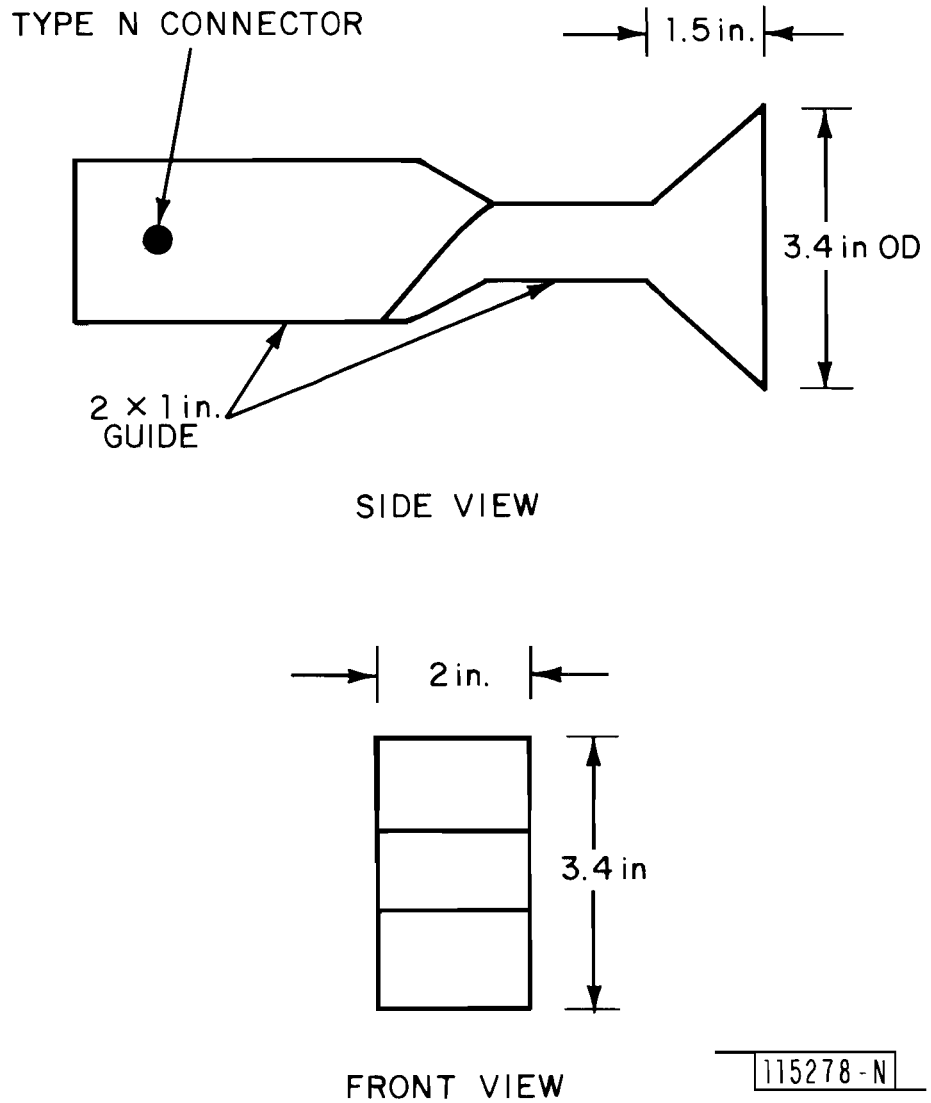

Fig. 2-7. Design dimensions for the C-band E-plane sectoral horn.

elements, the five RF front ends and other RF components (such as LO source, RF test signal source) are all contained in the same antenna array housing; as opposed to the situation in the L-band subsystem where each RF front end was individually packaged in a RF box due to the large physical size of the L-band antenna arrays. Thus, the received signal fed back to the van was at 60 MHz IF frequency, as for L-band. This arrangement of the C-band RF front ends was expected to yield better tracking among five receiver channels, as discussed in [6].

For the C-band receiver, the five RF front ends are shared by the 29 antenna elements. A SP10T* RF switch installed in each receiver channel (Fig. 2-3b) serves this time multiplexing purpose. Thus the recordings of the received signal at 29 antenna elements are grouped into eight modes: A, B, C, D, E, F, G, and H, as shown in Fig. 2-6. The antenna #30 is used as the phase reference antenna and is connected to the reference receiver channel #5 all the time. The remaining 28 antennas (#2 to #29) are time multiplexed into the receiver channels #1 to #4, as indicated in Fig. 2-6. In the normal measurement mode, recordings of the incoming signal are made in the sequence of ABCDEFGHAB at 10 Hz rate. Thus the time required to measure on all seven modes (H mode is a dummy recording mode) to collect the received signal at all 29 antennas is 0.7 second. So again, as in the L-band measurement, to ensure the negligible change in the multipath environment for this 0.7 second duration, the measurements were made with hovering or very slow descent/ascent flight paths.

---

*These SP10T RF switches were the used components from the ITT Gilfillan C-band elevation array. We only used the eight switch positions out of ten. Although each switch only has to serve 7 antenna elements (except in the reference received channel where only one reference antenna was connected to the switch), eight switch positions were used for the ease of binary counting in switch matrix logic. So, the eighth switch position was just terminated with a 50-Ω load.

3. IF Subsystem

This subsystem consists of 5-channel receiver IF for the signal amplitude and phase detections, system timing and control (STC), and the analog-to-digital (A/D) interface which includes a sample/hold circuit, a channel multiplexer and an A/D converter. Since this subsystem is essentially identical to the original PALM equipment (except the A/D converter and some minor modifications which we will discuss here), please see the reference [3] for the equipment/component description.

The new A/D converter is an 8-bit 20 MHz TRW TDC-1007J A/D converter. This 8-bit A/D converter gave us better amplitude and phase quantization than the 7-bit A/D converter we used to have. For the L-band and the C-band subsystems to share the same IF subsystem, a SP2T switch was installed at the input of each of the five IF receiver channels, as indicated by the L/C band switch in Fig. 2-3c. These L/C band switches are manually but synchronously controlled through a single toggle switch on the IF receiver front panel.

4. Calibration Subsystem

The components involved in the system calibration, such as the digital phase shifter and attenuator, test signal generator, etc., are mostly the original PALM equipment. However, the calibration network was slightly changed. The calibration test signals are injected both at the inputs of the IF receiver channels (IF calibration) and the RF front ends (RF calibration), as shown in Fig. 2-3. The IF calibration can be obtained with either CW source or the pulses from the ATC transponder (down mixed to 60 MHz IF), and is done in full dynamic range (0 to -80 dB for amplitude and 0° to 360° for phase). Also the IF calibration process has been automated. The RF calibration for the C-band subsystem is done with the CW test signal generated inside the C-band array housing, while that for the L-band subsystem can be done with either the CW test signal or the ATC transponder pulses generated inside the electronic van. The RF calibration is done only at one signal level.

5. Computer Subsystem

This subsystem serves the following purposes in a measurement mission: (1) monitoring the equipment calibration to see if the measurement system was functioning normally, (2) recording the measured data on its magnetic disks, and (3) performing the on-site processing of the measured data right after each measurement to see if the measurement was properly made. The computer is a Data General Eclipse S/200, operating with a 10-megabyte disk drive. The communication between the computer subsystem and the rest of the measurement system is one way from the IF subsystem to the computer subsystem and occurs only during the data recording which is controlled by the STC recording command.

B. System Calibration

We divide the system calibration into two parts, the internal (IF) calibration and the external calibration as indicated in Fig. 2-3. The IF calibration calibrates the system path from the output of the L/C-band switch down to the output of the A/D converter. This path is entirely inside our equipment van and mainly consists of the IF log-video and phase detectors, the channel multiplexer and the A/D converter. The external calibration (for either L or C band) calibrates the path from the input of the antenna down to the output of the L/C-band switch. This path contains the antenna element, RF cable, RF switch, RF front end, IF cable and a bandpass filter.

1. Internal Calibration

The IF amplitude calibration is accomplished by injecting the IF test signal at the output of the L/C-band switch and recording the A/D converter output of the log-video detector in A/D counts. The test signal is attenuated from 0 to 80 dB in 55 steps with a digital attenuator at the output of the test signal generator. The digital attenuator was calibrated on a network analyzer and the precise attenuation values (to 0.01 dB) for each attenuation setting were stored in a lookup table. Figure 2-8 shows some examples of the IF channel amplitude response curves obtained from the IF amplitude calibrations taken at various times. The IF amplitude calibration gives us

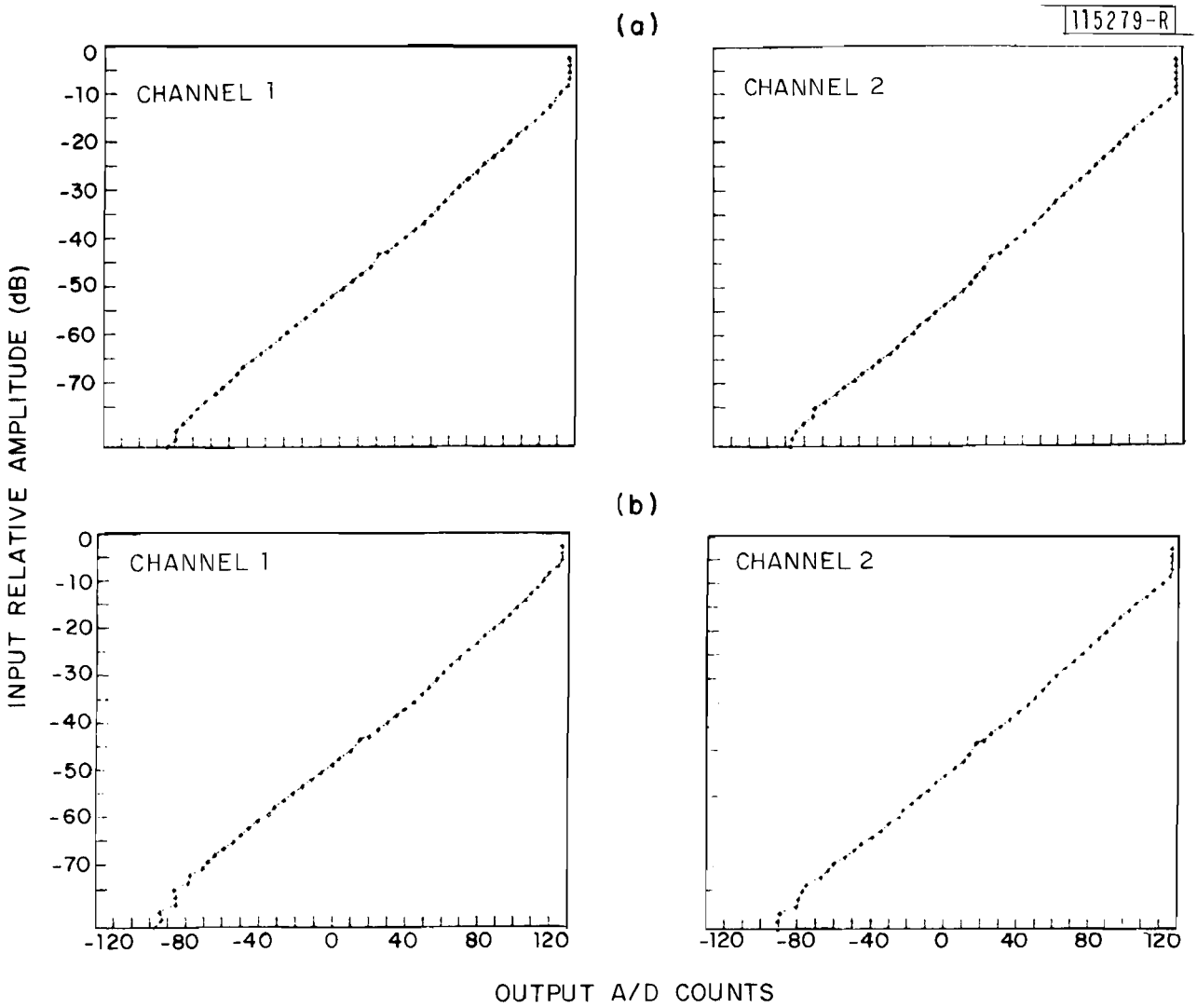

Fig. 2-8. IF channel amplitude response.

amplitude lookup tables to convert the recorded signal amplitude in A/D counts to the IF signal amplitude in dB which is supposed to be free of IF channel amplitude bias. The peak quantization error for the amplitude measurement with our current 8-bit A/D converter is about 0.2 dB.

The IF phase calibration is done by feeding the IF test signal to the output of the L/C-band switch and recording the phase detector output in A/D counts in terms of the in-phase (I) and the quadrature-phase (Q) components. The channel relative phase is varied from 0° to 360° in 32 steps, by means of a digital phase shifter in the reference IF channel. In the IF phase calibration, channel #5 was used as a phase reference channel. The digital phase shifter was calibrated on a network analyzer and precise phase values (to 0.05°) for each digital phase setting were stored in a lookup table. Examples of the IF channel phase response curves, together with the measured I and Q values, are shown in Fig. 2-9. The saturation as appeared in Fig. 2-9 on both I and Q curves was intentional in the design to obtain higher A/D quantization accuracy with the same 8-bit A/D converter, since we use both I and Q for phase detection. The IF phase calibration gives us phase lookup tables to convert the recorded phase in terms of I and Q values in A/D counts to the relative phase in degrees. The peak phase quantization error is about 0.3°.

For a given field measurement mission, which normally lasted from 4 to 6 hours, we made at least two IF calibrations, premission and postmission, to see how stable our IF receiver is for the short term. As can be seen in Figs. 2-8 and 2-9 both amplitude and phase responses remain very much the same between the premission and postmission calibrations. We found that our IF receiver channels were very stable during any measurement mission; although sometimes we did notice the drift in the IF channel responses among various missions taken at different dates. This between-mission variation might be due to the component misalignment caused by the vibration during the transportation of our equipment van or due to temperature differences among various missions.

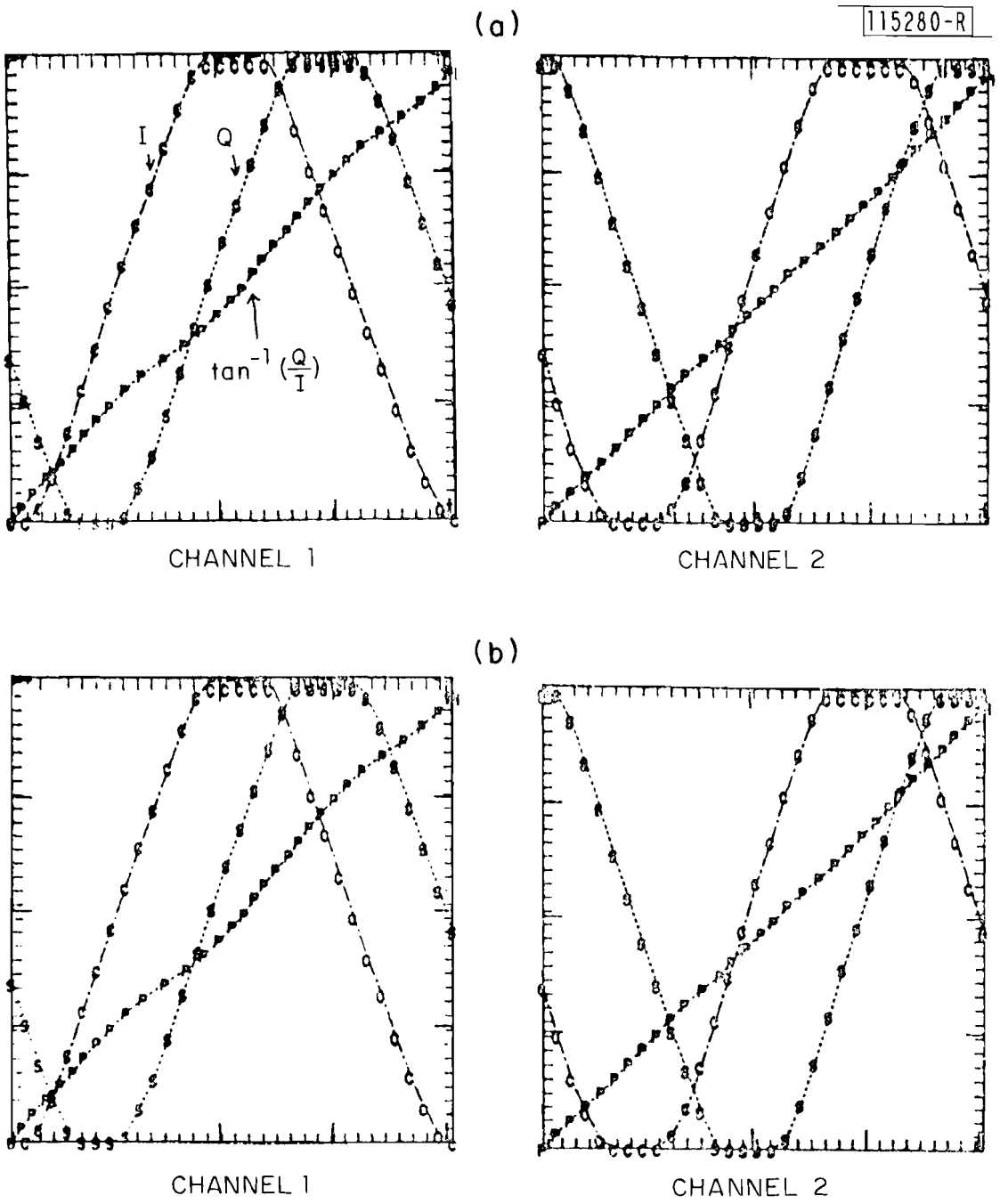

Fig. 2-9. External calibration by array collimation at antenna test range.

2. External Calibration

Now to calibrate the system from the input to the antenna down to the output of L/C-band switch, i.e., the external calibration, we made an array collimation at the Lincoln Laboratory antenna test range as shown in Fig. 2-10. The antenna test range was graded to a flatness of better than ±1" over a 200-foot by 2000-foot area. The measured cross-range field strength variation* at the receiving end was well below 0.5 dB for either our L-band or C-band arrays. At the antenna test range, our antenna array (either L-band or C-band) was arranged in such a way that we could use a common far field source to uniformly illuminate the entire array with a single plane wave at normal incidence. Thus, we knew that the amplitudes and phases of the incoming plane wave at all antenna elements are the same. So, any differences in the measured amplitude and phase values among antenna/receiver channels would be the amplitude and phase biases from various antenna/receiver channels. Hence, the external calibration with the array collimation at the antenna test range gives us a phase and amplitude lookup table to remove the antenna/receiver channel phase and amplitude biases from the field measurement data.

The external calibration by array collimation at the antenna test range eliminates the phase and amplitude biases; however this cannot be done at the field measurement sites. The compromise we made is to accomplish an external calibration by array collimation at the antenna test range in several different times of year, e.g., summer, fall and winter and apply appropriate external calibration data to process various field measurement data taken at different times of year. To compensate for any drift in the external calibration part of the system due to temperature and humidity changes or some other reasons, we take the so-called RF calibration, as indicated in Fig. 2-3, when we do the external calibration by array collimation at the antenna test range and when we take field data at any given measurement mission.

---

*For L-band, the transmitting source was an 8-foot dish at 30-foot height and our L-band elevation array (30-foot long) was laid horizontally at 2-foot height. For C-band, the transmitting source was a 6 foot dish at 10-foot height and our C-band array (12-foot long) was laid horizontally at 4-foot height.

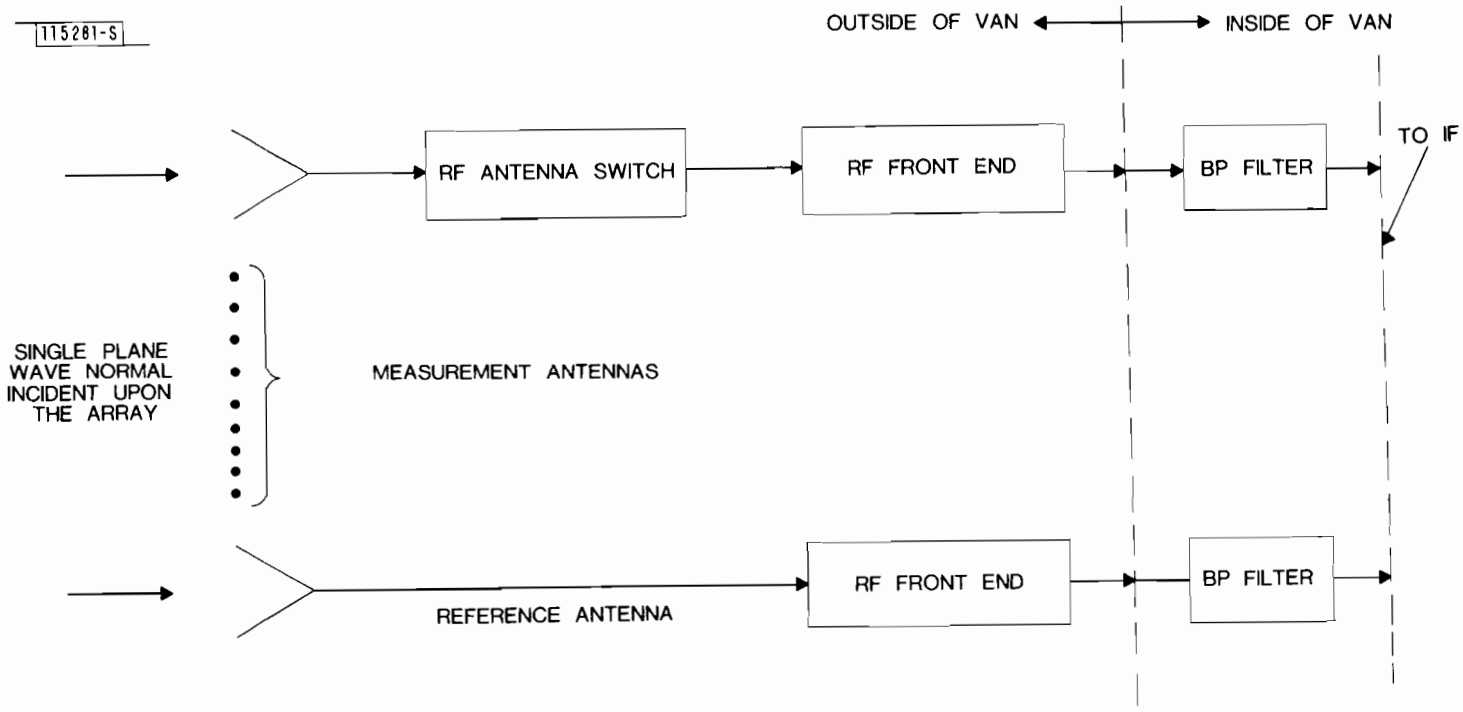

Fig. 2-10. Far field calibration/array collimation at antenna test range.

As shown in Fig. 2-3, the RF calibration is accomplished by injecting the RF test signal right behind the antenna element and recording the measured phase and amplitude for each antenna/receiver channel. In our current system, the C-band RF test signal is injected behind each of the twenty-nine horn antennas by a 40 dB slotted waveguide directional coupler through a common waveguide, as shown in Fig. 2-11. The directivity of the coupler is better than 20 dB. With this 20 dB directivity plus the minimum of 40 dB isolation between two neighboring horns, the injected test signal would be mainly coupled back toward the output of the RF front end for the desired RF calibration.

The L-band RF test signal is injected through a coaxial directional coupler to only one of the four antenna channels in the same RF front end. The choice of one antenna channel over all four antenna channels for the RF test signal injection is based on the following reasons:

(1) It is much simpler to build the RF test signal distribution for one antenna channel than for the four antenna channels (one 5-way power divider, 5 10-foot RF cables and 5 directional couplers versus one 17-way power divider, 17 15-foot RF cables and 17 directional couplers). So, the temperature tracking among the test signal paths should be better for the one antenna channel case.

(2) Since the short RF cables in four antenna channels which share the same RF front end are of equal length and very temperature stable, RF calibration for one antenna channel should suffice for the other three antenna channels using the same RF front end.

By comparing the RF calibration values taken at any given measurement mission with those taken during the external calibration (by array collimation) at the antenna test range, drifts in the channel phase and amplitude biases obtained from the external calibration can be properly accounted for.

Table 2-1 shows two sets of external calibration values taken about six hours apart for our C-band elevation antenna system which has a total of 29 antenna/receiver channels. Also shown in this table is the corresponding RF calibration values. Table 2-2 gives the similar results for the L-band anten-

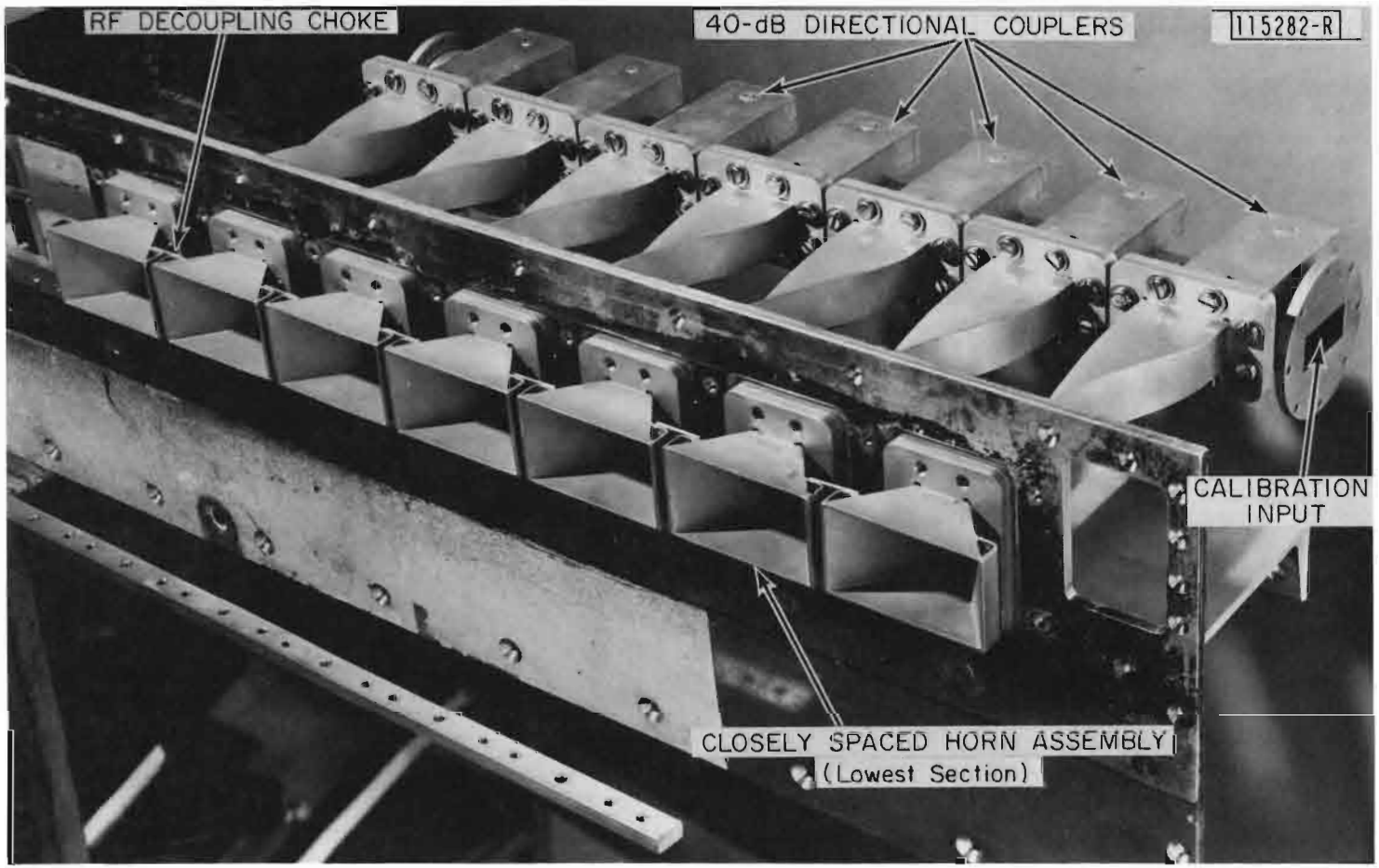

Fig. 2-11. Coupling arrangement of C-band RF test signal.

TABLE 2-1

EXTERNAL AND RF CALIBRATION VALUES: C-BAND ANTENNA SYSTEM

DATE: 8/15/80

(a) External calibration values AMP1/AMPR and PH1/PHR: relative amplitude and phase values from two external calibrations taken six hours apart

ANT.	AMP1	AMPR	AMP1-AMPR	PH1	PHR	PH1-PHR
2	-0.15	-0.30	0.15	265.54	268.99	-3.45
3	-0.81	-0.98	0.17	226.44	230.37	-3.93
4	-1.83	-2.10	0.27	253.44	256.78	-3.34
5	-1.23	-1.39	0.16	244.71	248.18	-3.41
6	-0.30	-0.30	0.00	245.88	249.30	-3.42
7	-0.81	-0.98	0.17	290.74	293.70	-2.96
8	-0.93	-1.05	0.12	270.76	273.30	-2.54
9	0.04	-0.30	0.34	277.72	279.53	-1.81
10	-0.63	-0.84	0.21	297.13	298.71	-1.58
11	0.04	-0.27	0.31	286.47	288.13	-1.66
12	0.42	-0.03	0.45	291.45	292.99	-1.54
13	1.57	1.23	0.34	304.71	305.73	-1.02
14	0.42	0.12	0.30	282.07	283.66	-1.59
15	-0.84	-0.93	0.09	263.57	265.34	-1.77
16	1.83	1.23	0.60	274.56	275.36	-0.80
17	1.27	0.90	0.37	301.51	302.47	-0.96
18	0.93	0.51	0.32	297.44	298.09	-0.65
19	0.38	0.00	0.38	312.13	312.95	-0.82
20	0.80	0.51	0.28	300.56	300.97	-0.41
21	0.83	0.48	0.35	325.81	325.98	-0.17
22	0.83	0.51	0.32	305.09	305.64	-0.55
23	3.03	2.82	0.21	272.40	273.77	-1.37
24	2.82	2.76	0.06	276.88	278.42	-1.54
25	1.83	1.56	0.27	255.45	257.52	-2.07
26	1.50	1.26	0.24	263.74	265.39	-1.65
27	2.49	2.55	-0.06	283.80	285.62	-1.82
28	2.06	1.89	0.17	289.29	290.59	-1.30
29	1.17	0.90	0.27	236.66	238.11	-1.45
30	0.0	0.0	0.0	0.00	0.00	0.00

(b) RF calibration values AMP1/AMPR and PH1/PHR: relative amplitude and phase values from two RF calibrations taken six hours apart

ANT.	AMP1	AMPR	AMP1-AMPR	PH1	PHR	PH1-PHR
2	0.71	0.04	0.67	261.83	263.60	-1.77
3	-0.53	-1.21	0.68	41.80	44.38	-2.44
4	-2.22	-2.74	0.52	242.96	245.12	-2.16
5	-0.98	-1.59	0.66	49.55	52.12	-2.57
6	0.26	-0.27	0.53	224.73	227.12	-2.39
7	-1.13	-1.93	0.80	94.96	96.48	-1.52
8	-1.10	-1.87	0.77	252.49	254.56	-2.07
9	1.36	0.50	0.86	79.82	81.98	-2.15
10	0.34	-0.35	0.69	278.84	280.83	-1.99
11	-0.38	-1.10	0.72	354.99	357.21	-2.22
12	0.34	-0.42	0.76	92.20	93.72	-1.52
13	1.44	0.58	0.86	195.26	197.10	-1.84
14	-0.15	-1.02	0.87	264.46	266.12	-1.66
15	-1.04	-1.96	0.92	332.66	334.79	-2.13
16	1.32	0.62	0.70	74.06	74.05	0.01
17	0.61	-0.19	0.80	193.28	193.48	-0.18
18	0.55	-0.19	0.74	278.83	280.28	-1.45
19	-0.66	-1.59	0.92	19.85	21.58	-1.73
20	0.79	0.12	0.67	102.34	102.30	0.04
21	0.91	0.19	0.71	218.42	217.29	1.13
22	0.79	0.00	0.79	284.80	284.87	-0.07
23	2.69	2.29	0.40	336.94	339.22	-2.28
24	2.89	2.24	0.65	80.23	82.84	-2.60
25	2.69	2.24	0.45	150.36	152.81	-2.45
26	1.48	0.85	0.62	248.14	251.41	-3.27
27	2.64	2.19	0.45	356.08	358.00	-1.92
28	2.21	1.44	0.77	96.26	98.43	-2.17
29	1.24	0.47	0.78	131.69	134.04	-2.35
30	0.0	0.0	0.0	0.00	0.00	0.00

TABLE 2-2

EXTERNAL AND RF CALIBRATION VALUES: L-BAND ANTENNA SYSTEM
DATE: 7/23/80

(a) External calibration values AMP1/AMPR and PH1/PHR: relative amplitude and phase values from two external calibrations taken six hours apart

	ANT.	AMP1	AMPR	AMP1-AMPR	PH1	PHR	PH1-PHR
elevation array	9	-3.24	-3.86	0.68	301.61	301.76	-0.15
	8	-3.21	-3.64	0.43	306.80	307.46	-0.66
	7	-3.09	-3.71	0.62	340.10	341.26	-1.16
	6	-1.89	-2.38	0.49	358.31	359.43	-1.12
	5	0.10	-0.37	0.47	838.03	840.75	-2.72
	4	-0.23	-0.61	0.37	192.92	194.61	-1.69
	3.5	-0.96	-1.18	0.22	812.02	813.30	-1.28
	3	0.59	0.19	0.41	345.09	348.23	-3.14
	2.5	-1.41	-1.56	0.16	145.68	147.79	-2.11
	2	-1.08	-1.39	0.31	283.19	285.07	-1.88
	1	0.00	0.00	0.00	0.00	0.00	0.00
azimuth array	6	-13.24	-13.50	0.25	78.86	80.78	-7.92
	5	-13.28	-14.18	0.90	121.32	129.84	-8.52
	4	-12.33	-12.37	0.04	226.78	833.91	-7.13
	3	-16.49	-17.04	0.54	305.08	317.18	-12.10
	2	-10.27	-10.67	0.40	11.03	18.62	-7.59
	1	-11.41	-11.97	0.55	273.99	881.55	-7.56

(b) RF calibration values AMP1/AMPR and PH1/PHR: relative amplitude and phase values from two RF calibrations taken six hours apart

	ANT.	AMP1	AMPR	AMP1-AMPR	PH1	PHR	PH1-PHR
elevation array	9	-2.89	-4.05	1.16	313.37	313.30	0.07
	8	-2.89	-4.05	1.16	313.37	313.30	0.07
	7	-2.89	-4.05	1.16	313.37	313.30	0.07
	6	-2.89	-4.05	1.16	313.37	313.30	0.07
	5	-0.38	-1.50	1.13	268.24	271.90	-3.66
	4	-0.38	-1.50	1.13	268.24	271.90	-3.66
	3.5	-0.38	-1.50	1.13	268.24	271.90	-3.66
	3	-0.38	-1.50	1.13	268.24	271.90	-3.66
	2.5	-1.50	-3.19	1.69	810.81	813.00	-2.19
	2	-1.50	-3.19	1.69	210.81	213.00	-2.19
	1	0.00	0.00	0.00	0.00	0.00	0.00
azimuth array	6	-9.65	-10.93	1.28	116.01	125.28	-9.27
	5	-9.65	-10.93	1.28	116.01	125.28	-9.27
	4	-9.65	-10.93	1.28	116.01	125.28	-9.27
	3	-9.65	-10.93	1.28	116.01	125.28	-9.27
	2	-8.99	-10.46	1.47	303.50	305.75	-2.25
	1	-8.99	-10.46	1.47	303.50	305.75	-2.25

na system which has 11 elevation and 6 azimuth antenna/receiver channels. From examining the external array collimation data and the corresponding RF calibration data obtained during the past year, we found that both our C-band and L-band elevation antenna systems had been fairly stable in the short term (4-6 hours), while the L-band azimuth antenna system showed notable drift in the channel phase bias which often could not be explained by the corresponding RF calibration value. This larger channel phase bias variation obvserved in the L-band azimuth array channels probably is due to the type of antenna element we used in the L-band azimuth array. Contrary to the simple horn antenna used in the C-band elevation antenna system and the conventional dipole antenna used in the L-band elevation antenna system, the L-band azimuth antenna is a printed circuit type of dipole array whose more complicated feed structure apparently makes it more sensitive to temperature and humidity changes.

Figure 2-12 describes how various system calibration data are used to obtain the correct signal amplitude and phase at each antenna element, i.e., the measured amplitude and phase values which are free of channel amplitude and phase biases. Judging from the system calibration data we have accumulated and from simulation results for various field measurements with known signal environment, the accuracy in our estimated amplitude and phase at the antenna element is about 1 dB and 3 to 5 degrees, respectively. These errors are believed to be primarily from the drift in the channel amplitude and phase biases which we are unable to account for with our RF calibration procedure and the non-real time nature of our system calibration.

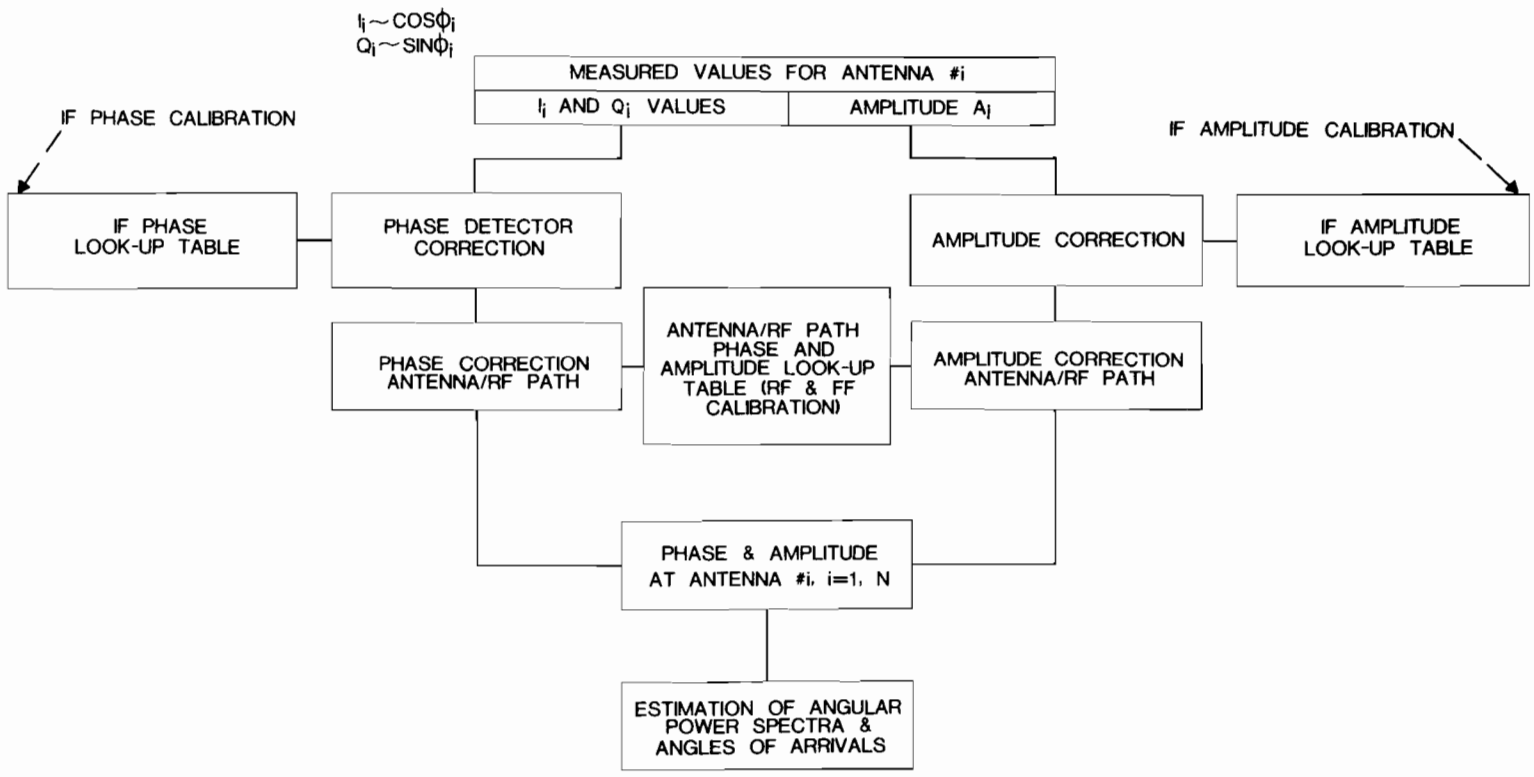

Fig. 2-12. Correction of channel amplitude and phase biases from the measured data.

III. METHODS

A. For Propagation Model Validation

For the validation of terrain multipath propagation models used in the MLS computer simulation program, the comparison between the field measured data and the MLS computer simulation predicted results will be made on the angular power spectra, as we did before [2]. With this approach, in addition to the multipath levels (i.e.,M/D ratios) and/or the angle errors which are conventionally used in the comparison between the field measured and simulated data, several other features in the received signal can be used for comparison, such as the number and the arrival angles of the multipath components.

Here, the angular power spectrum is referred to the distribution of the received signal power for a given helicopter position as a function of the elevation angle (for elevation array) or the azimuth angle (for azimuth array). For the field measurements, this approach involves the estimation of the angular power spectrum from the measured complex signal (i.e., the RF phase and amplitude) at each antenna element of the receiving antenna array. For the MLS simulation results, before the angular power spectrum can be estimated, the complex signal at each antenna element has to be generated first from the output of the MLS multipath simulation model [1,7]. The MLS multipath simulation run uses as its input an appropriate ground model for the terrain involved in the field measurements. Thus, an important part of the validation effort involved the development of ground models based on measurements of the terrain profiles.

In the results presented in the following Chapter V, three angular power spectral estimates, namely, the beamsum (BS), the maximum likelihood (ML), and the maximum entropy (ME), were calculated from both the field measured data and the corresponding MLS multipath simulation runs. They are basically the same spectral estimation methods as those used in our earlier terrain reflection study [2], except that here the "modified" covariance matrix is used in obtaining the ML and ME spectra to yield better resolution of signal arrivals. Since these spectral estimation methods have been widely discussed in the literature [8,9,10] and most recently in another Lincoln report [6],

here we will only very briefly put down the expressions for calculating these spectra and say a few words about how we used them. Also, in this subsection, we will discuss the approach which we took to construct the ground model used in the MLS multipath simulation.

1. Spectral Estimation Methods

Let $P_{BS}(\theta)$, $P_{ML}(\theta)$, and $P_{ME}(\theta)$ be the angular power spectrum estimated from the BS, ML and ME methods, respectively. They can be simply expressed as follows*:

$$P_{BS}(\theta) = \underline{V}^* \underline{\underline{R}}\, \underline{V} \tag{3-1}$$

$$P_{ML}(\theta) = (\underline{V}^* \underline{\underline{R}}^{-1} \underline{V})^{-1} \tag{3-2}$$

$$P_{ME}(\theta) = P_N \Delta / |\underline{V}^* \underline{\Gamma}|^2 \tag{3-3}$$

where the asterisk (*) denotes conjugate transposition.

The column vector $\underline{V}$ represents the steering vector whose i^{th} element is given by

$$V_i = \exp[jkz_i \sin\theta] \tag{3-4}$$

where

$j = \sqrt{-1}$

k = wave number

z_i = distance of i^{th} antenna element from the array origin

θ = elevation or azimuth angle.

---

*It is understood that here we are only dealing with the linear antenna arrays with equally spaced elements. Thus the expression (3-3) for the ME spectrum is only valid for that case.

The square matrix $\underline{\underline{R}}$ is the signal covariance matrix. In our previous report on the terrain multipath [2], $\underline{\underline{R}}$ was estimated by the sample covariance matrix $\hat{\underline{\underline{R}}}$, i.e.,

$$\underline{\underline{R}} \approx \hat{\underline{\underline{R}}} = \underline{S}^{*}\underline{S} \tag{3-5}$$

where the column vector $\underline{S}$ represents the complex sensor outputs from the receiving antenna array, i.e., S_i is the complex signal received at i^{th} antenna element. For the terrain reflection data, it was found that the $P_{ML}(\theta)$ using $\hat{\underline{\underline{R}}}$ would only yield signal resolution similar to $P_{BS}(\theta)$ [2]. Consequently, the $P_{ML}(\theta)$ for the results presented in this report was obtained with the so-called "modified" covariance matrix, $\tilde{\underline{\underline{R}}}$.

$$\underline{\underline{R}} \approx \tilde{\underline{\underline{R}}} = \frac{1}{M} \sum_{m=1}^{M} \hat{\underline{\underline{R}}}_m \tag{3-6}$$

where $\hat{\underline{\underline{R}}}_m$ is the sample covariance matrix for the subarray m in a given antenna array. All subarrays, m=1, M, consist of the same number of antenna elements and two neighboring subarrays have the same antenna elements except the one antenna element at the one end of each subarray (see Fig. 3-1). The $P_{ML}(\theta)$ using $\tilde{\underline{\underline{R}}}$ appears to give much better signal resolution than that using $\hat{\underline{\underline{R}}}$ [6].

In (3-3), Δ is the spacing between two neighboring antenna elements. P_N and $\underline{\Gamma}$ are the solution of the following matrix equation:

$$\underline{\underline{R}}\ \underline{\Gamma} = \underline{P} \tag{3-7}$$

where

$$\underline{\Gamma} = \begin{bmatrix} 1 \\ a_2 \\ \vdots \\ a_N \end{bmatrix} \qquad \underline{P} = \begin{bmatrix} P_N \\ 0 \\ \vdots \\ 0 \end{bmatrix}$$

In our previous report on the terrain multipath [2], the P_N and a_i's were determined directly from the complex antenna outputs, i.e., $\underline{S}$, using the so-called Burg technique [11,12]. The Burg technique for obtaining $P_{ME}(\theta)$ is

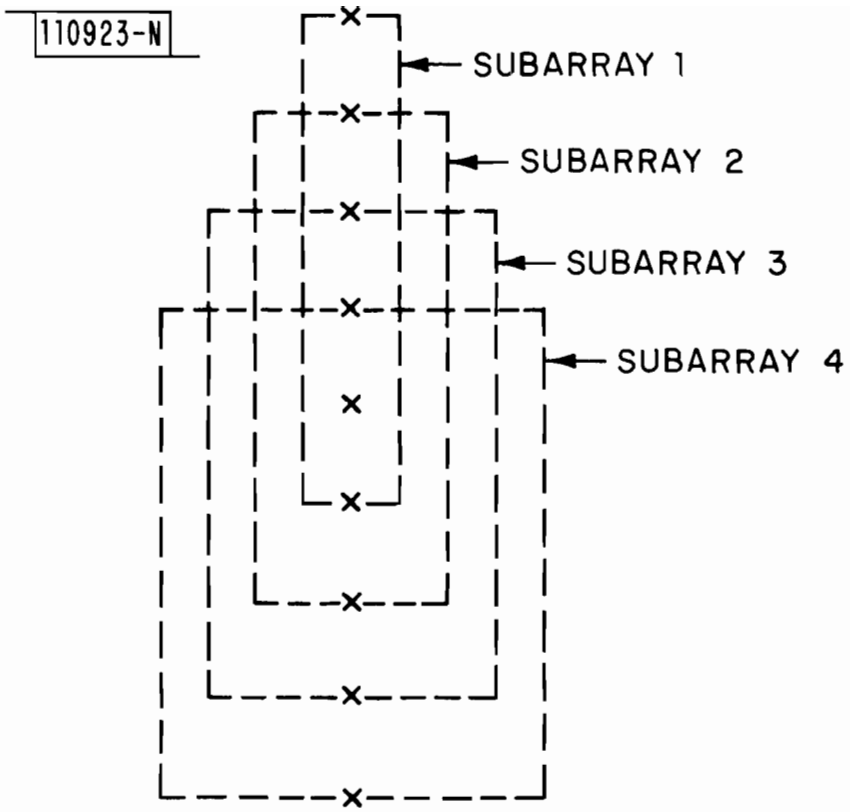

Fig. 3-1 6-element subarrays from a 9-element array.

attractive in terms of its computation efficiency. However, some problems have been observed in the Burg $P_{ME}(\theta)$, such as the spectral peak splitting and the bias in the arrival angle estimation of various signal components [13,14,15]. So, the $P_{ME}(\theta)$ for the results presented in this report was obtained through the so-called modified covariance method [4,6]. The computation efficiency with the modified covariance method is compatible to that with the Burg technique while no peak splitting and angle biasing problems were observed. For detailed discussion, especially the mathematical description, of the modified covariance method, please see the references [4] and [6].

2. Ground model for MLS Computer Simulation

Figure 3-2 shows a terrain height profile for the ground in front of our receiving antenna array at one of our measurement sites. For the MLS multipath simulation run, the ground was modelled as a series of rectangular plates with their along-range slopes coincident with the surveyed terrain height profile and with their cross-range slopes coincident with the surveyed ground cross tilts. As shown in Fig. 3-2, for this particular ground, the terrain height profile was fitted with eight straight line segments with various slopes (indicated as X-Z projection in the figure). The cross tilt of a particular rectangular plate is indicated as Y-Z projection. Taking into account of these various terrain heights and cross tilts, the total number of rectangular plates used to model this particular terrain was ten, as indicated in the top view X-Y projection.

As mentioned earlier, in our previous report on the terrain multipath measurement [2], the terrain at a given measurement site was only surveyed for its along-range height profile. Consequently, the rectangular plates in the ground model were assumed to have no cross tilts and were treated as the tilted building plates in the MLS multipath simulation run. The main reason that we handled the ground plates as tilted building plates was that the focusing ground option of the ground reflection calculation [1] in the MLS multipath simulation was not fully operative then. The validity of treating the ground plates as tilted building plates was discussed then; and the

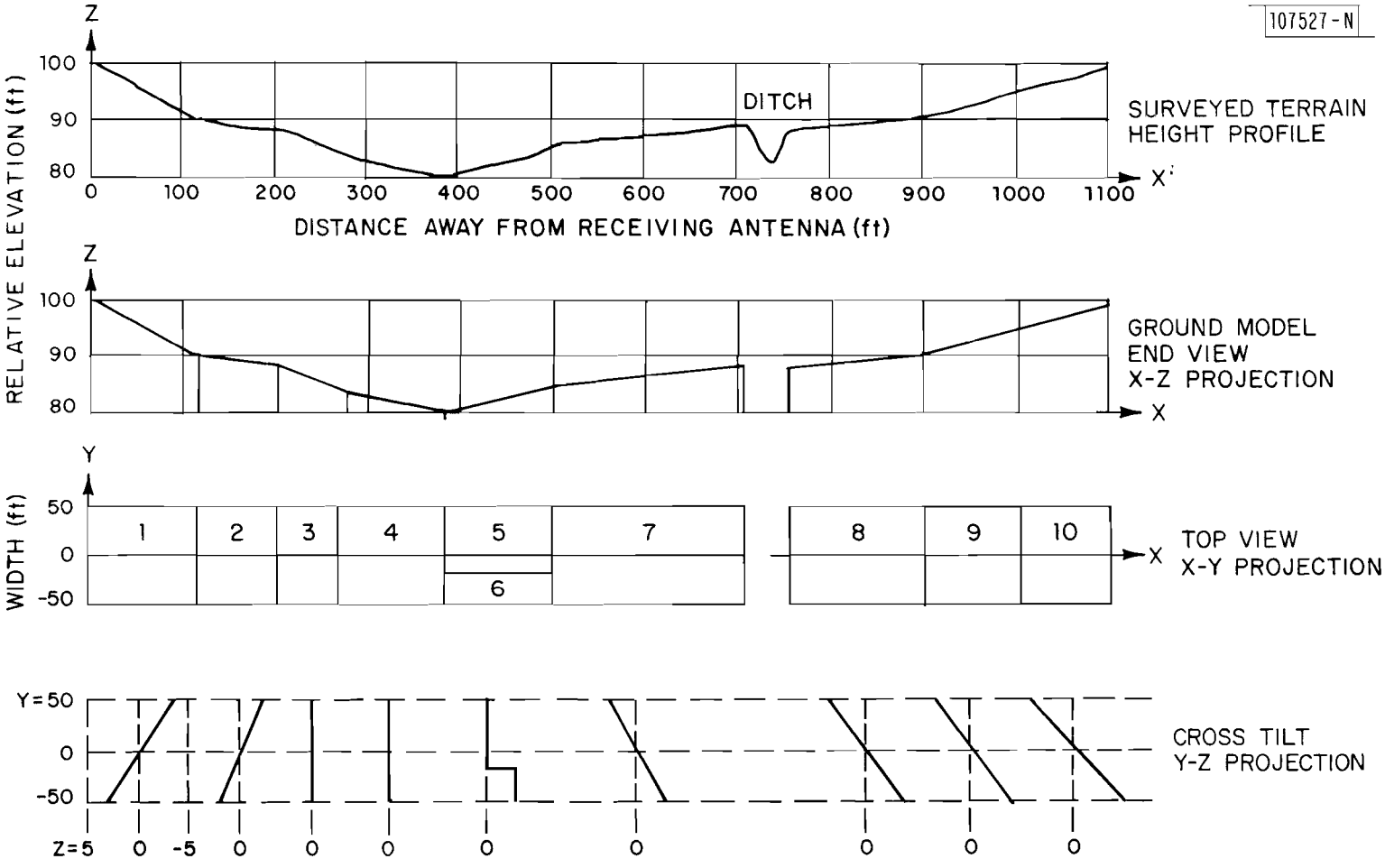

Fig. 3-2. Construction of the ground model from the terrain survey.

favorable comparison between the field measured results and the corresponding MLS simulation results were observed, especially for the measurement sites with no significant terrain cross tilts [2].

Thus, for the measurement sites without obvious terrain cross-range tilts, the MLS simulation results were obtained in two ways: (1) the ground plates were treated as the tilted building plates using building reflection calculation as we did before, and (2) the ground plates were handled as ground plates using the ground reflection calculation with the focusing ground option. However, for the measurement sites with significant terrain cross tilts, only the latter approach was used in obtaining the simulation results.

B. For Elevation Angle Estimation

The results on the elevation angle estimation were primarily for the comparative study of the angle estimation accuracy versus antenna array aperture size. Therefore, our main objective here was not to compare the performances of various elevation angle estimation techniques. Rather, we were interested in the angle estimation accuracy obtainable from antenna arrays of various aperture sizes for a given angle estimation technique in various terrain multipath environments. Thus, the two elevation angle estimators (A and B), which we used in producing the angle estimation results given in Chapter VI, were chosen because of their use in the MLS angle processing. The angle estimator A (θ_A) corresponds to the conventional MLS (TRSB) angle processor. The angle estimator B (θ_B) corresponds to the MLS "single edge" flare processor (SEP) [16].

We implemented both elevation angle estimators based on the beamsum (BS) angular power spectrum of the received signal. The BS spectrum was calculated according to equation (3-1), with a -30 dB sidelobe level based on the Dolph-Tchebyscheff design. The angle estimator A takes the angular position of the largest spectral peak of the received signal BS spectrum in the positive elevation angle as the direct signal angle (i.e., the helicopter elevation angle θ_d). That is,

$$\theta_d \approx \theta_A = \theta_{BS\text{-}peak} \tag{3-8}$$

where $\theta_{BS\text{-}peak}$ is the largest BS spectral peak location, as illustrated in Fig. 3-3. Since the BS spectral peak corresponding to the direct signal (PK_d) is typically biased by the terrain multipath on the side of the peak towards the multipath (i.e., at the angles less than that of the direct signal), angle estimators which primarily rely on the less distorted portion of the PK_d (i.e., that at angles above the direct signal angle) seem sensible. The angle estimator B is such an estimator.

The angle estimator B obtains its estimation of the direct signal angle by locating the angular position of a given slope along the main lobe of the received signal BS spectrum. The slope was chosen to be -1.86 dB/0.1 BW which corresponds to the point 6 dB below the nominal BS spectral peak.* Thus, the direct signal angle θ_d given by the angle estimator B is

$$\theta_d \approx \theta_B = \theta_{slope} - \theta_{cor} \tag{3-9}$$

where θ_{slope} is the angular position of the point with -1.85 dB/0.1 BW slope along the main lobe of the BS spectrum, as indicated in Fig. 3-3. θ_{cor} is the difference between the direct signal angle and the θ_{slope} when only the direct signal is present.

To see the performances of these two angle estimators with various antenna aperture sizes under the known signal environment, we first applied them to a simple synthetic data case consisting of two plane wave arrivals. The synthetic data were obtained from one plane wave arriving at angle θ (to simulate the direct signal) with amplitude 1 and the other plane wave arriving at angle $-\theta$ (to simulate the ground reflected signal) with amplitude 0.9 and 0° phase relative to the direct signal. The signal environment in this synthetic data case would correspond to the terrain multipath environment for a perfectly flat ground. Four antenna arrays of different aperture sizes

---

*To reduce the sidelobe multipath effect on θ_B, the slope of -1.86 dB/0.1 BW was chosen instead of -3 dB/0.1 BW slope (corresponding to the point 9 dB below the nominal BS spectral peak) which was used in the MLS single edge flare processor developed by Calspan [16].

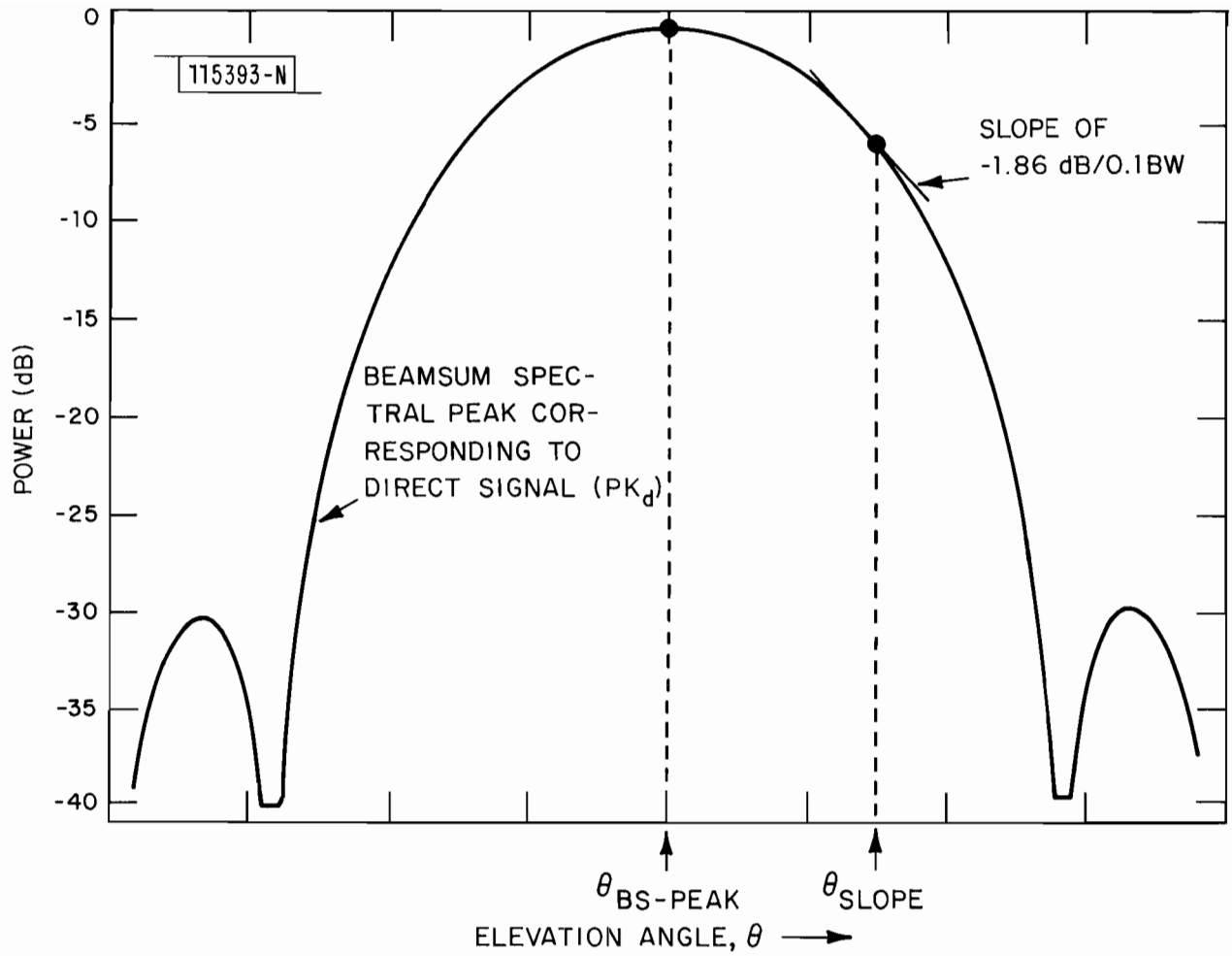

Fig. 3-3. Angular positions of points on the beamsum spectrum used for the estimation of direct signal angle.

(yielding beamwidths (BW) of 1°, 2°, 3°, and 4°), as described in Section II, were used. Figure 3-4 shows the angle errors (i.e., $\theta_A - \theta_d$ or $\theta_B - \theta_d$) versus the direct signal angle. For a given array aperture size, the angle estimator B yields much smaller error than the angle estimator A, as expected for this simple multipath situation. For a given angle estimator, the angle error in degree decreases with increasing array aperture size, but the amount of the angle error reduction depends on the separation angle. For example, for the angle estimator A, no significant error reduction was obtained with increasing aperture size from 4° BW to 2° BW at θ_d = 1°, while a large error reduction was observed at θ_d = 1.5°.

C. Data Reduction Procedure

The procedure involved in processing the field measured data and that in obtaining the MLS computer simulation results to be compared with the field measured results are the same as those described in our previous report on terrain reflection measurements [2]. So, here we just show a more up-to-date block diagram of our data reduction procedure in Fig. 3-5.

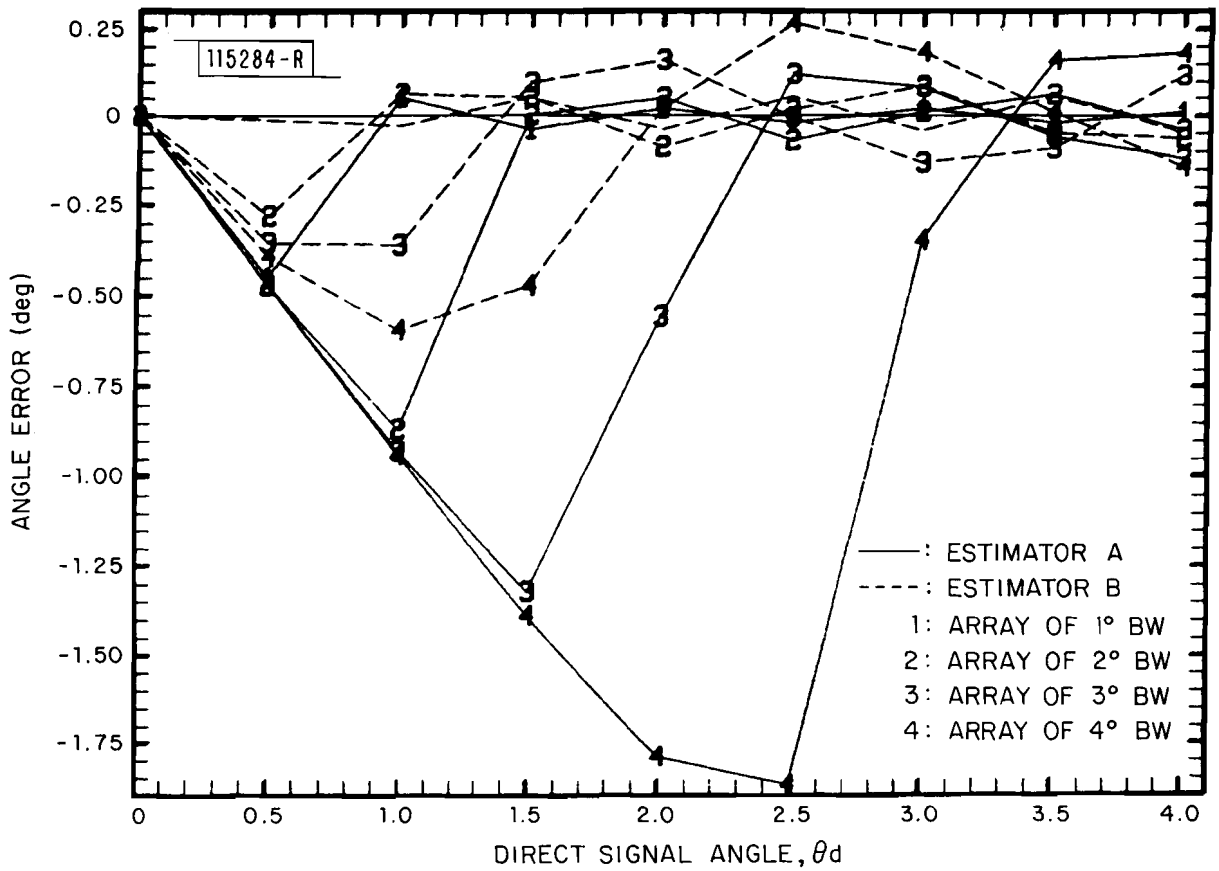

Fig. 3-4. Angle estimation results: synthetic data case.

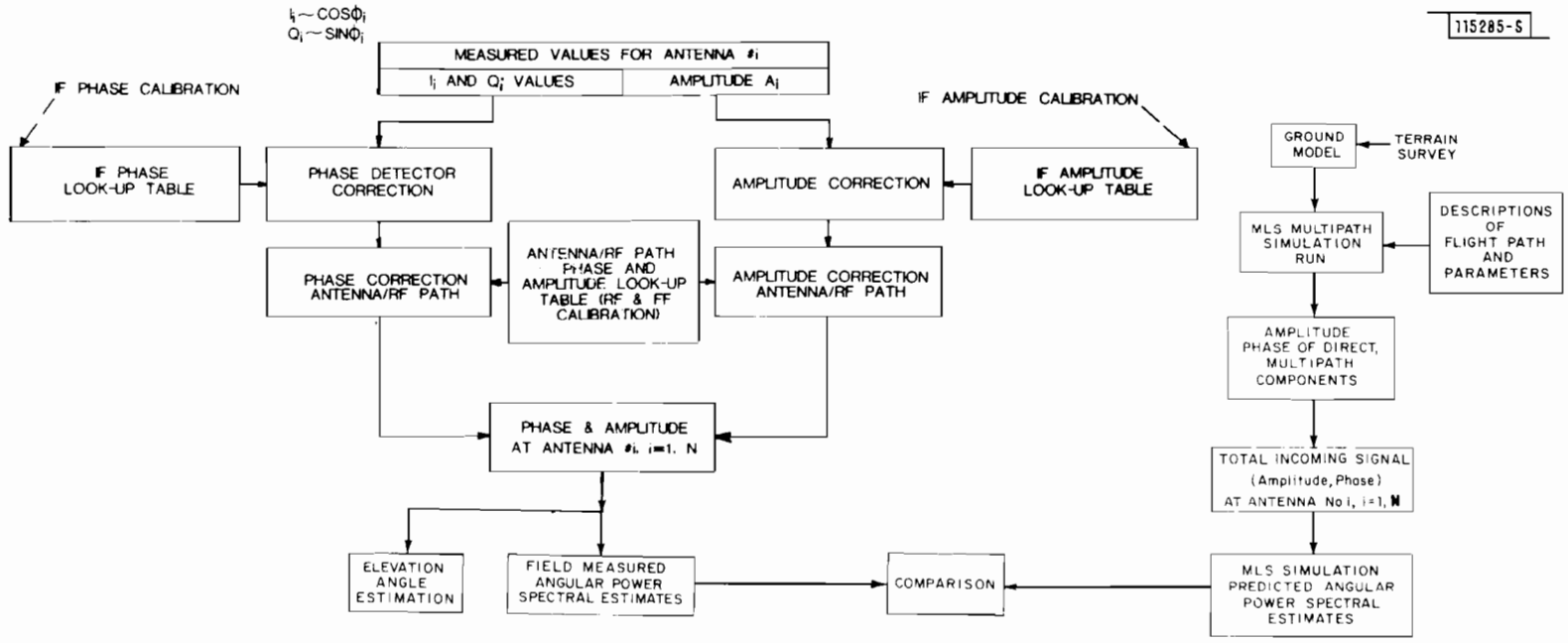

Fig. 3-5. Data reduction procedure.

IV. FIELD MEASUREMENT SITES

Field measurement results presented in the next two chapters were obtained from the measurements conducted at various test sites in 1980. This chapter describes the terrain conditions and the flight profiles involved in the measurements for the various test sites we visited. Also a summary of field measurements taken during 1980 is given here. Five sites in Massachusetts were visited. They are: (1) Hanscom Airport, (2) Fort Devens golf course, (3) Camp Edwards J2 Range, (4) Camp Edwards Gibbs Road at entrance, and (5) Camp Edwards Gibbs Road next to N Range.

A. Hanscom Airport

Figure 4-1 shows a simple map around the measurement site at Hanscom airport. Also shown in this figure is the terrain height profile (both surveyed and modelled for the MLS multipath simulation runs) along one of the radial lines from the receiving antenna array. The ground in front of our receiving antenna arrays was fairly flat (terrain height variation less than 2 feet in 1000 foot range) and had no cross-range tilts. The ground was mostly covered with grass of varying heights*, as can be seen in Fig. 4-2. To the south of the overrun area at Hanscom runway 11-29 is a fairly high (100 foot) hill (Pine Hill). This hill is covered by conifers and hence was not modeled on the grounds that the heavy vegetation would absorb the incident radiation.

Several measurement missions** were conducted at this site for both the L-band and the C-band measurements. The measurements were taken with a helicopter. The flight profiles for the helicopter were the continuous vertical descent at three drop points (0.5 nmi, 1 nmi and 2 nmi) along the 270° radial line. The 270° radial line was chosen because it gave us the lowest elevation obstruction. At 0.5 nmi drop point, our theodolite could track the helicopter down to the ground. For proper data collection with our equipment, as dis-

---

*Normally, after the airport people cut the grass, the grass was uniformly short.

**One measurement mission refers to one day of field measurements with at least some successful data recording.

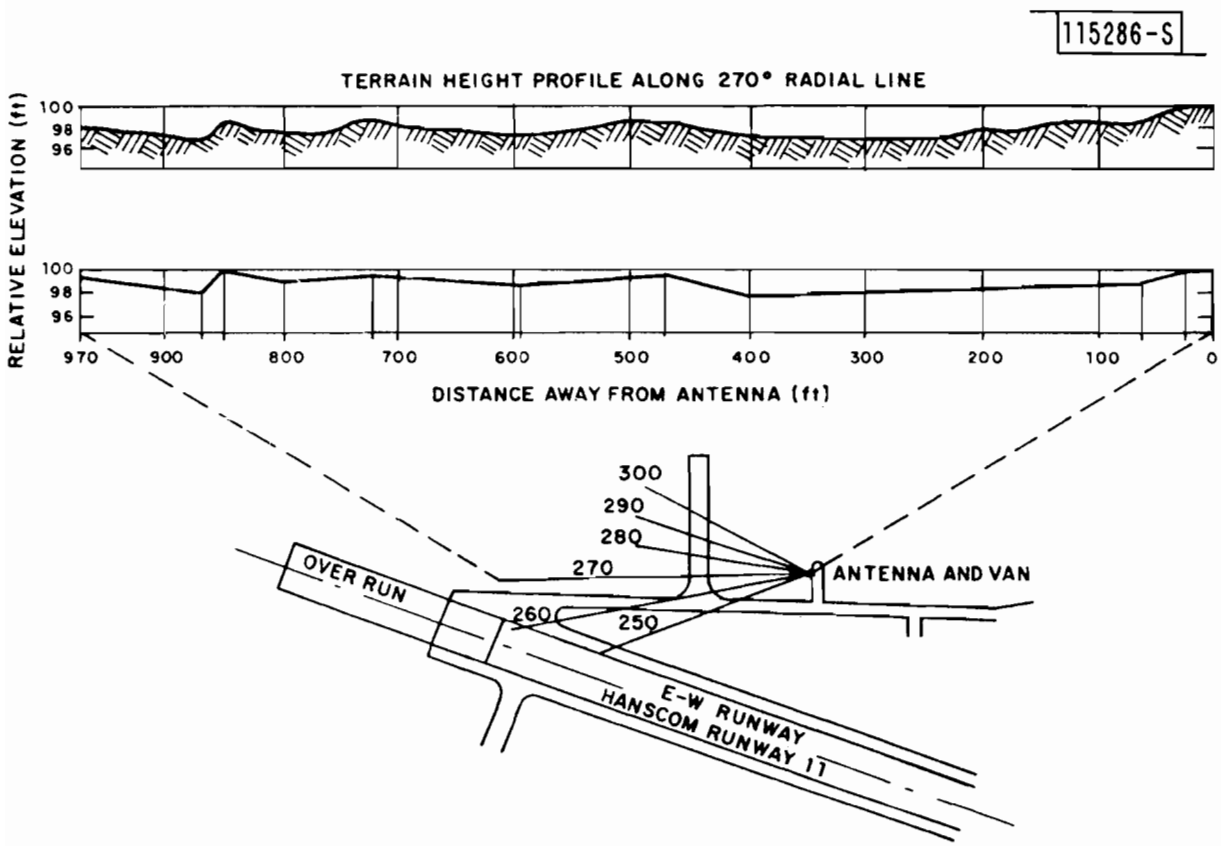

Fig. 4-1. Measurement site at Hanscom Air Force Base.

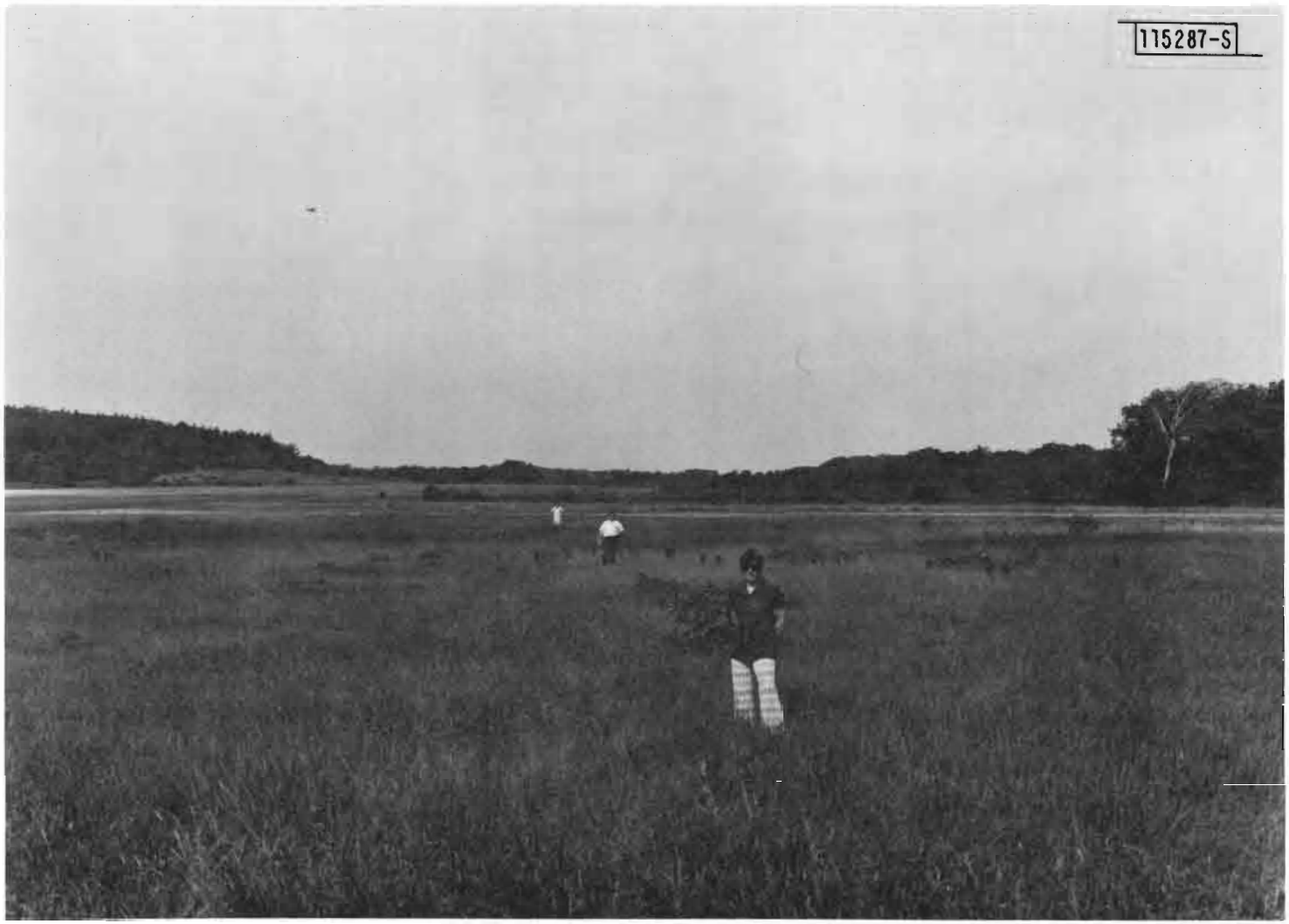

Fig. 4-2. Hanscom Air Force Base: ground in front of the receiving antenna towards overrun area.

cussed in Chapter II, the helicopter had to maintain a very slow descent rate of about 2 to 3 feet per second, especially with the C-band receiving antenna array at the closer range (0.5 nmi and 1 nmi). The elevation angle coverage in the measurements was from 8° down to the elevation angle where our theodolite could not track the helicopter due to obstructions. At this site, the lowest elevation angle reached was close to 0° at 0.5 nmi drop point and about 1° at 2 nmi point.

B. Fort Devens Golf Course

Figure 4-3 shows a map around the measurement site at the golf course. As we did before [2], six measurement points (at two ranges: 0.6 nmi and 1.5 nmi) along three radial lines centered at our receiving antenna array were chosen. Terrain surveys were made along these three radial lines, both for the along-range height profile and the cross-range tilt. Figures 4-4 through 4-6 present the surveyed height profiles, together with the corresponding ground models used in the MLS multipath simulation runs. The variations of the along-range terrain height were fairly similar among three radial lines. The ground in front of the receiving antenna array had a noticeable downward slope, followed by an upward slope, within a roughly level horizon. However, the cross-range tilts were somewhat different among three radial lines, with the radial line O-A having the most variation in the ground cross tilt. The ground was covered very uniformly with short grass as can be seen in Fig. 4-7.

Two measurement missions were conducted at this site, with both the L-band and the C-band antenna arrays. The measurements were taken with a helicopter, making continous vertical descent at the measurement points, again at very slow descending rate. Data were taken from the high elevation angle of about 8° down to obstruction height along a given radial line. The elevation obstruction angles along these three radial lines were at 1.5° (radial lines O-A and O-B) and about 3° (radial line O-C).

C. Camp Edwards

Figure 4-8 shows a map covering three measurement sites at Camp

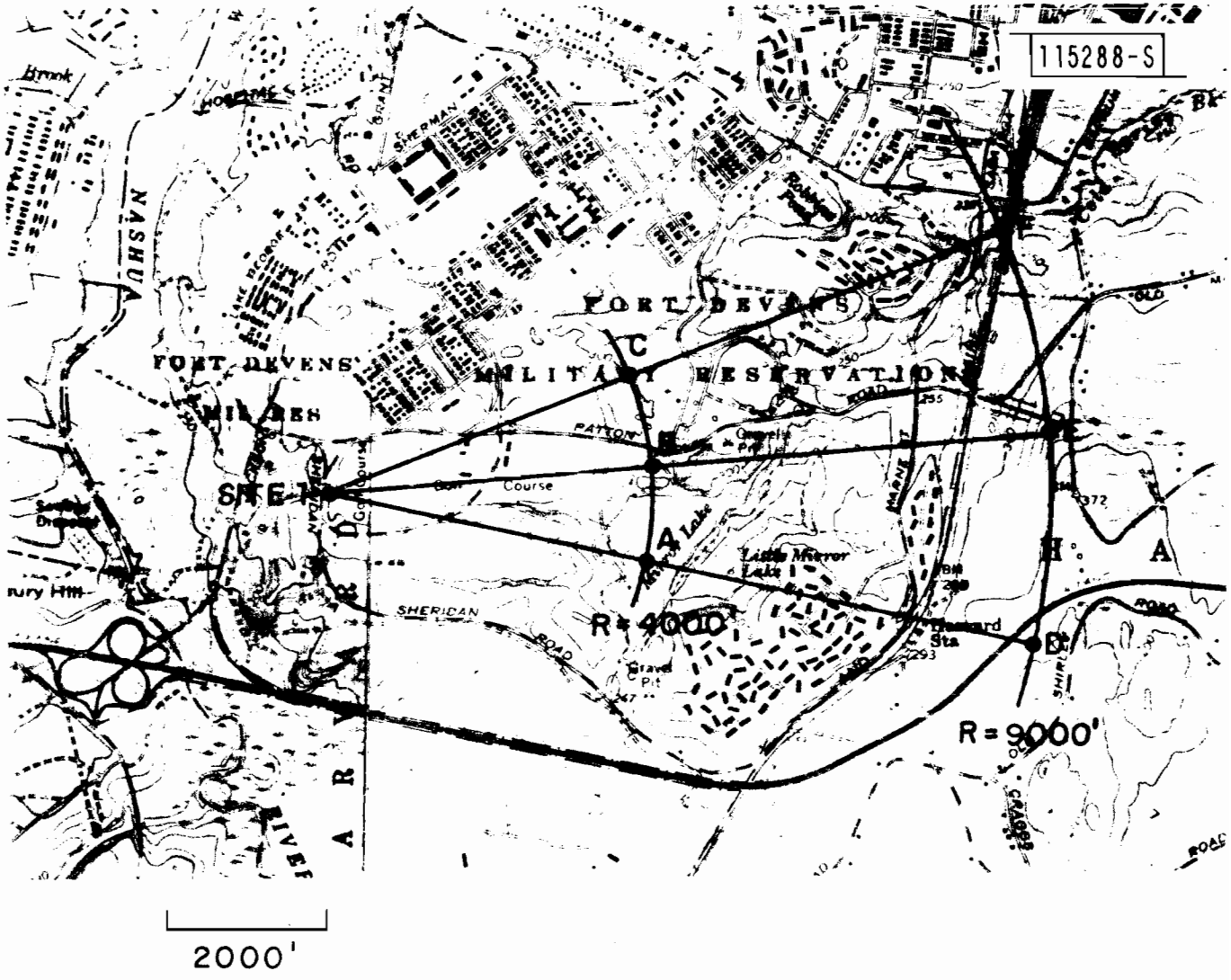

Fig. 4-3. Measurement site at Fort Devens golf course.

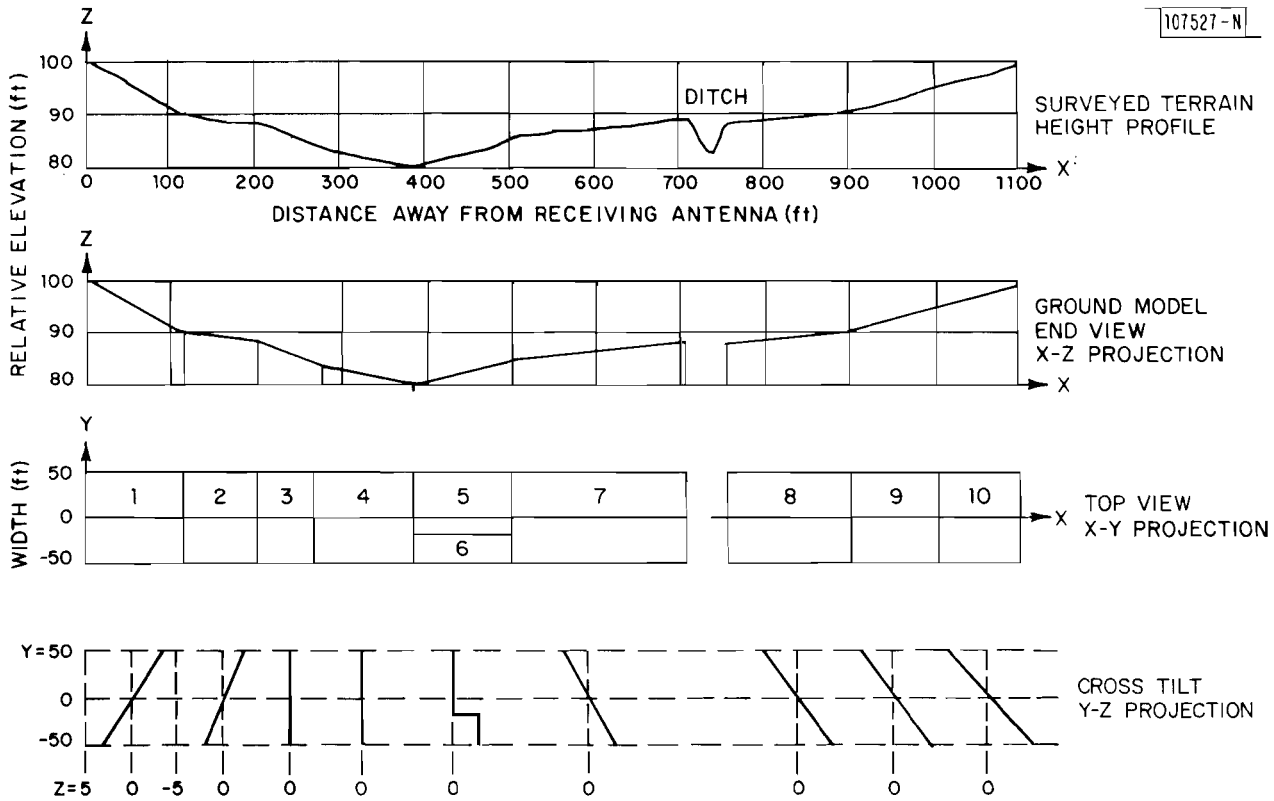

Fig. 4-4. Terrain height profile at Fort Devens golf course: radial line O-A.

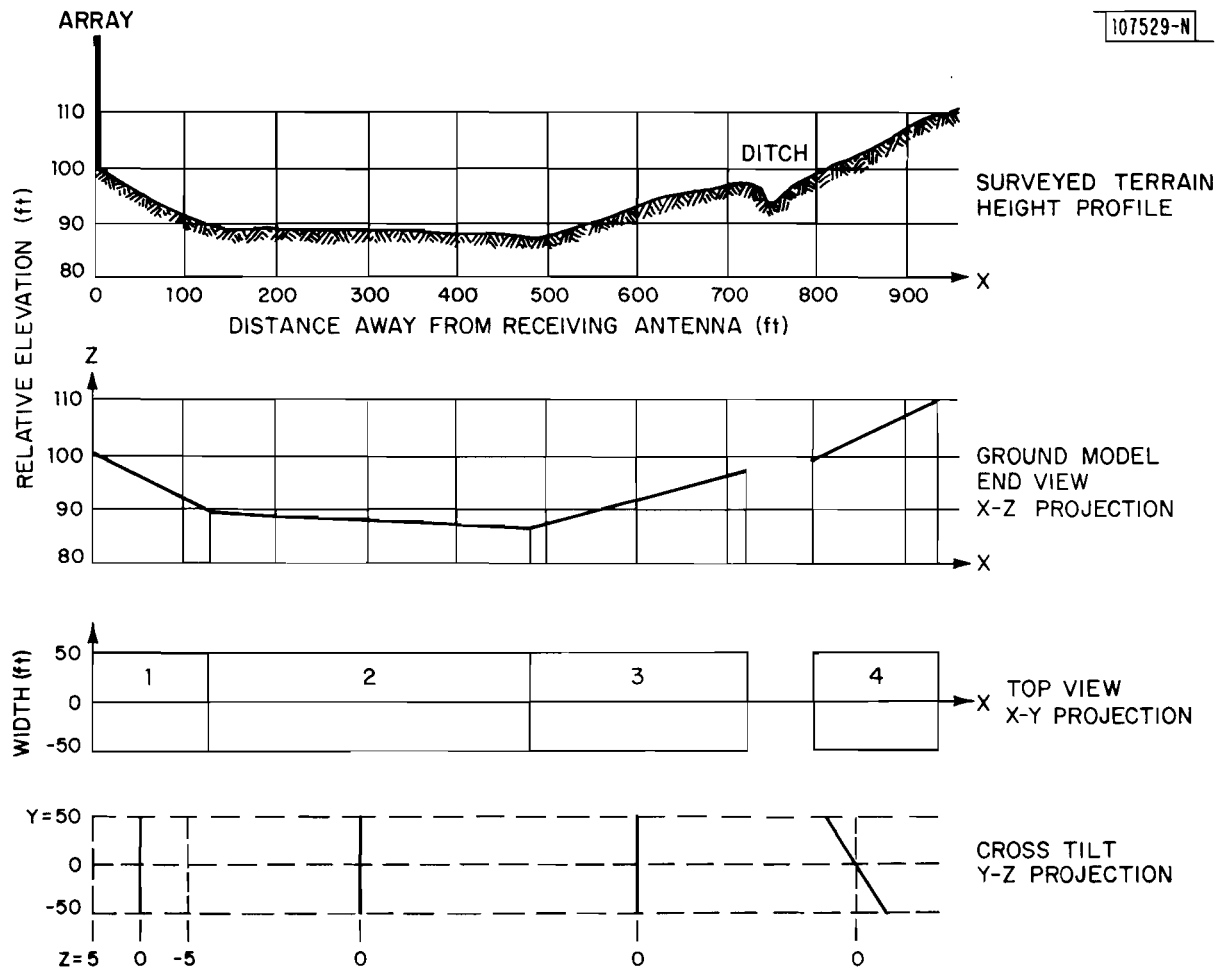

Fig. 4-5. Terrain height profile at Fort Devens golf course: radial line 0-B.

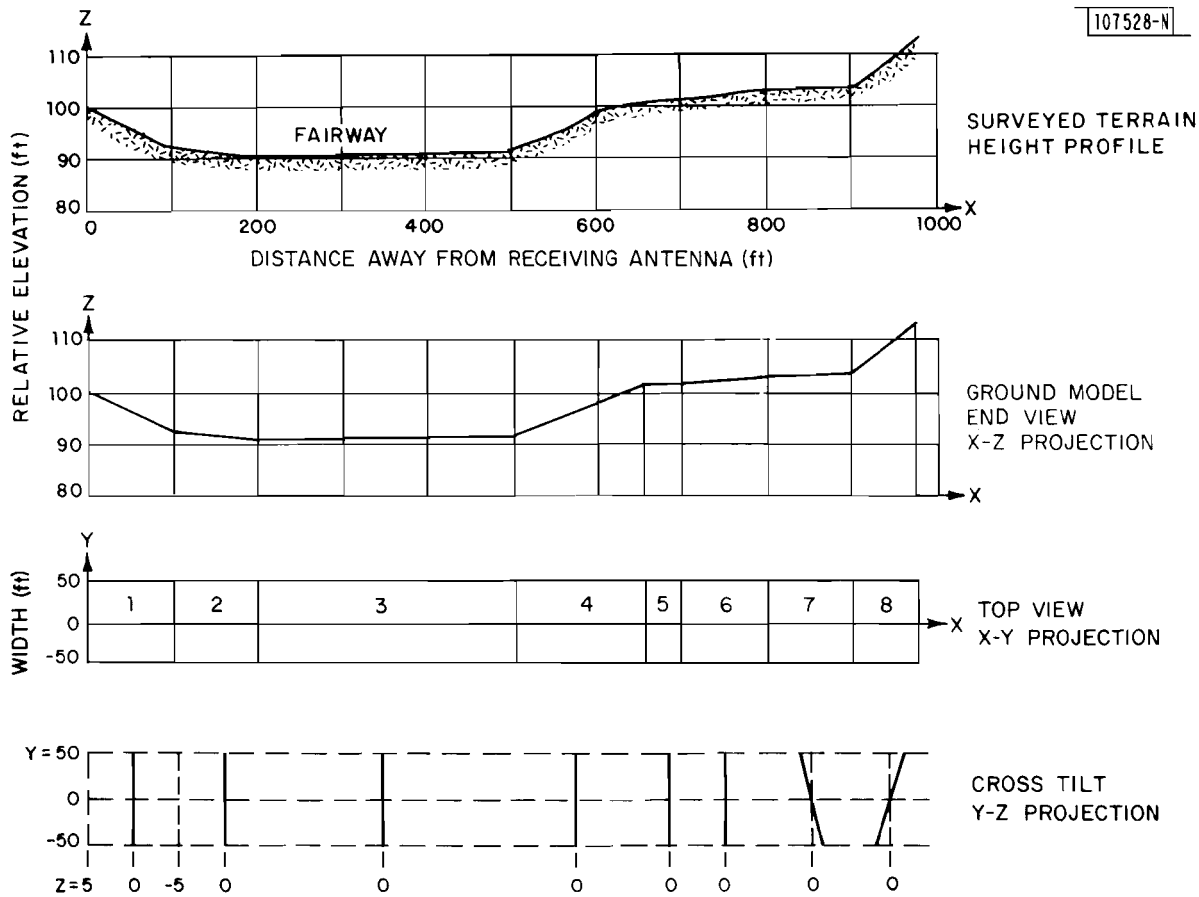

Fig. 4-6. Terrain height profile at Fort Devens golf course: radial line O-C.

Fig. 4-7. Fort Devens golf course: ground in front of the receiving antenna along radial line O-B.

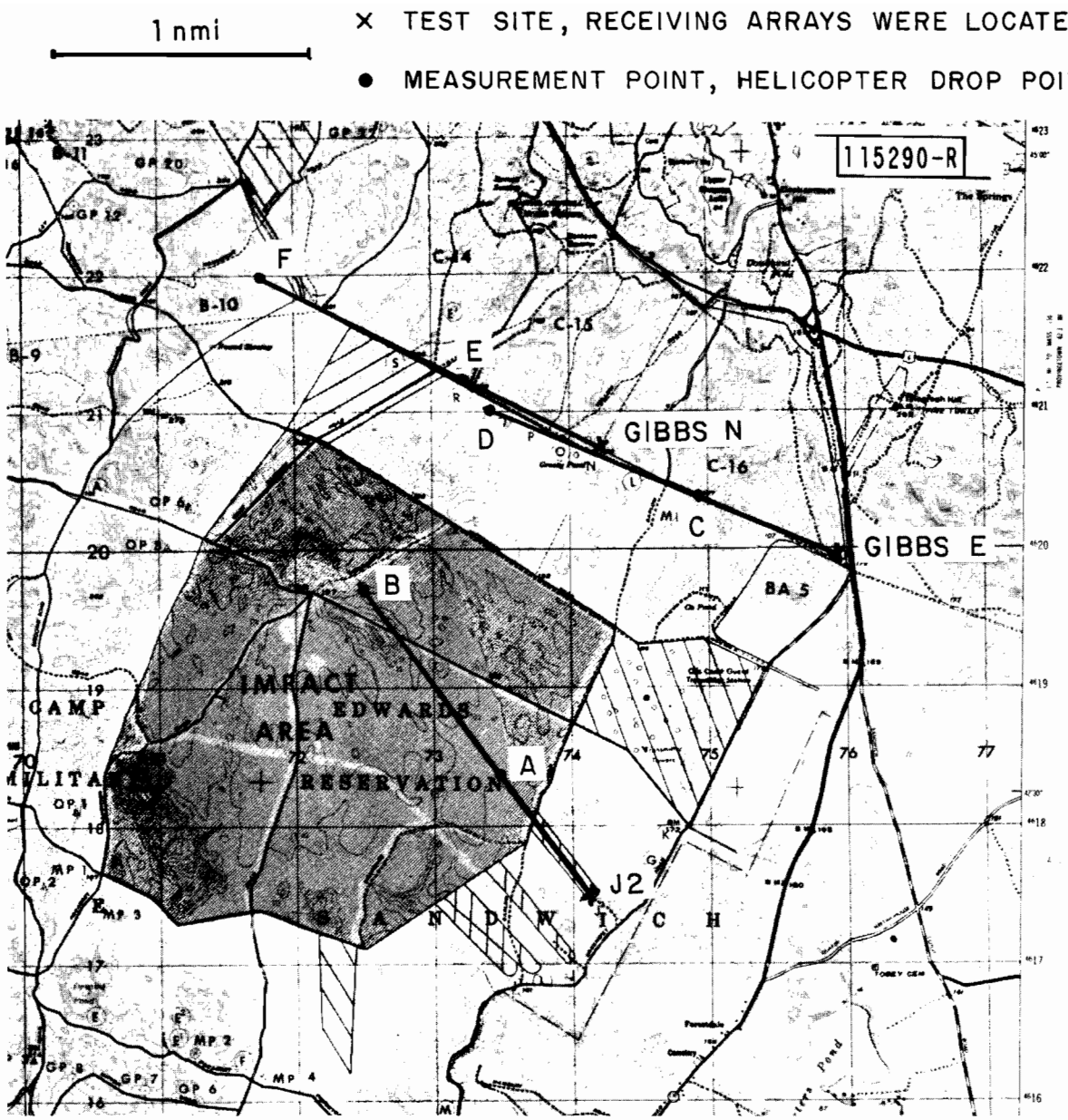

Fig. 4-8. Measurement sites at Camp Edwards.

Edwards. Measurements were only taken along one radial line for two measurement points at each site, due to the narrow open air space at these three sites. Again, the terrain surveys were made for both the along-range height profile and the cross-range tilt.

Figure 4-9 gives the surveyed height profile at the J2 Range site. Also shown in the figure is the three projections of the ground model which was derived from the surveyed ground heights/cross tilts for the MLS multipath simulation. The ground here was fairly flat (along-range height variation less than 2 feet in more than 1000 foot range), but some minor cross tilts (in the order of along-range height variation) were observed at various ranges. One distinct terrain feature at this site was that the ground surface was fairly rough, especially for the C band. As can be seen in Fig. 4-10, which was a photograph taken at the receiving array location toward the measurement points in the Impact Zone, the ground surface was basically composed of small sandy dirt mounts with various sizes and was covered unevenly with grass of various heights.

Figure 4-11 shows the surveyed terrain height profile at the Gibbs Road entrance site, together with the ground model being used in the MLS multipath simulation. The terrain here had a very similar feature as that at the Fort Devens golf course, i.e., the upsloping and downsloping local slope within a roughly level horizon. However, here the ground height varied in a much larger scale than that at the Fort Devens Golf Course. Here, the variation of the along-range height was as large as 80 feet in 1000 foot range. Also, the large cross-range tilts existed almost everywhere (10 foot tilt in 50 foot cross range). The ground surface was fairly smooth, especially along the Gibbs Road, as can be seen in Fig. 4-12. The road surface consisted of gravel and the off-road area was unevenly covered with grass of various heights on the sandy dirt.

Figure 4-13 shows the surveyed terrain height profile at the Gibbs Road next to N Range and the corresponding ground model for the MLS multipath simulation. The terrain here had more rolling features than that at the Gibbs Road entrance site, as can be seen in the height profile. However, the ter-

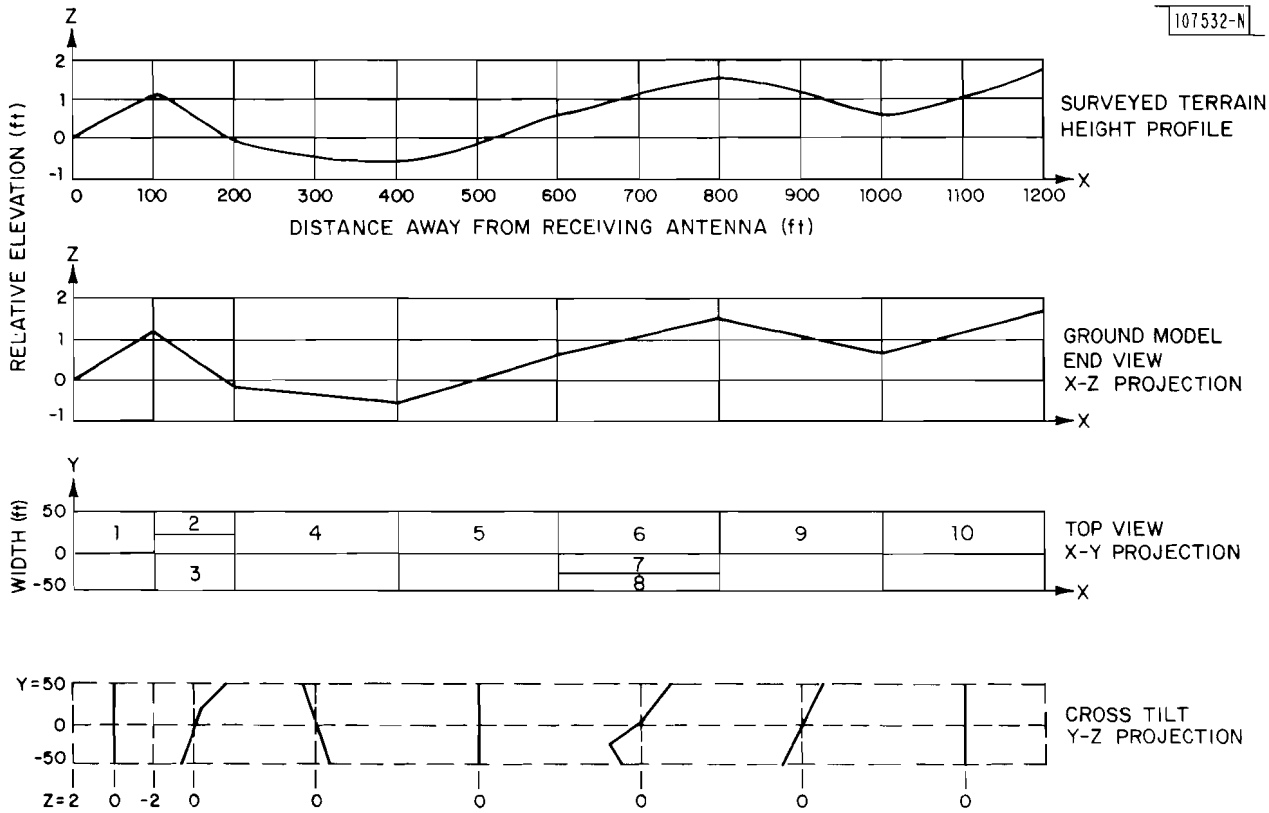

Fig. 4-9. Terrain height profile at Camp Edwards J2 Range.

Fig. 4-10. Camp Edwards J2 Range: ground in front of the receiving antenna.

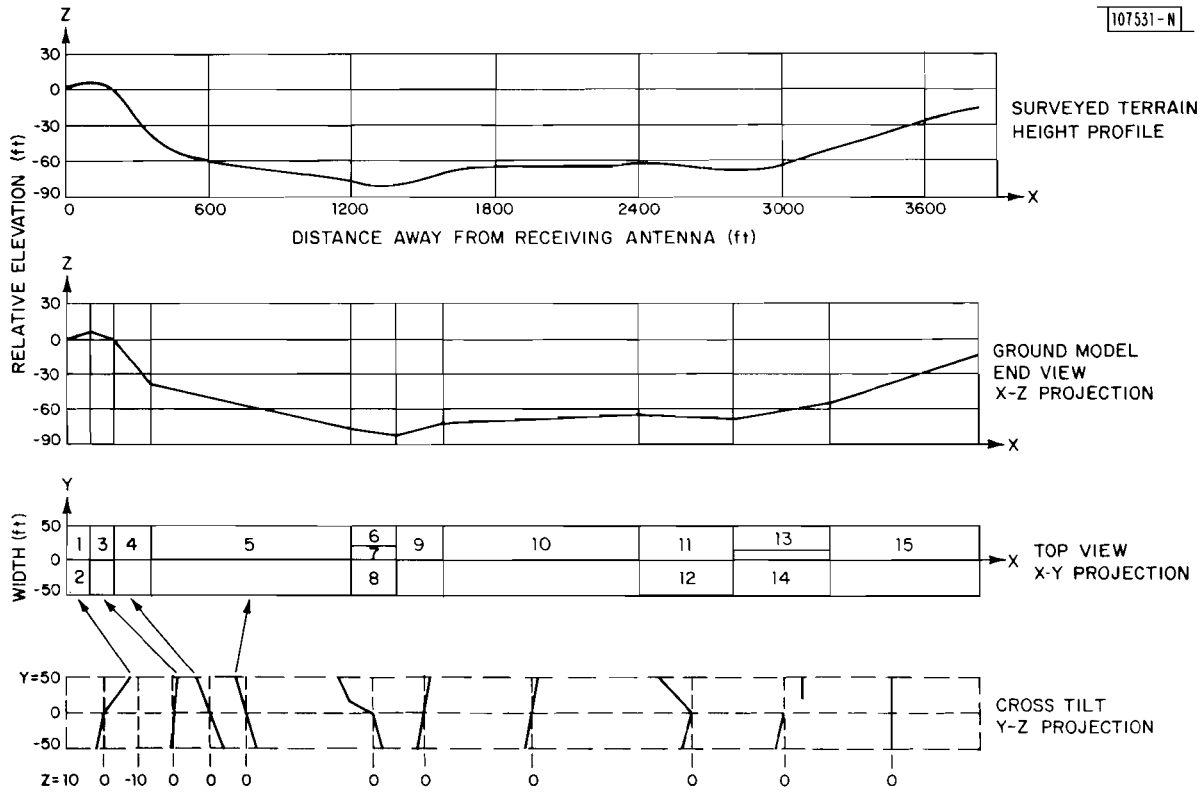

Fig. 4-11. Terrain height profile at Camp Edwards Gibbs Road entrance.

Fig. 4-12. Camp Edwards Gibbs Road entrance: ground in front of the receiving antenna.

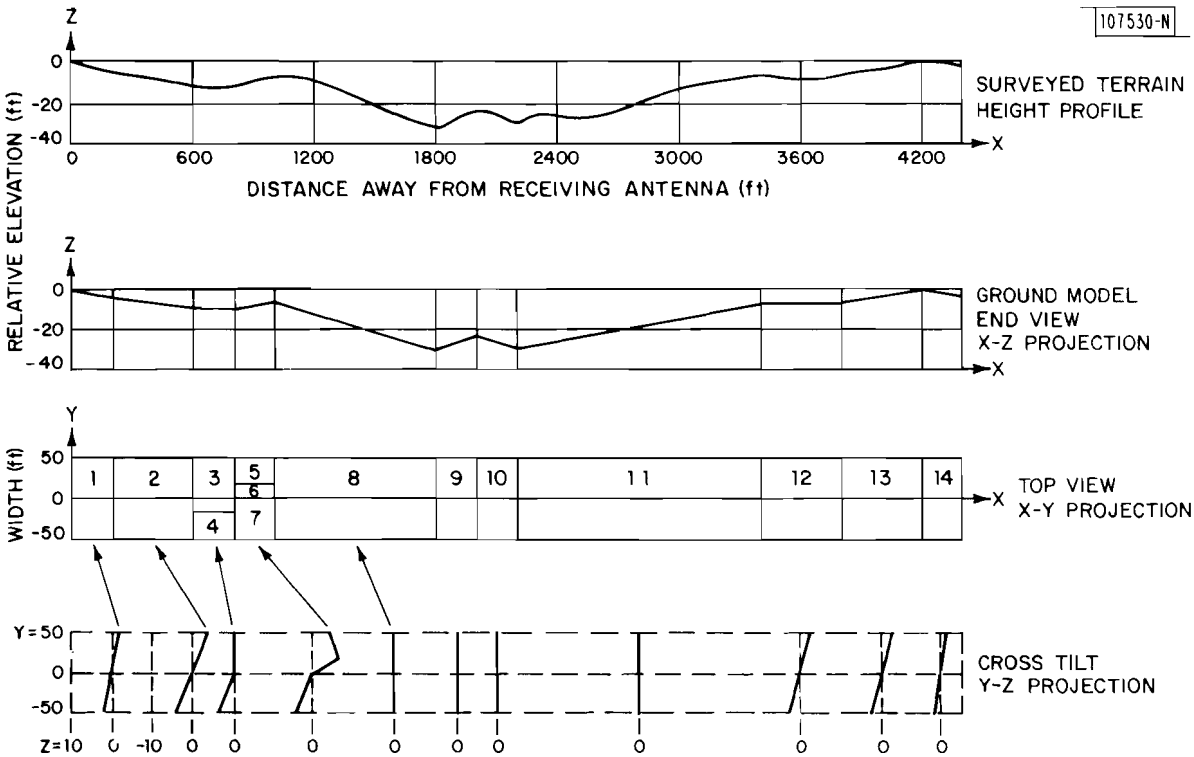

Fig. 4-13. Terrain height profile at Camp Edwards Gibbs Road N Range.

rain along-range heights changed much more gradually and only went down 30 feet in about 2000 foot range. Nevertheless, this site had the similar cross-tilt features as the Gibbs Road entrance site. Also, the ground surface of this site was very similar to that at the previous site, i.e., gravel on the road surface and sandy dirt with unevenly covered grass on the off-road area (Fig. 4-14).

A total of five measurement missions were conducted at three Camp Edwards sites. Both the L-band and the C-band measurements were taken at the first two sites (J2 Range and Gibbs Road entrance), however, only L-band measurements were made at the last site due to the C-band antenna failure. Again, the measurements were taken with a helicopter. However, in addition to the continuous vertical descent flights as those at Hanscom Airport and Fort Devens, data were also taken for the hovering flights at various elevation angles. The continuous vertical descent flights covered elevation angles from 8° and down to the obstruction height. The lowest elevation angles reached for the measurements were 0.5° at the J2 Range and around 1° at the other two sites.

D. Summary of Field Measurements Taken During 1980

Table 4-1 summarizes the field measurement missions conducted during 1980. This yielded the field data base for the field measurement results presented in the next two chapters. Reasonable efforts were made to obtain both the L-band and the C-band data at all five measurement sites. To ensure the data repeatability and to increase the successful rate of data collection at any given measurement point, duplicate measurements were taken for two identical helicopter flight paths. Also, for the meaningful comparison between the L-band and the C-band results, the fight paths involved in the L-band and the C-band measurements at a given measurement point were made as identical as possible*.

*Helicopter vertical descent flights were guided by the measured range displayed on the range indicator inside the measurement van and by the theodolite azimuth angle (relative to the fixed landmark or the first flight at a given measurement point).

Fig. 4-14. Camp Edwards Gibbs Road N Range: ground in front of the receiving antenna.

TABLE 4-1

SUMMARY OF FIELD MEASUREMENTS TAKEN DURING 1980

Measurement Site	Number of Missions	Date(s)	Terrain Type	Remarks
Hanscom Airport	4	2/26 -4/7	Flat and smooth, with no crosstilts	L/C-band data slow descending flights
Fort Devens golf course	2	5/21 -6/6	Rolling and smooth, with almost no cross-tilts (O-B, O-C) with crosstilts (O-A)	L/C-band data slow descending/ arc flights
Camp Edwards J2 Range	2	8/18 -8/28	Flat and rough, with small crosstilts	L/C-band data slow descending/ hovering flights
Camp Edwards Gibbs Road E	2	9/8 -9/10	Rolling and smooth, with large height variation and signif-icant crosstilts	Same as above
Camp Edwards Gibbs Road N	1	9/11	Rolling and smooth, with medium-height variation and signif-icant crosstilts	L-band data only slow descending/ hovering flights

Although only five measurement sites were visited, several varieties of commonly encountered terrain conditions were included. These are:

(1) Flat (along-range height variation less than 2 feet in 1000 foot range) and smooth terrain with no cross range tilts: Hanscom Airport Site,

(2) Flat and fairly rough terrain with some cross-range tilts (less than 2 feet in 50 foot cross range): Camp Edwards J2 Range,

(3) Rolling and smooth terrain with small along-range height variation (10 feet in 1000 foot range) and almost no cross-range tilts: Fort Devens golf course radial lines O-B and O-C,

(4) Rolling and smooth terrain with medium along-range height variation (20-30 feet in 1000 foot range) and significant cross-range tilts (more than 5 feet in 50 foot cross range): Fort Devens golf course radial line O-A and Camp Edwards Gibbs road next to N. Range, and

(5) Rolling and smooth terrain with large along-range height variation (80 feet in 1000 foot range) and significant cross-range tilts: Camp Edwards Gibbs Road entrance.

V. EXPERIMENTAL RESULTS FOR TERRAIN MULTIPATH

Data analysis results presented in this chapter were obtained from the field measured data and the corresponding MLS multipath simulation runs for the measurements taken at various sites, as described in Chapter IV. The angular power spectrum was presented for the helicopter at waypoints of every 0.5° interval in elevation angle along a given flight path, starting at around 6° elevation angle. These angular power spectra were thought to be representative for a given flight path. To obtain the best possible angular resolution of various multipath arrivals from the angular power spectral estimate, the largest available array apertures in our L-band and C-band arrays were used to process the field measured data and the corresponding MLS multipath simulated data. For the L-band data, the 9 element equally spaced elevation (EL) array (beamwidth of 2°) and the 6 element equally spaced azimuth (AZ) array (beamwidth of 4°) were used. For the C-band data, the 19 element equally spaced EL array (beamwidth of 1°) was used.

Comparison between the field measurement results and the corresponding MLS multipath simulation predicted results was made on the following features: (1) the general appearances of all three kinds of angular power spectra (i.e., beamsum (BS), maximum likelihood (ML) and maximum entropy (ME)), and (2) the number, the arrival angles and the multipath levels (i.e., M/D ratios) of the multipath arrivals indicated in the angular power spectrum. The second feature was estimated from the ME angular power spectrum, since it offered the highest resolution among three kinds of spectral estimates used. The M/D ratios of the multipath signals to the direct signal were estimated based on the least-squares fitting scheme [5], using the multipath angles estimated from the ME spectrum. Comparison was also made along the similar lines between the L-band results and the corresponding C-band results at a given measurement point. This would show the change in the terrain multipath environment due to the frequency change from L band to C band.

The MLS multipath simulation results were obtained in either one or both of the following ways, as discussed in Chapter III, depending on the terrain condition at a given measurement site. (1) For the terrain with no cross range tilts such as at Hanscom airport, the ground plates in the ground model

were treated as the tilted building plates using building reflection calculation (for reflection ray X-O-R only [1,2]) in the multipath simulation runs. This is to take the advantage of the building reflection calculation which can handle the maximum of fifty rectangular reflection plates (as opposed to fifteen plates in the ground reflection calculation) [1]. So, the terrain can be modelled in more detail with a greater number of rectangular plates. (2) For the terrain with significant cross-range tilts, such as at Camp Edwards, the ground plates in the ground model were handled as ground plates using the ground reflection calculation with the focusing ground option [1] in the mulipath simulation runs. For the terrain with minimal cross-range tilts, such as at Fort Devens (radial lines O-B and O-C), simulation predicted results were obtained in both ways. So, some reasonable comparison could be made between the results obtained from two approaches.

As we emphasized before [2], in making the comparison, one cannot expect the detailed spectral shape (e.g., the sidelobe structure, the background spectral level) to be identical. This is because of some of the conditions in the field measurements were not exactly known and were not taken into account in the MLS multipath simulation runs, such as the possible diffuse scattering, the exact flight path and noise interference. Also, as we did before [2], we again made the assumption of plane wave arrivals in constructing the sensor outputs of the receiving antenna array from the multipath components predicted by the MLS multipath simulation run. Although this time the terrain cross-tilt was accounted for in modelling the ground, the ground reflection calculation with the focusing ground option in the multipath simulation limited the maximum number of 15 rectangular plates in the ground model. This prevented us from modelling the detailed terrain along-range height variation. Taking these factors into consideration in making the comparison, in most cases, the MLS multipath simulation predicted results could generally explain the major features observed in the field measurement results, such as the number of multipath arrivals, their arrival angles and M/D ratios.

In calculating the ME spectrum, no attempt was made to determine an "optimal order"* for the autoregressive (AR) model. Instead, we used the maximum order which was consistent with the dimension of the modified covariance matrix. The model order that we used was around NANT/3, where NANT is the number of antenna elements in a given array. Thus, for the L-band data, order of 2 to 3 was used with the azimuth array and order of 3 to 4 was used with the elevation array. For the C-band data, order of 6 to 7 was used.

In the following, the results from the comparison between the field measurement results and the corresponding MLS multipath simulation predicated results will be discussed and some representative angular power spectra will be given. To facilitate the comparison, in each figure shown below, the angular power spectra obtained from the field measured data are shown at the top and those predicted by the MLS multipath simulation are given at the bottom. Also, in each figure, the L-band and the C-band results are shown side by side. The BS, ML and ME angular power spectrum are shown in the dashed line (-----), the solid line (_____) and the dotted line (. . . .), respectively. The power levels (relative to the direct signal) of various multipath arrivals are indicated by the symbol "X" at their arrival angles. The true elevation angle of the direct signal** is indicated by a vertical line with the symbol "C".

A. Hanscom Airport

Examples of the elevation (EL) angular power spectral estimates for the measurements taken at Hanscom airport are shown in Figs. 5-1 to 5-6. As described in Chapter IV Section A, terrain at this measurement site is mainly a fairly flat grass field. Thus, the expected EL multipath environment should be primarily a single specular reflection. This was found to be the case in

---

*Such as via Akaike's FPE [17]. It appeared that the AR model determination was not practical for our terrain reflection data.

**For the field measurement results, this angle was calculated from the theodolite tracking angle, taking into account the height difference between the theodolite and the array phase center.

Field Measured

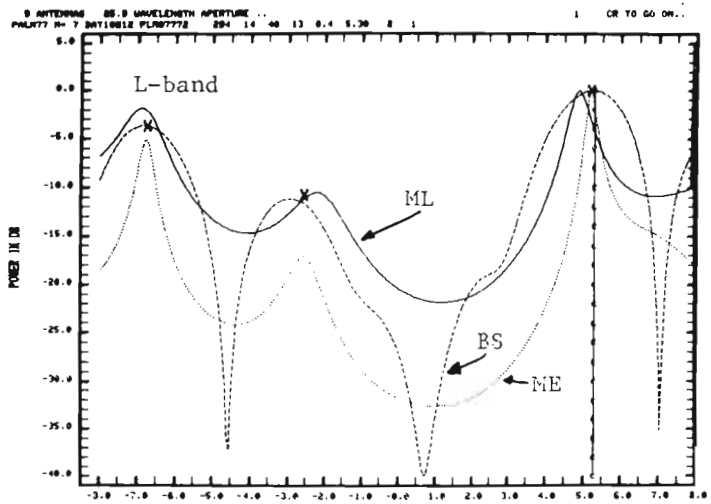

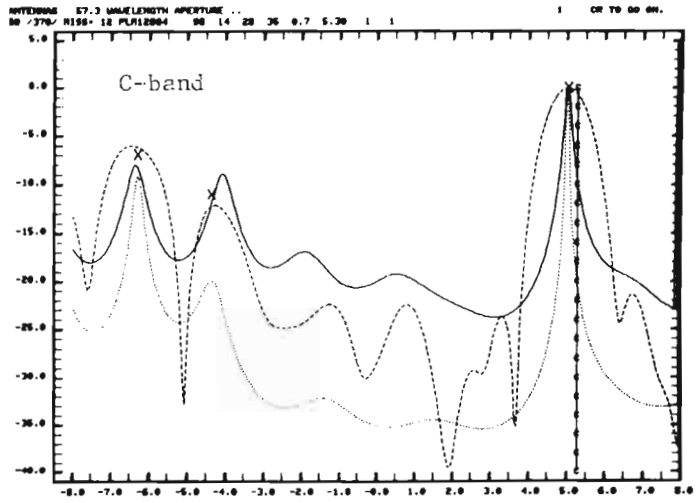

Simulation Predicted

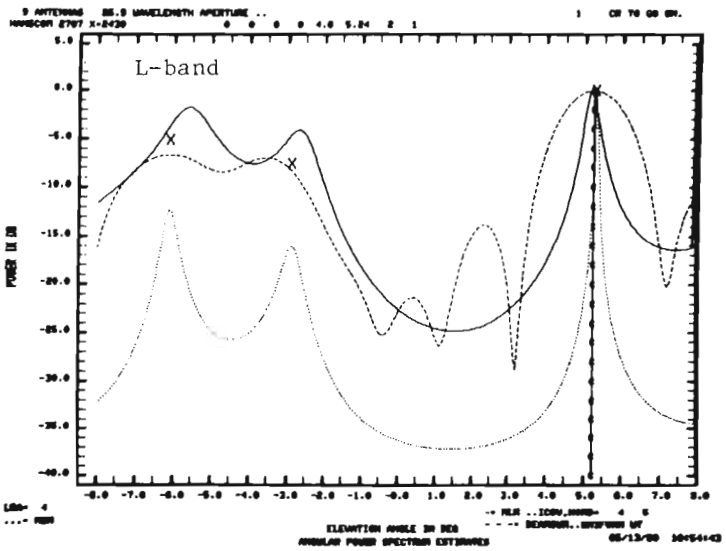

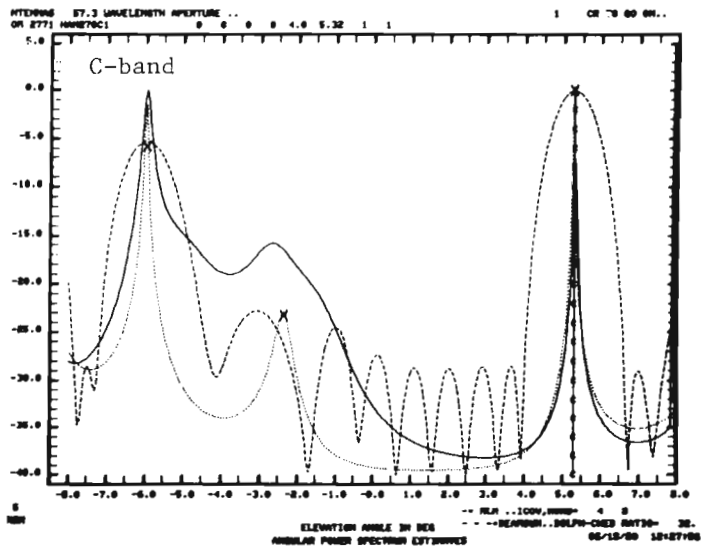

Fig. 5-1. Hanscom airport measurement: L- and C-bands elevation arrays, helicopter at $\theta_{EL} \simeq 5.3°$.

Field Measured

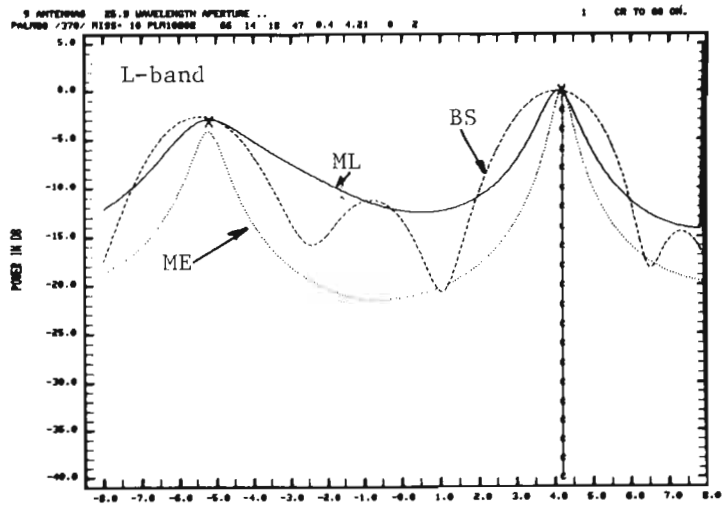

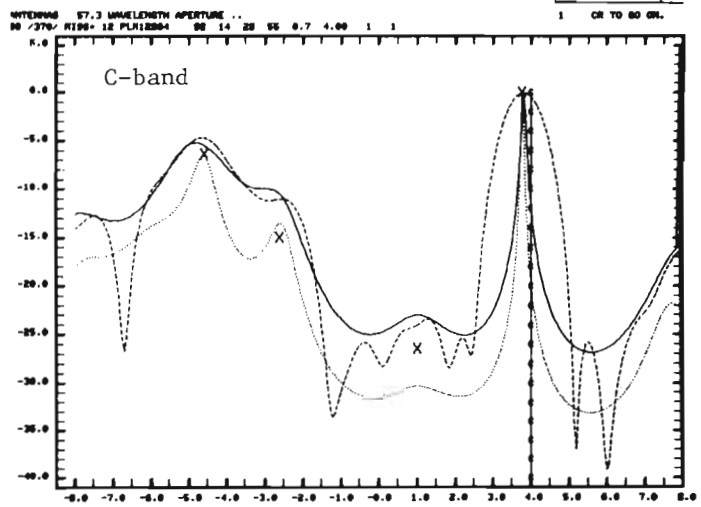

Simulation Predicted

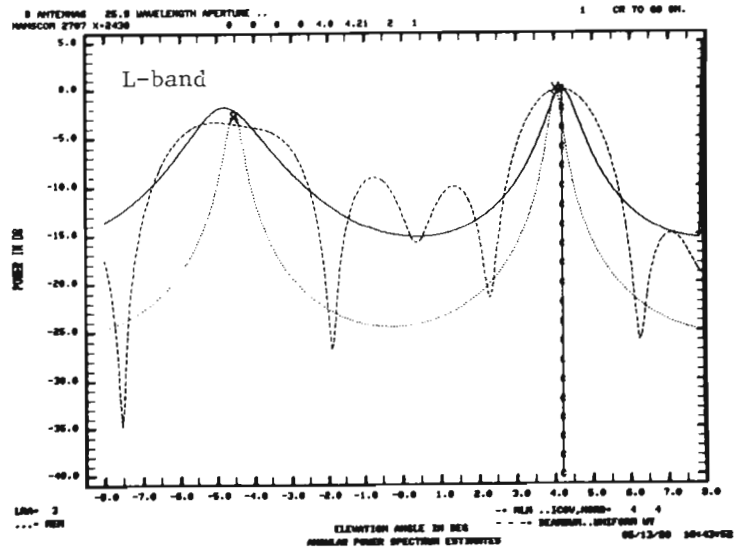

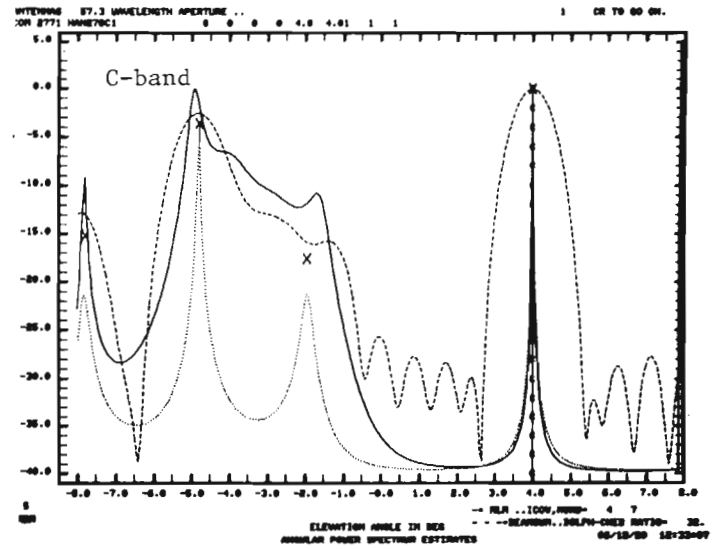

Fig. 5-2. Hanscom airport measurement: L- and C-bands elevation arrays, helicopter at $\theta_{EL} \simeq 4°$.

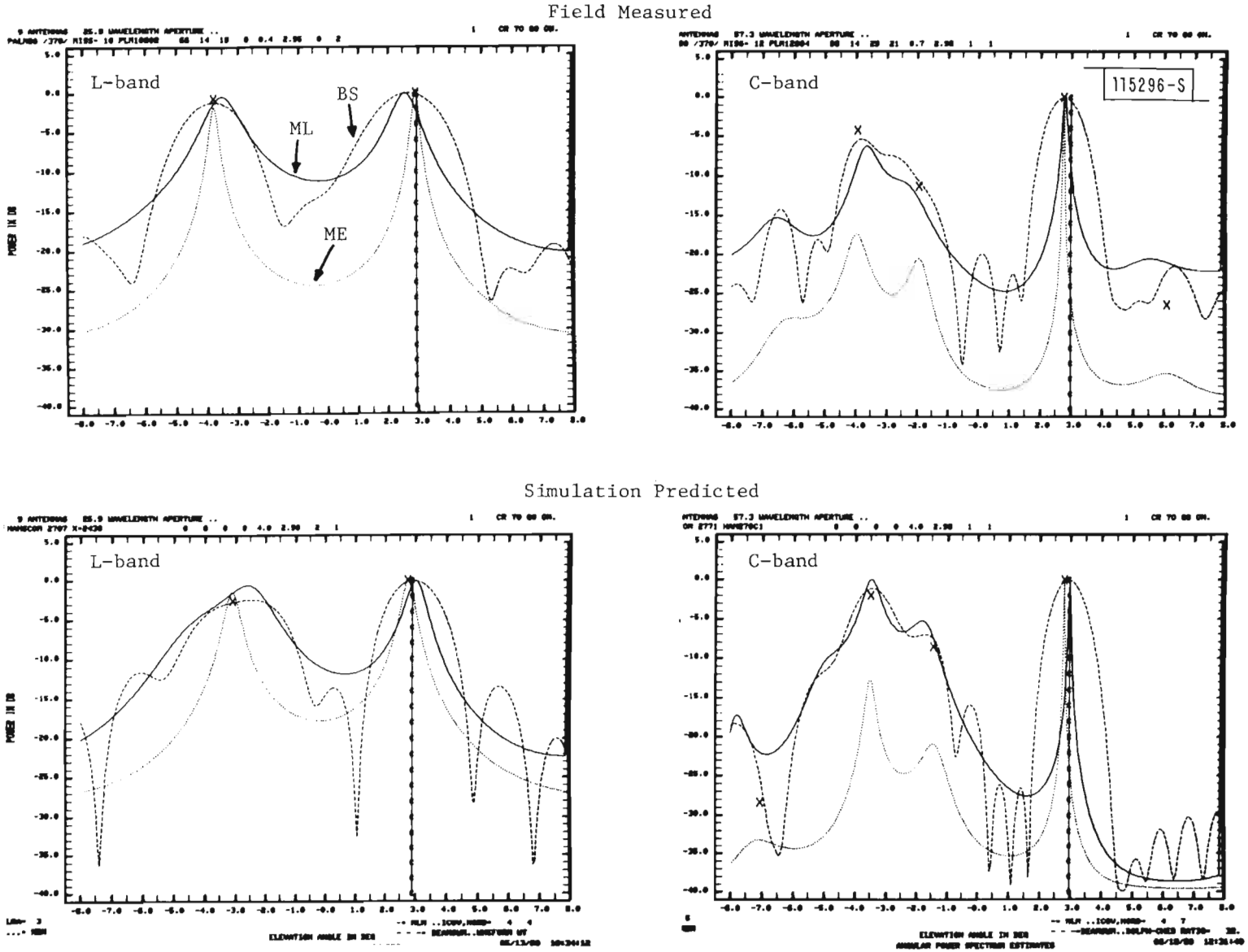

Fig. 5-3. Hanscom airport measurement: L- and C-bands elevation arrays, helicopter at $\theta_{EL} \simeq 3°$.

Field Measured

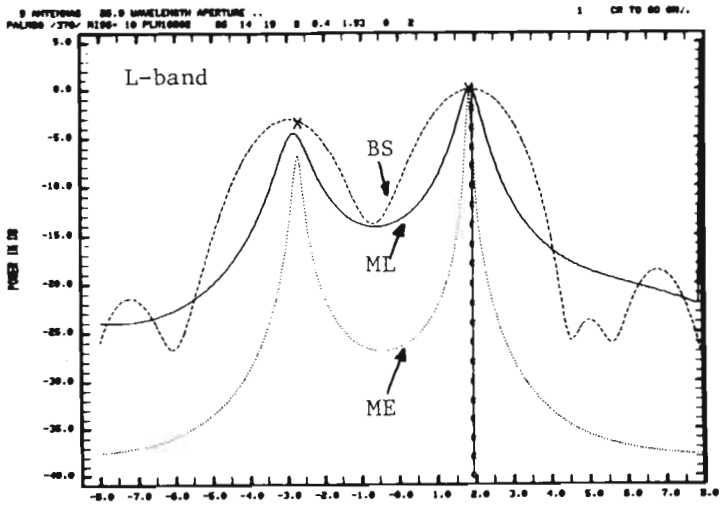

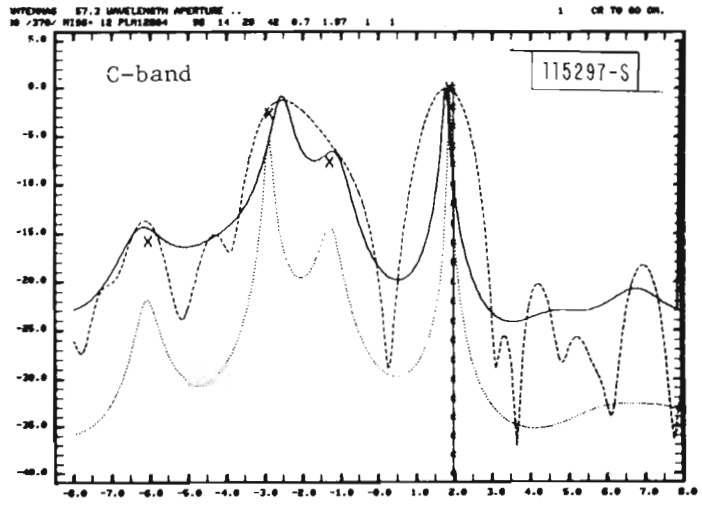

Simulation Predicted

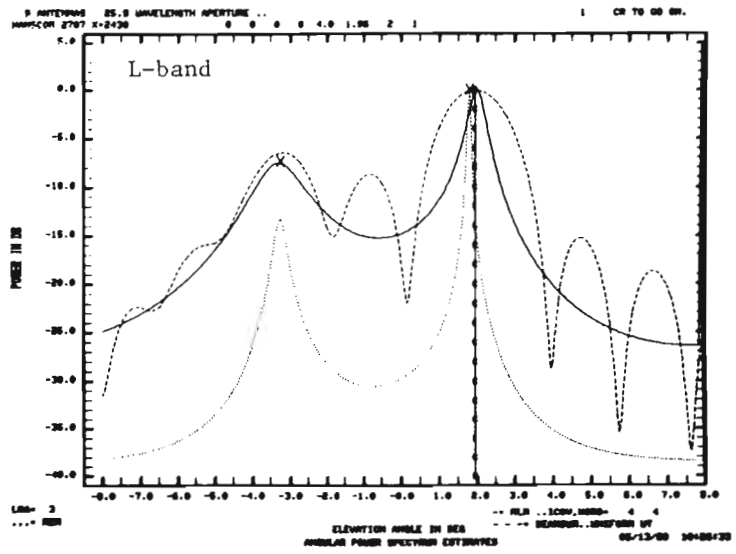

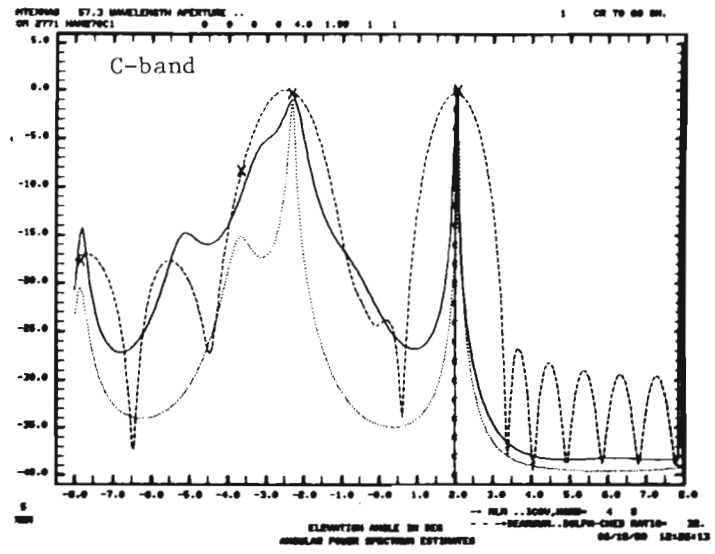

Fig. 5-4. Hanscom airport measurement: L- and C-bands elevation arrays, helicopter at $\theta_{EL} \simeq 2°$.

Field Measured

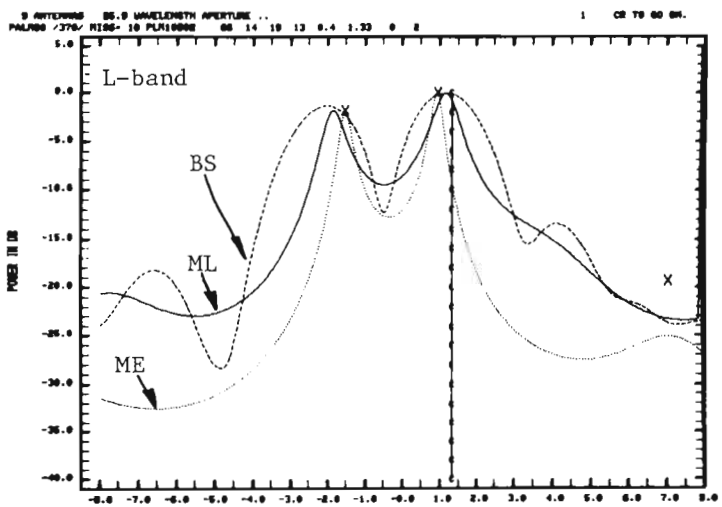

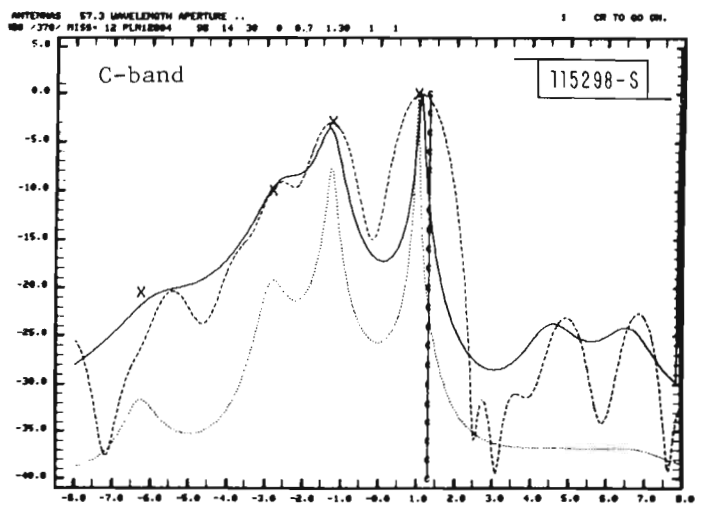

Simulation Predicted

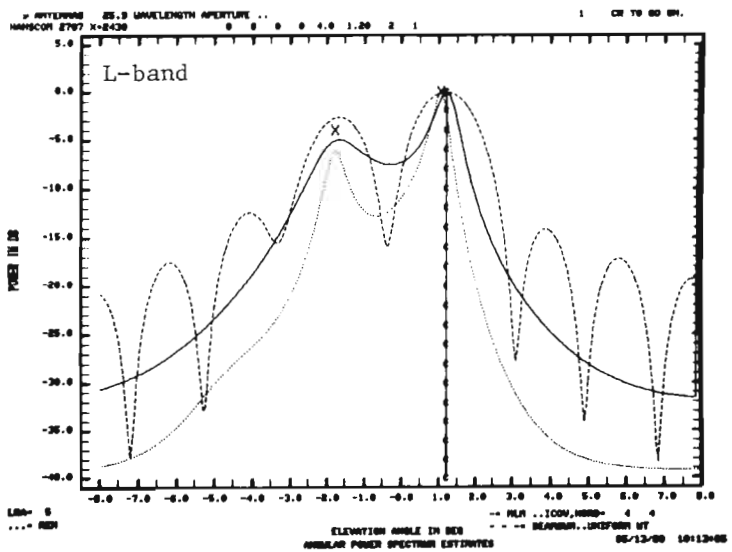

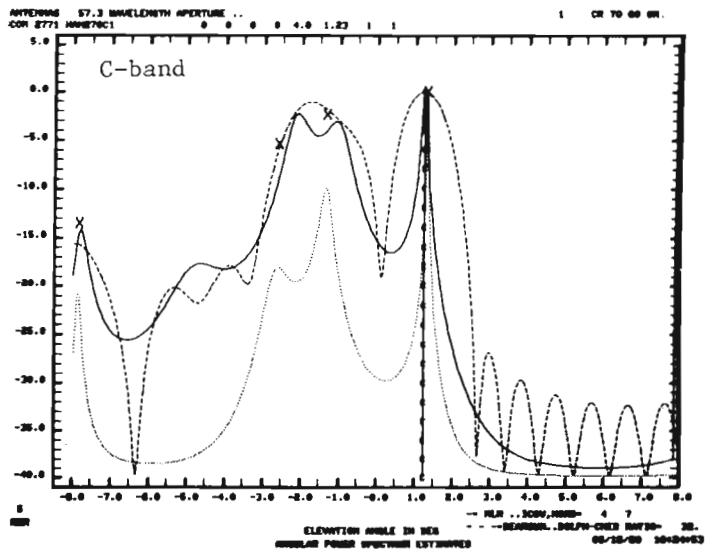

Fig. 5-5. Hanscom airport measurement: L- and C-bands elevation arrays, helicopter at $\theta_{EL} \simeq 1.2°$.

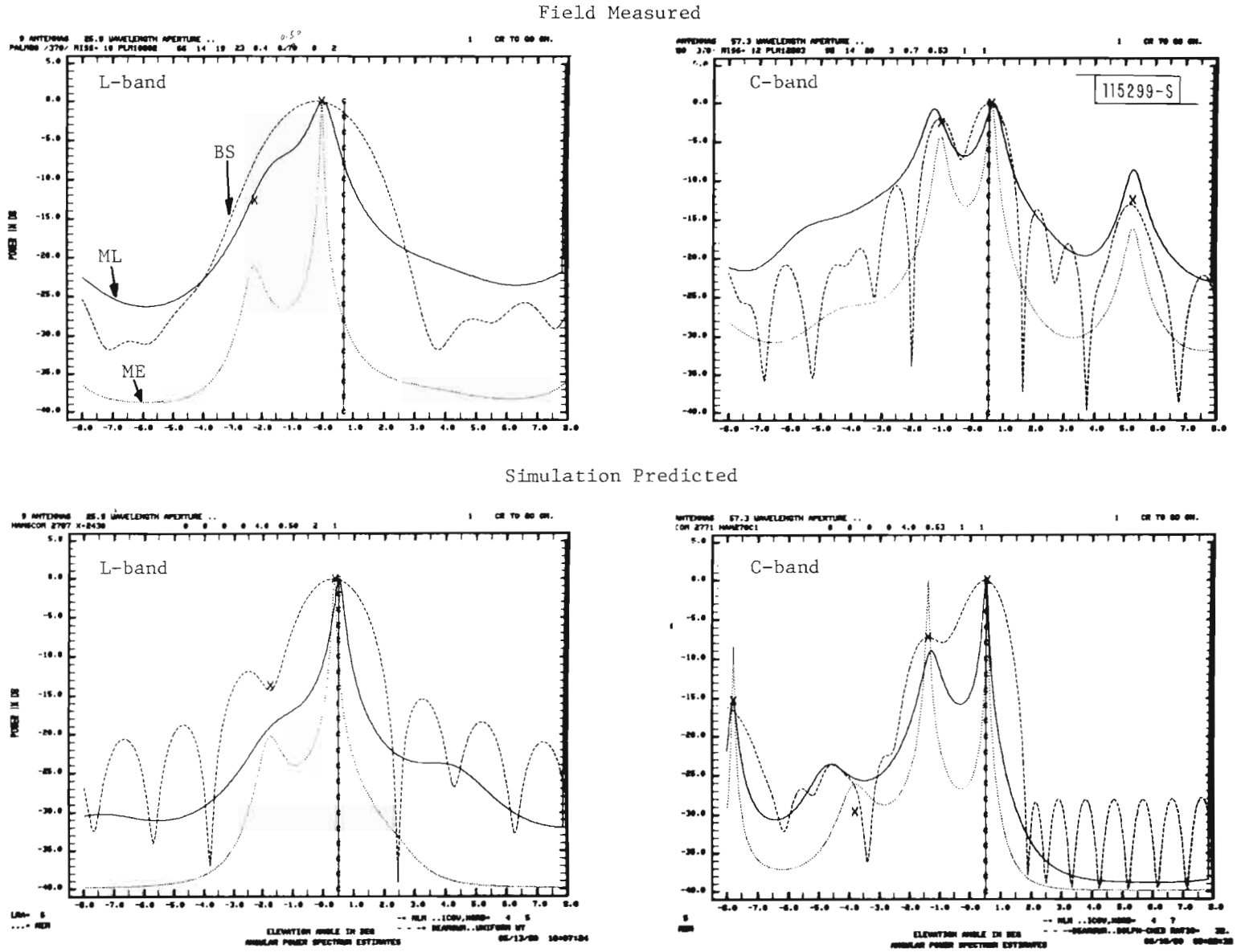

Fig. 5-6. Hanscom airport measurement: L- and C-bands elevation arrays, helicopter at $\theta_{EL} \simeq 0.5°$.

the L-band results reported previously [2] and those shown here. However, the C-band results consistently indicated more than one multipath arrival for various helicopter elevation angles, from 6° down to 0.5°. This suggests that the ground appearing to be flat at L band is not so flat at C band. In fact, if we take a look of the terrain height profile for this measurement site (Fig. 4-1), we do notice several segments of ground with slightly different slopes. These ground segments may be too small to produce any noticeable specular reflection at the L-band. They apparently are large enough at the C-band to yield significant reflection.

The observed L-band and C-band multipath environments appear to be different in terms of the number of multipath arrivals, however, they do have several common features. Ground reflection appears to be specular for both L band and C band, with high multipath level. For most of the flight path, the L band multipath level stays around -1 dB to -3 dB, while the C band multipath level increases from -6 dB at high elevation angles to -2 dB at low elevation angles. The arrival angle of the largest reflection at the C band is very much the same as that of the L-band reflection. This implies that the dominant specular reflection came from the same ground plate at both L band and C band. No diffuse multipath is evident in either the L-band or the C-band spectral estimates.

In our previous L-band measurements at Hanscom airport [2], we found that the agreement between the MLS multipath simulation predicted results and the field measurement results was very good. This good agreement, in terms of the number of the multipath arrivals, their arrival angles and multipath levels, is again very evident in the results shown here for both L band and C band*. Figure 5-7 shows the EL multipath level and EL angle error versus the direct signal EL angle for the field measured and MLS simulation predicted results.

---

*For the C-band result in Fig. 5-6, the apparent difference in the arrival angle of the second multipath indicated by the field data and that given by the simulation is due to the grating lobes of our C-band array. Since our C-band array has 17° grating lobe repetition, the arrival angle of 6° indicated in the field data actually could be -11° which is more in line with -8° given by the simulation.

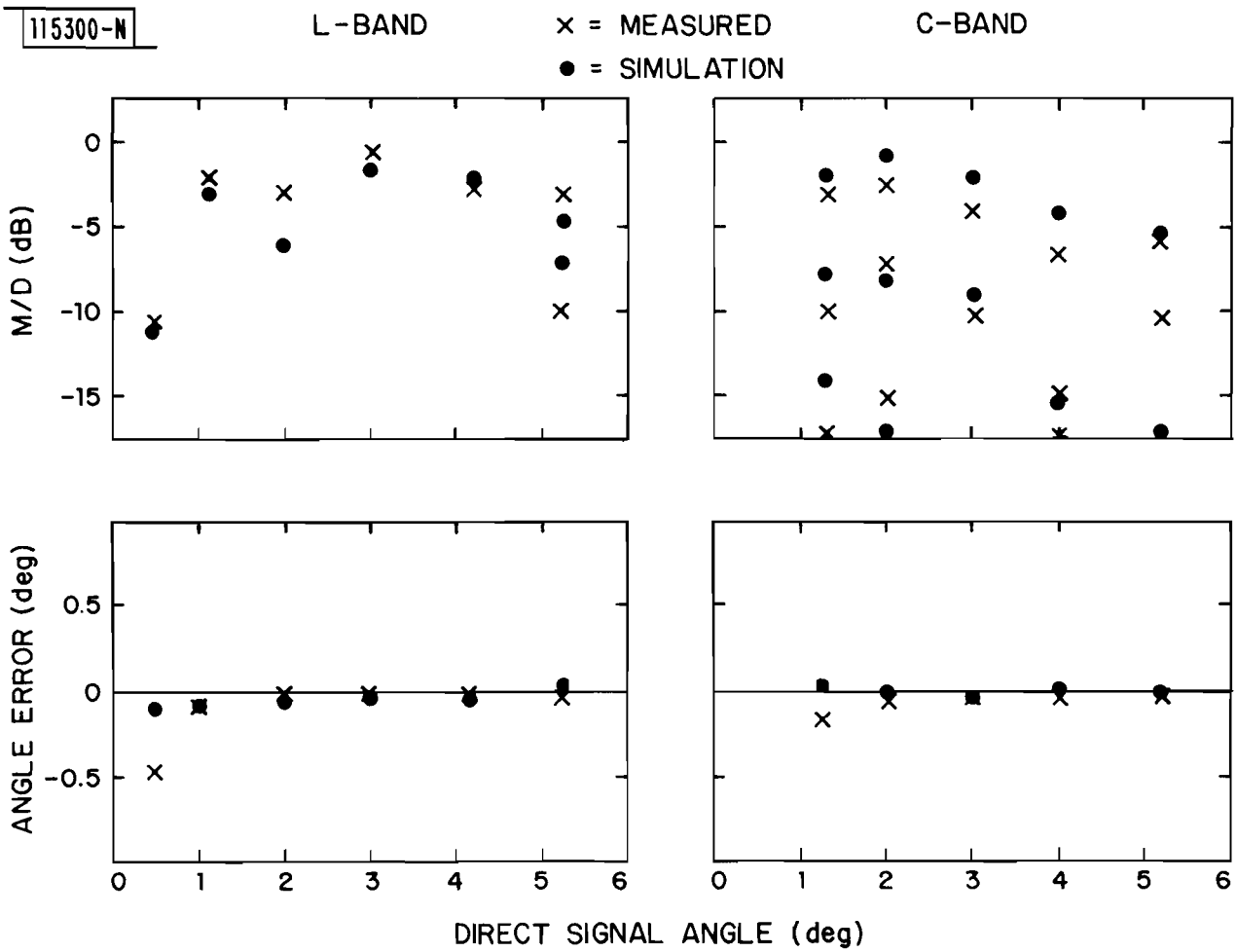

Fig. 5-7. Hanscom airport measurement: M/D ratios and angle errors.

Figure 5-8 shows L-band azimuth (AZ) angular power spectral estimates obtained with the L-band AZ array for two helicopter elevation angles. The AZ angular power spectrum gives the azimuthal distribution of the multipath arrivals for a given direct signal elevation angle. No simulation results are shown here, since for the ground model with no cross-range tilts the azimuthal arrival angles of the ground reflections will be the same as that of the direct signal. In fact, we do observe this fact in the field measured results shown in Fig. 5-8. The AZ angular power spectrum only shows a single spectral peak, indicating that all the signal arrivals (direct signal and multipath signals) came from the same azimuth angle*. Thus, for the flat terrain with no cross-range tilts as the one here, the terrain multipath should not affect the azimuth angle estimation of the direct signal arrival.

It should also be noted that no multipath is evident from Pine Hill, at an azimuth of 20° with respect to the direct signal. This suggests that even at L-band, tree covered hills are not significant multipath sources.

To show the data repeatability in our field measurements, Fig. 5-9 shows the L-band EL angular power spectrum for the measurement taken in 1980 and that in 1977, for the helicopter roughly at the same position. We notice that they look almost identical. This also indicates that the terrain multipath environment at Hanscom airport site has not changed.

B. Fort Devens Golf Course

As described in Chapter IV Section B, at this site measurements were taken along three radial lines O-A, O-B, and O-C (Fig. 4-3). The terrain conditions along these three radial lines were very different from the flat ground situation at Hanscom airport. We found in our previous L-band measurements at this site [2] that the terrain multipath environment was more

---

*The azimuth angle was measured relatively with respect to the AZ array boresight direction in the field measurement. For this particular flight, the helicopter was off array boresight by the angle indicated in Fig. 5-8. It is noted that the helicopter was drifting slightly in azimuth for this particular flight while making a vertical descent ($\theta_{AZ} \simeq -7°$ at $\theta_{EL} \simeq 3°$ while $\theta_{AZ} \simeq -5.5°$ at $\theta_{EL} \simeq 0.5°$.

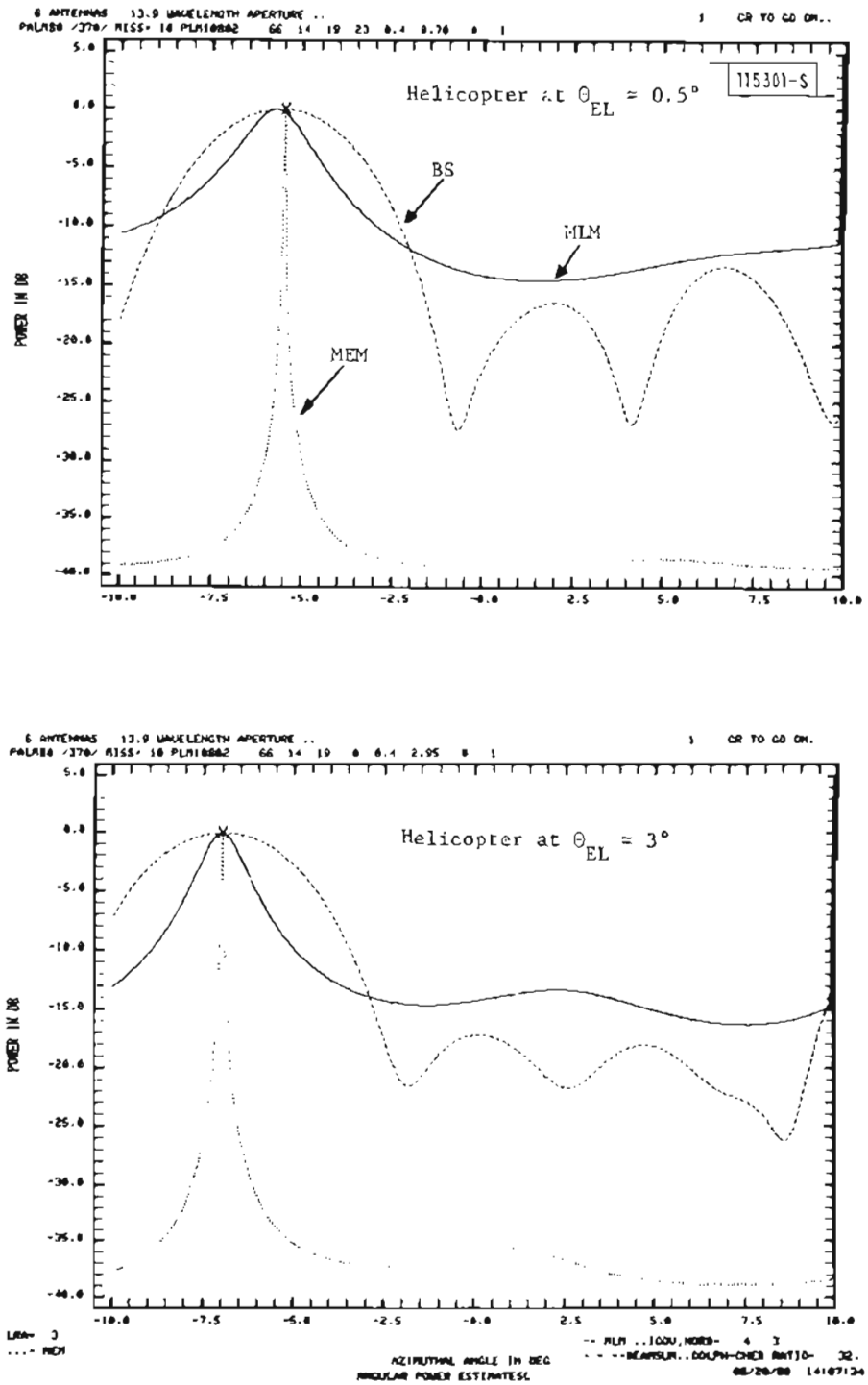

Fig. 5-8. Hanscom airport measurement: L-band azimuth array.

Measurement in 1977

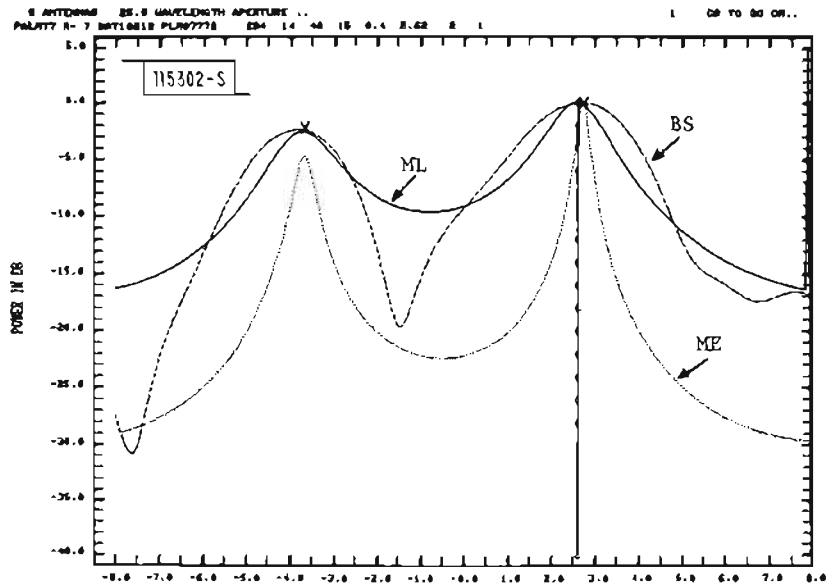

Measurement in 1980

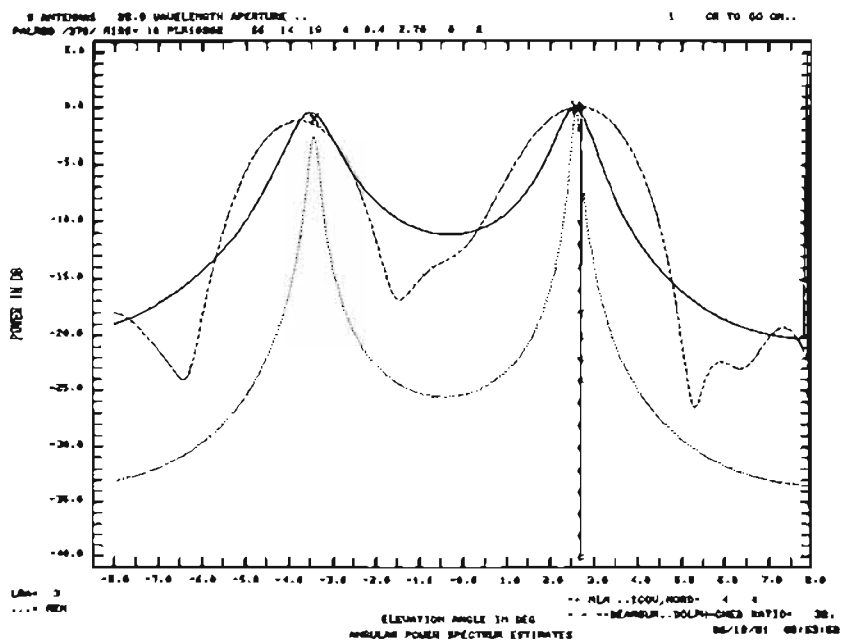

Fig. 5-9. Hanscom airport measurement: data repeatability, L-band elevation array.

complicated than that at Hanscom airport. The good agreement between the MLS multipath simulation predicted results obtained by the building reflection calculation and the field measured results was observed only for the measurements along the radial line O-B where almost no cross-range tilts were observed. Thus, this time, the MLS simulation results for the measurements at this site were obtained in two ways, as described earlier, i.e.: (1) using building reflection calculation which ignored the terrain cross-range tilts, and (2) using ground reflection calculation with focusing ground option which could take both the ground along-range height and cross-range tilt into consideration. So, in the following figures which show the EL angular power spectrum, parts (b) and (c) are both for the MLS simulation results, obtained in the above mentioned two ways, respectively.

1. Radial Line O-A

Figures 5-10 through 5-18 show the representative results of the EL angular power spectral estimates for the measurements taken along the radial line O-A. For the field measured results, in general, the C-band data show lower multipath level than the L-band data (maximum of -6 dB versus that of -3 dB). Although the focusing ground reflections (i.e., more than one specular reflection appear at the same time) are observed in both the C-band and the L-band results, the C-band results consistently indicate more multipath arrivals than the L-band results. However, unlike the cases in the Hanscom airport measurements where the dominant multipath arrivals in the L band and the C band appeared to come from the same ground plate, no such relation between the L-band and the C-band multipath arrivals is obvious here.

For both the L band and the C band, the MLS mulitpath simulation predicted results appear to be fairly different from the corresponding field measured results. In terms of the number of multipath arrivals, the agreement between the MLS multipath simulation predicted results and the field measured results seems fair. However, in terms of the arrival angles of various multipaths, the agreement in general is poor, especially for the simulation results obtained with the building reflection calculation (part (b) in each figure). The simulation result obtained with the focusing ground option of the ground

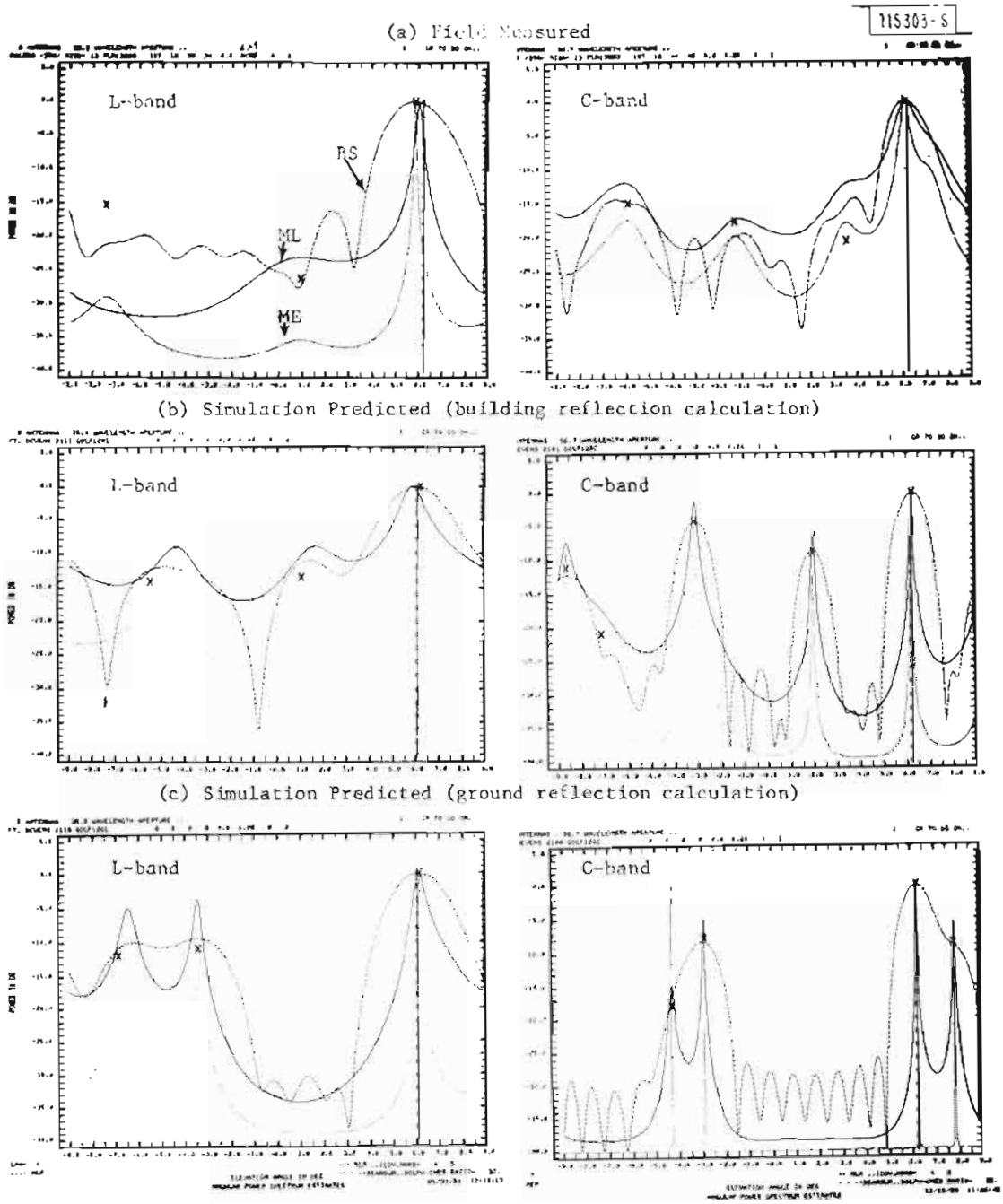

Fig. 5-10. Fort Devens measurement: radial line O-A, L-band and C-band elevation arrays, helicopter at $\theta_{EL} \approx 6°$.

(a) Field Measured

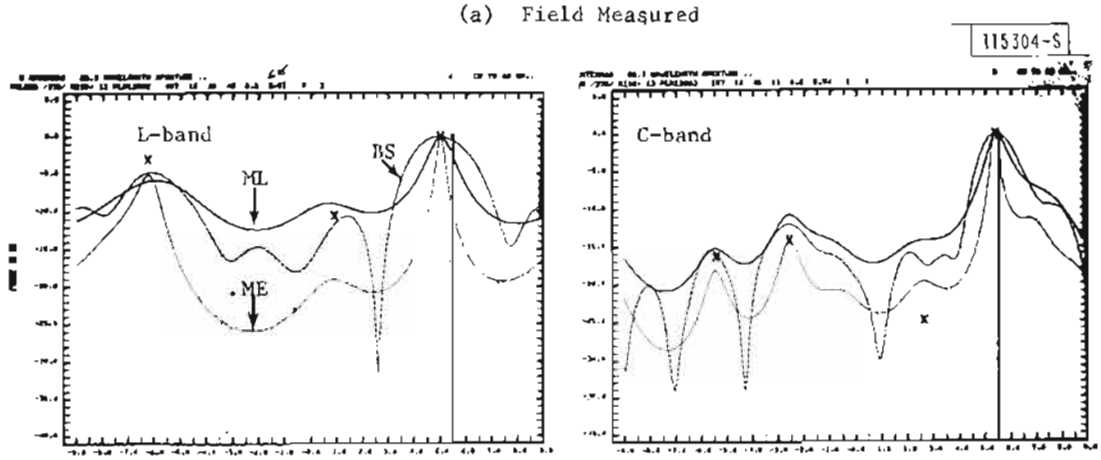

(b) Simulation Predicted (building reflection calculation)

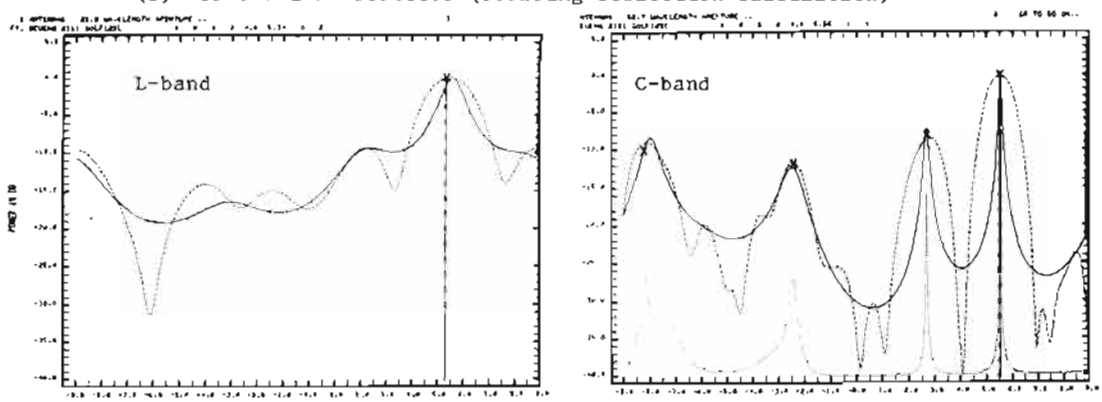

(c) Simulation Predicted (ground reflection calculation)

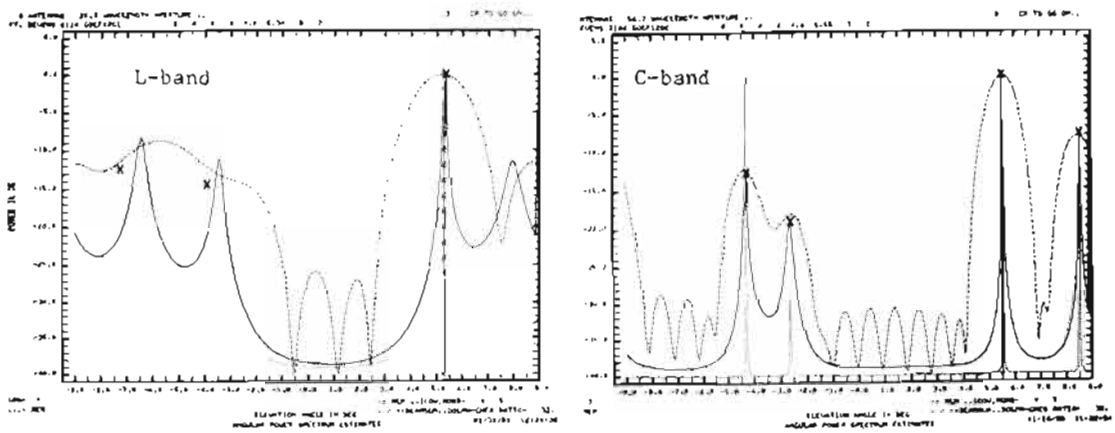

Fig. 5-11. Fort Devens measurement: radial line O-A, L-band and C-band elevation arrays, helicopter at $\theta_{EL} \approx 5.5°$.

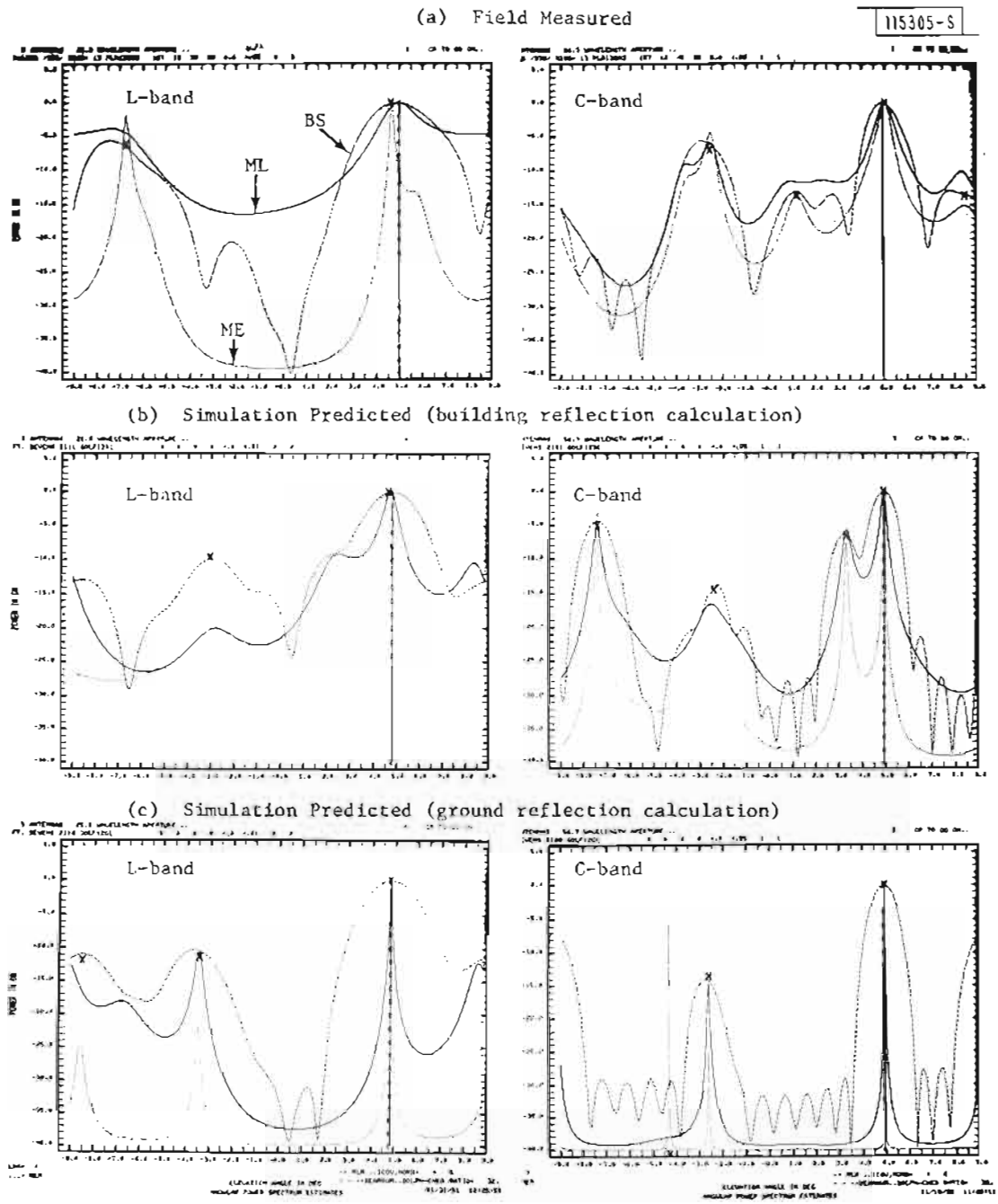

Fig. 5-12. Fort Devens measurement: radial line O-A, L-band and C-band elevation arrays, helicopter at $\theta_{EL} \simeq 5°$.

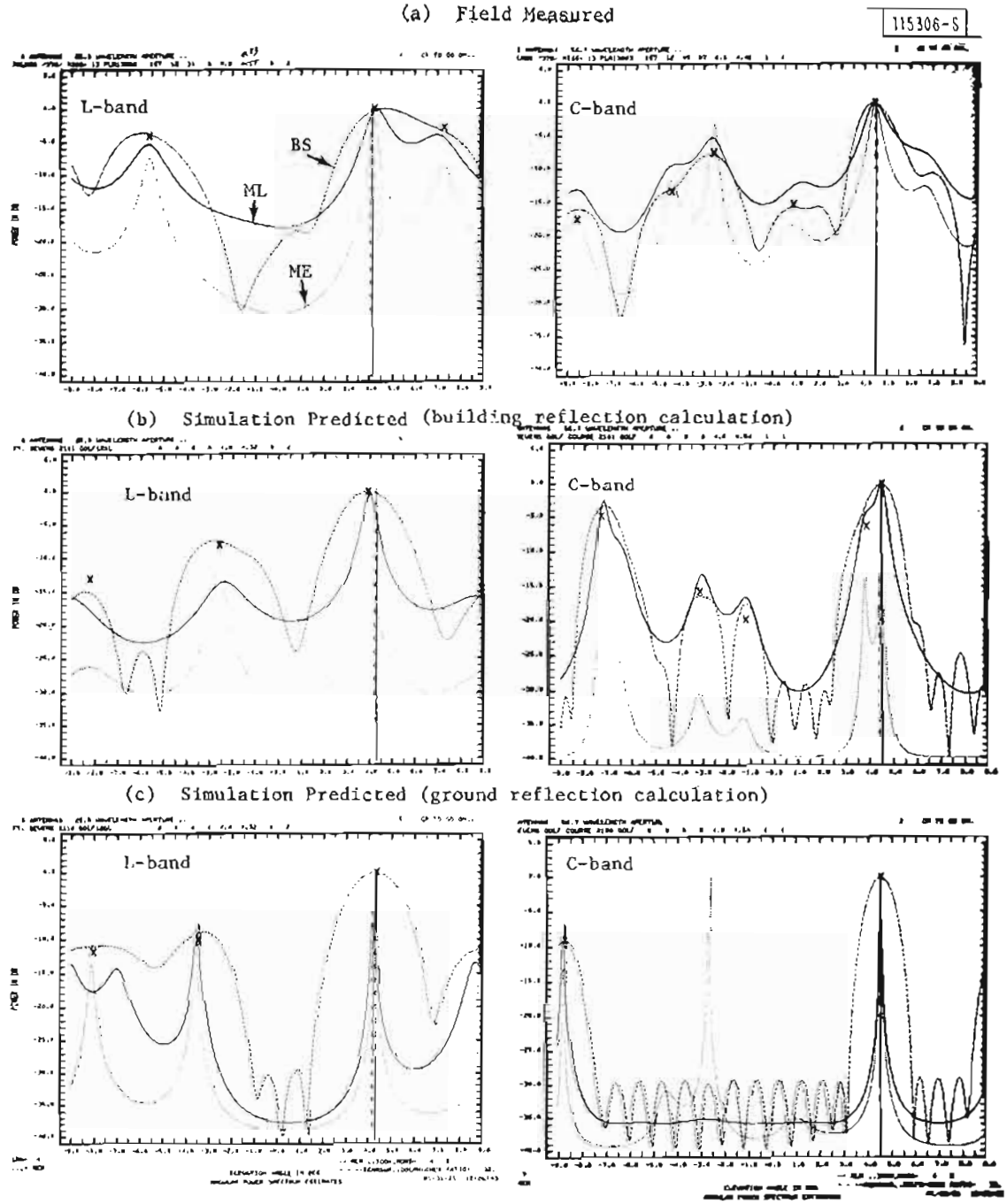

Fig. 5-13. Fort Devens measurement: radial line O-A, L-band and C-band elevation arrays, helicopter at $\theta_{EL} \approx 4.5°$.

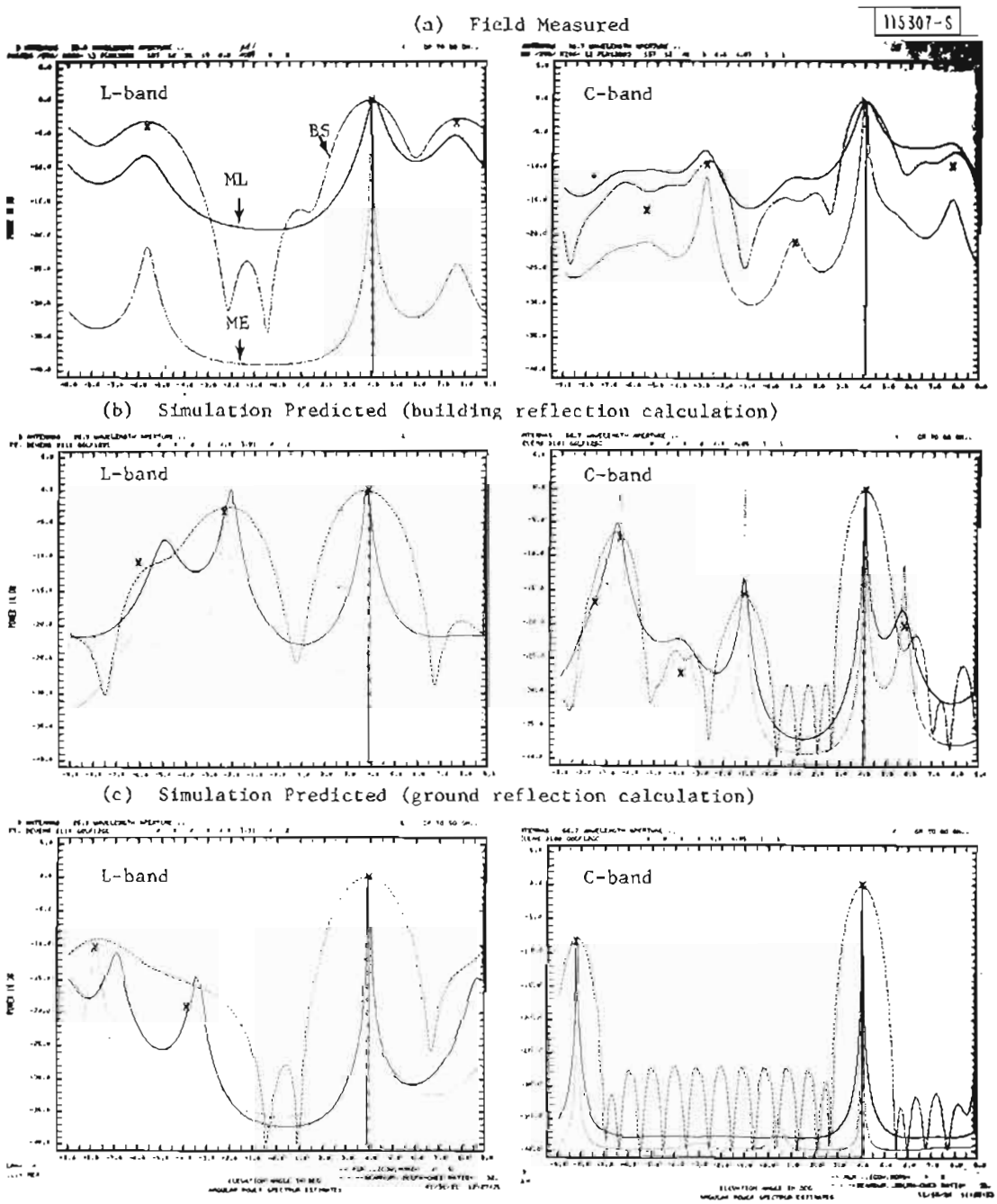

Fig. 5-14. Fort Devens measurement: radial line O-A, L-band and C-band elevation arrays, helicopter at $\theta_{EL} \simeq 4°$.

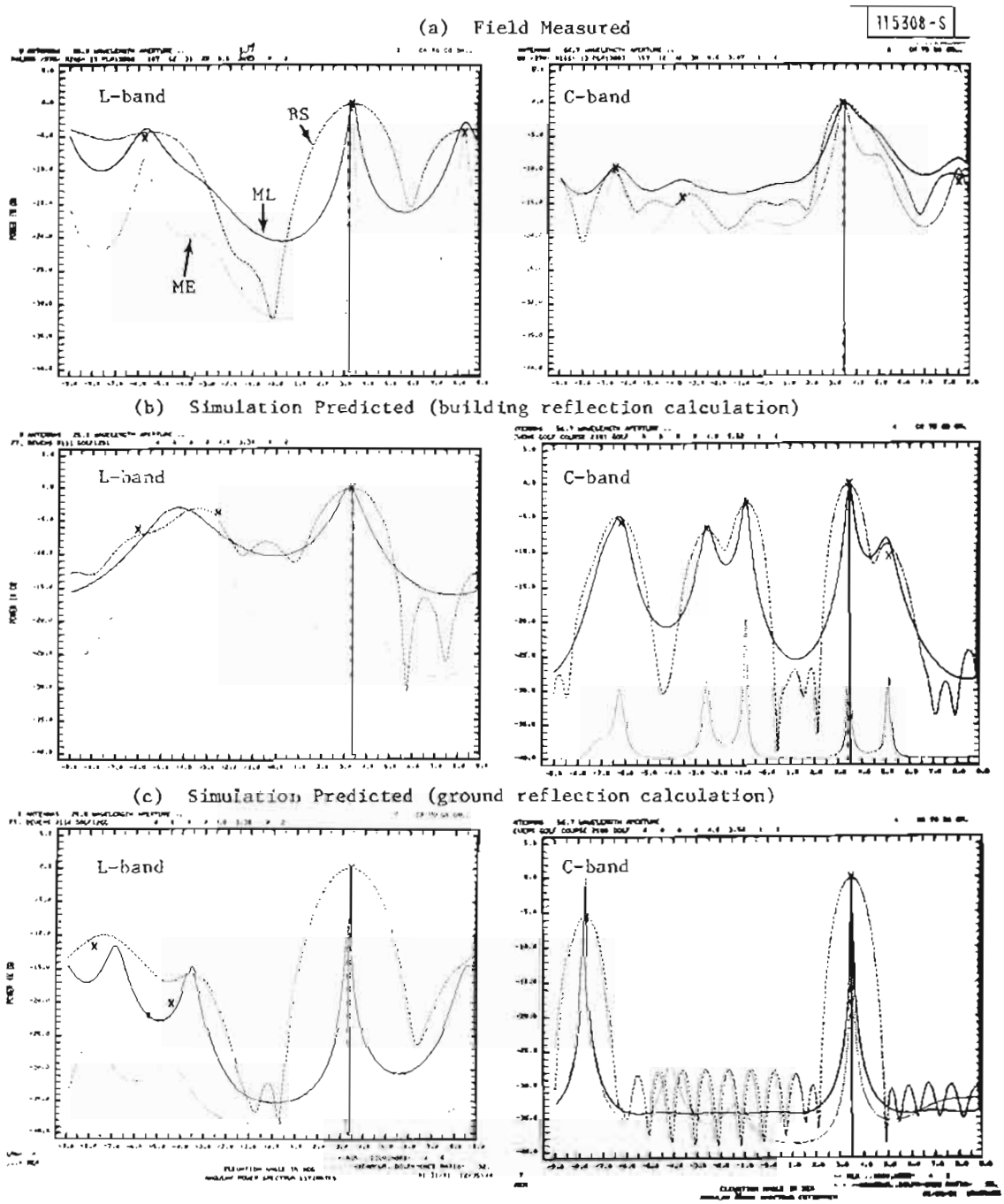

Fig. 5-15. Fort Devens measurement: radial line O-A, L-band and C-band elevation arrays, helicopter at θ_{EL} = 3.5°.

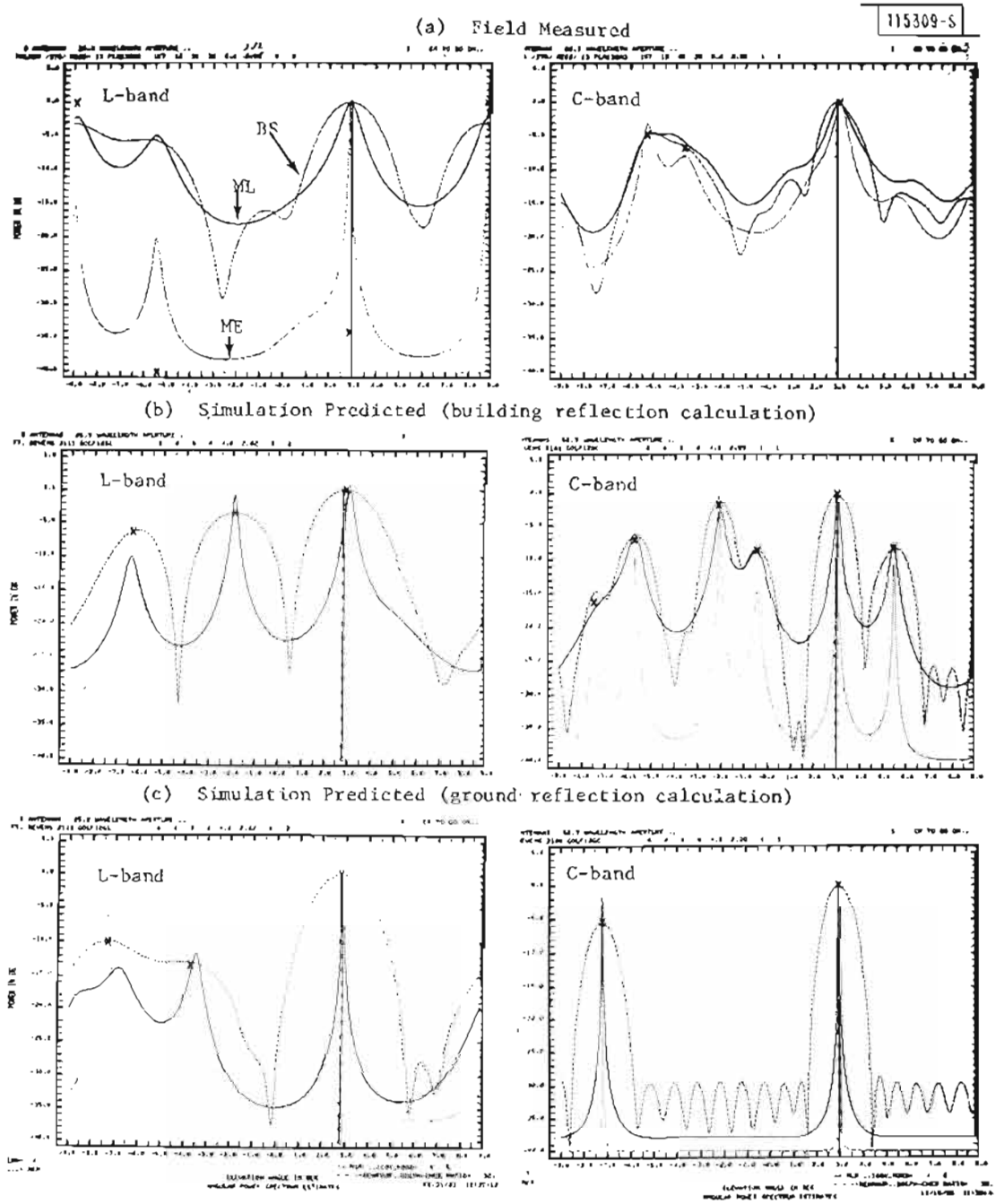

Fig. 5-16. Fort Devens measurement: radial line O-A, L-band and C-band elevation arrays, helicopter at $\theta_{EL} \approx 3°$.

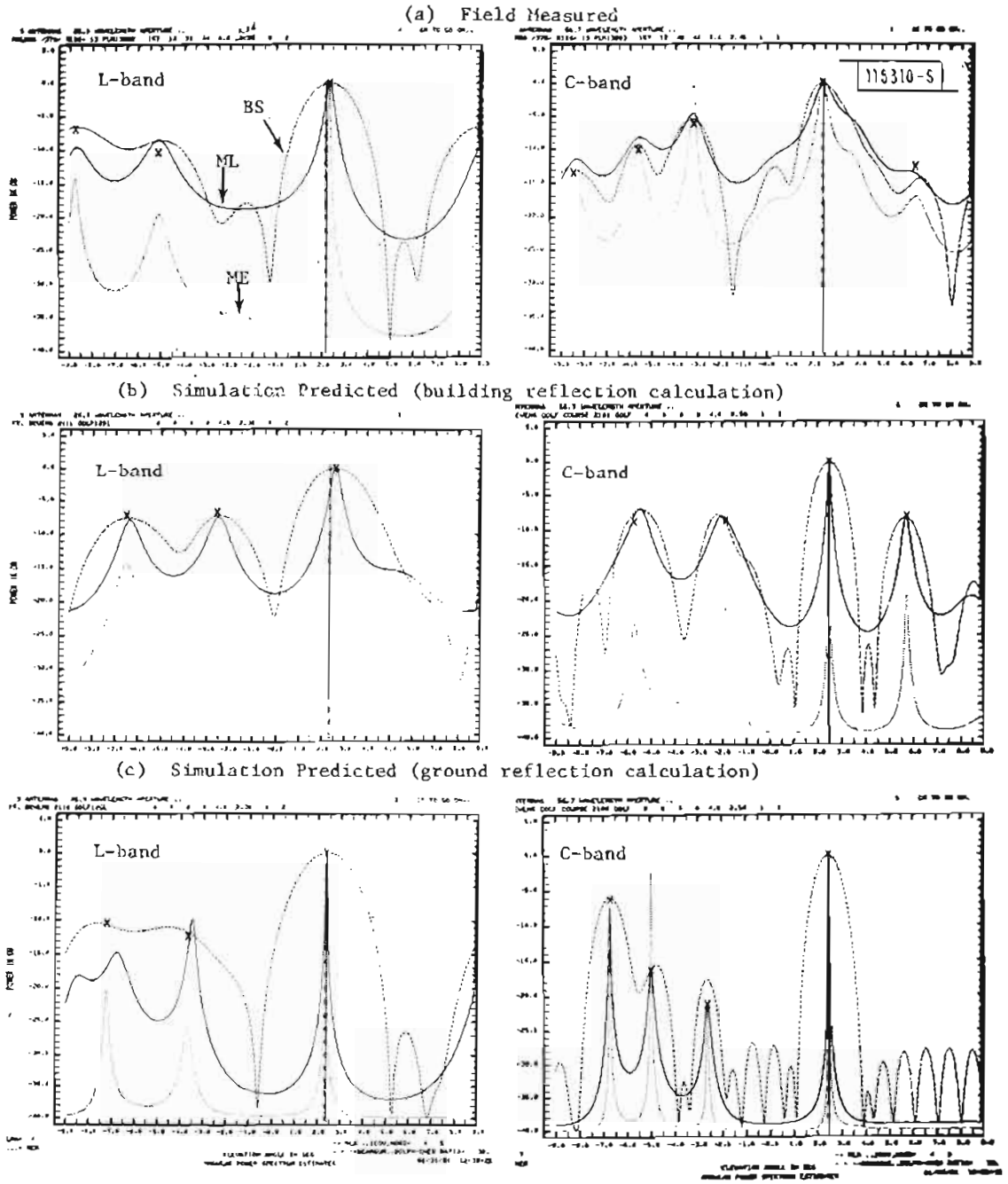

Fig. 5-17. Fort Devens measurement: radial line O-A, L-band and C-band elevation arrays, helicopter at $\theta_{EL} \approx 2.5°$.

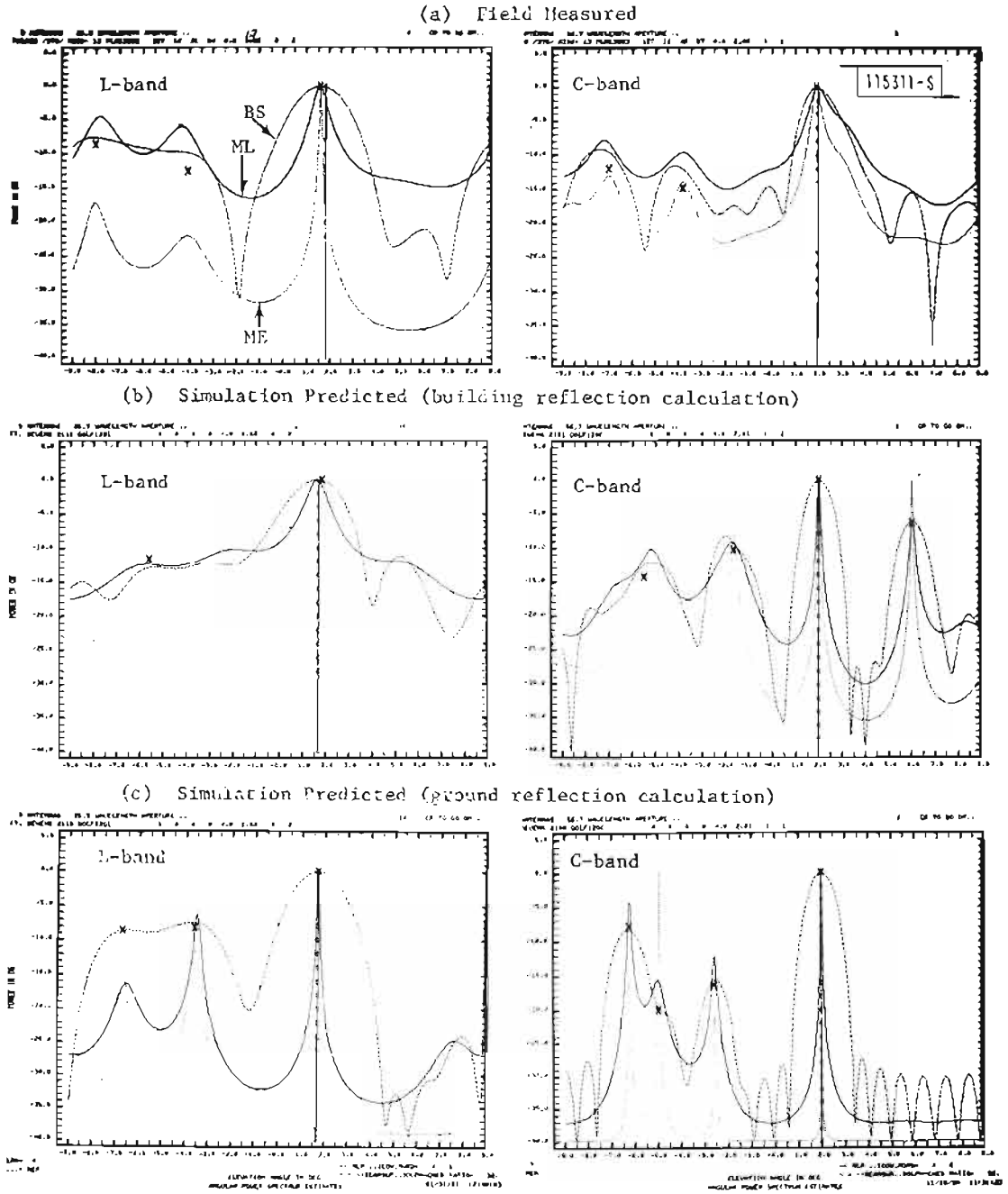

Fig. 5-18. Fort Devens measurement: radial line O-A, L-band and C-band elevation arrays, helicopter at $\theta_{EL} \approx 2°$.

reflection calculation (part (c) in each figure) generally have sharper spectral peaks (ME and ML spectral estimates) than those obtained with the building reflection calculation. The causes for this apparent difference probably are: (1)* the number of rectangular ground plates in the ground model used for the building reflection calculation was larger than that used for the ground reflection calculation with the focusing ground option and (2) the same AR model order was used for both calculations in producing the ME spectral estimate. Between the simulation results obtained with the building reflection calculation and those with the focusing ground option of the ground reflection calculation, the latter appears to agree better with the field measured results. This seems reasonable, since the latter considered the ground cross-range tilts while the former did not and the terrain along this radial line did have various cross-range tilts. Figure 5-19 shows the EL multipath level and EL angle error versus direct signal EL angle for the field measured results and the simulation predicted results (parts (a) and (c) in Figs. 5-10 to 5-18).

Figures 5-20 and 5-21 show L-band AZ angular power spectral estimates for two helicopter elevation angles. The observed offset** between the azimuth arrival angle of the direct signal in the field measured results ($\theta_{AZ} \simeq 5°$) and that in the simulation results ($\theta_{AZ} = 0°$) is due to the fact that no azimuthal theodolite tracking of the helicopter was made in the field measurements and, consequently, the helicopter was taken to be along the L-band AZ array boresight (i.e., $\theta_{AZ} = 0°$) in the MLS multipath simulation run. Thus, in making the comparison between the field measured results and simulation results, the actual AZ angles of various signal arrivals indicated in the

---

*As discussed earlier in this chapter, this was done because (1) the maximum number of rectangular plates which could be handled by the building reflection calculation was fifty (50) while that with the ground reflection calculation was fifteen (15) and (2) we would like to model the real terrain with as many rectangular plates as practically possible to see if the additional detail would produce better agreement.

**This type of offset in the direct signal azimuth angles applies to all AZ angular power spectral estimates shown here.

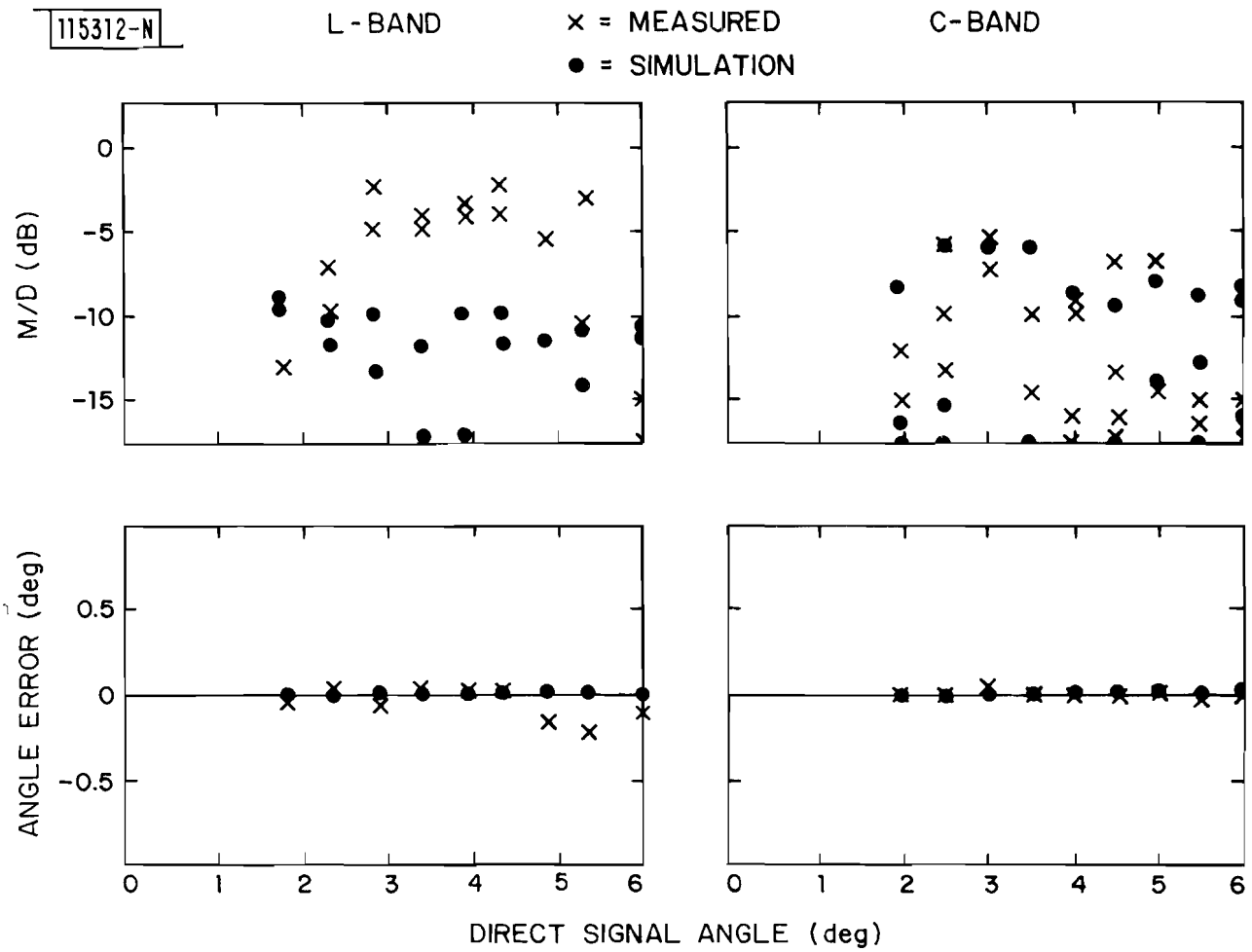

Fig. 5-19. Fort Devens measurement: radial line O-A, L-band and C-band elevation arrays, M/D ratios and angle errors.

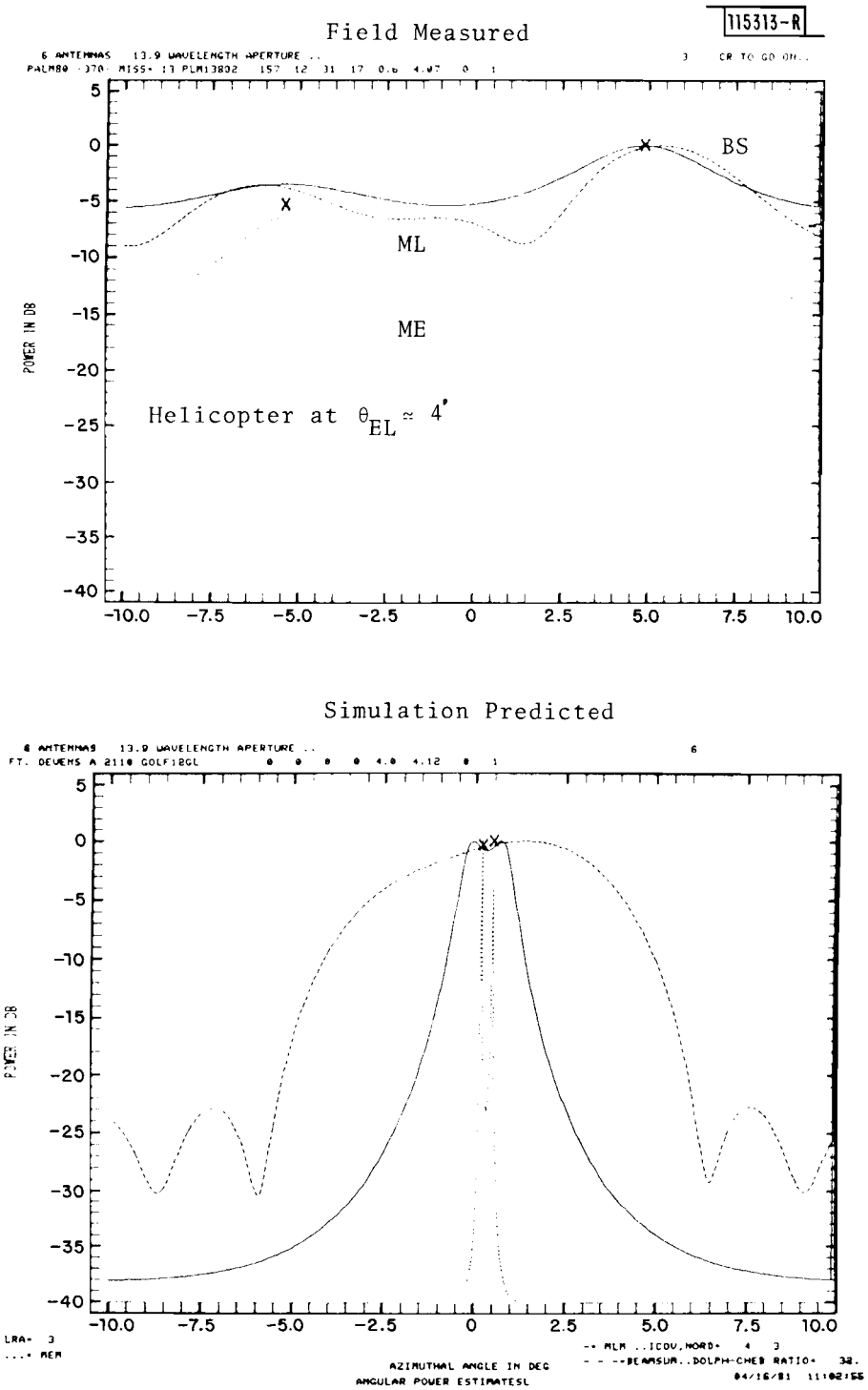

Fig. 5-20. Fort Devens measurement: radial line O-A, L-band azimuth array, $\theta_{EL} \simeq 4°$.

Field Measured

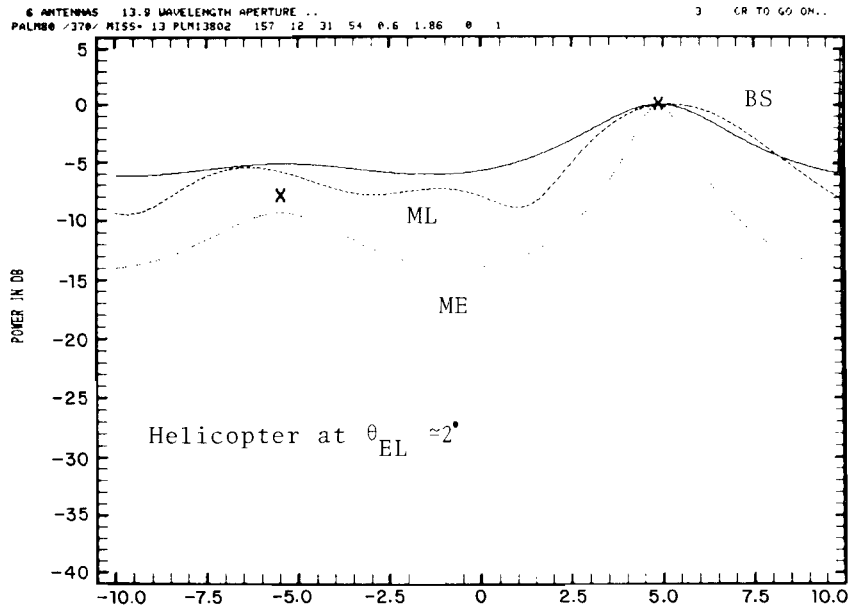

Simulation Predicted

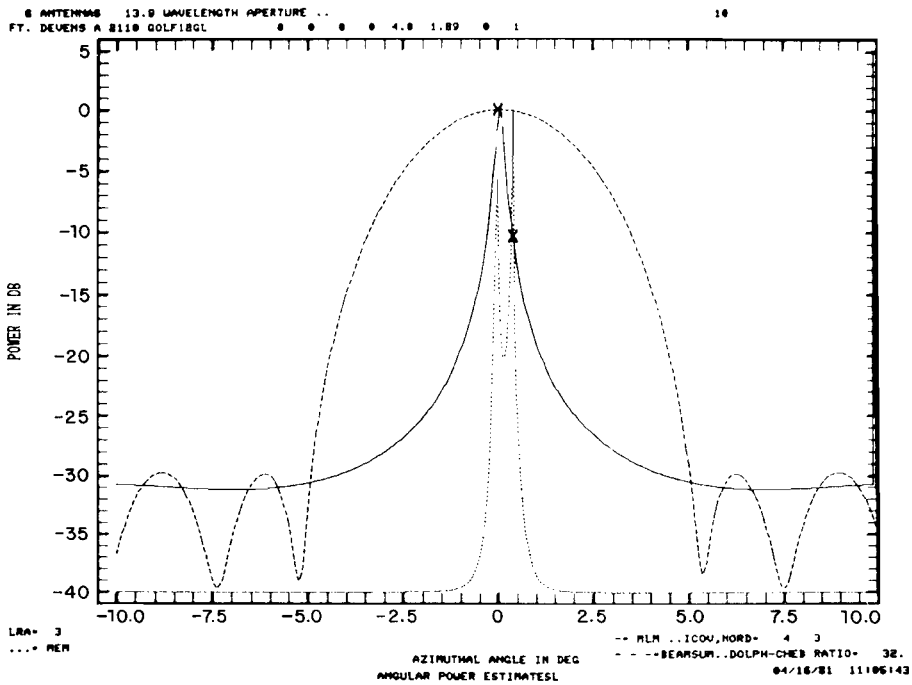

Fig. 5-21. Fort Devens measurement: radial line O-A, L-band azimuth array, $\theta_{EL} \simeq 2°$.

spectral estimates are not important. The relevant information is the angular separation between the direct signal arrival and the multipath arrival(s) (if there is any). Since the terrain here did show various cross-range tilts (Fig. 4-4), we did expect that there would be more than one spectral peak in the AZ angular power spectral estimate* and the AZ arrival angles of the direct signal and the multipath signal might be different. Both the field measured results and the simulation predicted results show two spectral peaks. However, the angular separation between two spectral peaks in the field measured results and that indicated by the simulation results are very different. Also, the spectral peaks are much wider in the field measured results. These apparent differences between the field measured results and the simulation results can be explained as follows:

(1) With the terrain cross-range tilts indicated in Fig. 4-4, the azimuth separation angle between the direct and multipath arrivals should be around 0.5° to 1° degrees like that indicated in the simulation result, instead of 10° shown in the field measured data. Thus, the spectral peak around -5° in the field measured results probably was the multipath arrivals from some nearby hills or tall buildings which we did not model in the simulation.

(2) There might be multipath arrival around the direct signal AZ arrival angle at 5°, but they could not be resolved because at most we could only use a 2-pole AR model to calculate the ME spectrum, as explained above.

These apparent differences in the AZ angular power spectral estimates might explain the poor agreement between field measured results and the simulation results that we observed in the EL angular power spectral estimates. If, indeed, the second spectral peak at -5° in the AZ spectral estimate was due to the multipath arrivals from some nearby hills as we conjectured above

*On the assumption that the separation angle between the direct signal and the multipath signal was large enough such that they could be resolved with the ME angular power spectral estimate. However, at most we could only expect to see two spectral peaks, since our L-band AZ array only had six antenna elements and consequently we calculated the ME angular power spectrum using a 2 pole AR model.

the multipath arrivals indicated in the EL angular power spectral estimates might not be entirely coming from the terrain reflections from the ground** which was modelled in the MLS multipath simulation run (Fig. 4-4).

2. Radial Line O-B

Figures 5-22 to 5-29 show examples of the EL angular power spectral estimates for the measurements taken along the radial line O-B. For the field measured results (part (a) in each figure), the C-band data indicate much lower multipath levels than the L-band data, similar to what we observed for the radial line O-A. Here, the highest multipath level is around -1 dB for the L band and is about -7 dB for the C band. Although the multipath level is much lower at C band, the C-band results consistently suggest more multipath arrivals. Again, here the phenomenon of the focusing ground reflections is very evident in both the L-band and the C-band results.

For the L band, agreement between the field measured results and the corresponding simulation predicted results is very good, in terms of the number of multipath arrivals, their EL arrival angles and M/D ratios. For the C band, good agreement is also observed in terms of the number of multipath arrivals and their arrival angles. However, the simulation predicted results indicate much higher M/D ratios than the field measured results. This seems understandable, since in the multipath simulation runs, the ground was assumed to be perfectly smooth*. Although the ground at this site appears to be physically smooth as can be seen in Fig. 4-7 and seems electrically smooth at the L band, the apparent difference in the M/D ratios between the C-band field measured results and the simulation results suggests that the ground probably

---

**As indicated in Fig. 4-4, the cross-range dimension of the rectangular ground plate was taken to be 100 feet.

*The MLS simulation model permits one to incorporate a rms roughness for each plate into the terrain reflectivity computations.

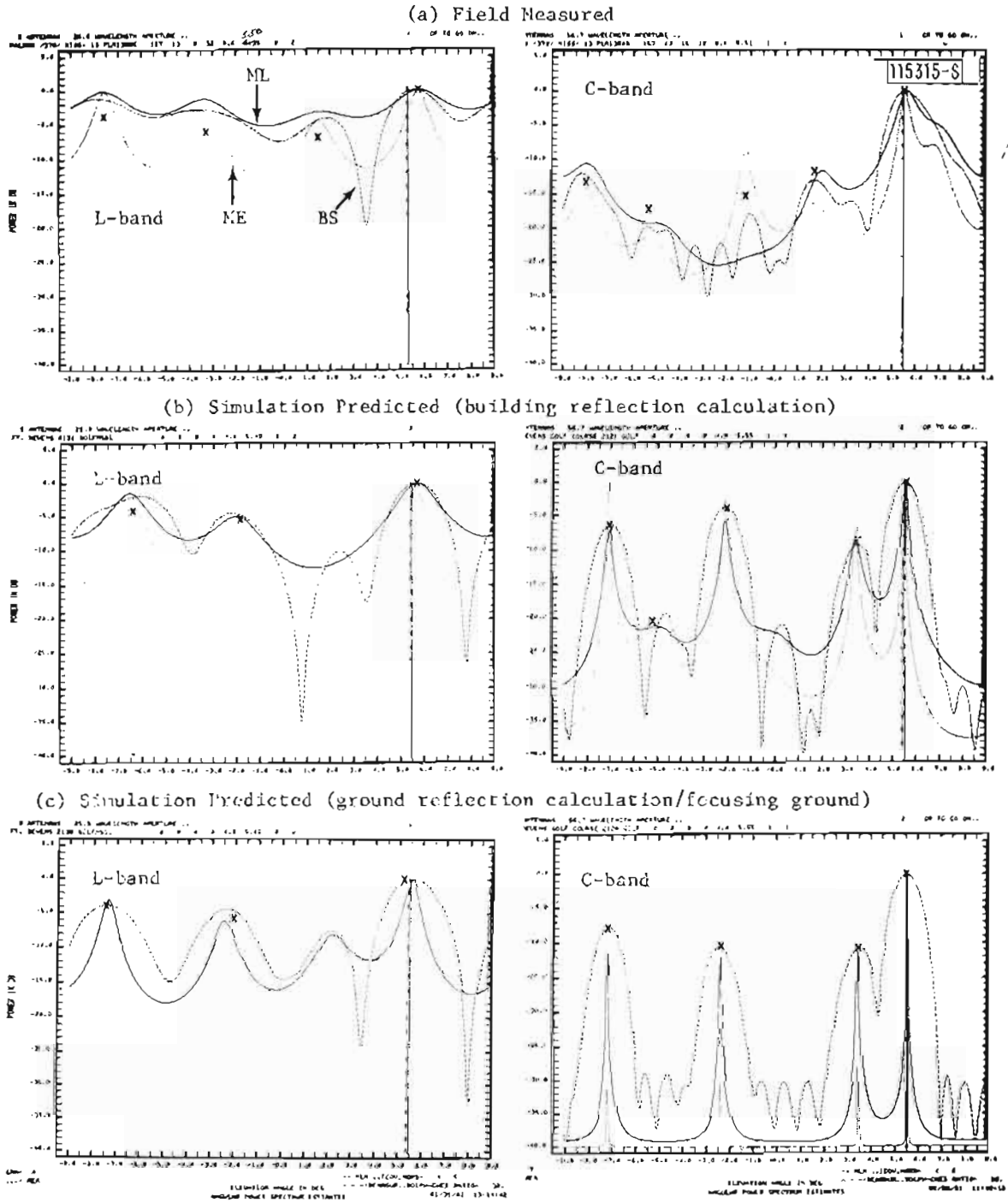

Fig. 5-22. Fort Devens measurement: radial line O-B, L-band and C-band elevation arrays, $\theta_{EL} \approx 5.5°$.

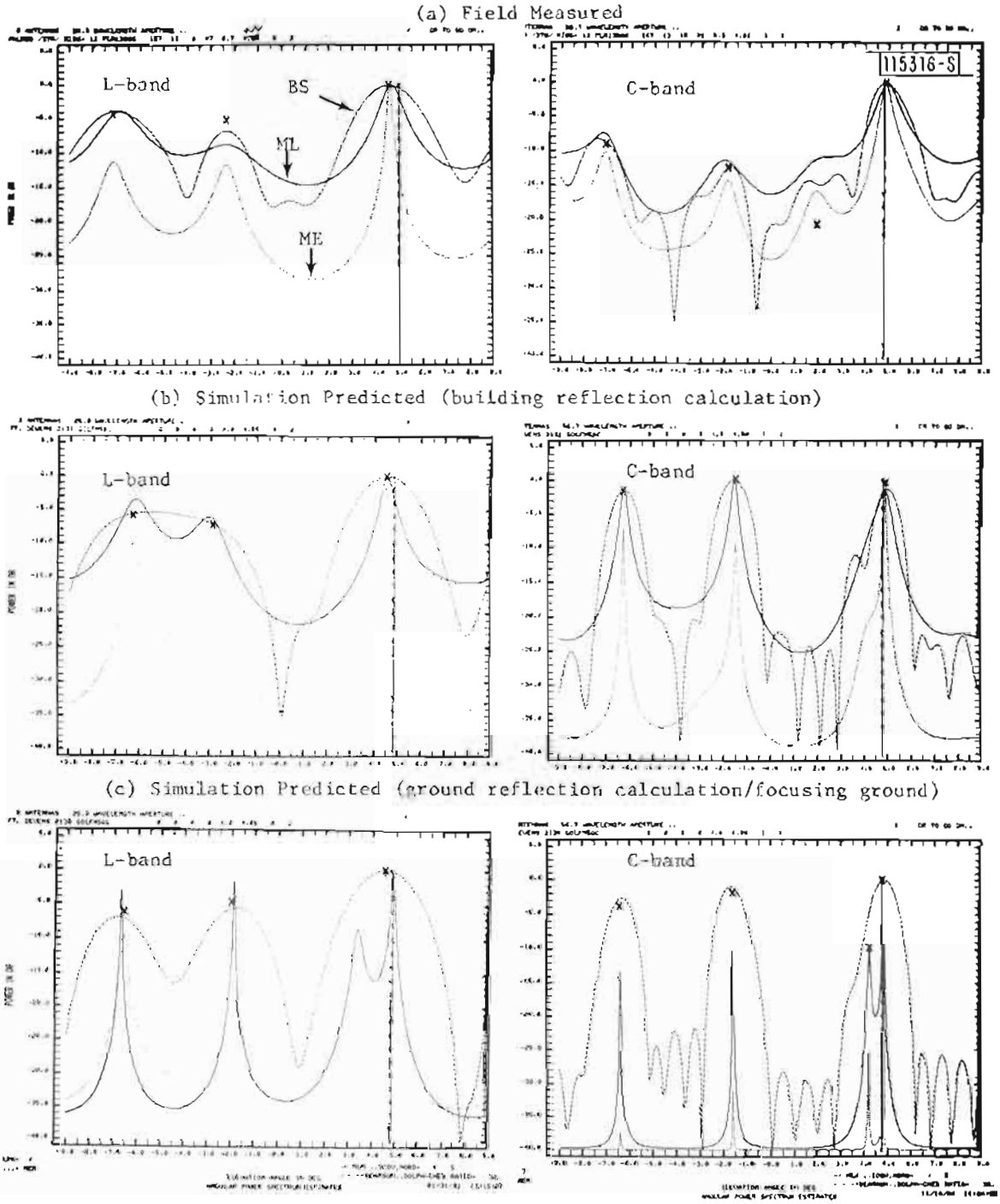

Fig. 5-23. Fort Devens measurement: radial line O-R, L-band and C-band elevation arrays, $\theta_{EL} \approx 4.8°$.

(a) Field Measured

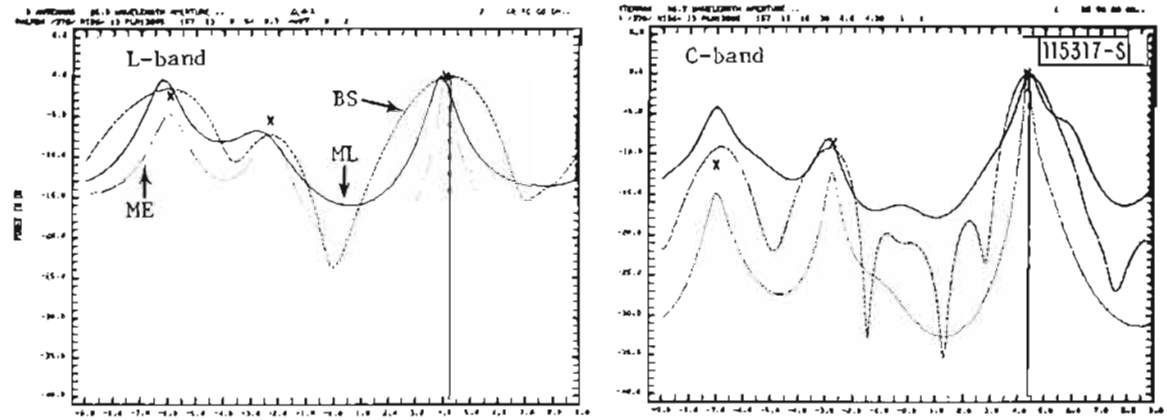

(b) Simulation Predicted (building reflection calculation)

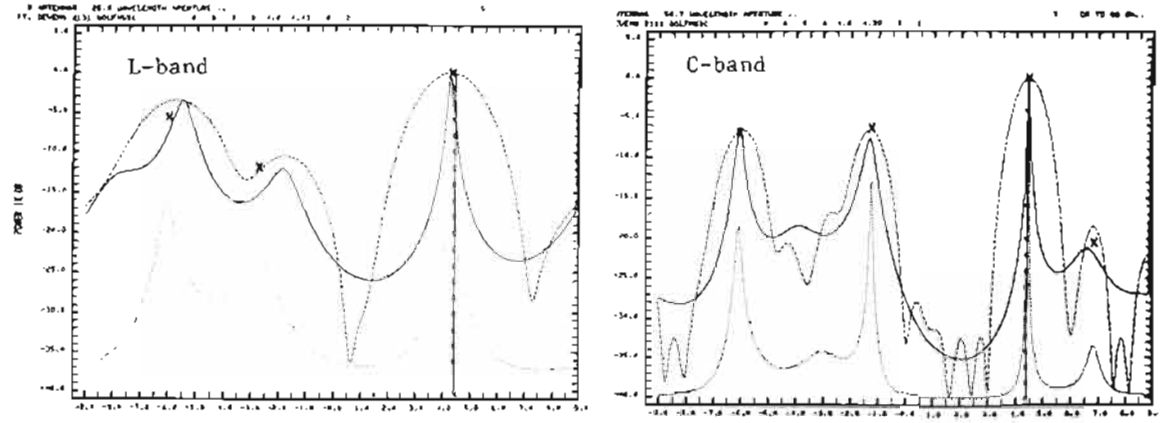

(c) Simulation Predicted (ground reflection calculation/focusing ground)

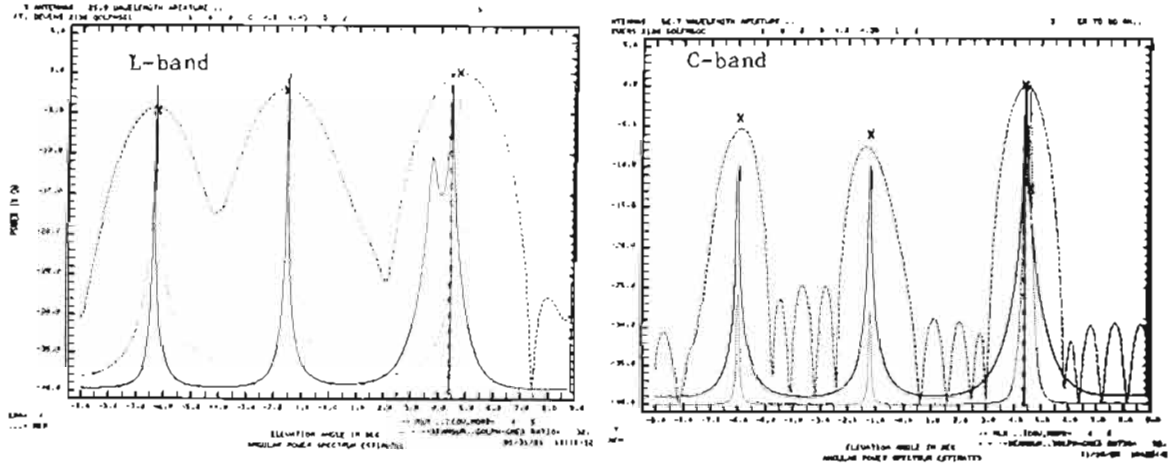

Fig. 5-24. Fort Devens measurement: radial line O-B, L-band and C-band elevation arrays, $\theta_{EL} \simeq 4.4°$.

(a) Field Measured

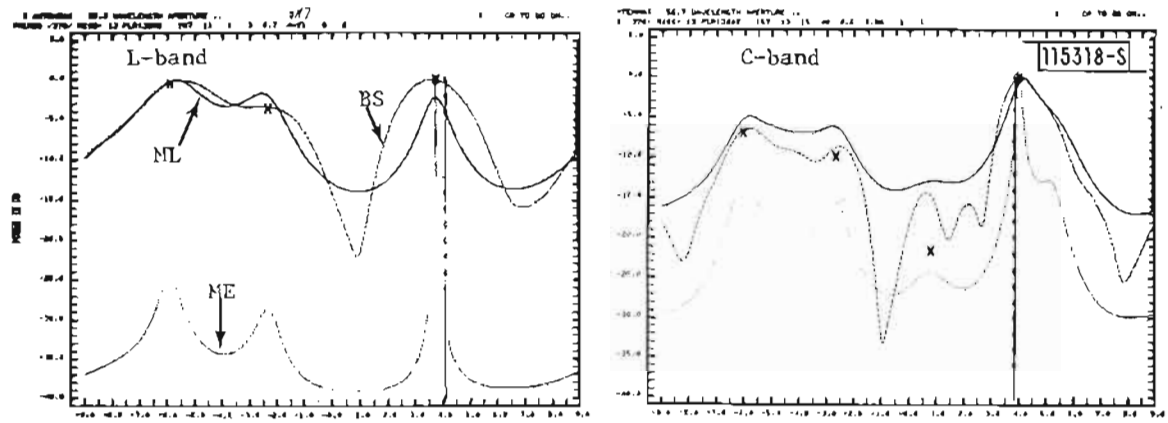

(b) Simulation Predicted (building reflection calculation)

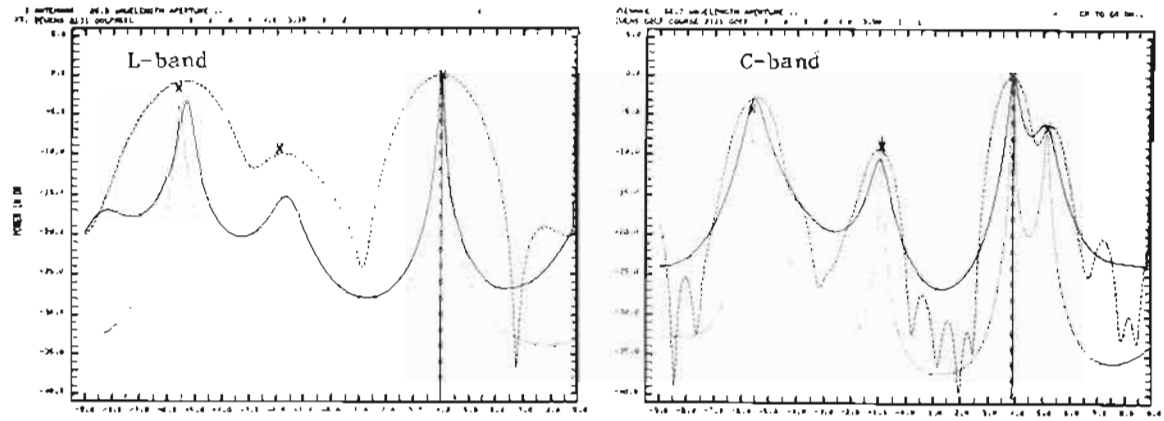

(c) Simulation Predicted (ground reflection calculation/focusing ground)

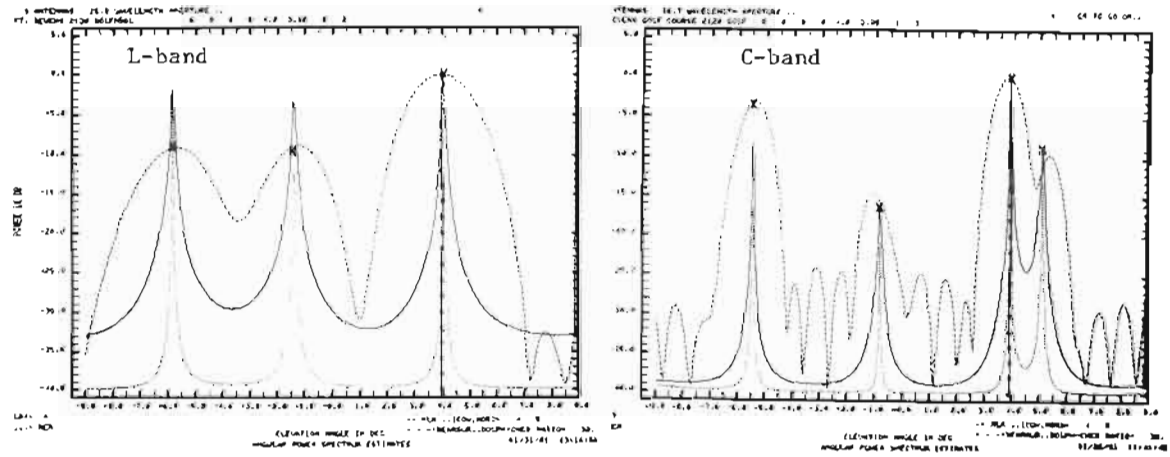

Fig. 5-25. Fort Devens measurement: radial line O-B, L-band and C-band elevation arrays, $\theta_{EL} \simeq 4°$.

(a) Field Measured

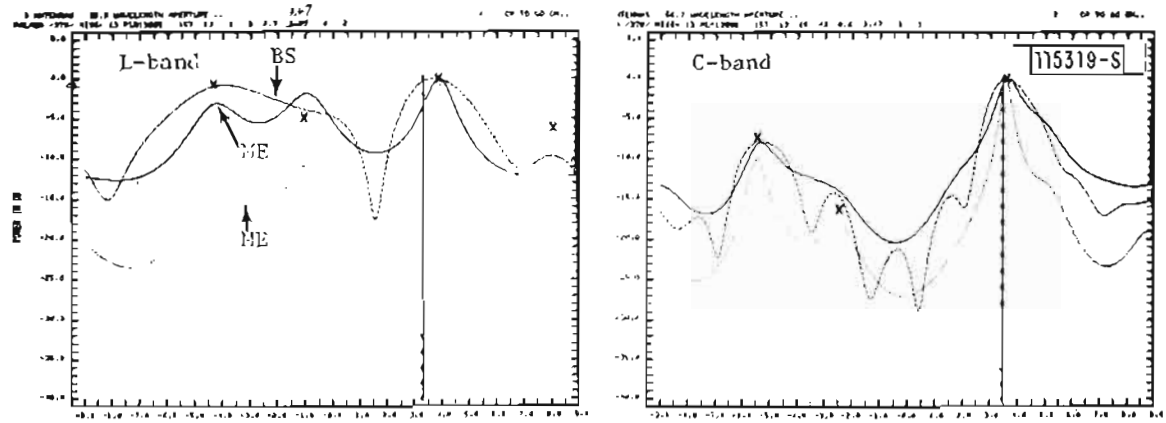

(b) Simulation Predicted (building reflection calculation)

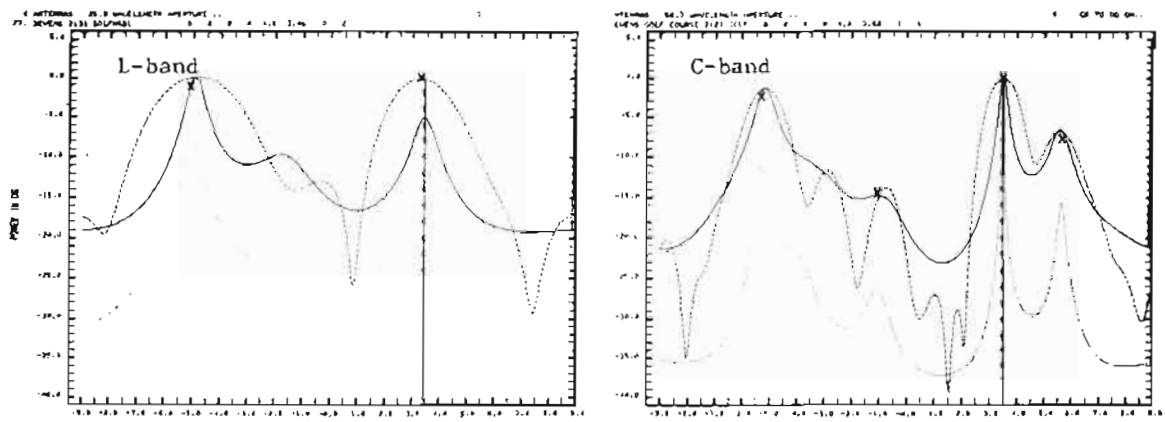

(c) Simulation Predicted (ground reflection calculation/focusing ground)

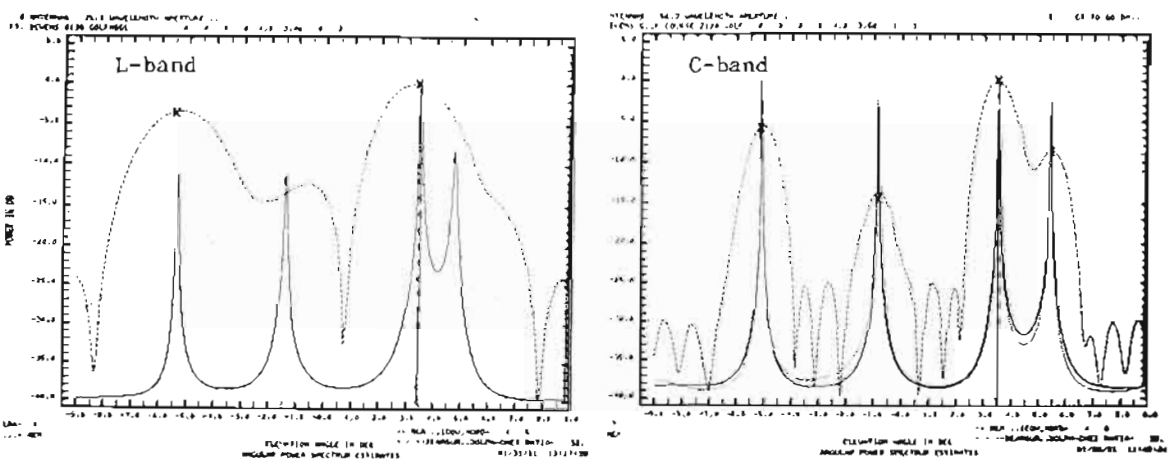

Fig. 5-26. Fort Devens measurement: radial line O-B, L-band and C-band elevation arrays, $\theta_{EL} \approx 3.5°$.

(a) Field Measured

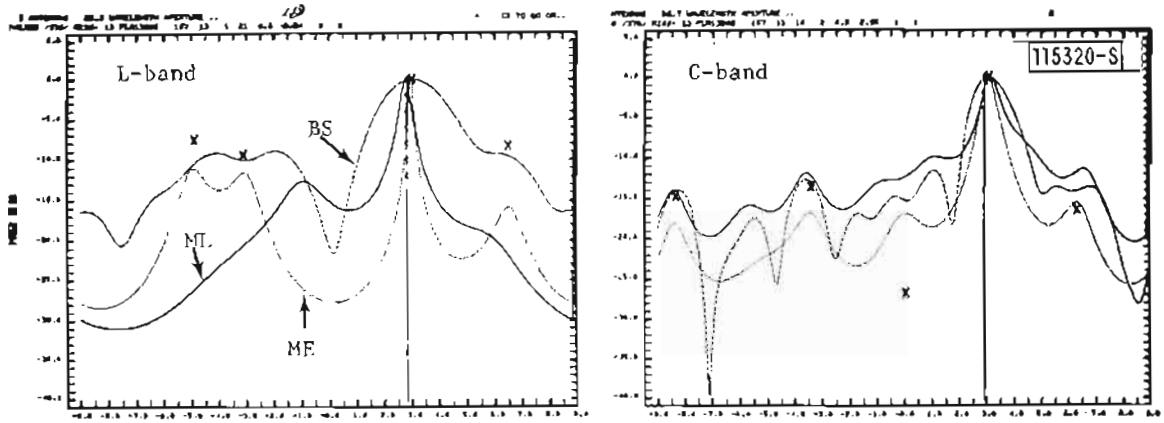

(b) Simulation Predicted (building reflection calculation)

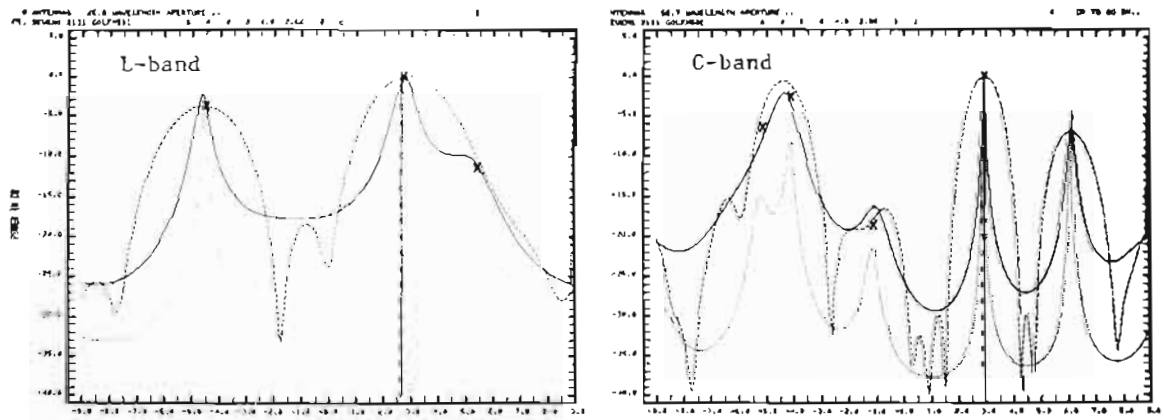

(c) Simulation Predicted (ground reflection calculation/focusing ground)

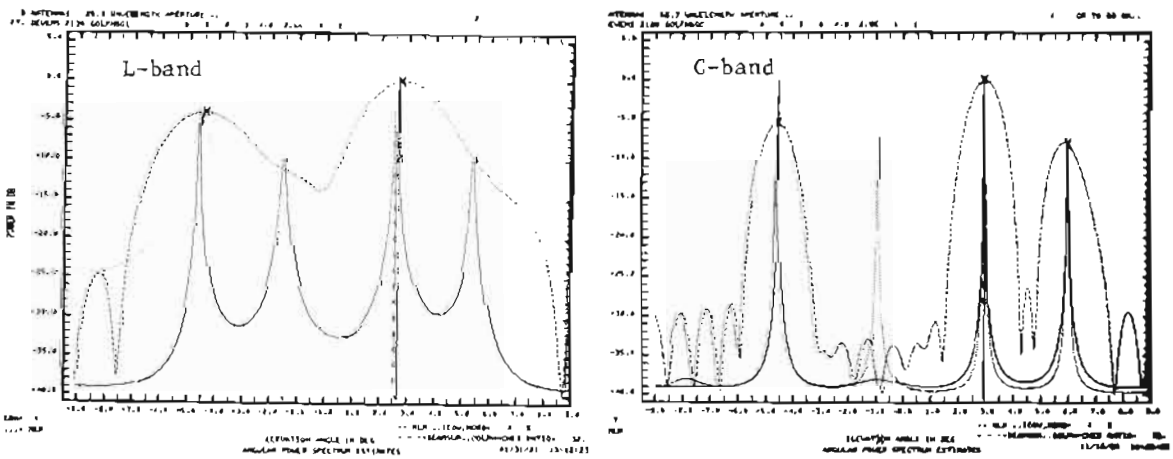

Fig. 5-27. Fort Devens measurement: radial line O-B, L-band and C-band elevation arrays, $\theta_{El} \simeq 3°$.

(a) Field Measured

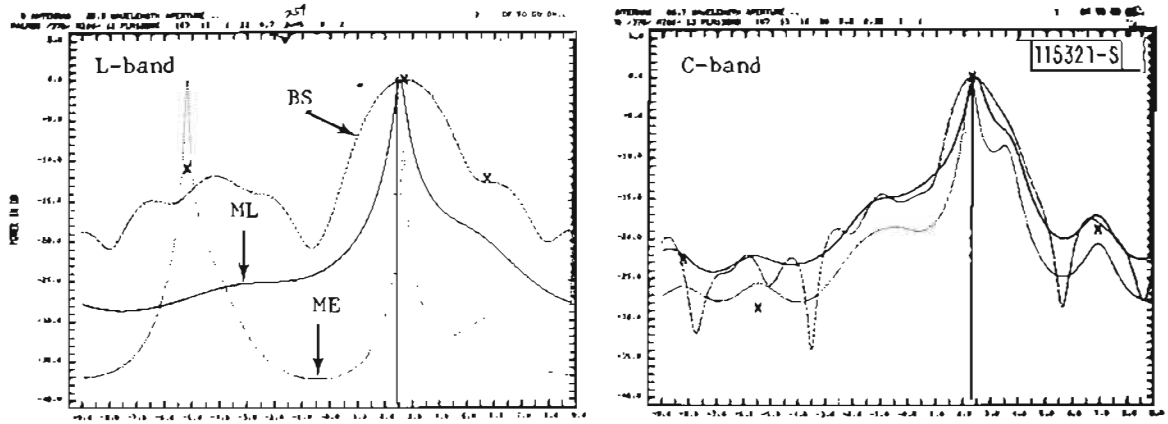

(b) Simulation Predicted (building reflection calculation)

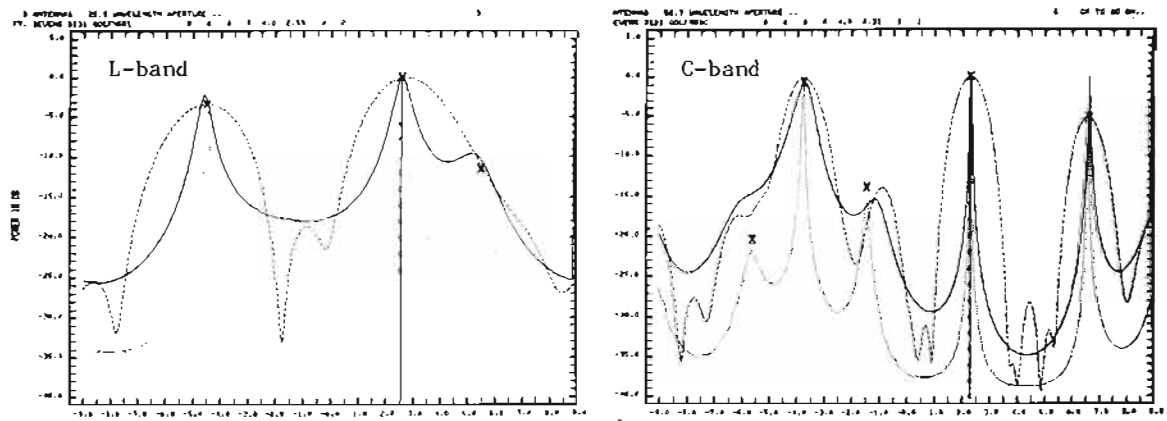

(c) Simulation Predicted (ground reflection calculation/focusing ground)

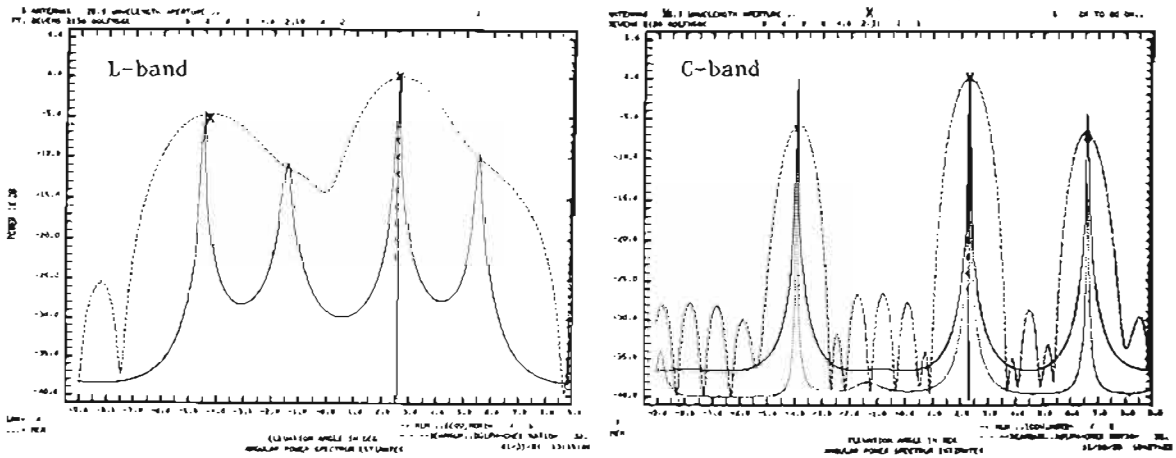

Fig. 5-28. Fort Devens measurement: radial line O-B, L-band and C-band elevation arrays, $\theta_{E1} \approx 2.5°$.

(a) Field Measured

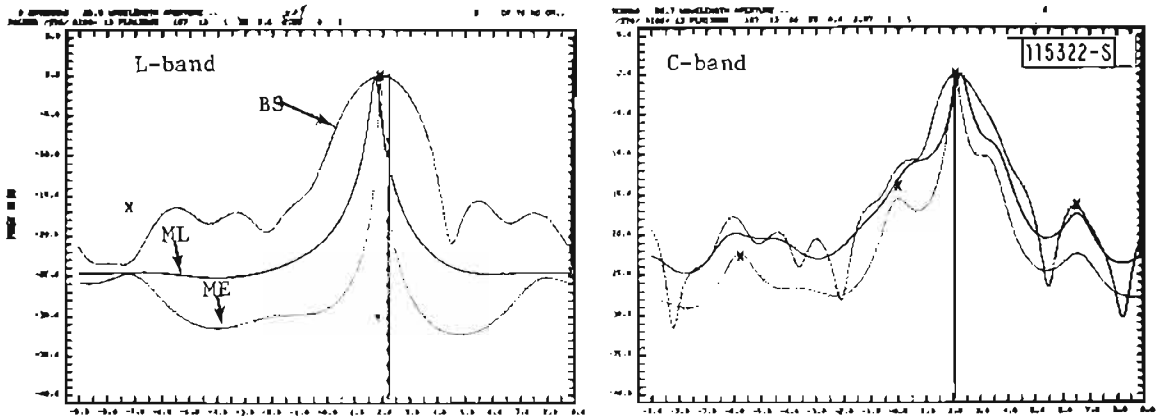

(b) Simulation Predicted (building reflection calculation)

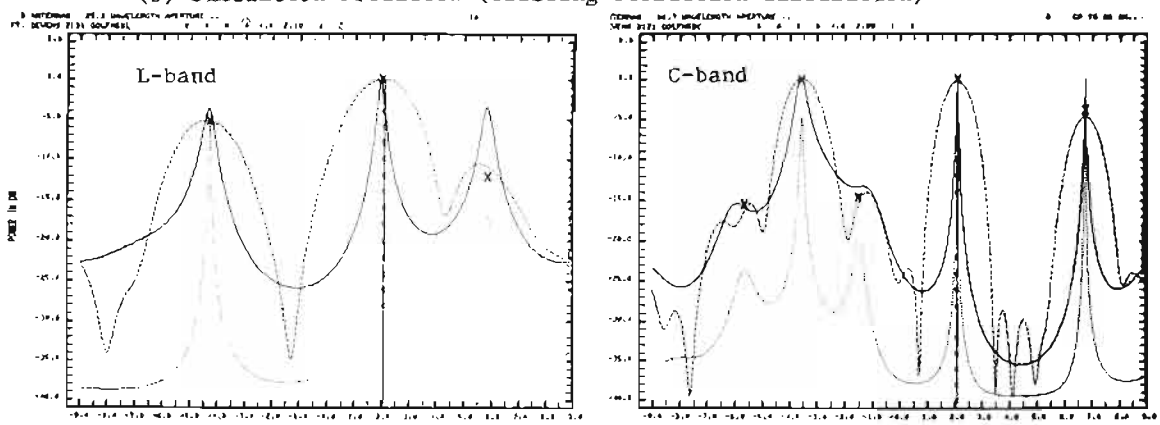

(c) Simulation Predicted (ground reflection calculation/focusing ground)

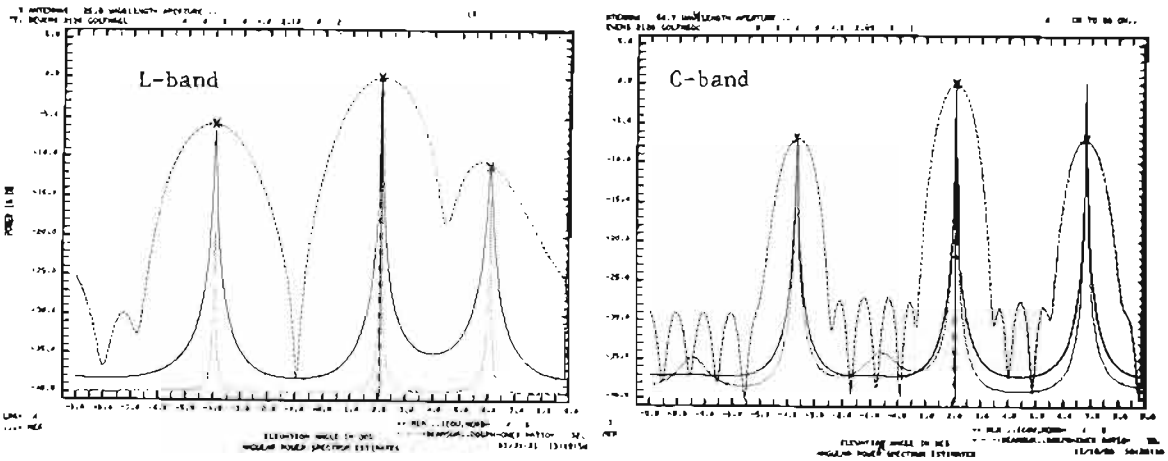

Fig. 5-29. Fort Devens measurement: radial line O-B, L-band and C-band elevation arrays, $\theta_{EL} \approx 2°$.

is electrically not so smooth at the C band. Figure 5-30 plots the EL multipath level and angle error versus direct signal angle for both the field measured results and the simulation predicted results (parts (a) and (b) in Figs. 5-22 to 5-29).

As described in Chapter IV Section B (Fig. 4-5), the terrain along this radial line has almost no cross-range tilts. This fact is reflected in the good agreement between the field measured results and the simulation results obtained with the building reflection calculation where the terrain cross-range tilts cannot be accounted for. For the terrain with no cross-range tilts, we should expect to see the similar simulation results obtained by the building reflection calculation and the ground reflection calculation with the focusing ground option. In fact, we have observed this similarity in the simulation results for the measurement along this radial line, as shown in Figs. 5-22 through 5-29. Except for the difference in the sharpness of the spectral peak that we previously encountered in Chapter V Section B.1, two sets of simulation results indicate the similar multipath environment, in terms of number of multipath arrivals, their arrival angles and M/D ratios.

Figures 5-31 and 5-32 shows L-band AZ angular power spectral estimates for two helicopter elevation angles. Since terrain along this radial line has almost no cross-range tilts, the direct signal and various terrain multipath signals which were suggested by the L-band EL angular power spectral estimates should all arrive at the same azimuth angle. That is the case in the simulation results shown in Figs. 5-31 and 5-32. However, the field measured results again show a second spectral peak around -6.5°, similar to what we observed in the field measured results along radial line O-A. This difference between the field measured results and the simulation results can be similarly explained as we did before. That is, this second spectral peak probably was due to the multipath arrivals from the nearby hills or tall buildings which were not considered in the ground model used in the MLS multipath simulation run.

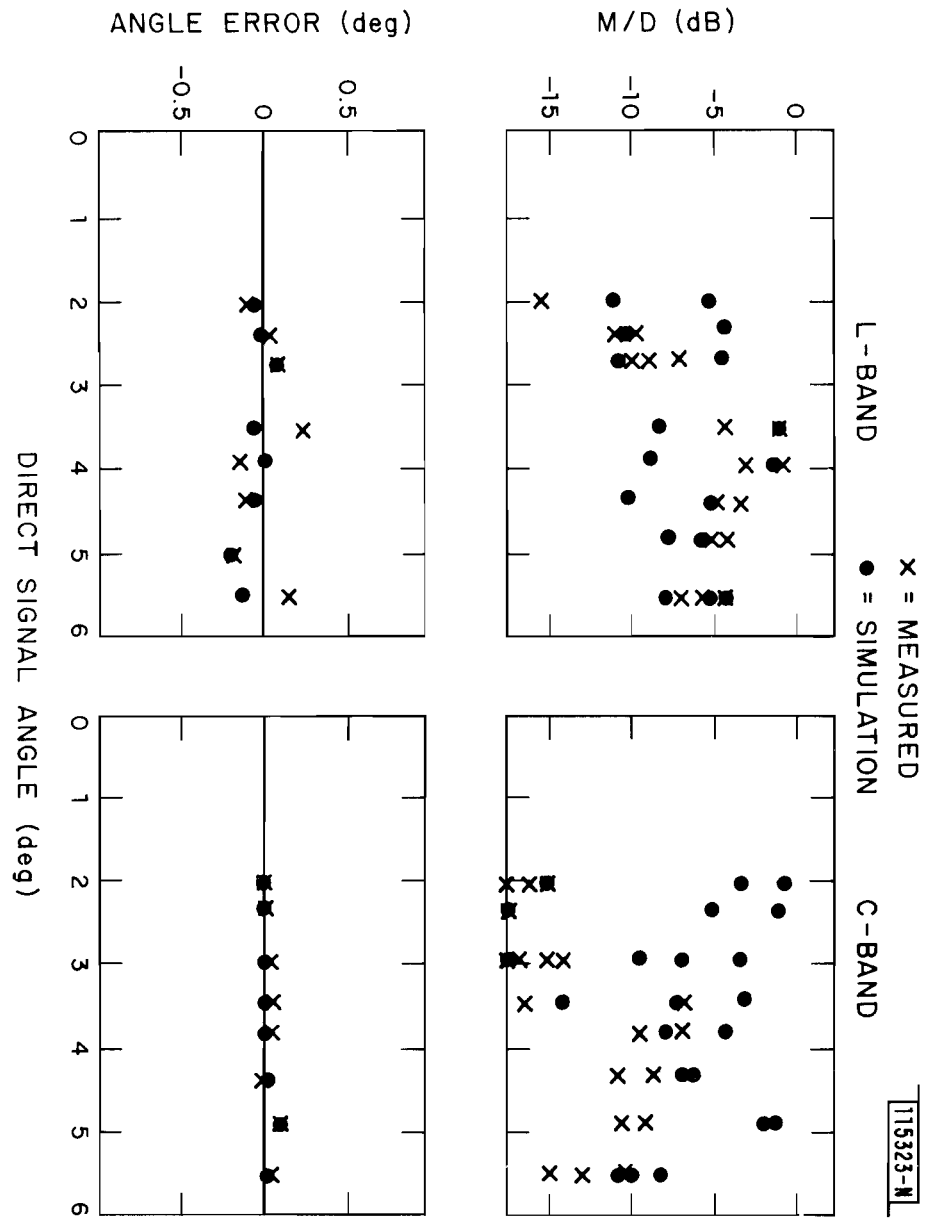

Fig. 5-30. Fort Devens measurement: radial line O-B, L-band and C-band elevation arrays, M/D ratios and angle errors.

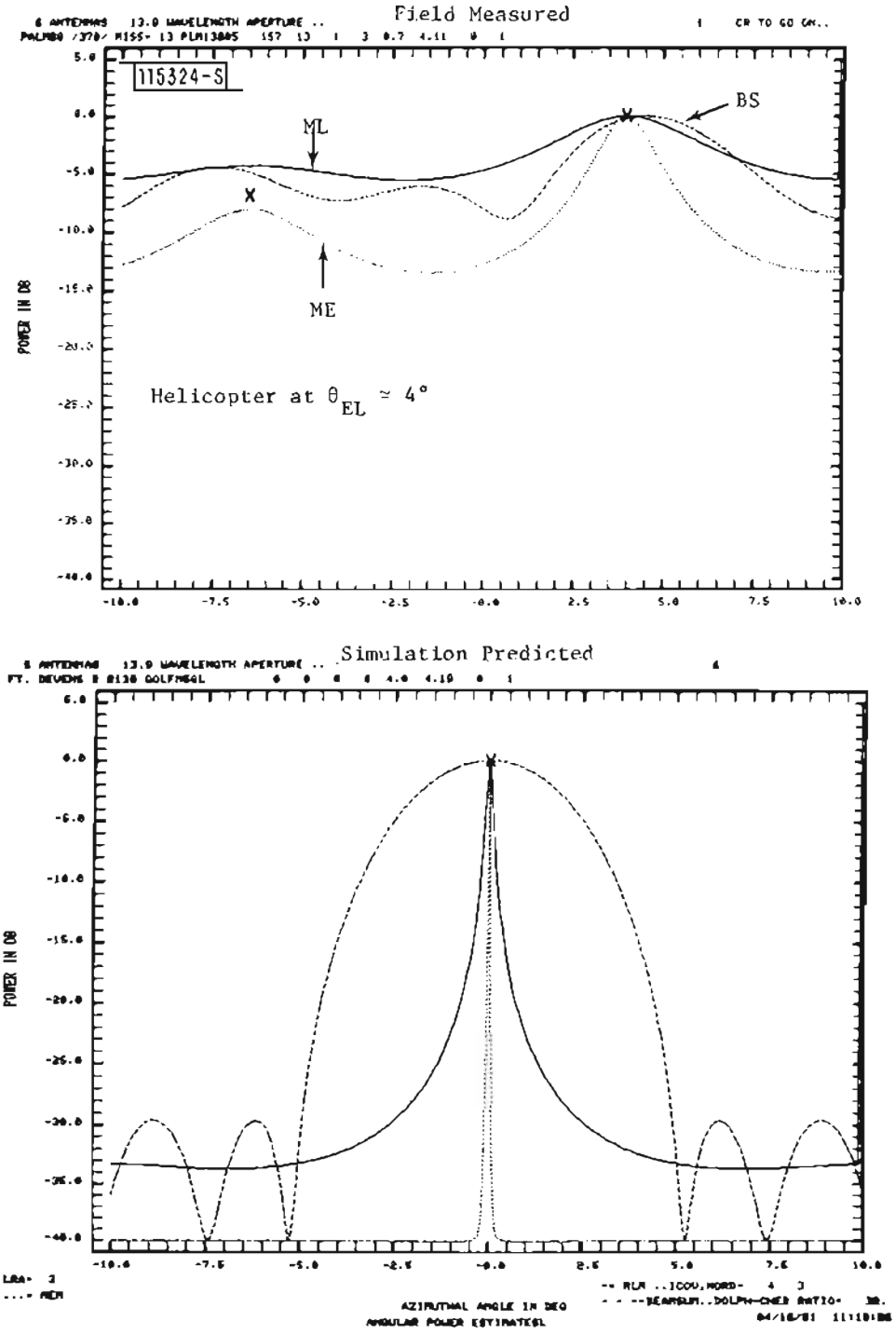

Fig. 5-31. Fort Devens measurement: radial line O-B, L-band azimuth array, $\theta_{EL} \simeq 4°$.

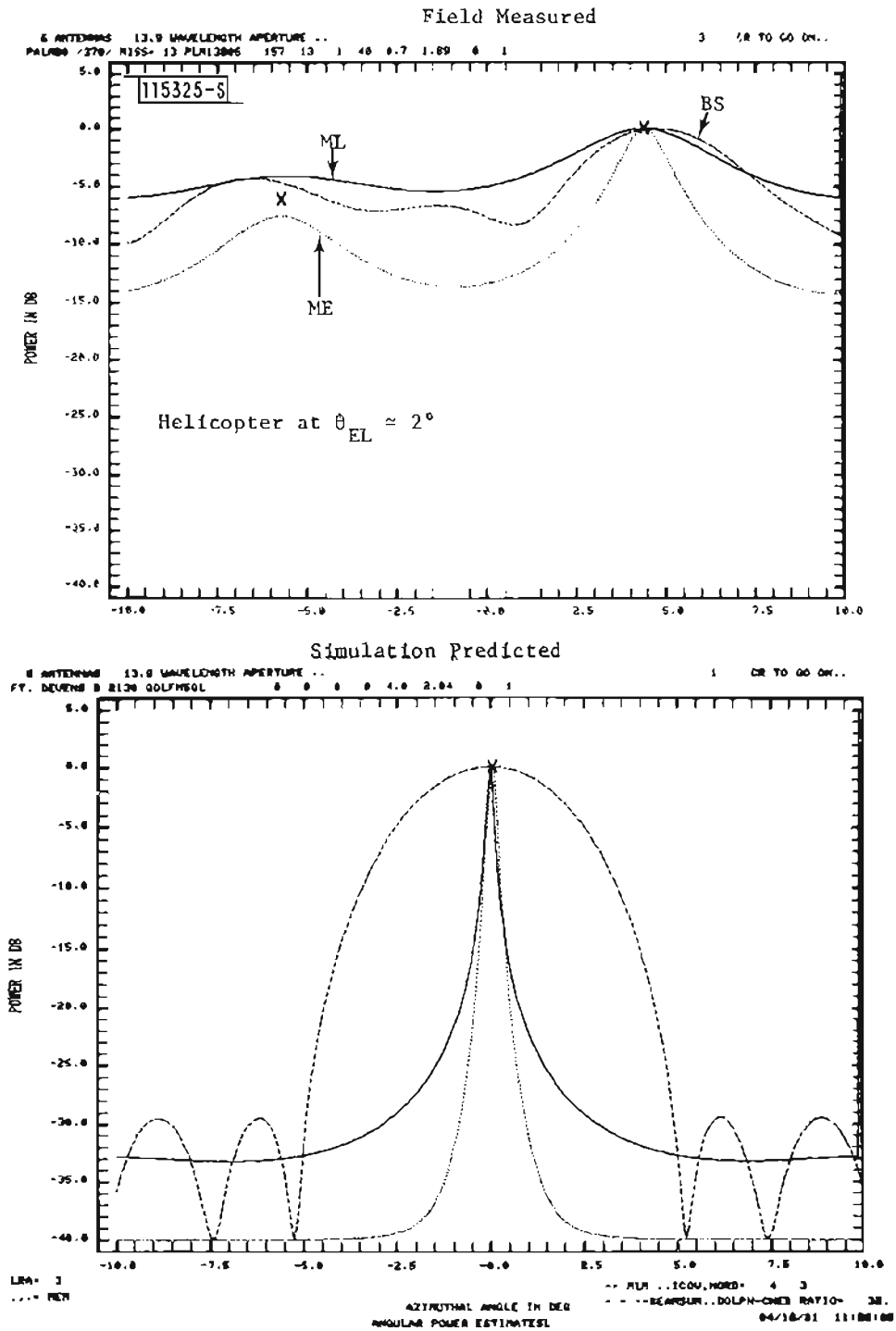

Fig. 5-32. Fort Devens measurement: radial line O-B, L-band azimuth array, $\theta_{EL} \simeq 2°$.

3. Radial Line O-C

Figures 5-33 to 5-38 show some results of the EL angular power spectral estimates for the measurements taken along the radial line O-C. As previously observed in the measurement results for the radial lines O-A and O-B, again we notice that the C-band field measured results show significantly much lower multipath levels than the corresponding L-band results. The field measured C-band multipath level is well below -10 dB, while the L-band multipath level is around -2 to -5 dB (part (a) in Figs. 5-33 to 5-38). This suggests that the terrain here appearing to be smooth for the L band probably is electrically rough for the C band. The small scale roughness in the terrain can reduce the specular reflection levels. Scattering theory [18] suggests that the reduced specular reflection levels due to the terrain roughness should be accompanied by a wide region of diffuse reflections with the largest levels near the horizon. We can see some indication of this phenomenon in the C-band results for the helicopter elevation angle $\theta_{EL} < 4°$ (Figs. 5-36 to 5-38). Again, here the phenomenon of the focusing ground reflection is very evident in both the L-band and the C-band results.

For the L band, the simulation predicted results (part (c) in each figure) which were obtained through the focusing ground option of ground reflection calculation, agrees reasonably well with the field measured results. The simulation predicted results using the building reflection calculation (part (b) in each figure) appear to give less satisfactory agreement with the field measured results. This probably is due to the similar situation that was discussed previously for the radial line O-A. That is, the simulation results obtained with the building reflection calculation could not and did not account for the possible terrain cross tilts. In terms of ground cross-range tilt, although the terrain along the radial line O-C here is not as complicated as that along the radial line O-A, it does have some cross-range tilts, as indicated in Fig. 4-6. For the C band, the agreement between the field measured results and the simulation predicted results is poor, especially in the multipath levels. This probably has to do with the possible diffuse reflections which were indicated in the C-band field measured results and which were not considered in the MLS multipath simulation here. Figure 5-39

(a) Field Measured

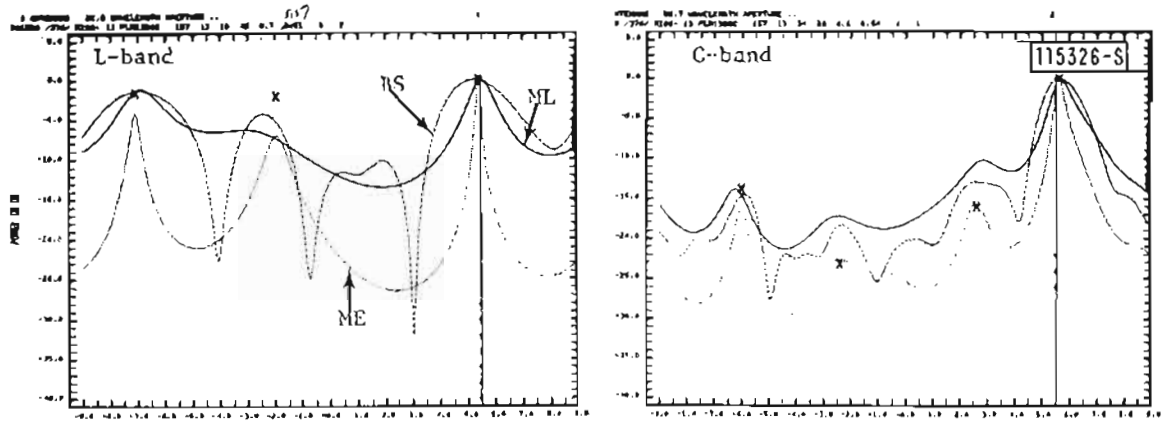

(b) Simulation Predicted (building reflection calculation)

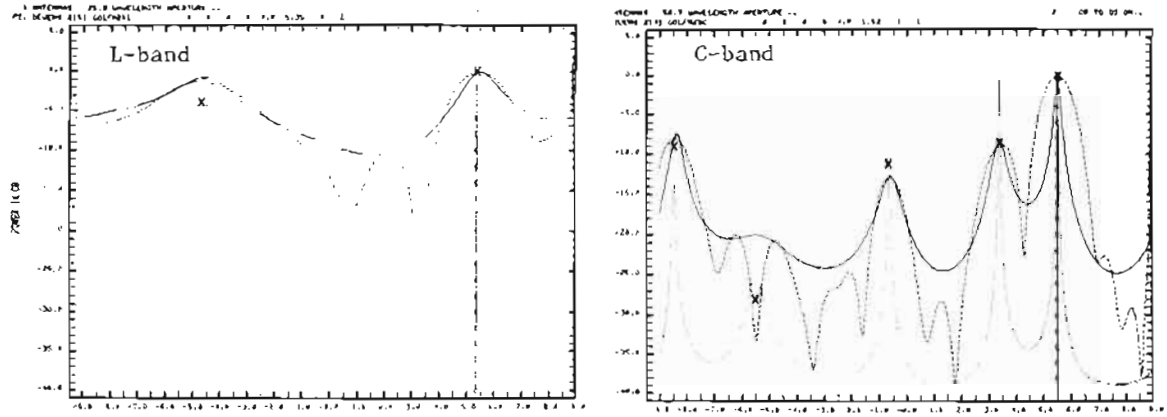

(c) Simulation Predicted (ground reflection calculation/focusing ground)

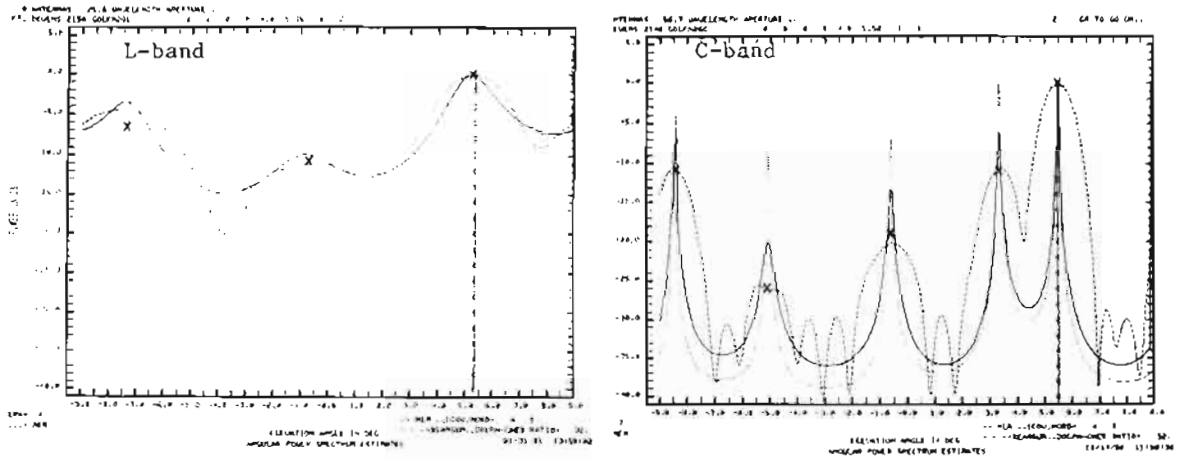

Fig. 5-33. Fort Devens measurement: radial line O-C, L-band and C-band elevation arrays, θ_{EL} = 5.5°.

(a) Field Measured

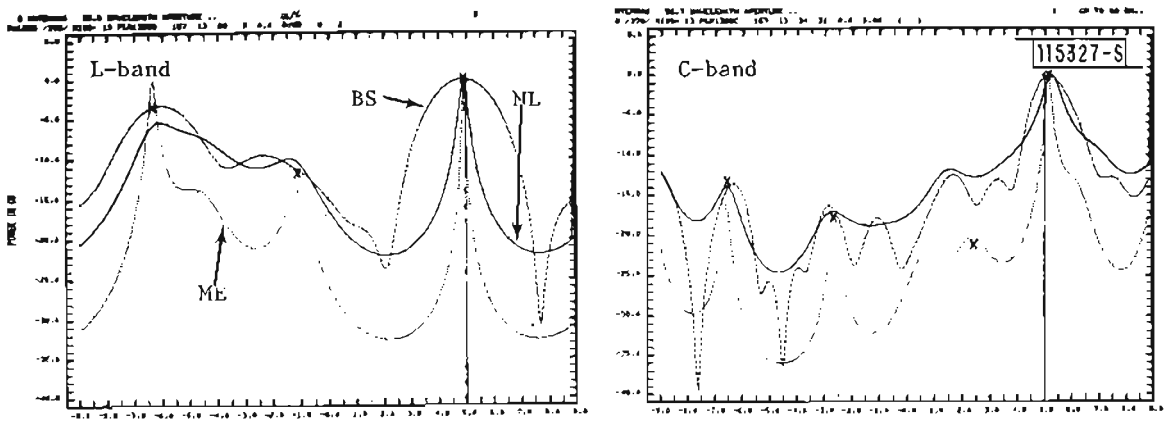

(b) Simulation Predicted (building reflection calculation)

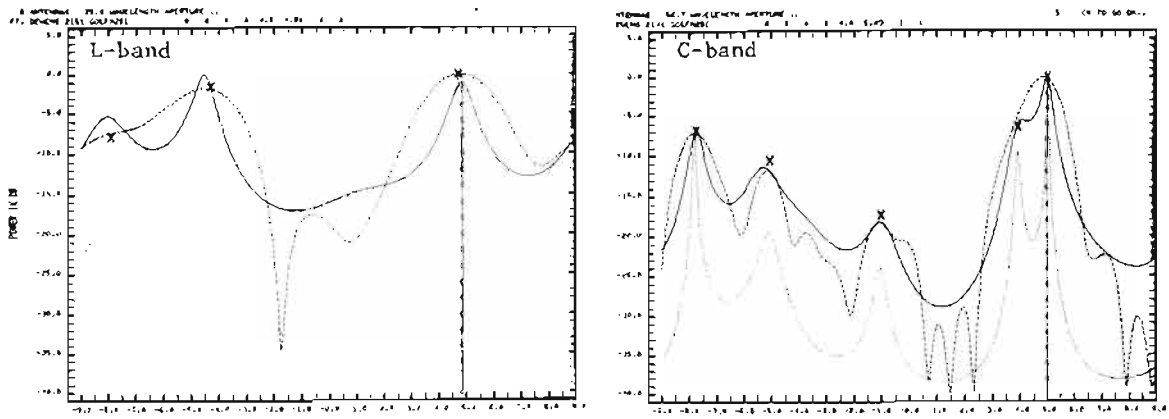

(c) Simulation Predicted (ground reflection calculation/focusing ground)

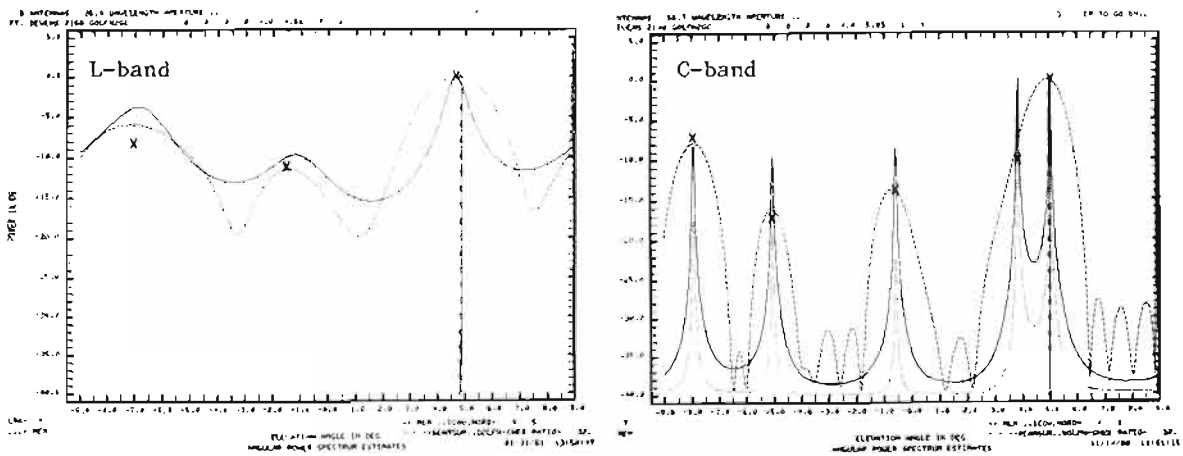

Fig. 5-34. Fort Devens measurement: radial line O-C, L-band and C-band elevation arrays, $\theta_{EL} = 5°$.

(a) Field Measured

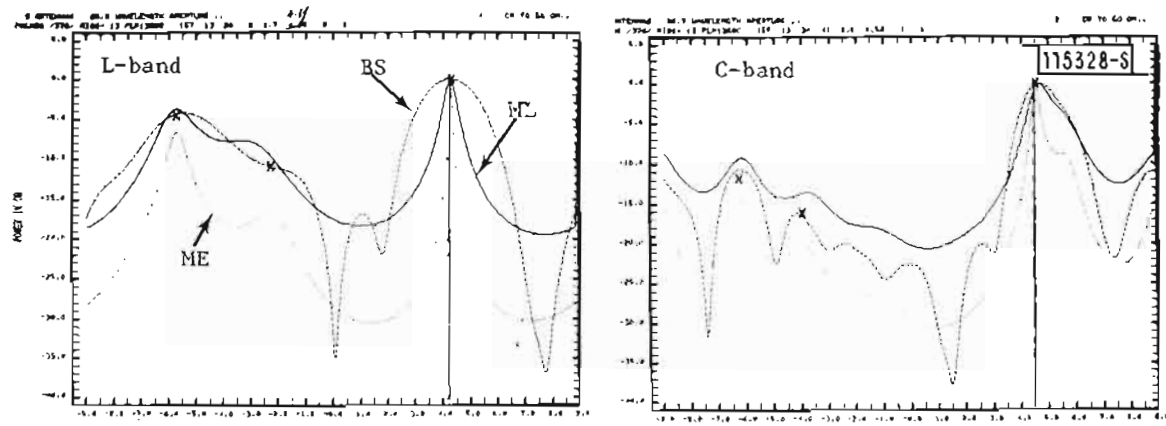

(b) Simulation Predicted (building reflection calculation)

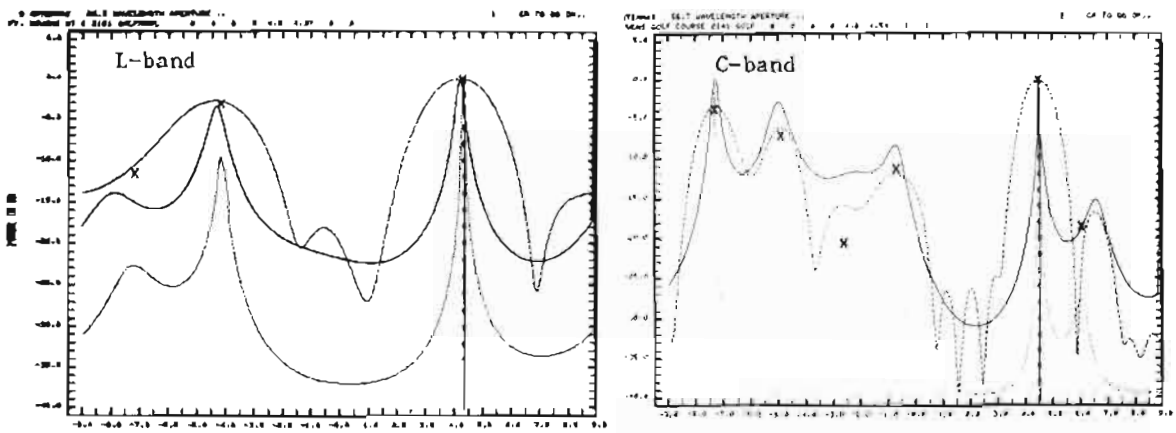

(c) Simulation Predicted (ground reflection calculation/focusing ground)

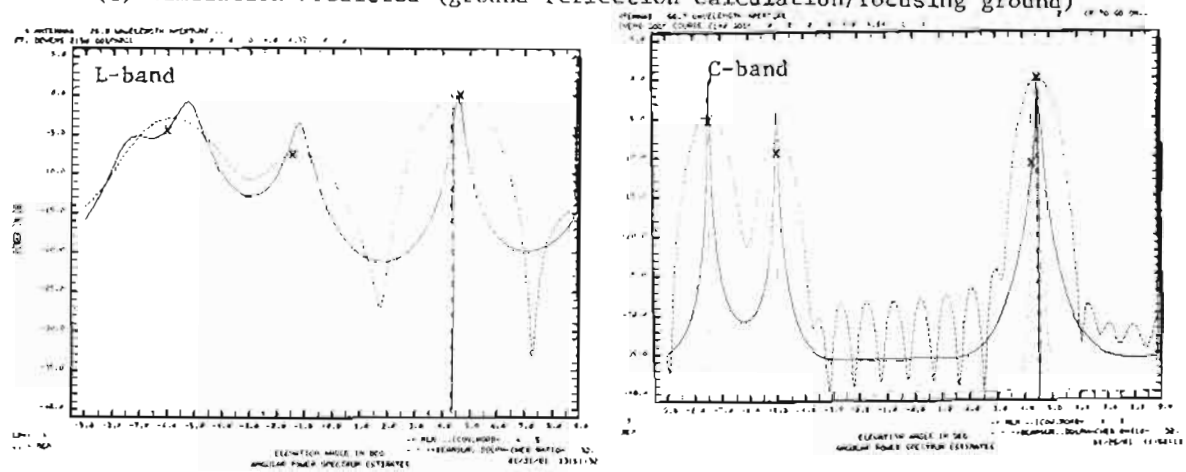

Fig. 5-35. Fort Devens measurement: radial line O-C, L-band and C-band elevation arrays, $\theta_{EL} \approx 4.5°$.

(a) Field Measured

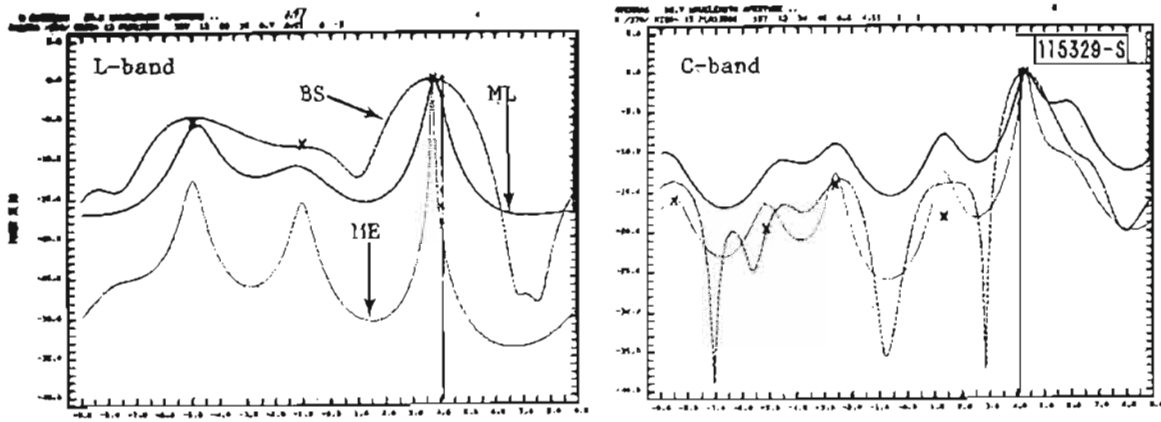

(b) Simulation Predicted (building reflection calculation)

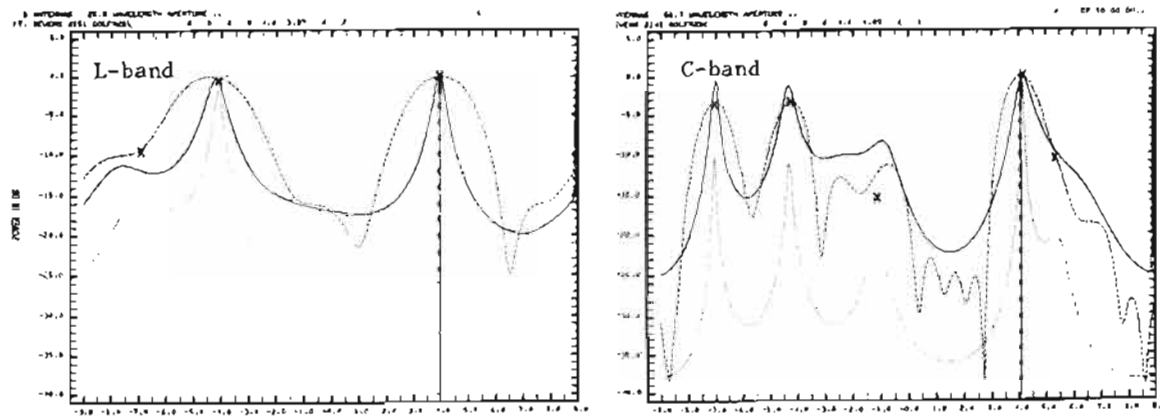

(c) Simulation Predicted (ground reflection calculation/focusing ground)

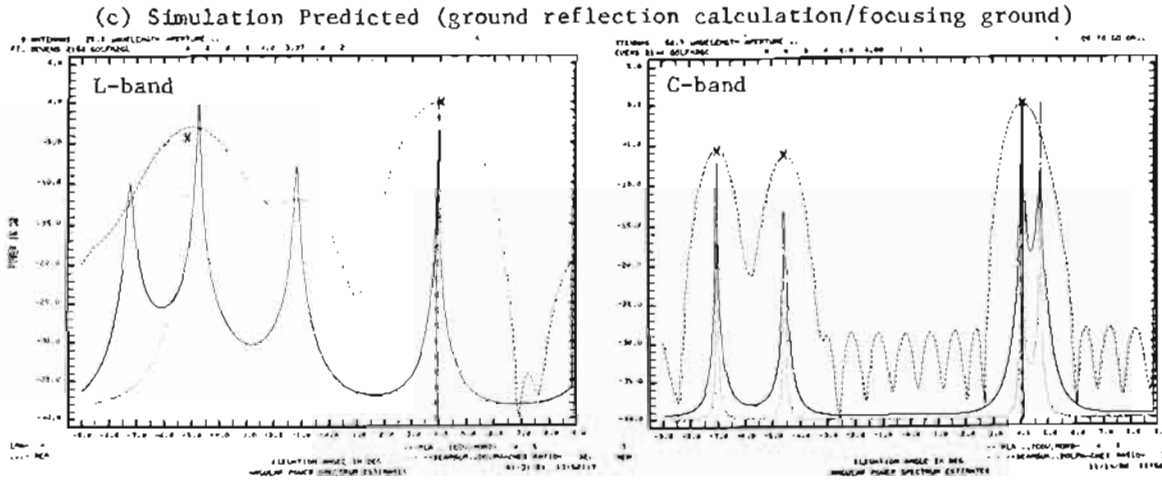

Fig. 5-36. Fort Devens measurement: radial line O-C, L-band and C-band elevation arrays, $\theta_{EL} \simeq 4°$.

(a) Field Measured

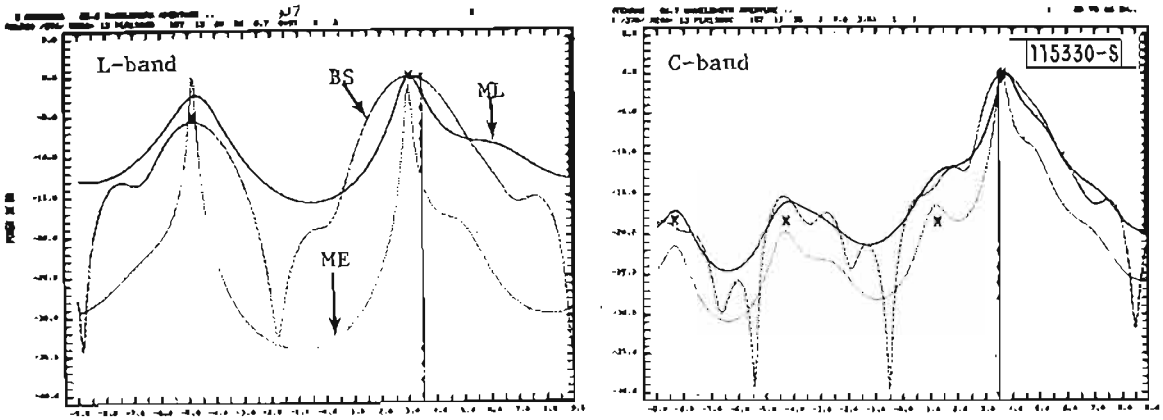

(b) Simulation Predicted (building reflection calculation)

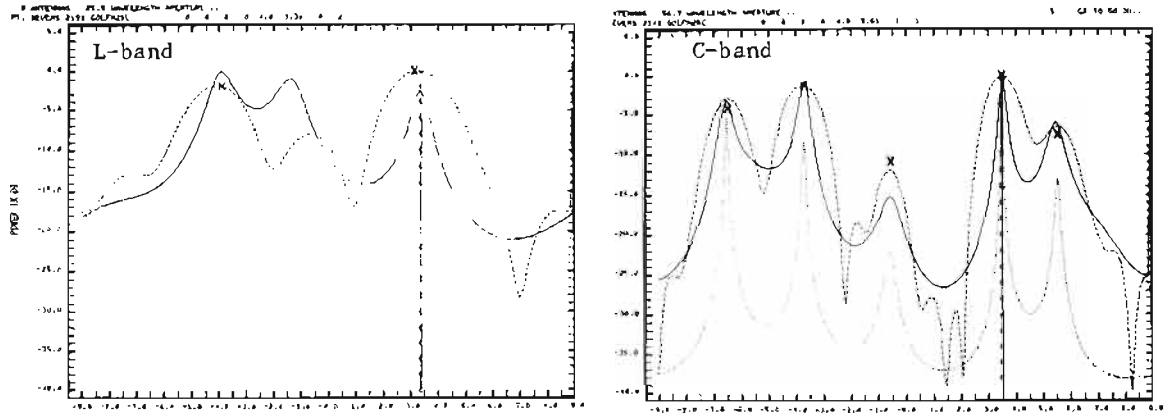

(c) Simulation Predicted (ground reflection calculation/focusing ground)

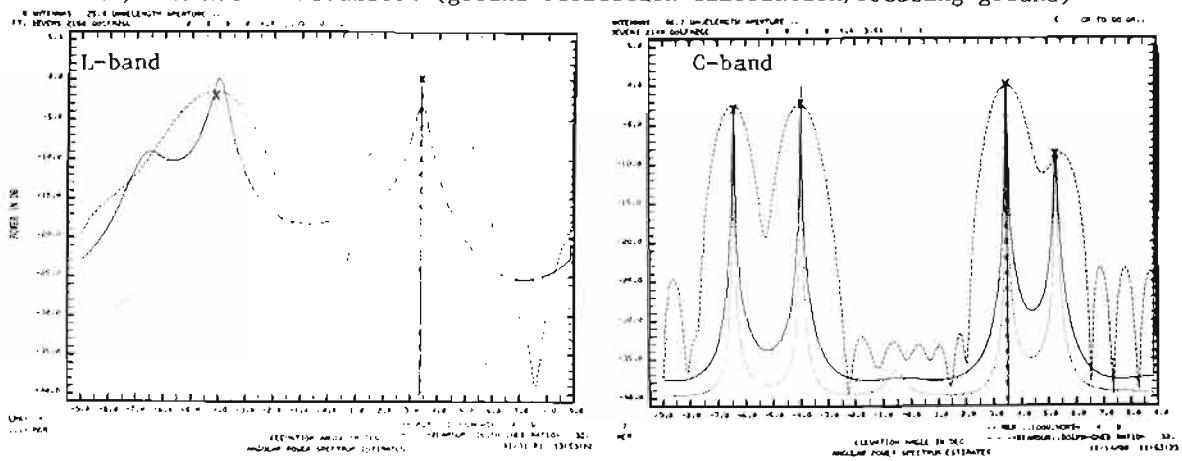

Fig. 5-37. Fort Devens measurement: radial line O-C, L-band and C-band elevation arrays, $\theta_{EL} \approx 3.5°$.

(a) Field Measured

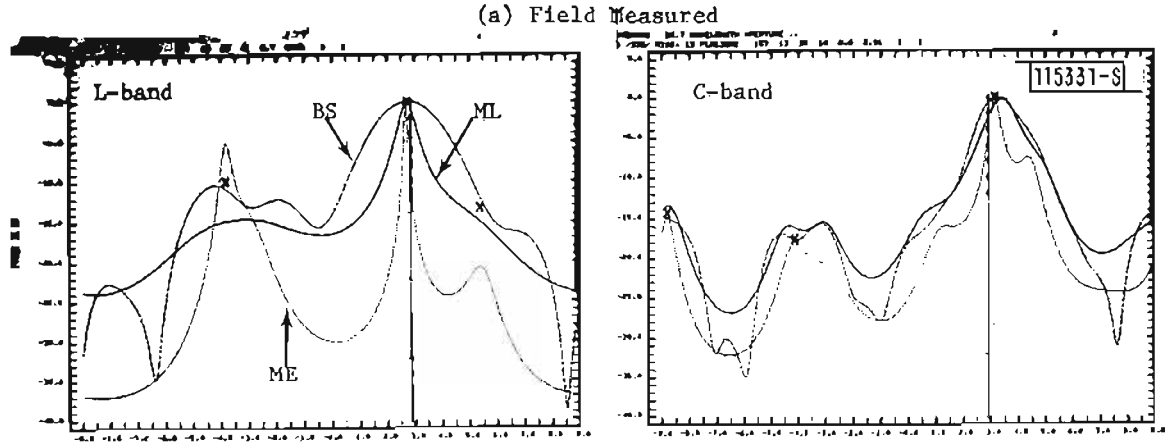

(b) Simulation Predicted (building reflection calculation)

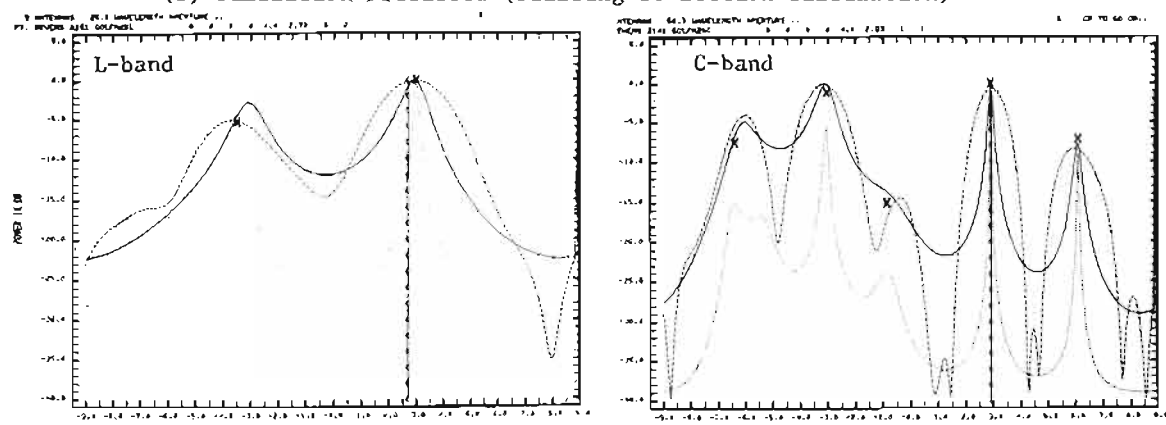

(c) Simulation Predicted (ground reflection calculation/focusing ground)

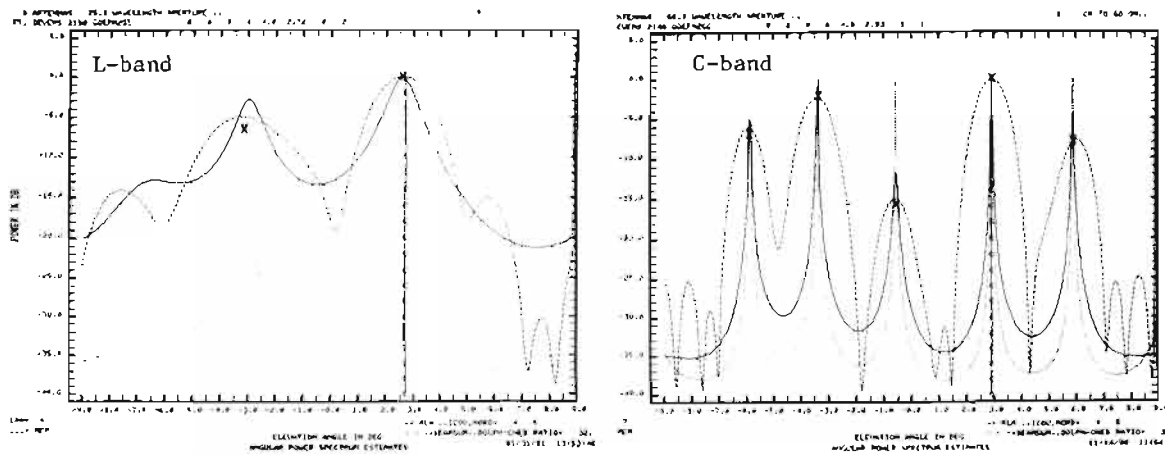

Fig. 5-38. Fort Devens measurement: radial line O-C, L-band and C-band elevation arrays, $\theta_{EL} \simeq 3°$.

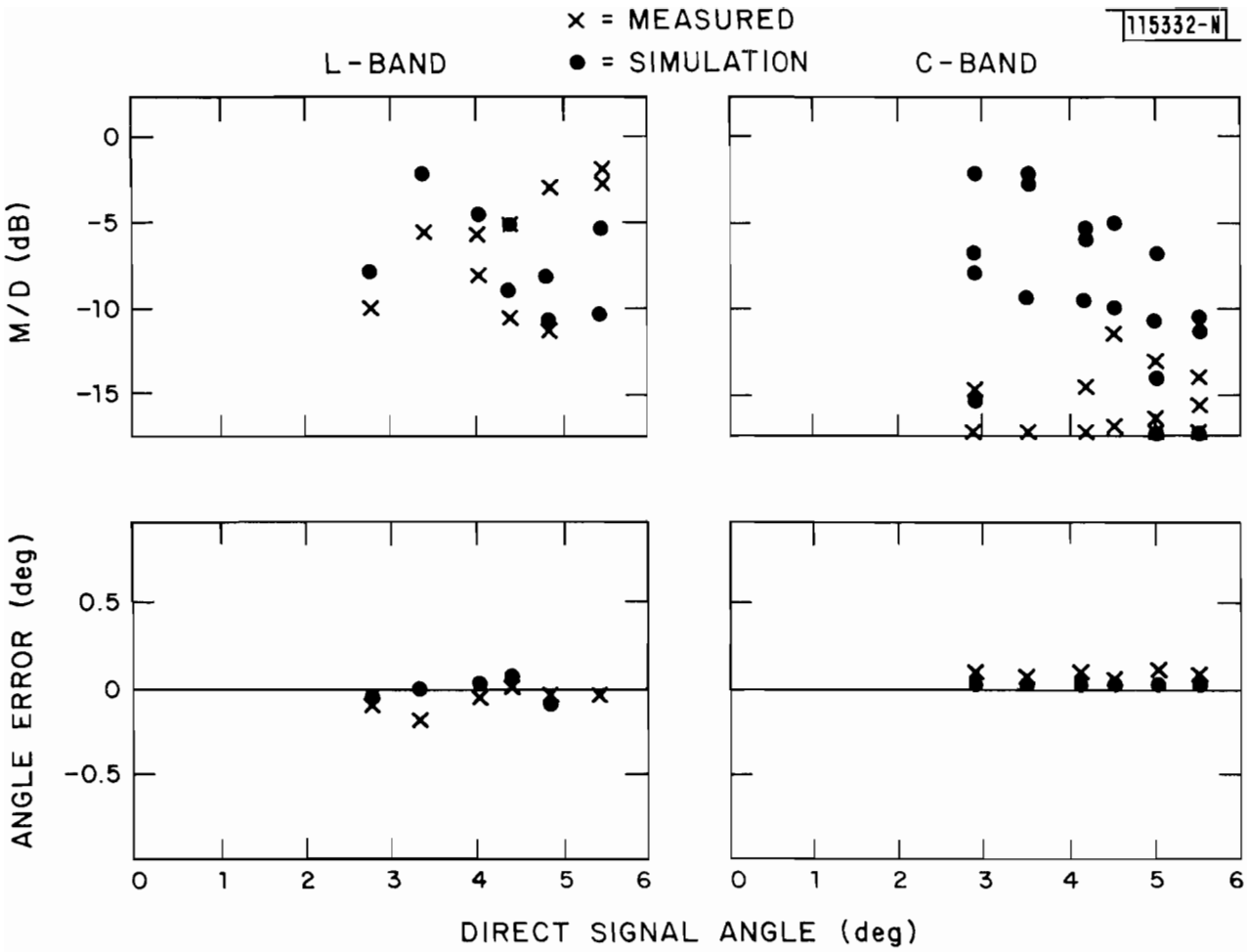

Fig. 5-39. Fort Devens measurement: radial line O-C, L-band and C-band elevation arrays, M/D ratios and angle errors.

shows the EL multipath level and angle error versus the direct signal angle for both the field measured results and the simulation predicted results (parts (a) and (c) in Figs. 5-33 to 5-38).

Figures 5-40 and 5-41 show the L-band AZ angular power spectral estimates for two helicopter elevation angles. Simulation predicted results only show one spectral peak at the direct signal AZ arrival angle. Although the terrain here has some cross-range tilts, apparently these cross-range tilts did not make the AZ arrival angles of various multipaths deviate too much from the direct signal AZ arrival angle. Thus the azimuthal angular separations between the direct signal and the multipath signals were too small to be resolved with the L-band 6 element AZ array. The field measured results again show a second spectral peak, similar to what we previously saw in the field measured results along the other two radial lines.

C. Camp Edwards

As described in Chapter IV Section C, terrains at three measurement sites in Camp Edwards have various cross-range tilts. Thus, for the field measurements at these three sites, the MLS multipath simulation predicted results were only obtained through the focusing ground option of the ground reflection calculation.

1. J2 Range

Figures 5-42 to 5-53 show some representative results of the EL angular power spectral estimates for the measurements taken at Camp Edwards J2 Range site. Terrain at this site was fairly flat with very minor cross-range tilts. However, significant small scale roughness existed throughout the entire terrain at this site. Nevertheless, the L-band field measured results show high multipath levels, ranging from -5 dB to 1 dB. The L-band multipath arrivals appear to be dominantly specular reflections. Thus, the physically rough terrain here seems to be electrically smooth for the L band. However, this small scale terrain roughness is clearly reflected in the C-band field measured results. The C-band field measured results indicate very low multipath levels, well below -20 dB for helicopter elevation angles $\theta_{EL} > 0.5°$.

115333-S

Field Measured

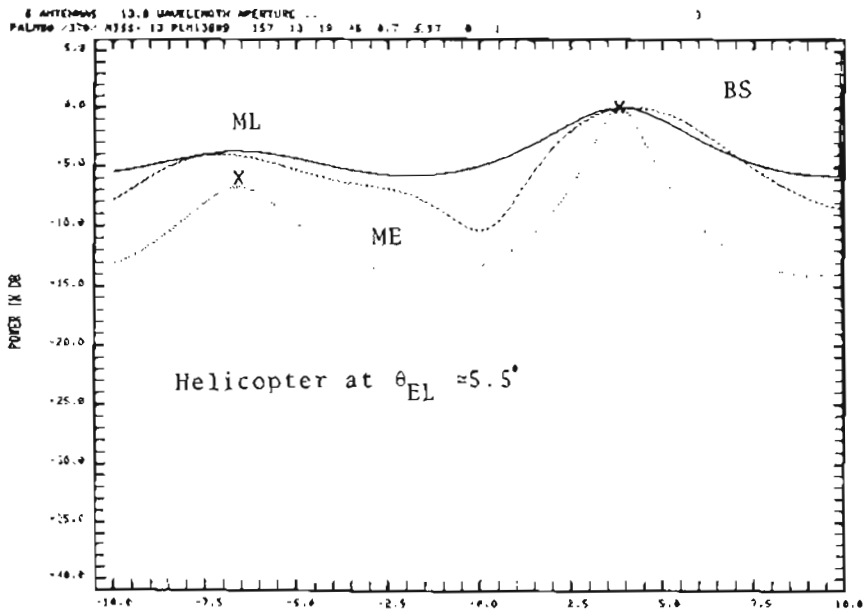

Simulation predicted (ground reflection calculation/focusing ground)

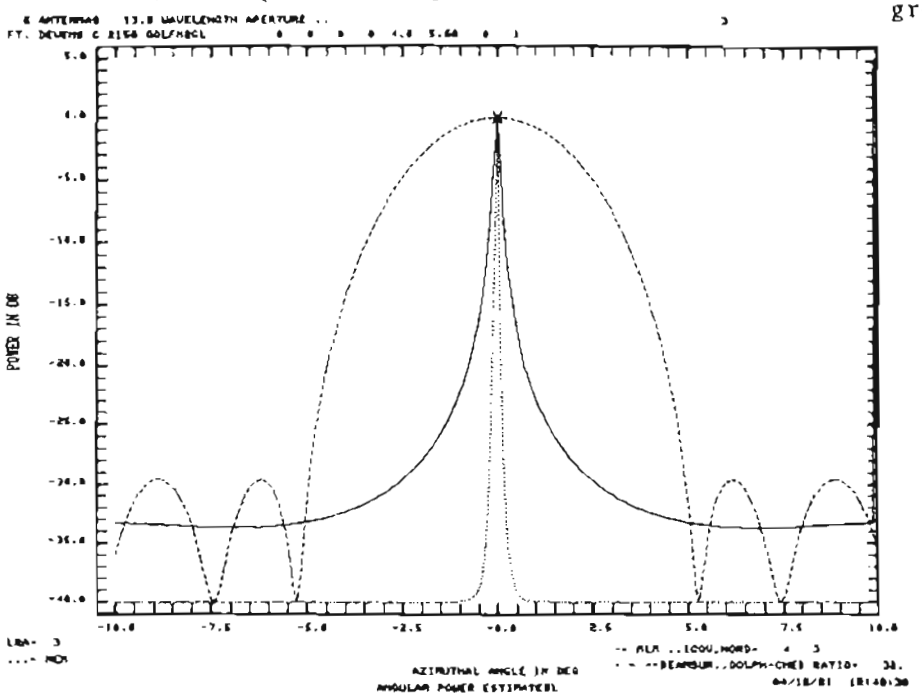

Fig. 5-40. Fort Devens measurement: radial line O-C, L-band and C-band azimuth array, $\theta_{EL} \approx 5.5°$.

Field Measured

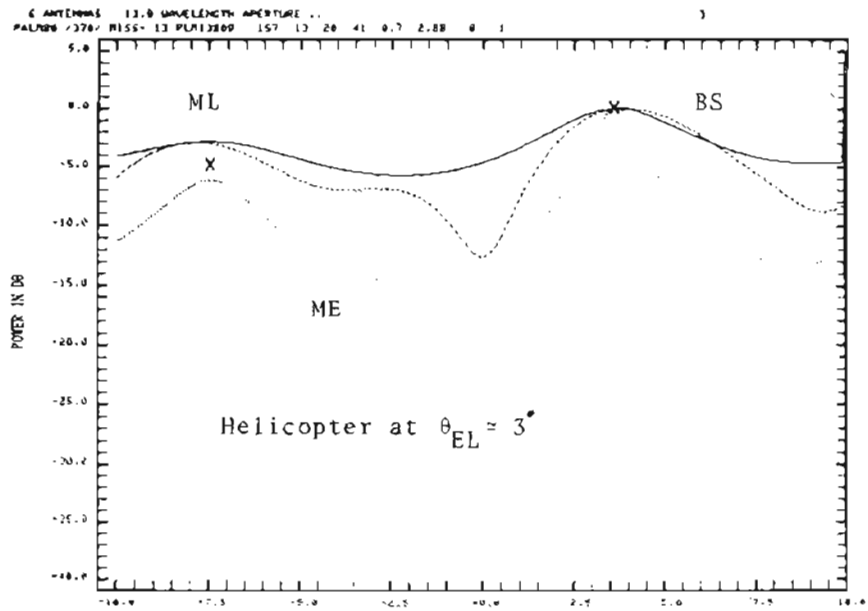

Simulation predicted (ground reflection calculation/focusing ground)

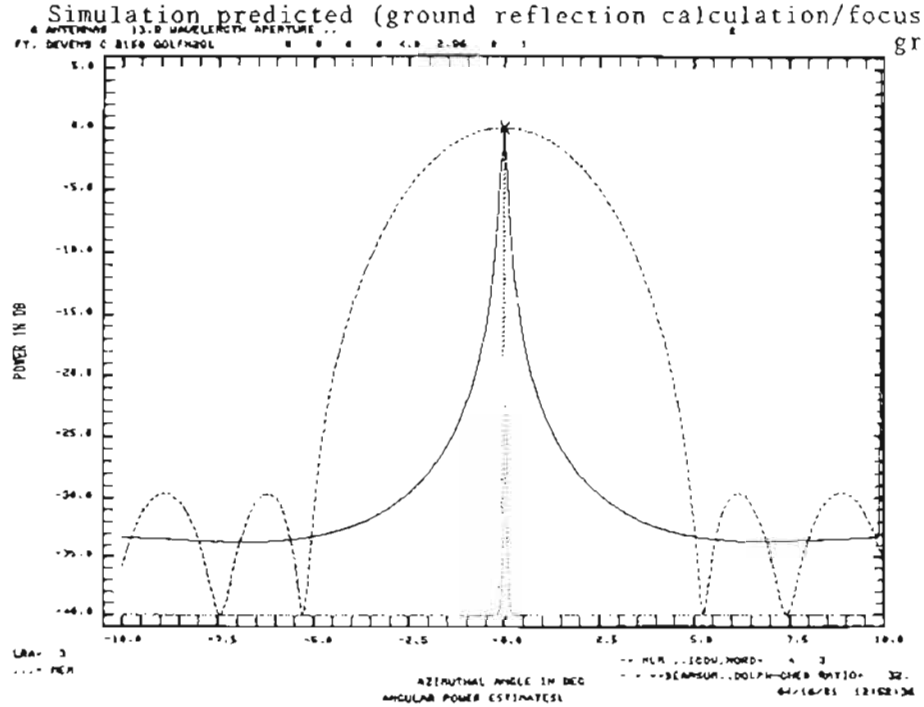

Fig. 5-41. Fort Devens measurement: radial line O-C, L-band and C-band azimuth array, $\theta_{EL} \approx 3°$.

Field Measured

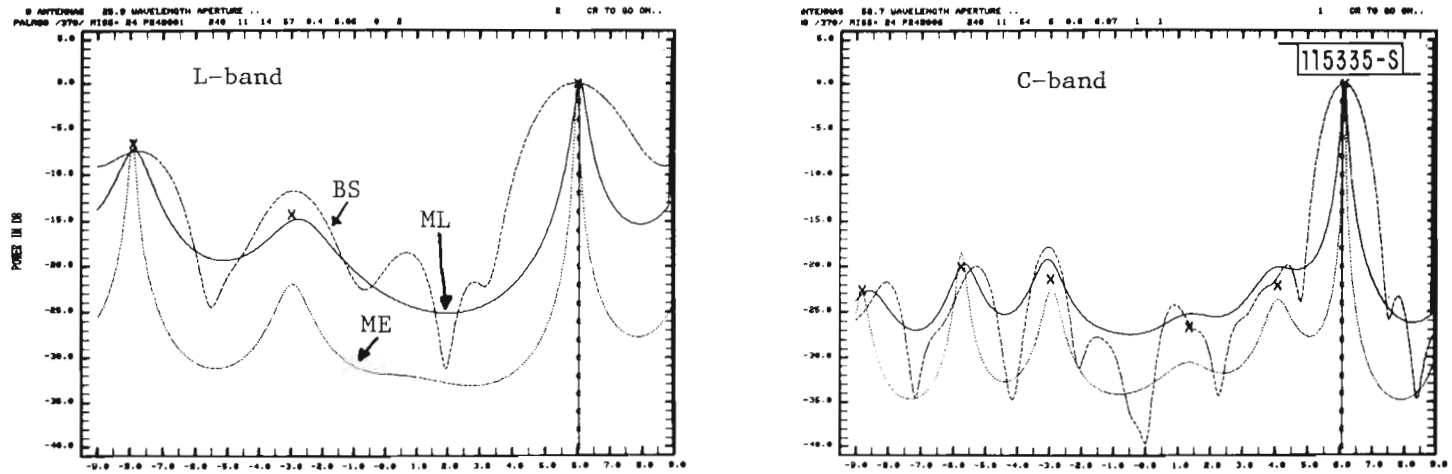

Simulation predicted (ground reflection calculation/focusing ground)

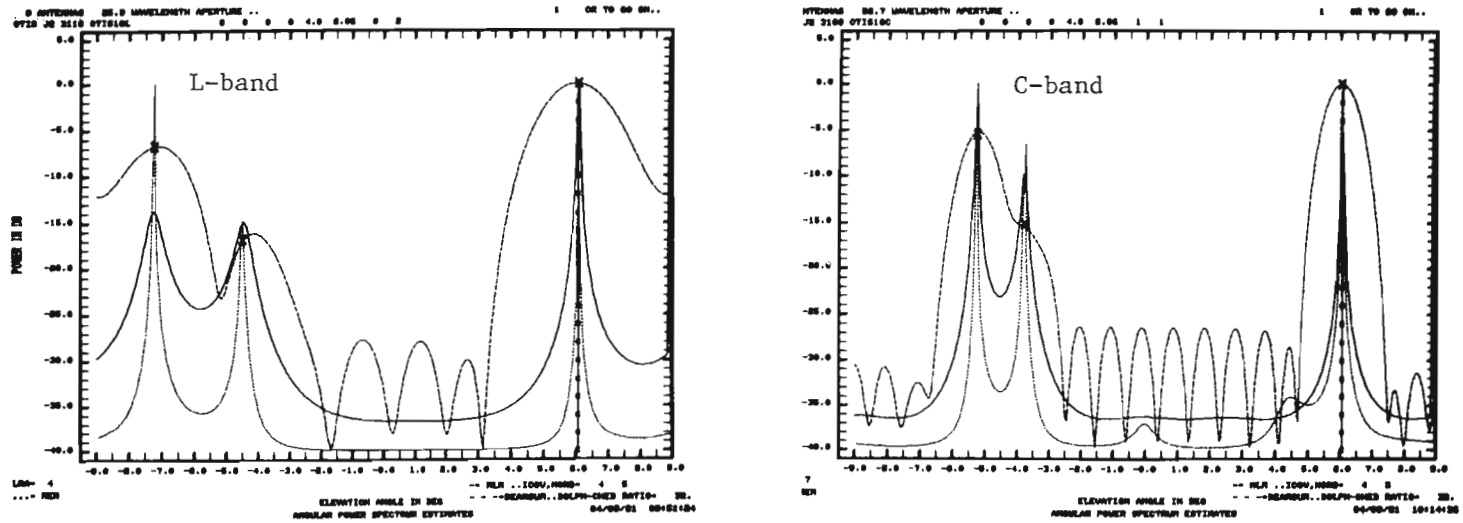

Fig. 5-42. Camp Edwards measurement: J2 range, L- and C-bands elevation arrays, $\theta_{EL} \simeq 6°$.

Field Measured

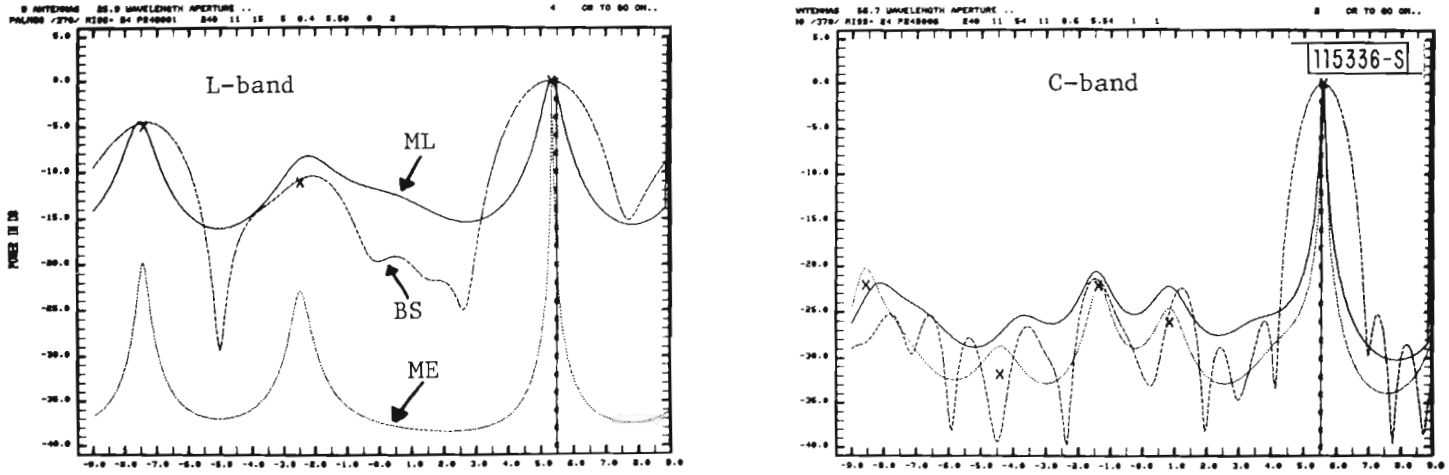

Simulation predicted (ground reflection calculation/focusing ground)

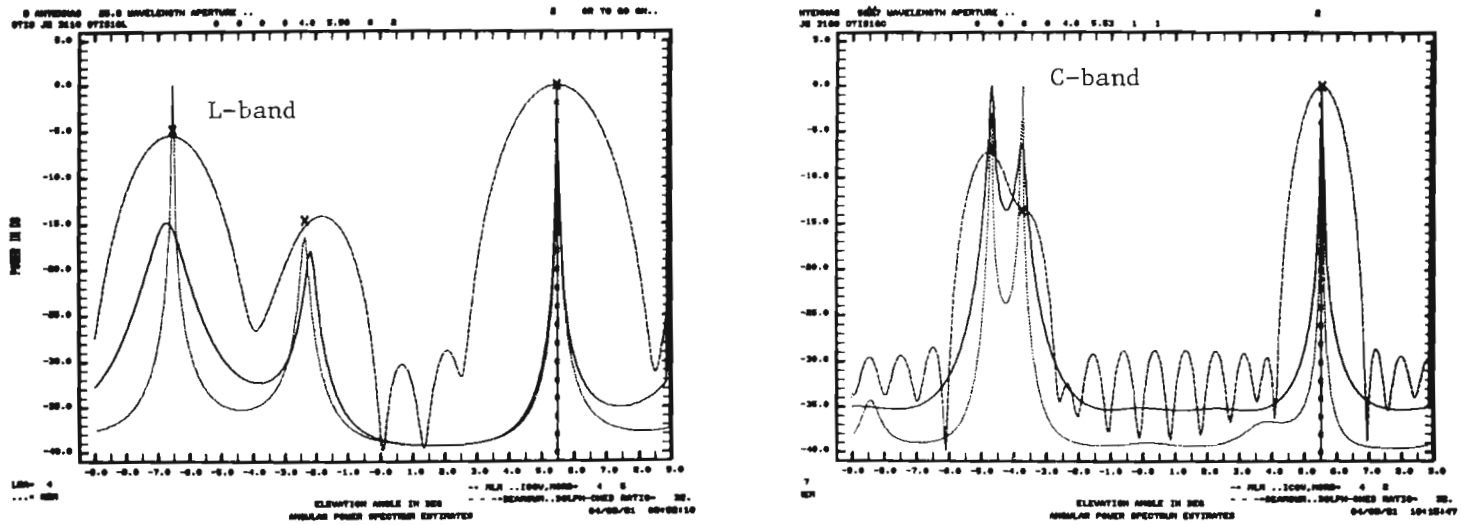

Fig. 5-43. Camp Edwards measurement: J2 range, L- and C-bands elevation arrays, $\theta_{EL} \simeq 5.5°$.

Field Measured

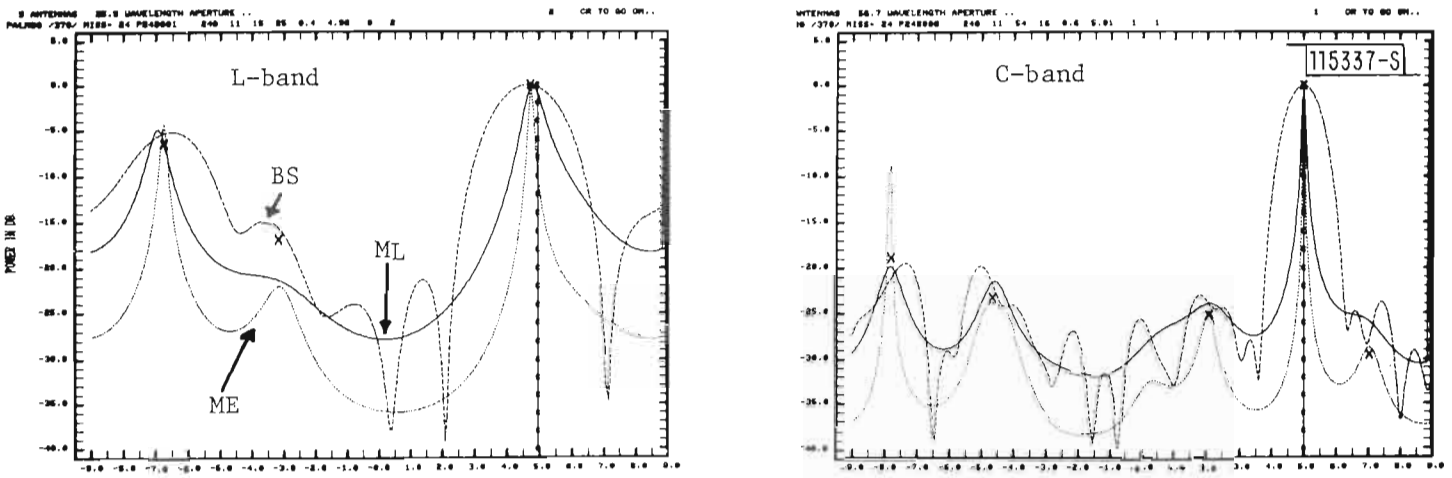

Simulation predicted (ground reflection calculation/focusing ground)

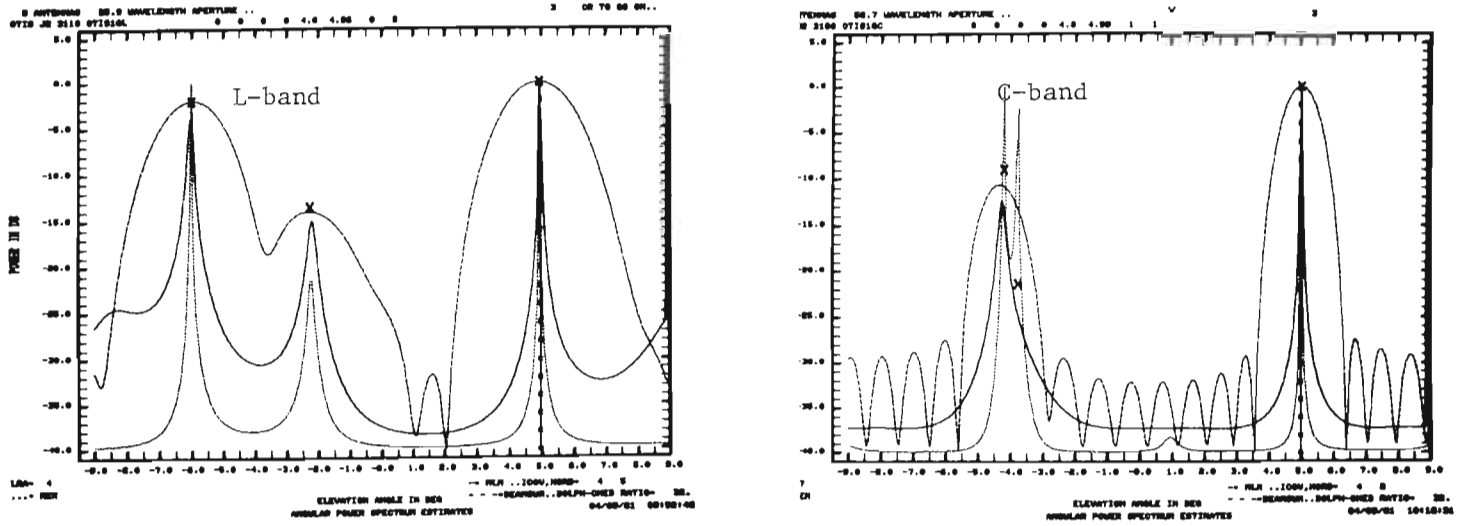

Fig. 5-44. Camp Edwards measurement: J2 range, L- and C-bands elevation arrays, $\theta_{EL} \simeq 5°$.

Field Measured

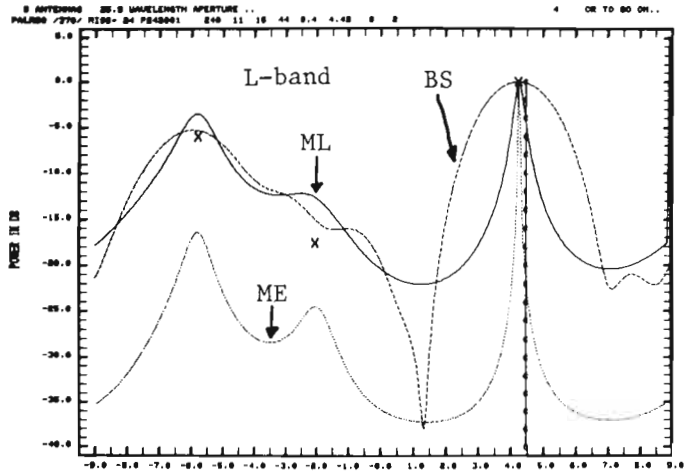

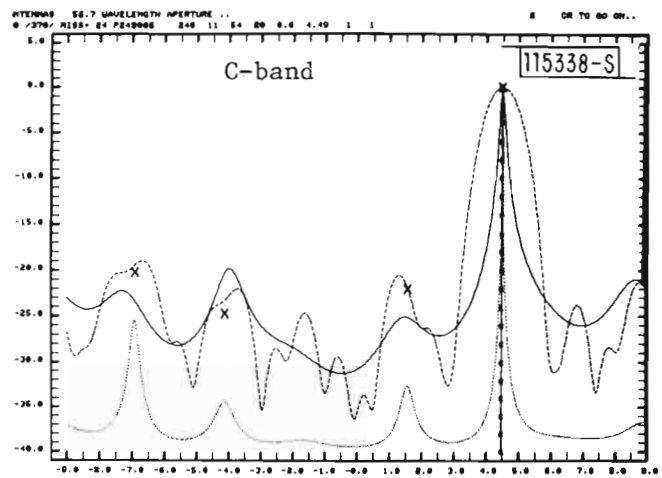

Simulation predicted (ground reflection calculation/focusing ground)

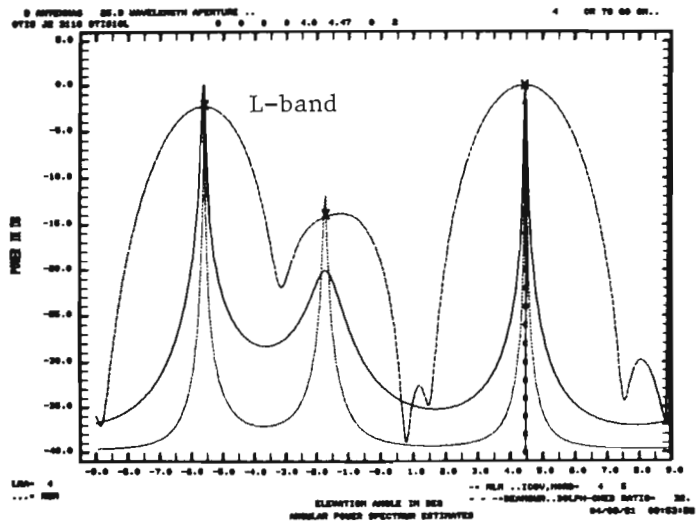

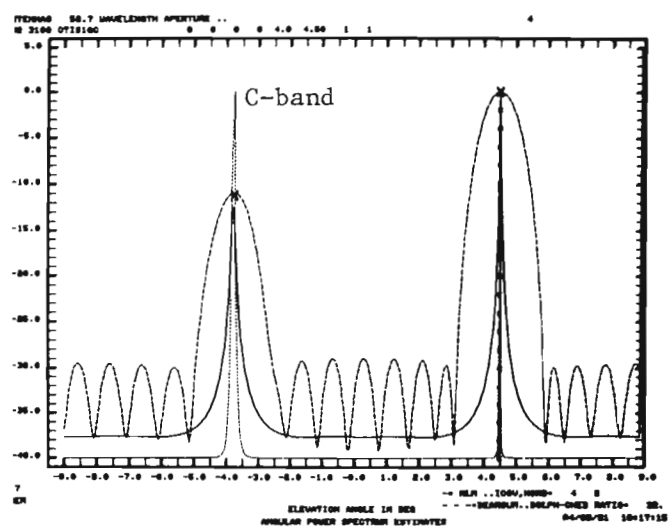

Fig. 5-45. Camp Edwards measurement: J2 range, L- and C-bands elevation arrays, $\theta_{EL} \simeq 4.5°$.

Field Measured

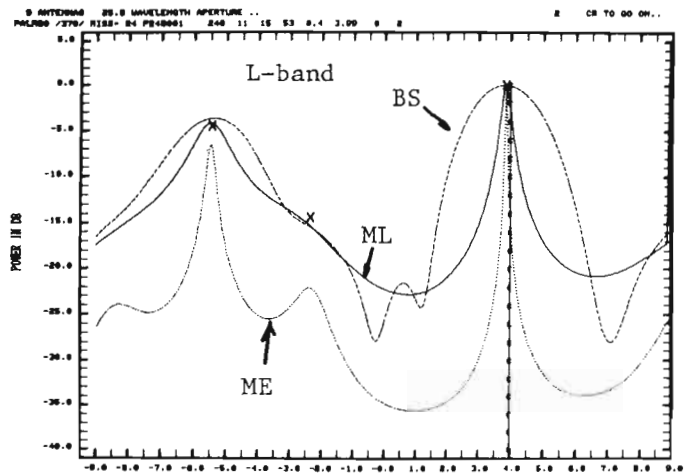

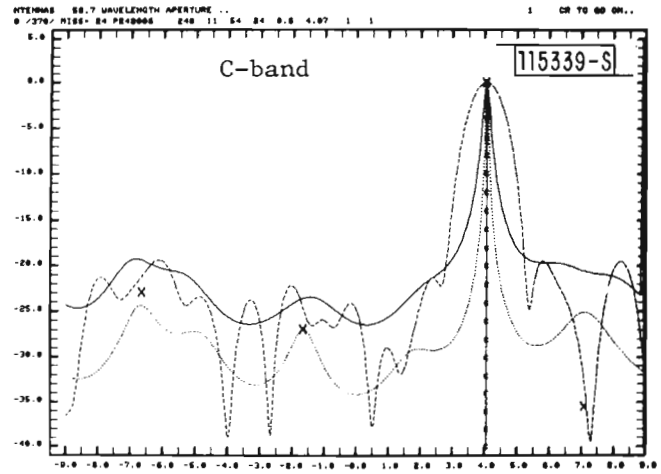

Simulation predicted (ground reflection calculation/focusing ground)

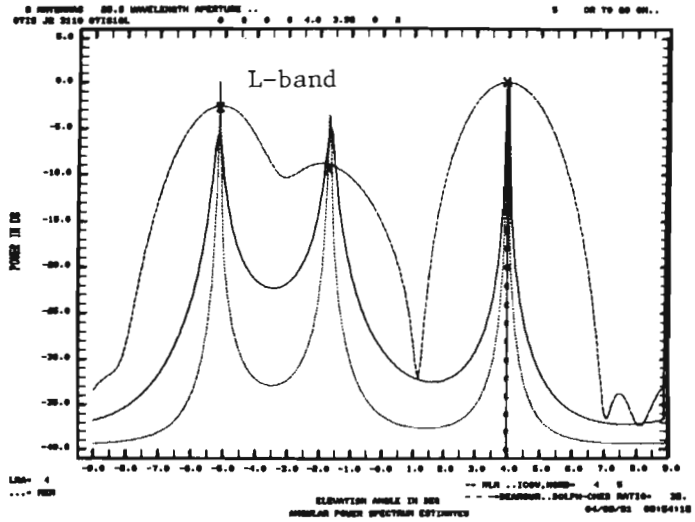

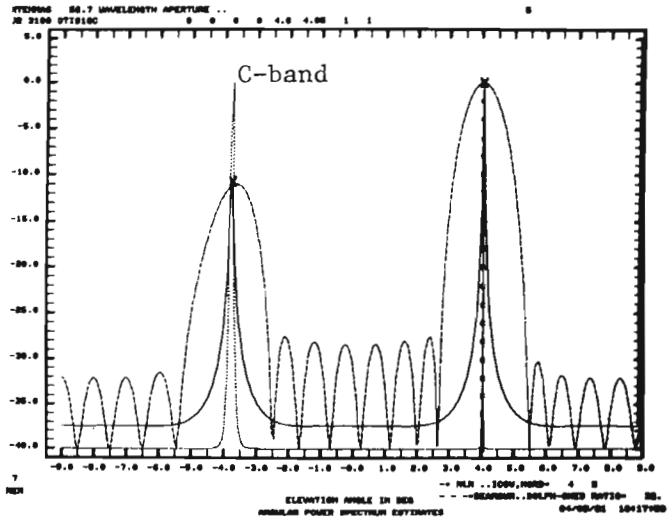

Fig. 5-46. Camp Edwards measurement: J2 range, L- and C-bands elevation arrays, $\theta_{EL} \simeq 4°$.

Field Measured

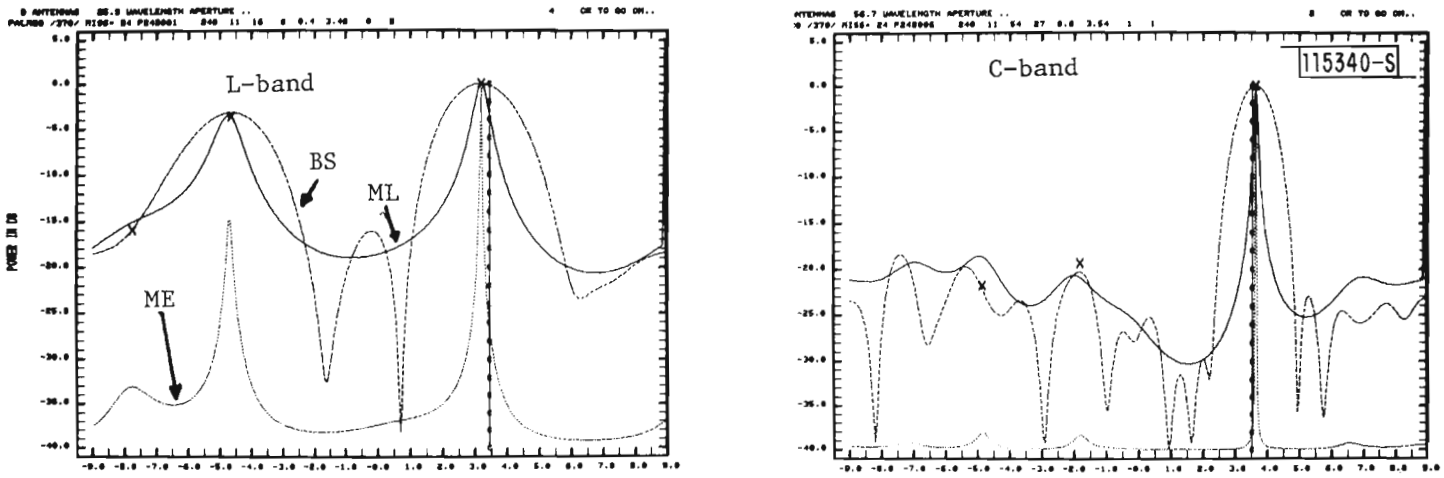

Simulation predicted (ground reflection calculation/focusing ground)

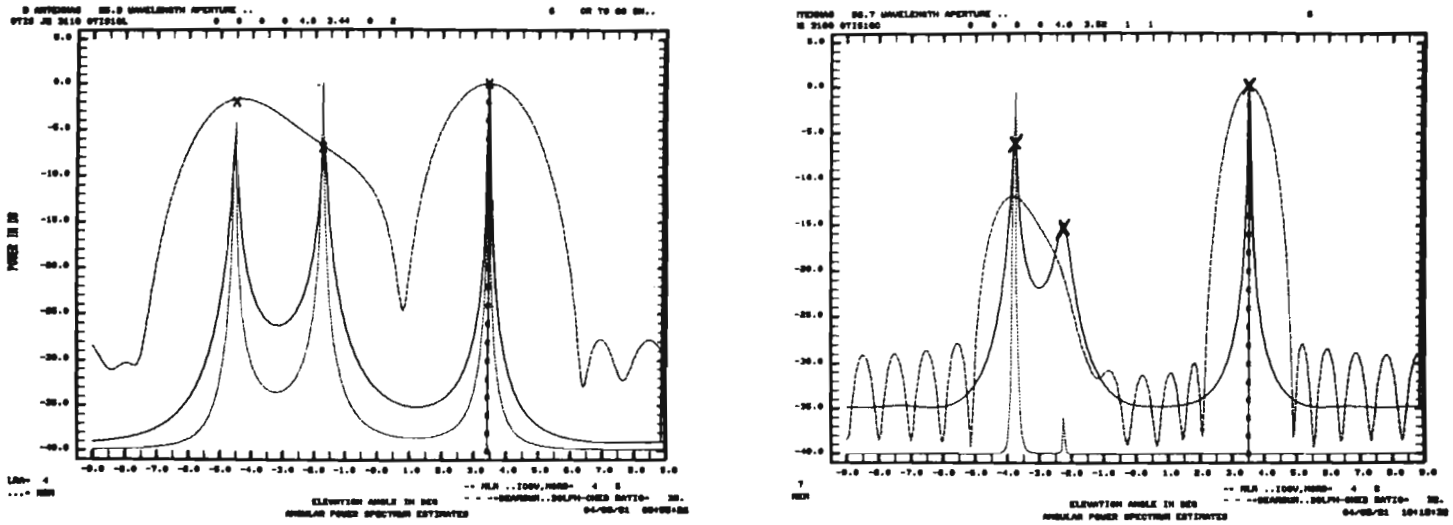

Fig. 5-47. Camp Edwards measurement: J2 range, L- and C-bands elevation arrays, $\theta_{EL} \simeq 3.5°$.

Field Measured

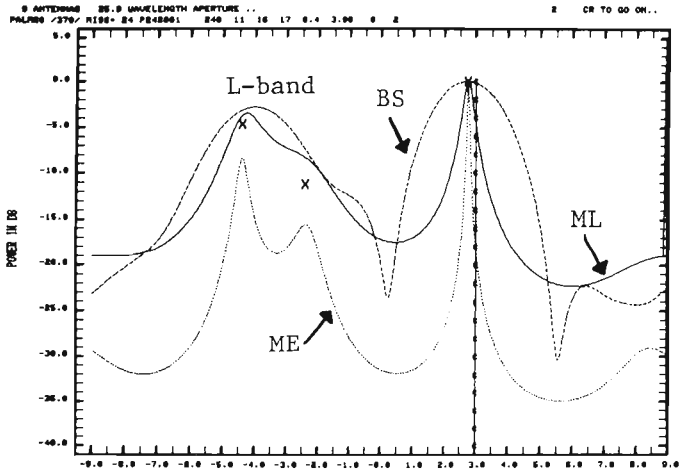

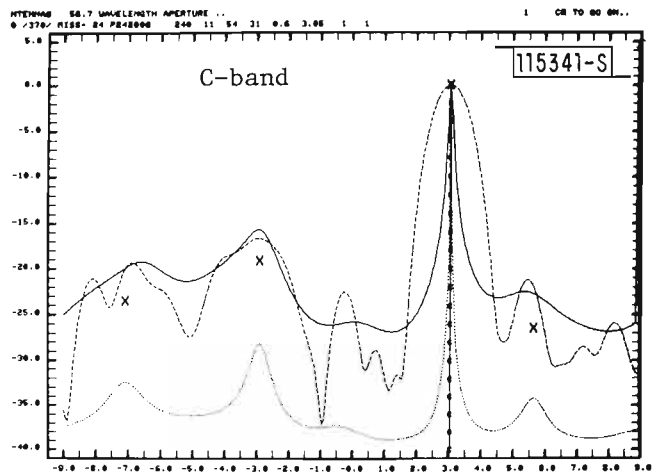

Simulation predicted (ground reflection calculation/focusing ground)

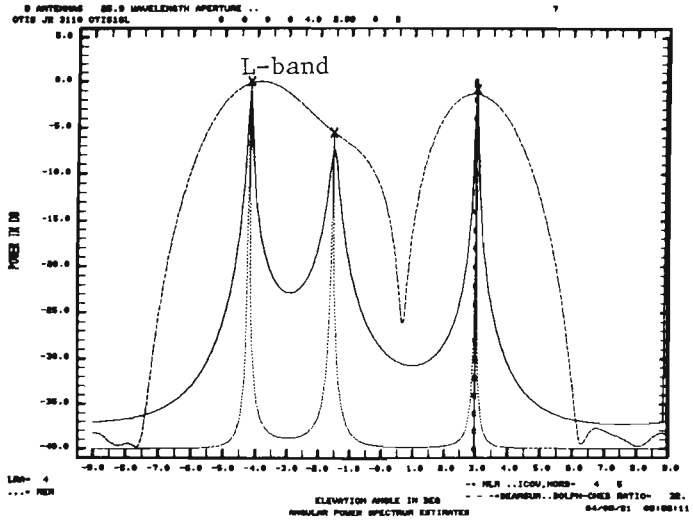

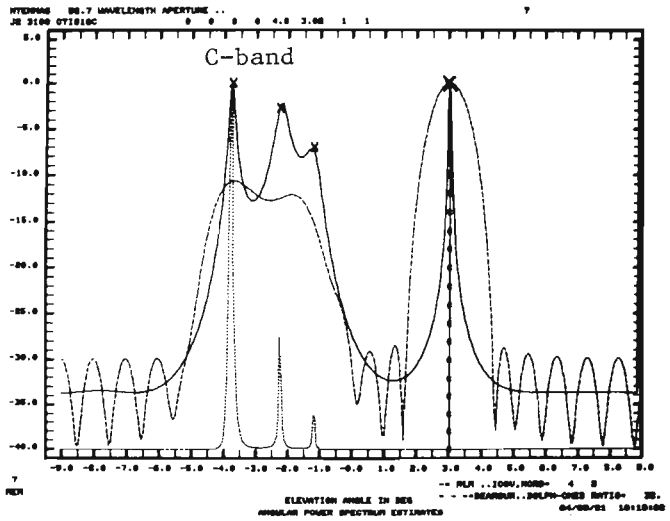

Fig. 5-48. Camp Edwards measurement: J2 range, L- and C-bands elevation arrays, $\theta_{EL} \simeq 3°$.

Field Measured

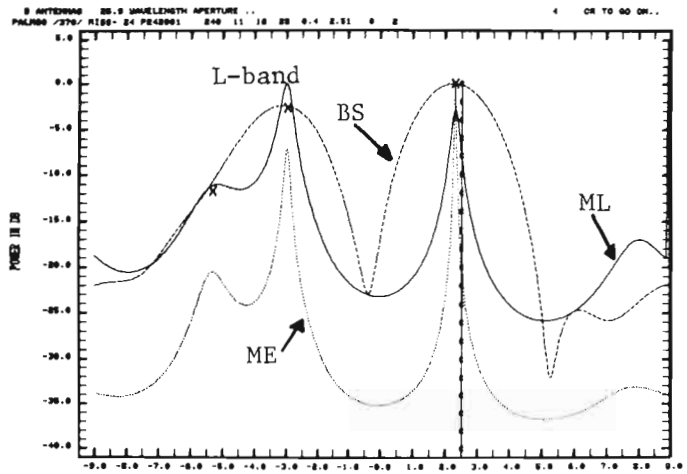

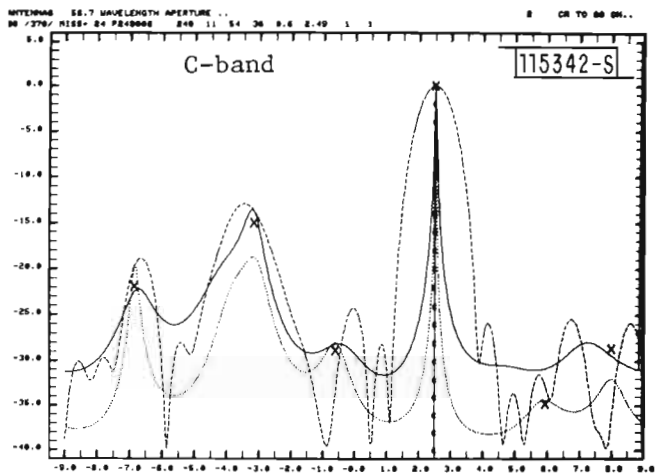

Simulation predicted (ground reflection calculation/focusing ground)

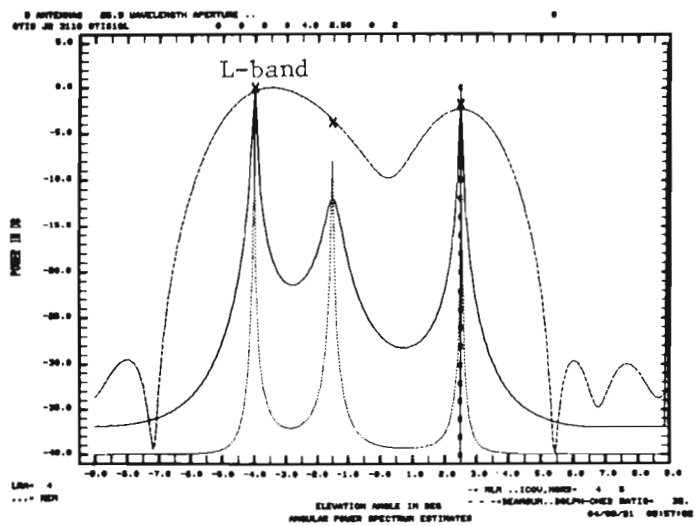

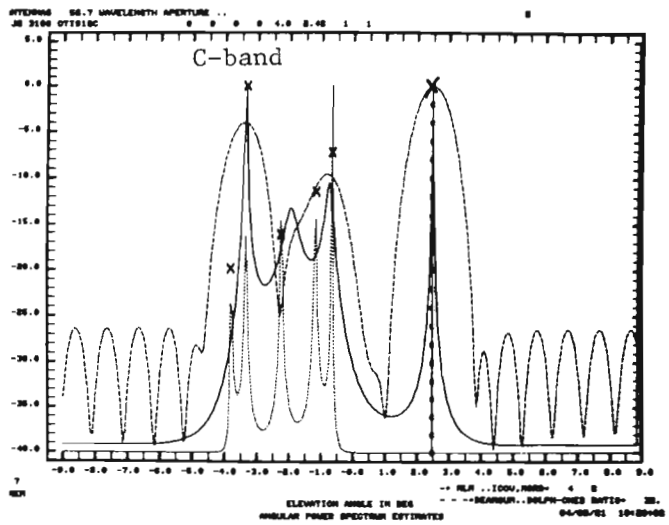

Fig. 5-49. Camp Edwards measurement: J2 range, L- and C-bands elevation arrays, $\theta_{EL} \simeq 2.5°$.

Field Measured

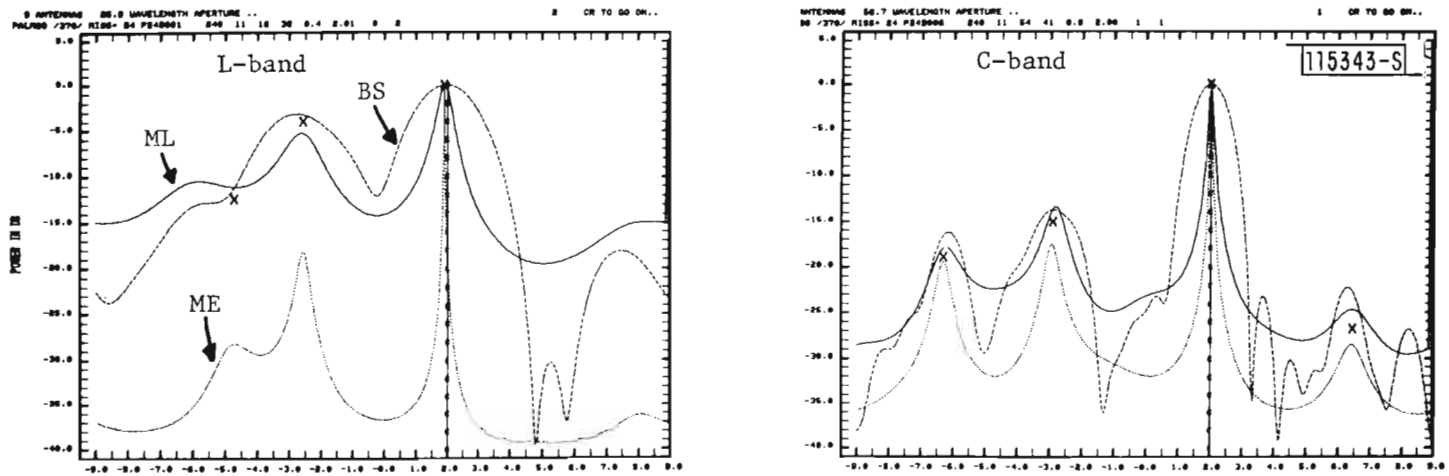

Simulation predicted (ground reflection calculation/focusing ground)

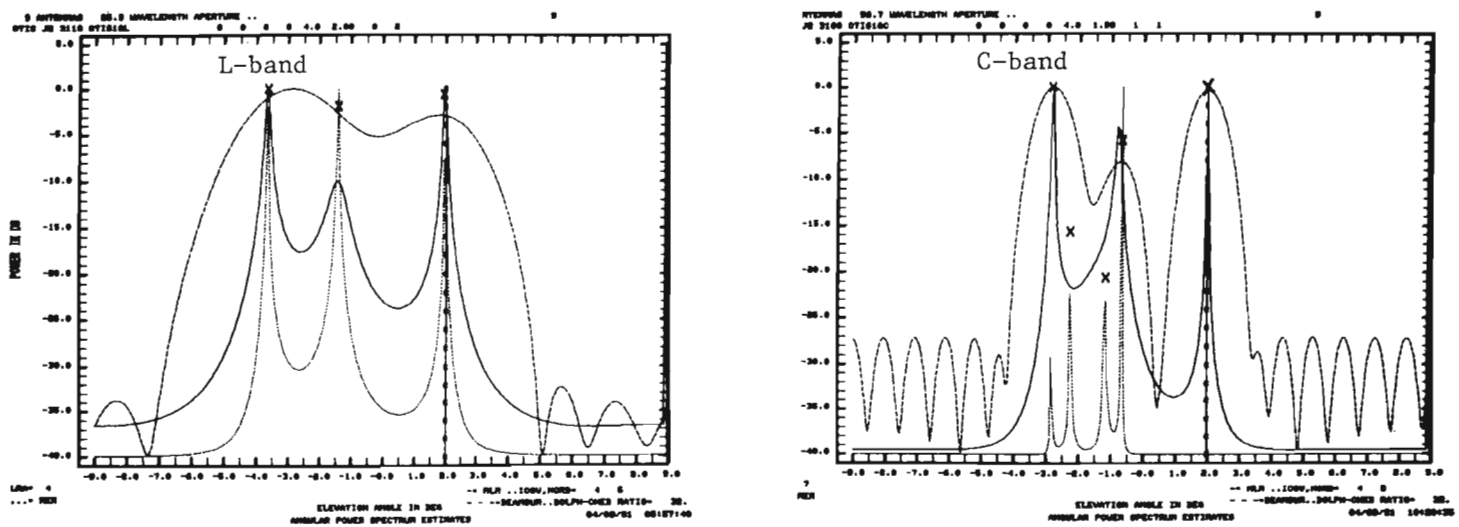

Fig. 5-50. Camp Edwards measurement: J2 range, L- and C-bands elevation arrays, $\theta_{EL} \simeq 2°$.

Field Measured

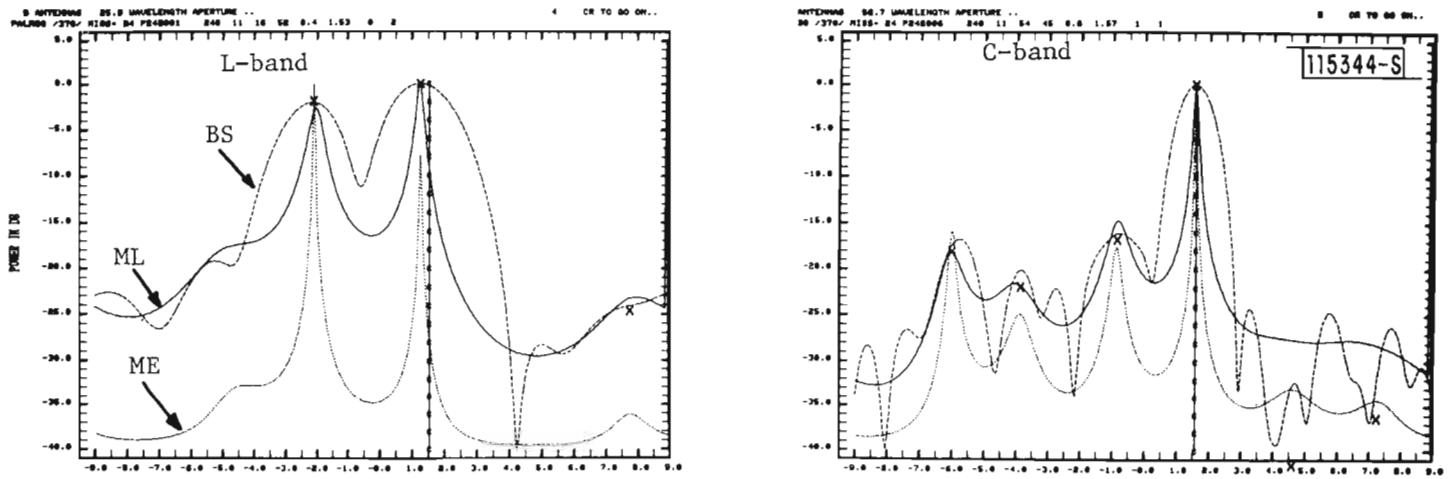

Simulation predicted (ground reflection calculated/focusing ground)

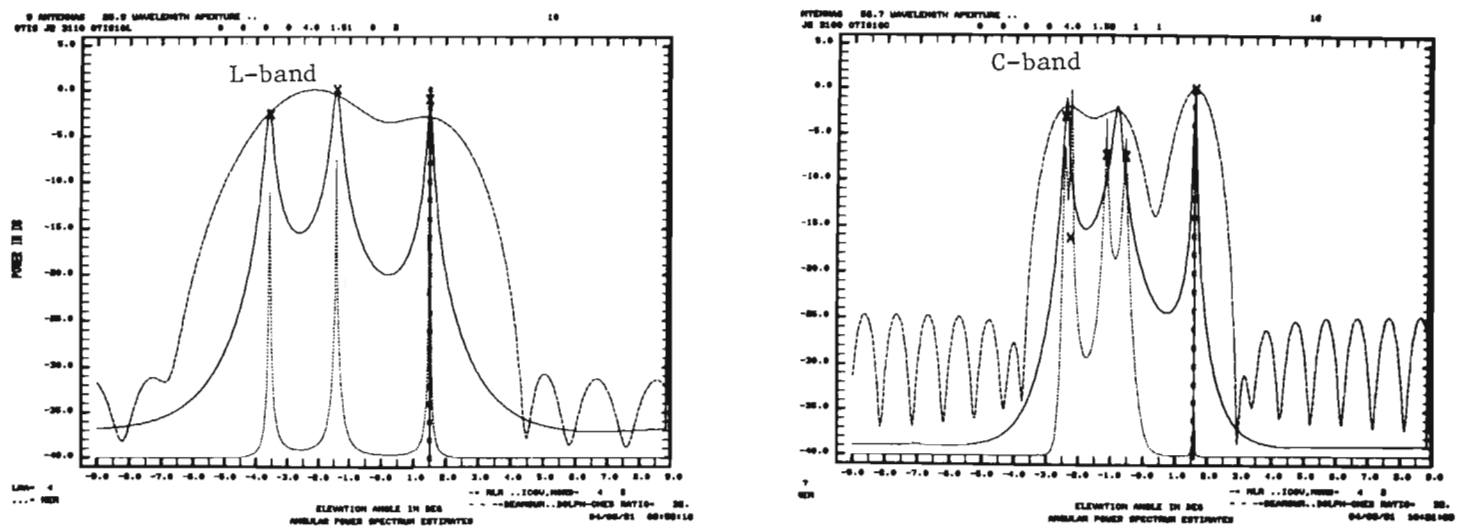

Fig. 5-51. Camp Edwards measurement: J2 range, L- and C-bands elevation arrays, $\theta_{EL} \simeq 1.5°$.

Field Measured

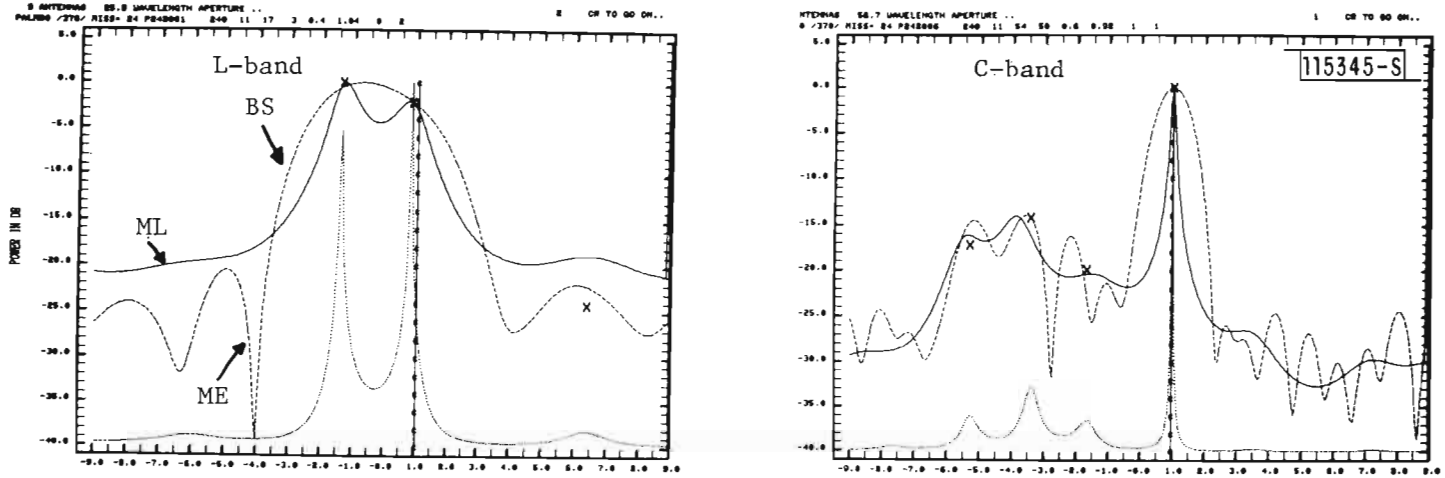

Simulation Predicted (ground reflection calculation/focusing ground)

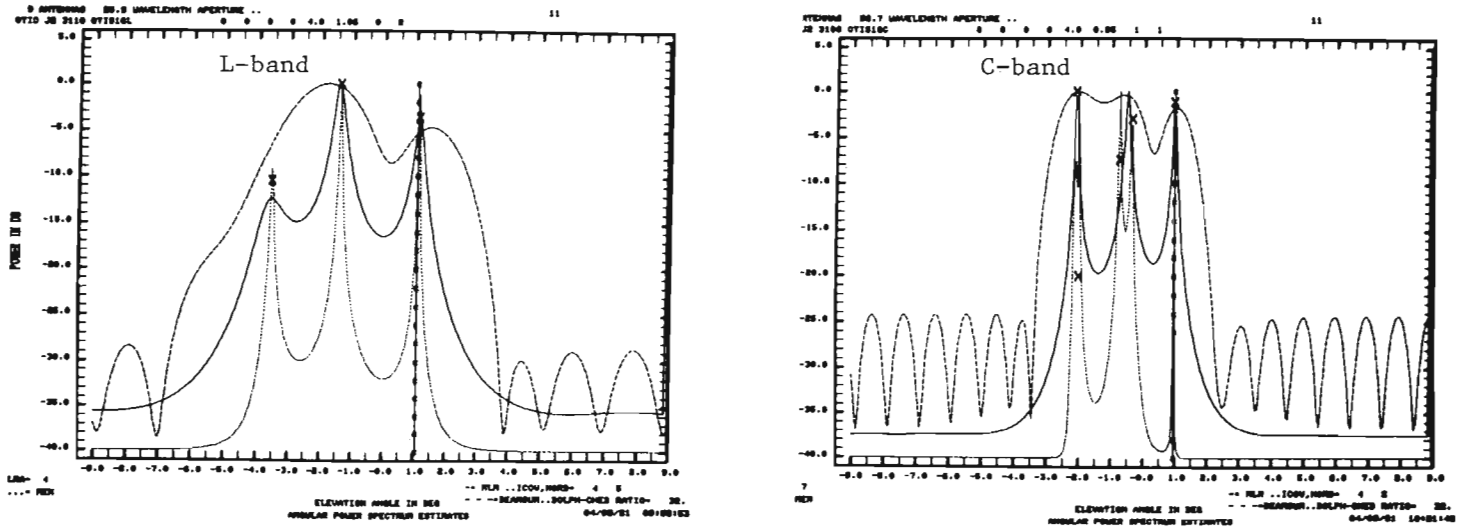

Fig. 5-52. Camp Edwards measurement: J2 range, L- and C-bands elevation arrays, $\theta_{EL} \simeq 1°$.

Field Measured

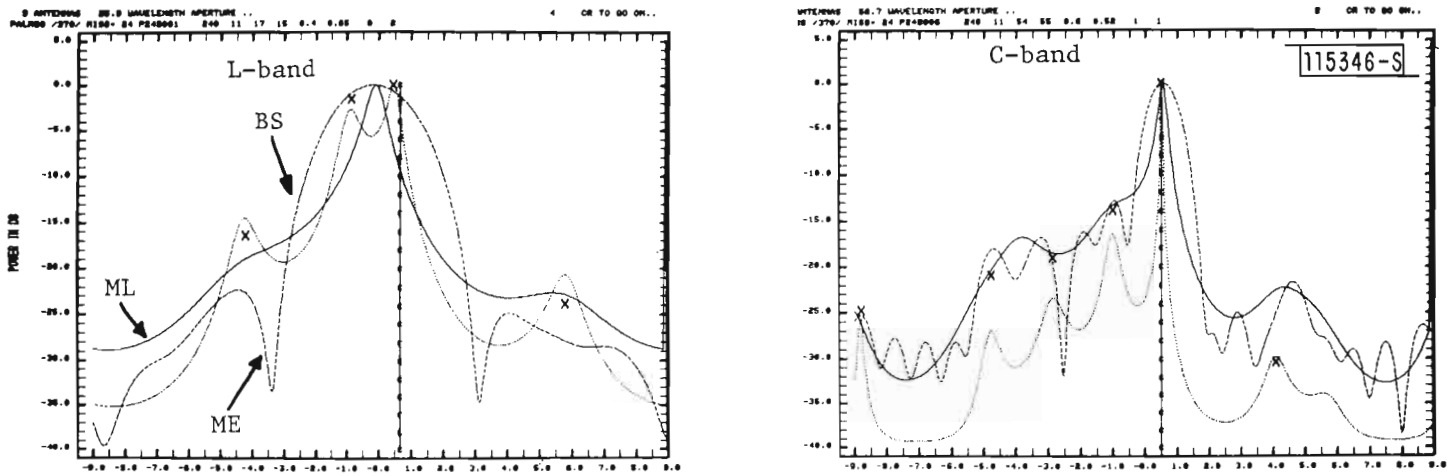

Simulation predicted (ground reflection calculation/focusing ground)

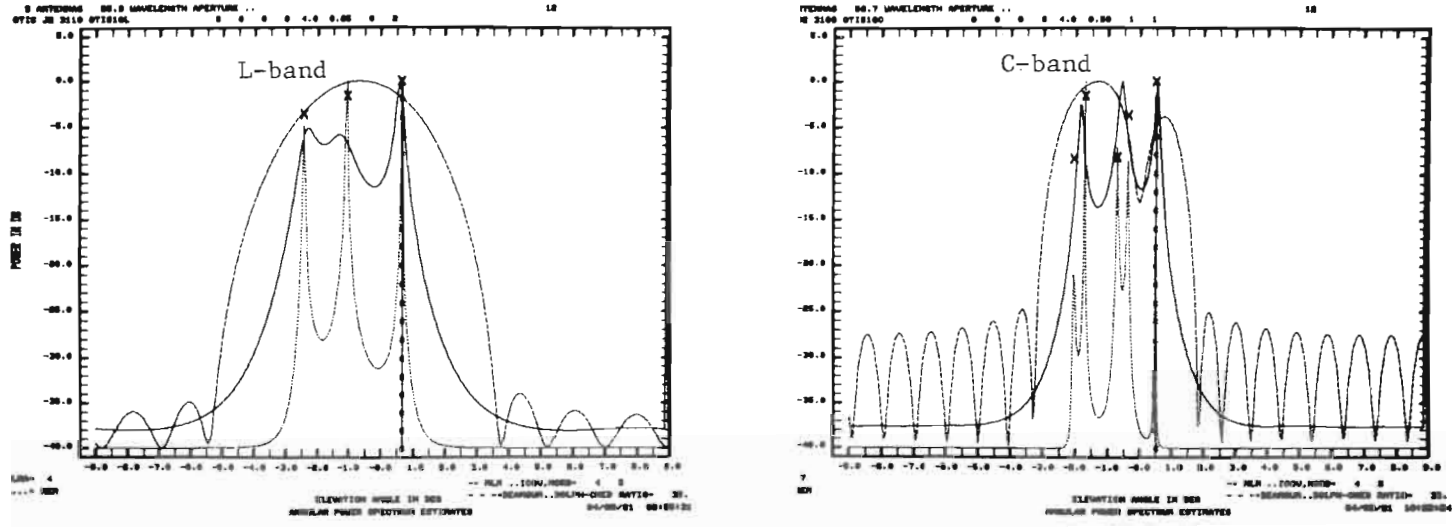

Fig. 5-53. Camp Edwards measurement: J2 range, L- and C-bands elevation arrays, $\theta_{EL} \simeq 0.5°$.

The indication of diffuse reflections in the C-band field measured results here is even stronger than that at the Fort Devens golf course radial line O-C. Only at very low helicopter elevation angles (θ_{EL} = 0.2° - 0.4°), the C-band field measured results start to show specular reflections at multipath levels of -8 dB to -2 dB (Fig. 5-54).

For the L band, the simulation predicted results agree fairly well with the field measured results, in terms of the number of multipath arrivals, their arrival angles and M/D ratios. However, the agreement for the C-band results is very poor. This poor agreement is not too surprising; since (1) the C-band field measured results strongly indicate that the C-band multipath environment here probably is dominated by the diffuse reflections, and (2) the simulation predicted results were obtained with the focusing ground option of the ground reflection calculation which only considered the specular ground reflections. Figure 5-55 plots the EL multipath level and the angle error versus the direct signal EL angle.

The L-band AZ angular power spectral estimates are given in Figs. 5-56 and 5-57 for two helicopter elevation positions. Both the simulation predicted results and the field measured results show one spectral peak. This suggests that the direct signal arrival and the multipath arrivals indicated in the L-band EL power spectral estimates all come from the same azimuth angle. This seems reasonable, since the terrain cross-range tilts are fairly small (Fig. 4-9).

2. Gibbs Road Entrance

Figs. 5-58 through 5-68 show examples of the EL angular power spectral estimates for the measurements taken at Camp Edwards Gibbs Road entrance site. The terrain here was rolling with large along-range height variation and significant cross-range tilts, as described in Chapter IV Section C (Fig. 4-11). Although the ground along Gibbs Road was fairly smooth, the off-road area was not quite so (Fig. 4-12). The L-band field measured results show moderate multipath levels around -5dB to -10dB for higher elevation angles ($\theta_{EL} > 2°$) and very high multipath level of 1 dB at low elevation angle of $\theta_{EL} \simeq 0.7°$. The C-band multipath level appears to vary in the similar manner

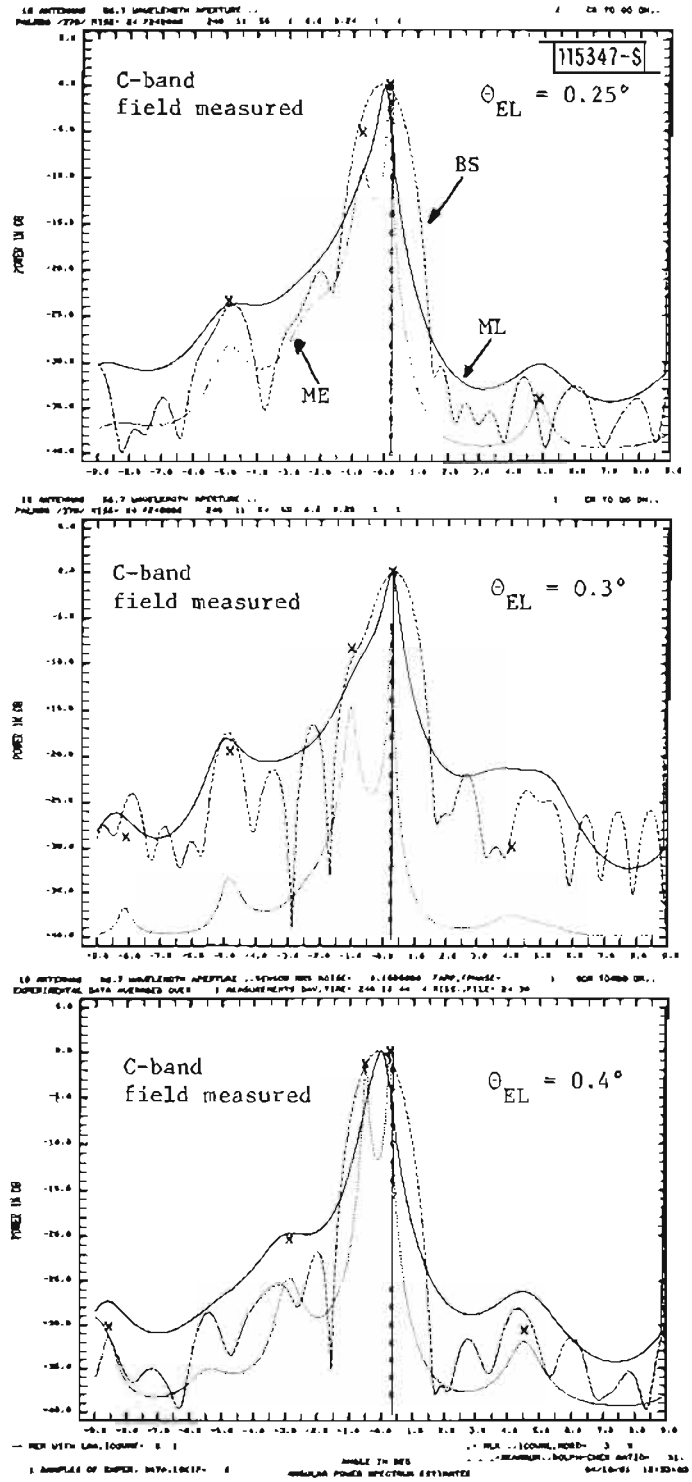

Fig. 5-54. Camp Edwards measurement: J2 range, L-band elevation array, $\theta_{EL} < 0.5°$.

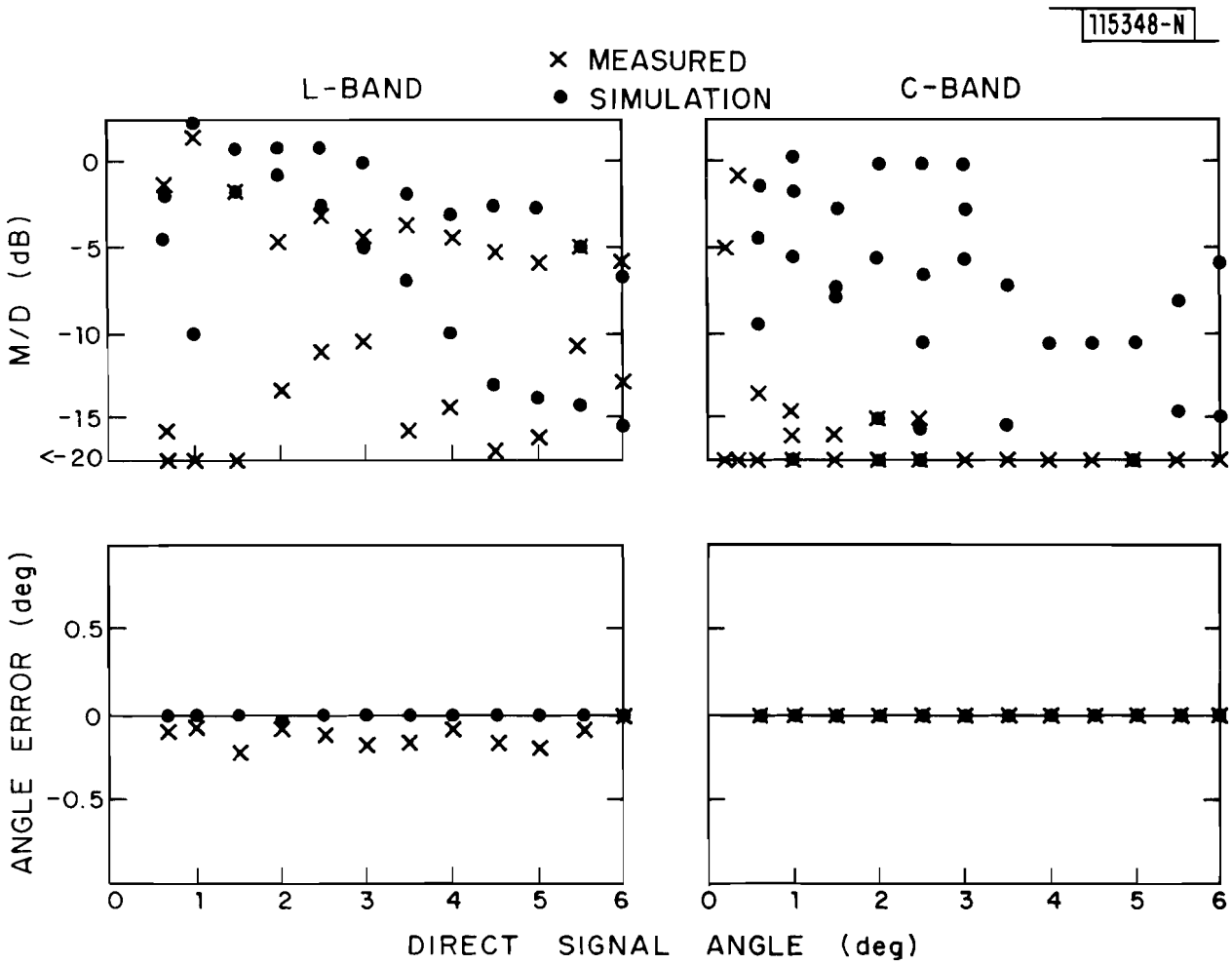

Fig. 5-55. Camp Edwards measurement: J2 range, L- and C-bands elevation arrays, M/D ratios and angle errors.

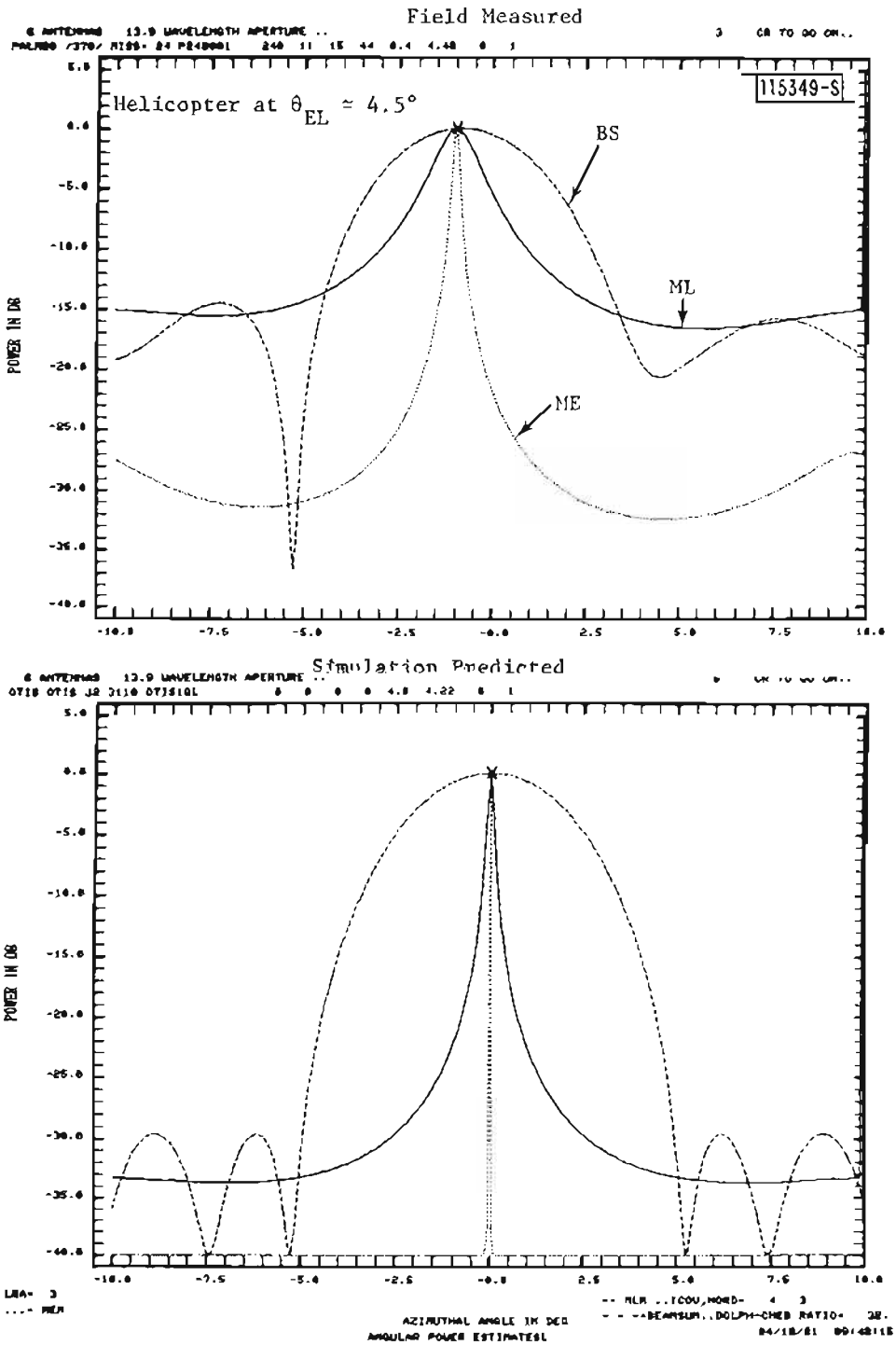

Fig. 5-56. Camp Edwards measurement: J2 range, L-band azimuth array, $\theta_{EL} \simeq 4.5°$.

Field Measured

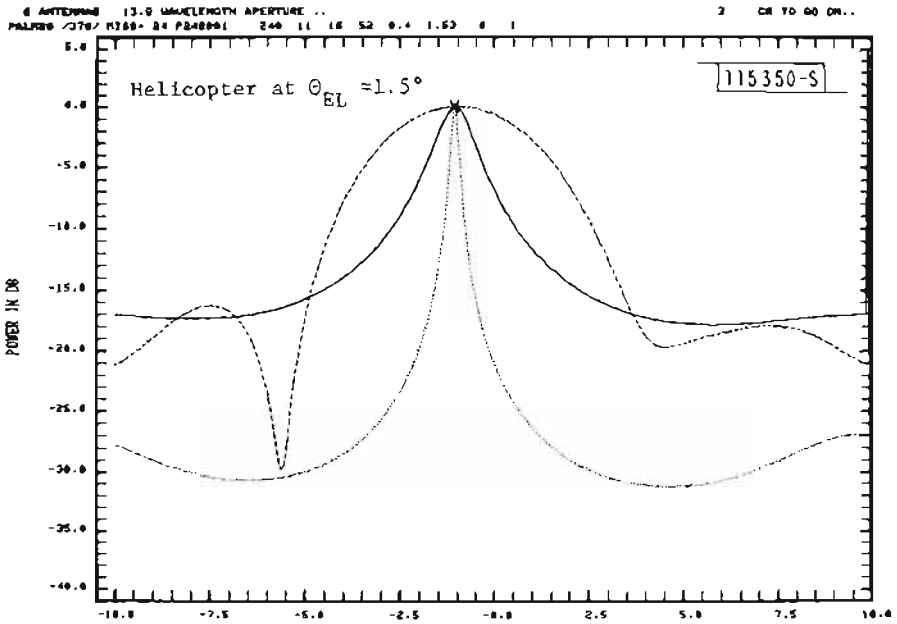

Simulation Predicted

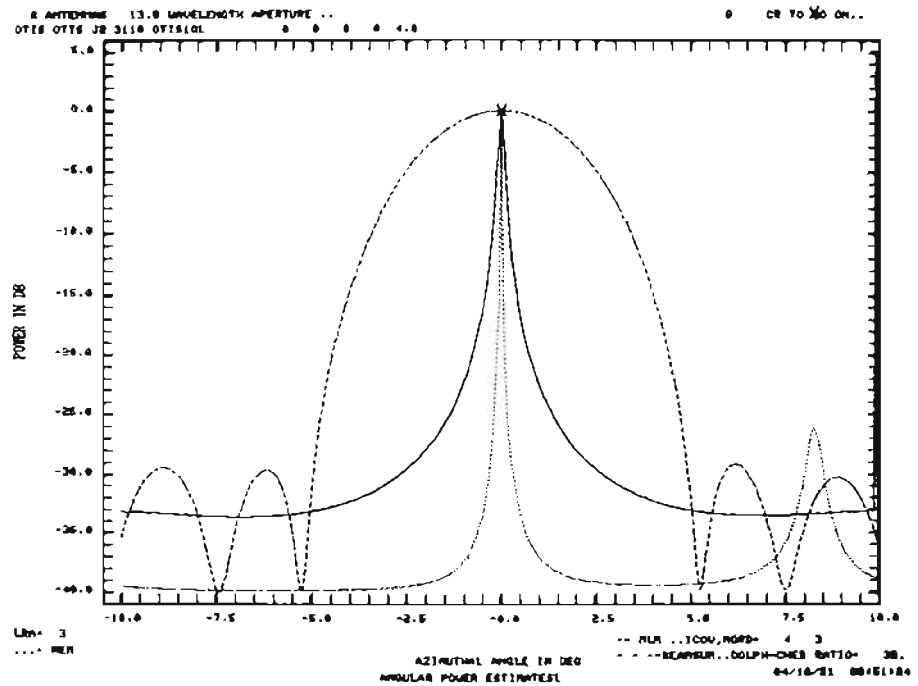

Fig. 5-57. Camp Edwards measurement: J2 range, L-band azimuth array, $\theta_{EL} \simeq 1.5°$.

Field Measured

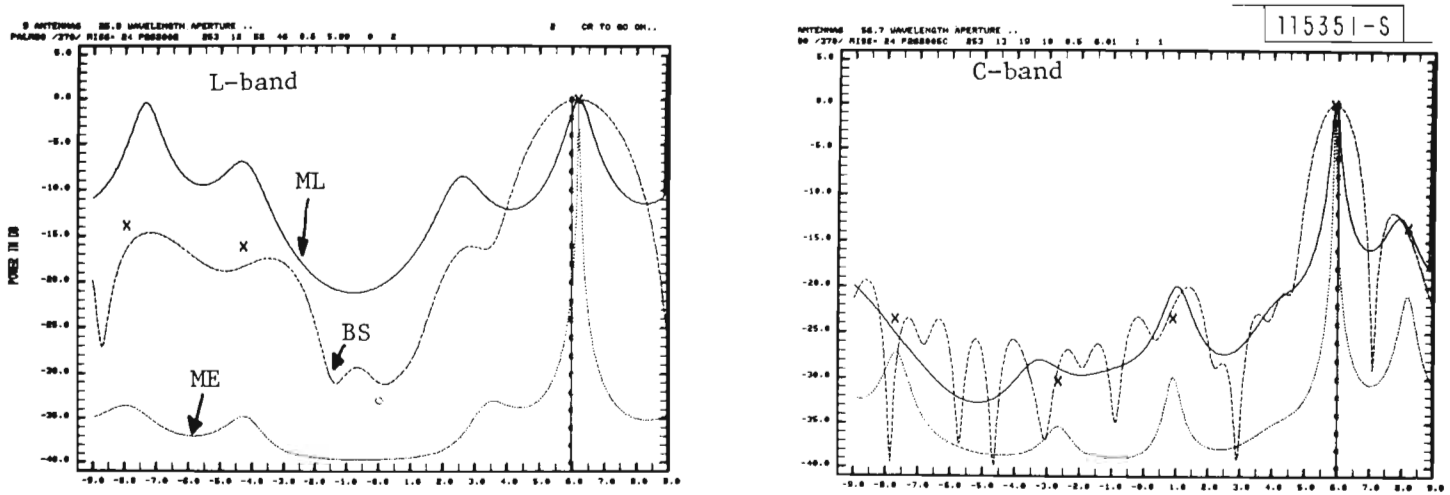

Simulation Predicted (ground reflection calculation/focusing ground)

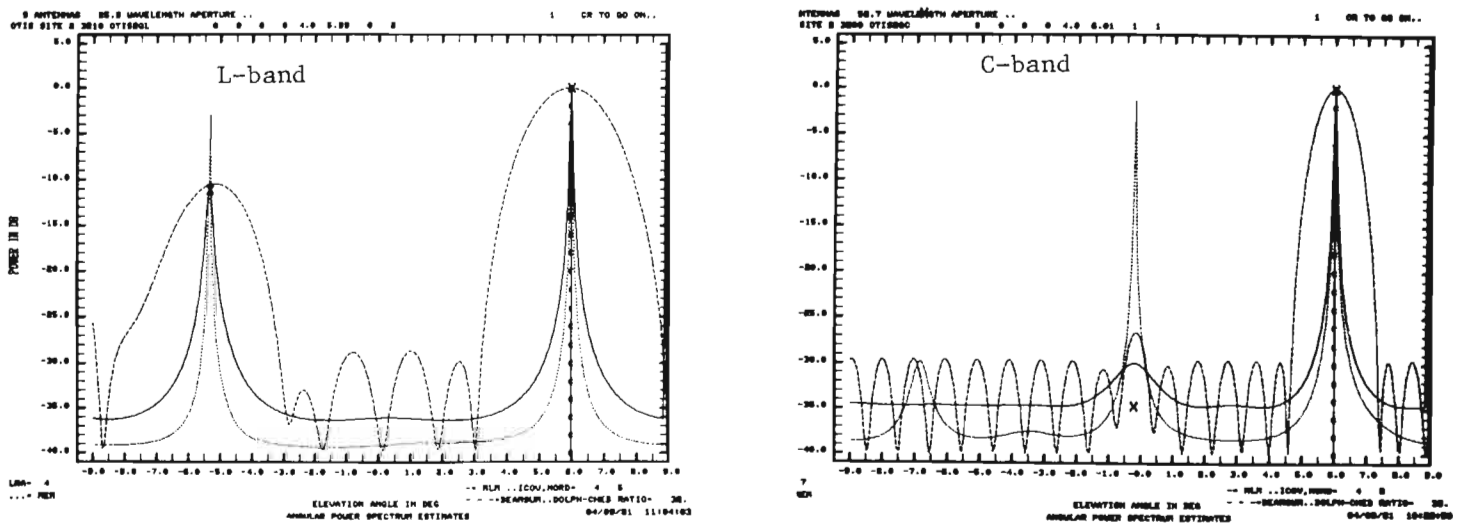

Fig. 5-58. Camp Edwards measurement: Gibbs Road E, L- and C-bands elevation arrays, $\theta_{EL} \simeq 6°$.

Field Measured

115352-S

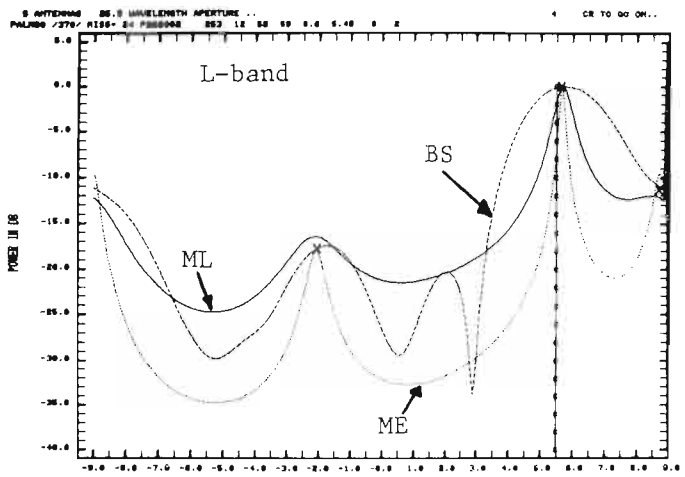

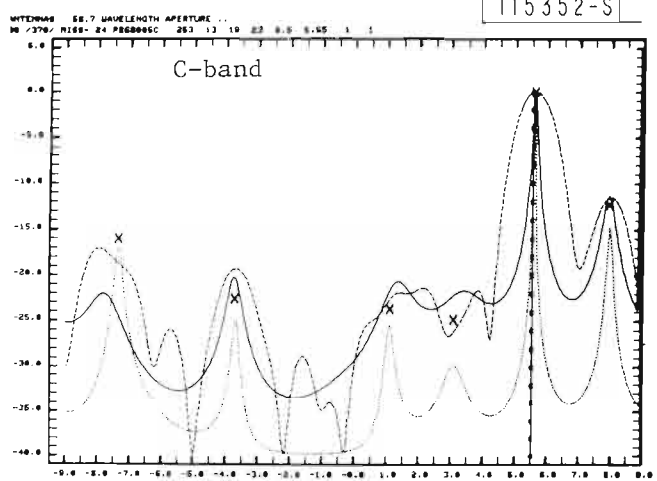

Simulation Predicted (ground reflection calculation/focusing ground)

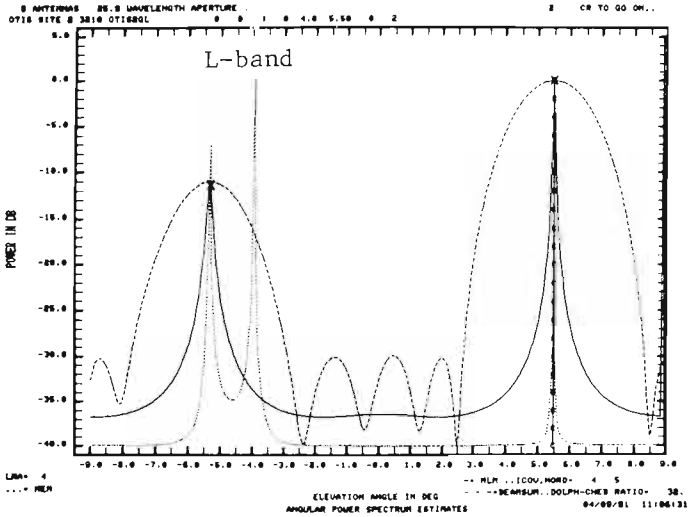

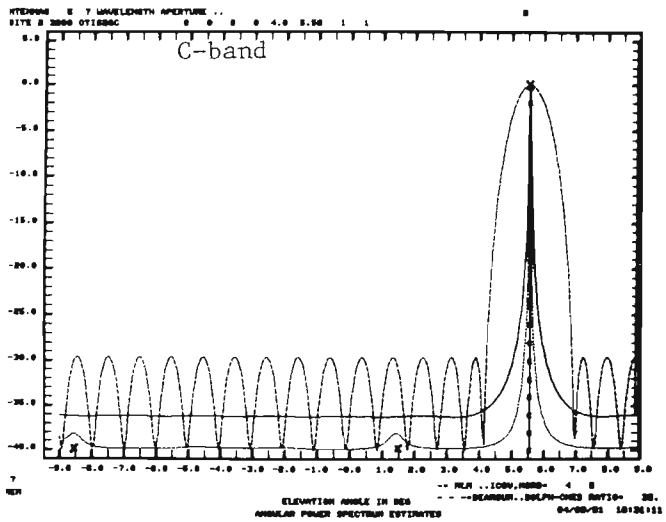

Fig. 5-59. Camp Edwards measurement: Gibbs Road E, L- and C-bands elevation arrays, $\theta_{EL} \simeq 5.5°$.

Field Measured

115353-S

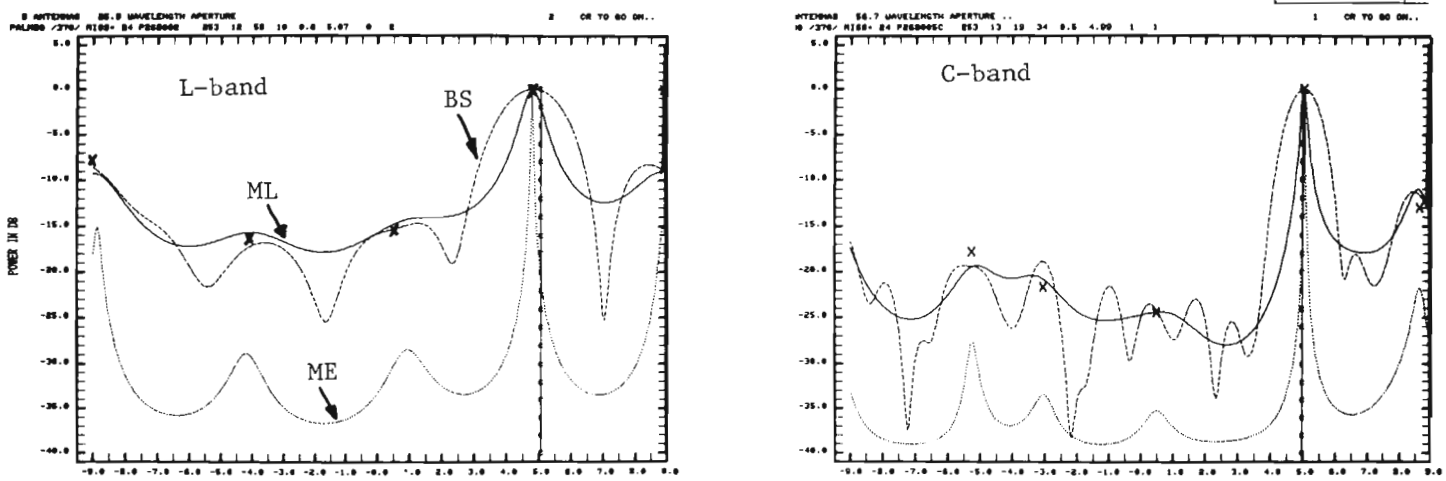

Simulation Predicted (ground reflection calculation/focusing ground)

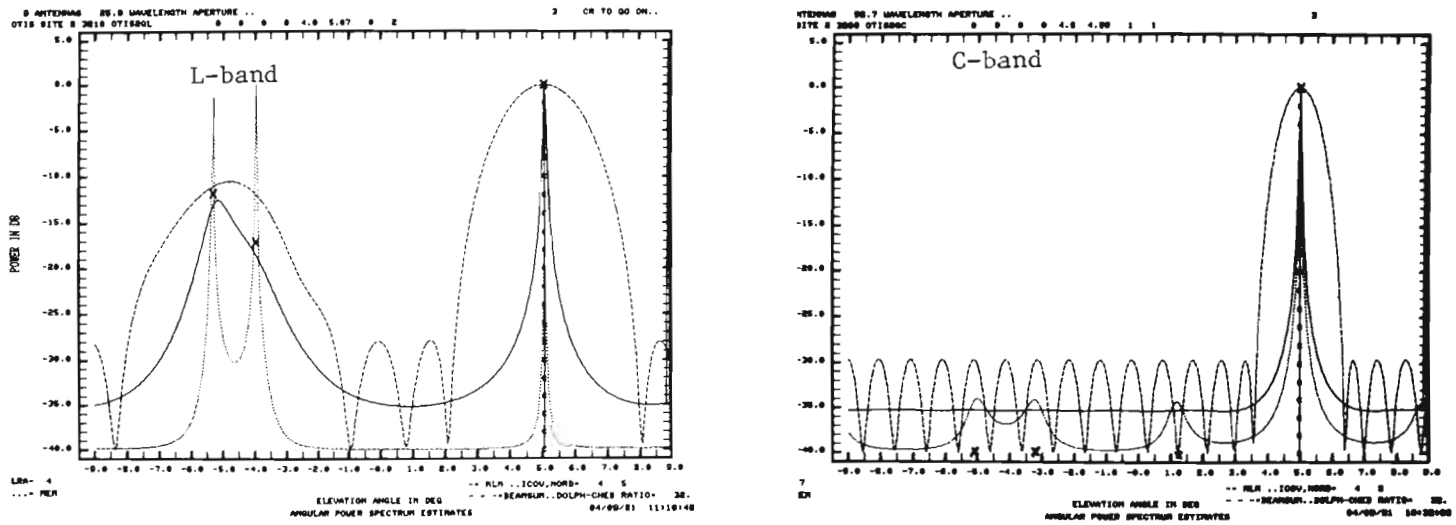

Fig. 5-60. Camp Edwards measurement: Gibbs Road E, L- and C-bands elevation arrays, $\theta_{EL} \simeq 5°$.

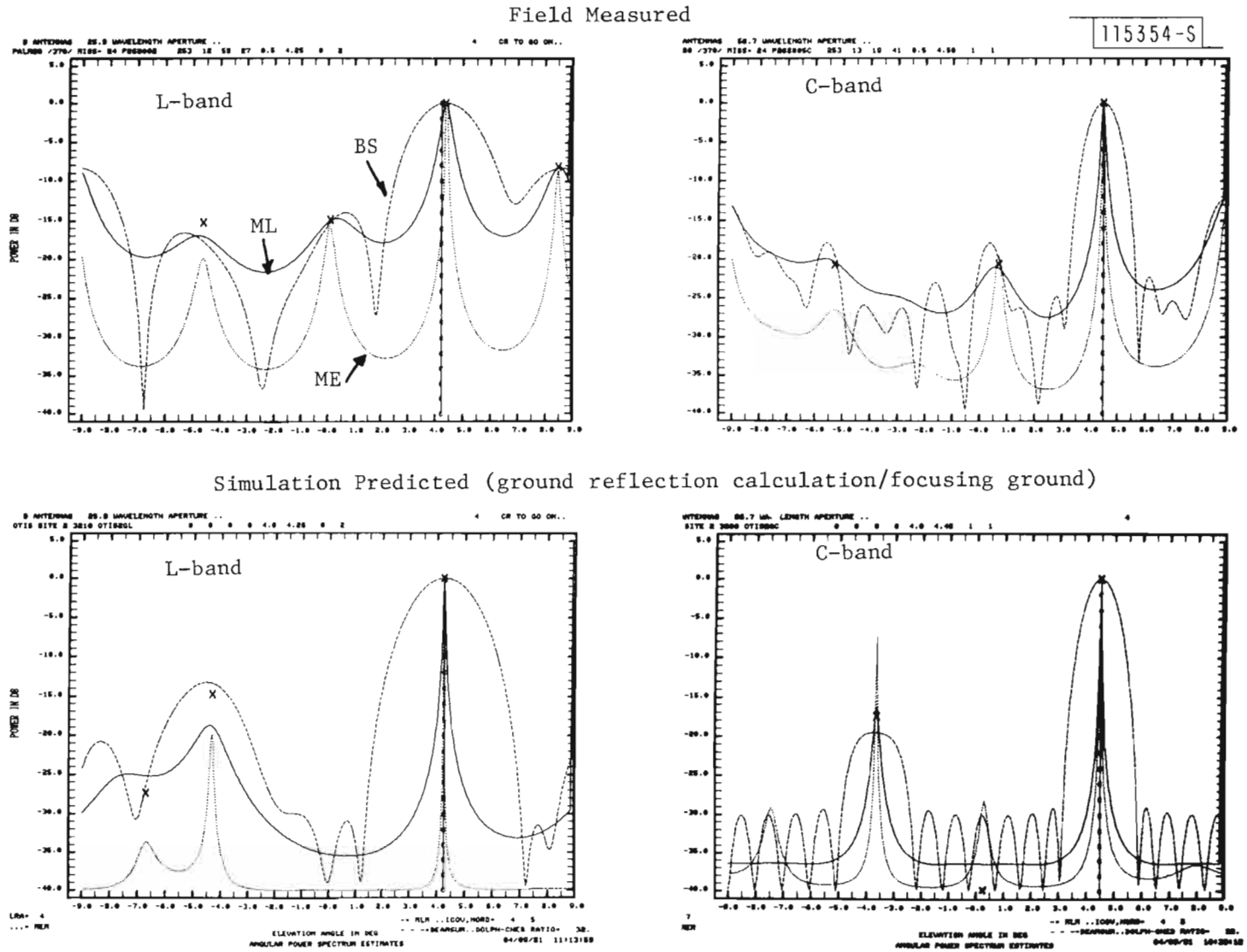

Fig. 5-61. Camp Edwards measurement: Gibbs Road E, L- and C-bands elevation arrays, $\theta_{EL} \simeq 4.5°$.

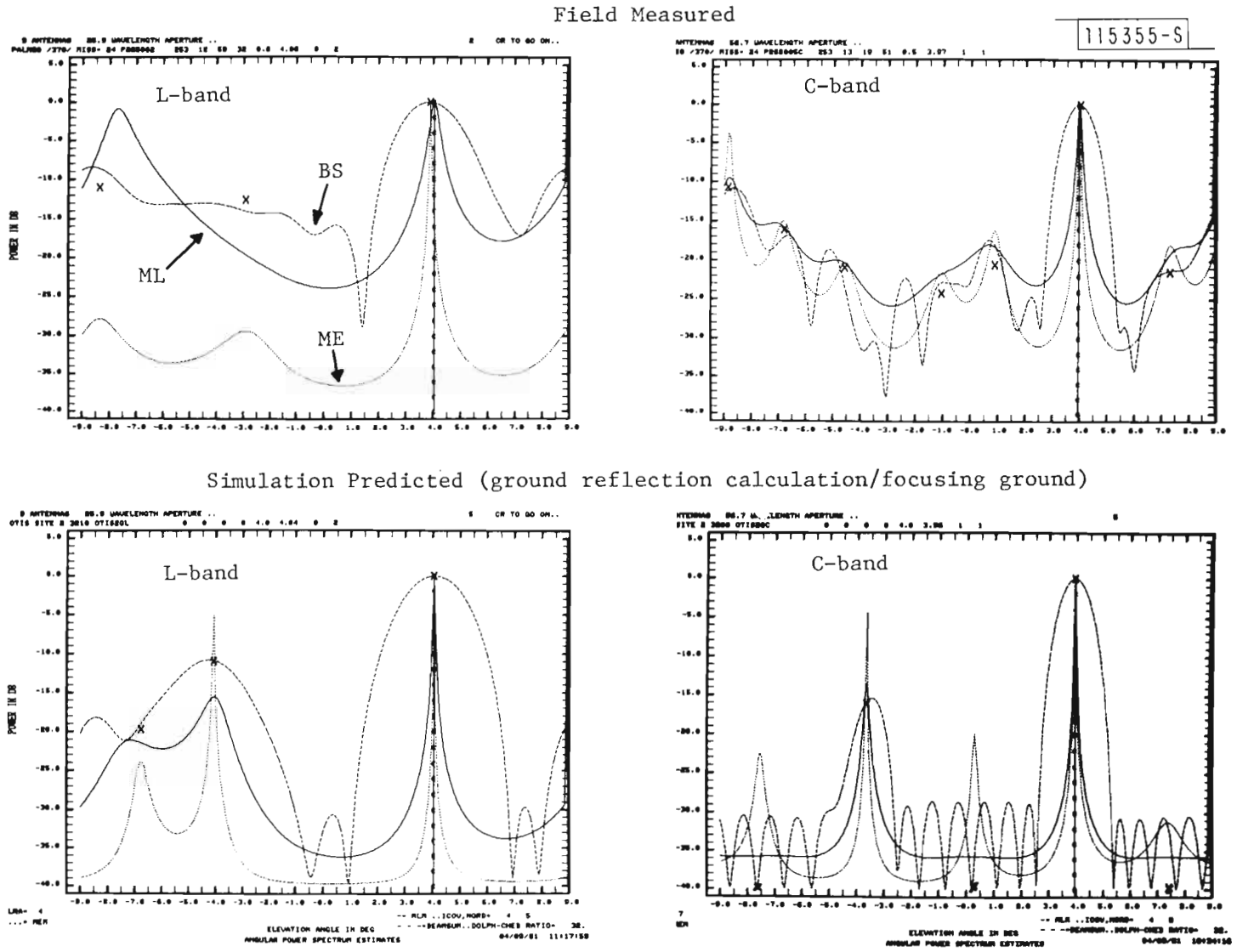

Fig. 5-62. Camp Edwards measurement: Gibbs Road E, L- and C-bands elevation arrays, $\theta_{EL} \simeq 4°$.

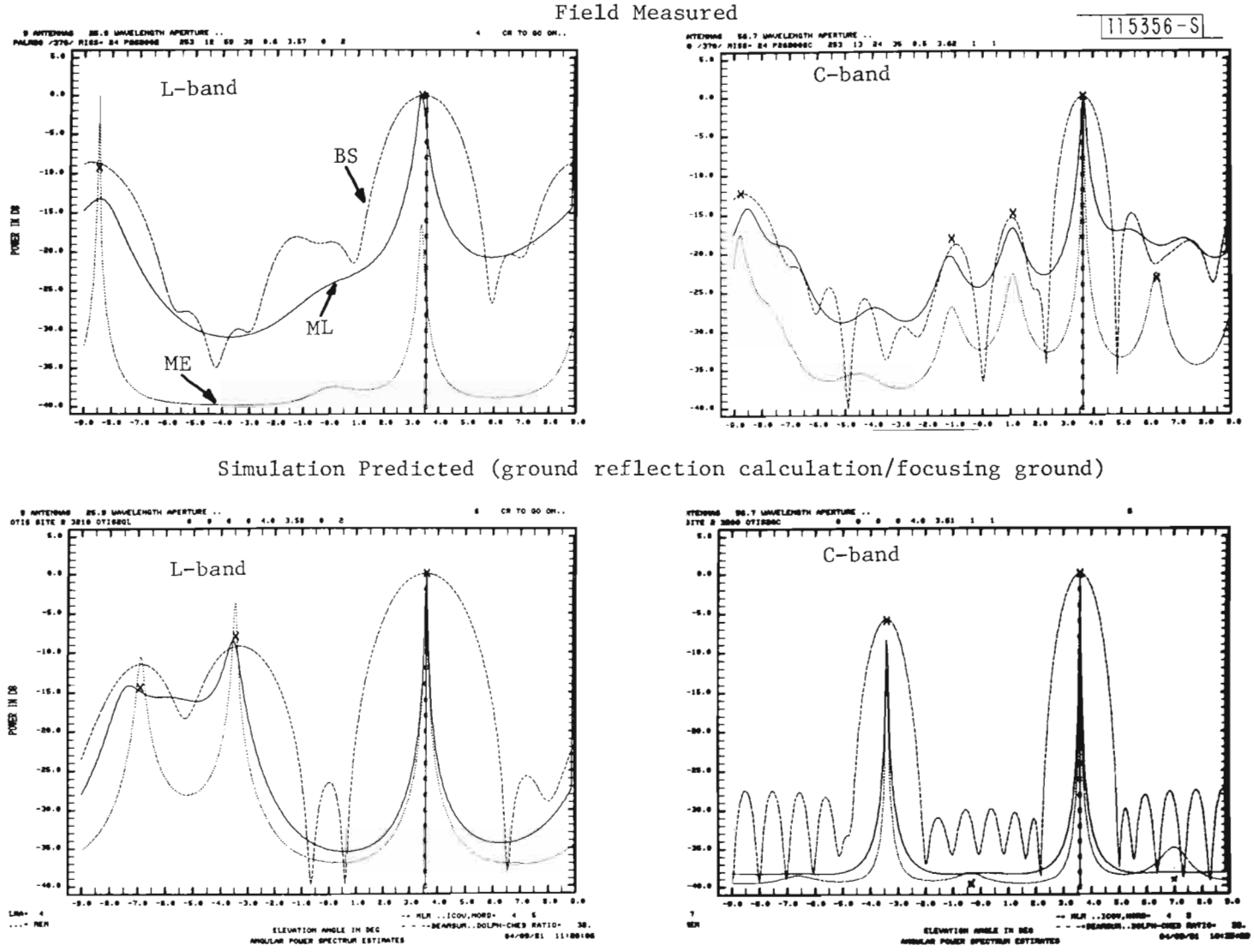

Fig. 5-63. Camp Edwards measurement: Gibbs Road E, L- and C-bands elevation arrays, $\theta_{EL} \simeq 3.5°$.

Field Measured

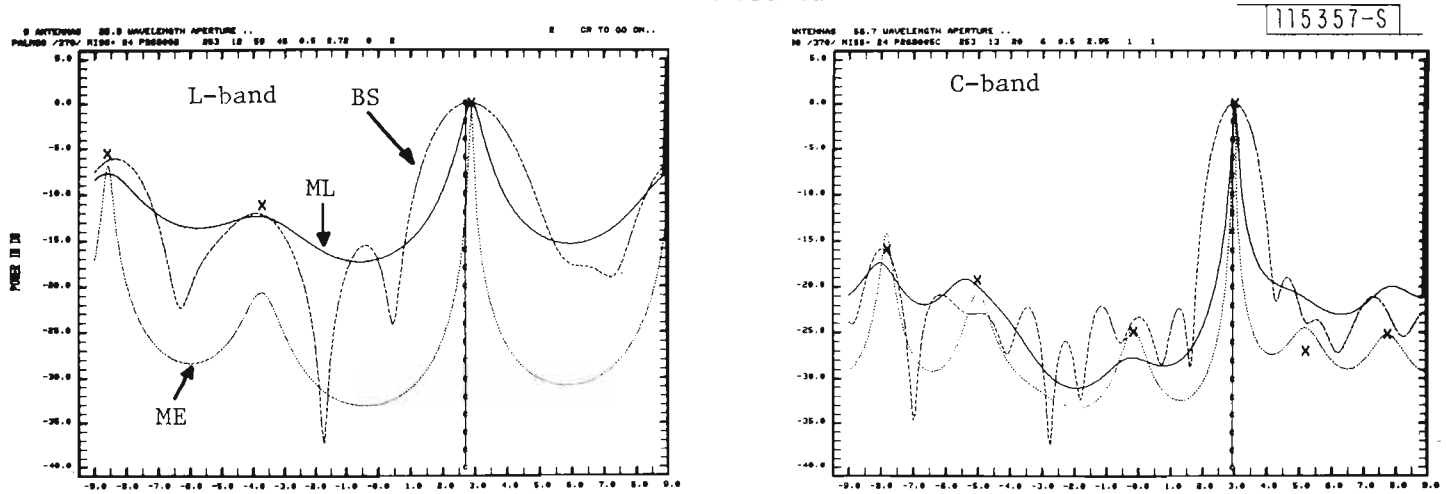

Simulation Predicted (ground reflection calculation/focusing ground)

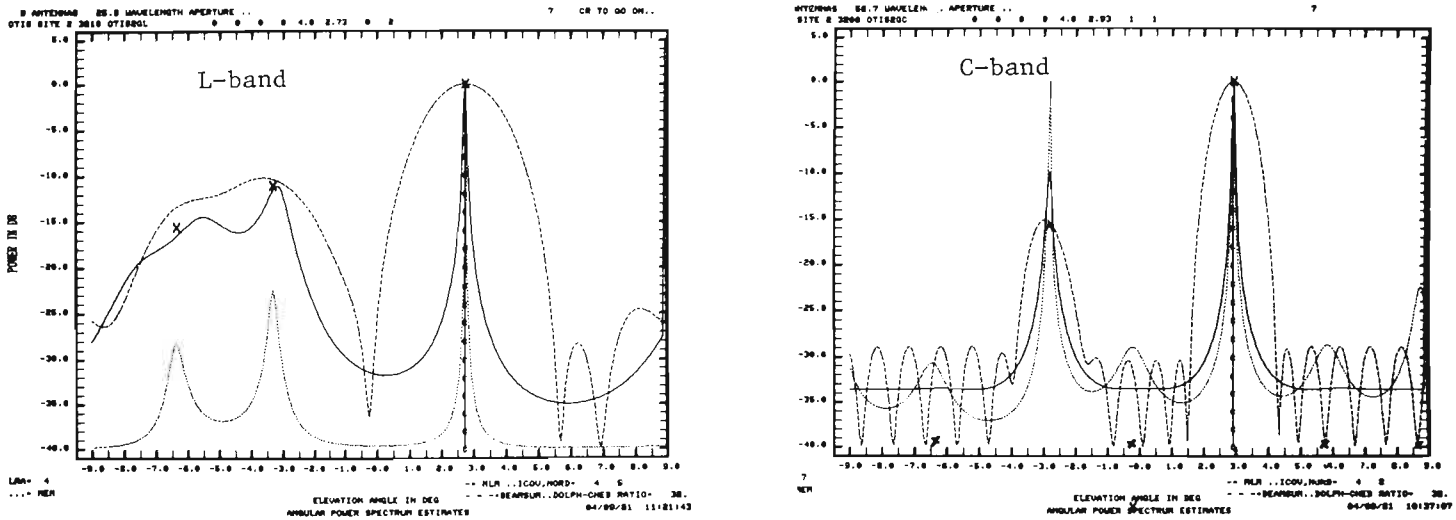

Fig. 5-64. Camp Edwards measurement: Gibbs Road E, L- and C-bands elevation arrays, $\theta_{EL} \simeq 3°$.

Field Measured

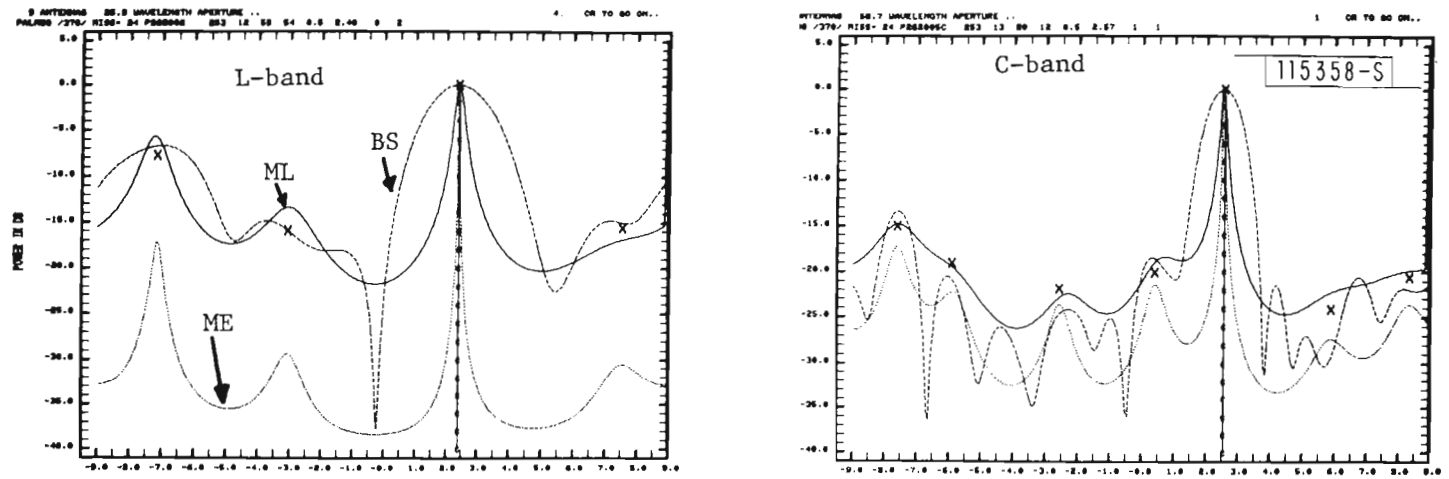

Simulation Predicted (ground reflection calculation/focusing ground)

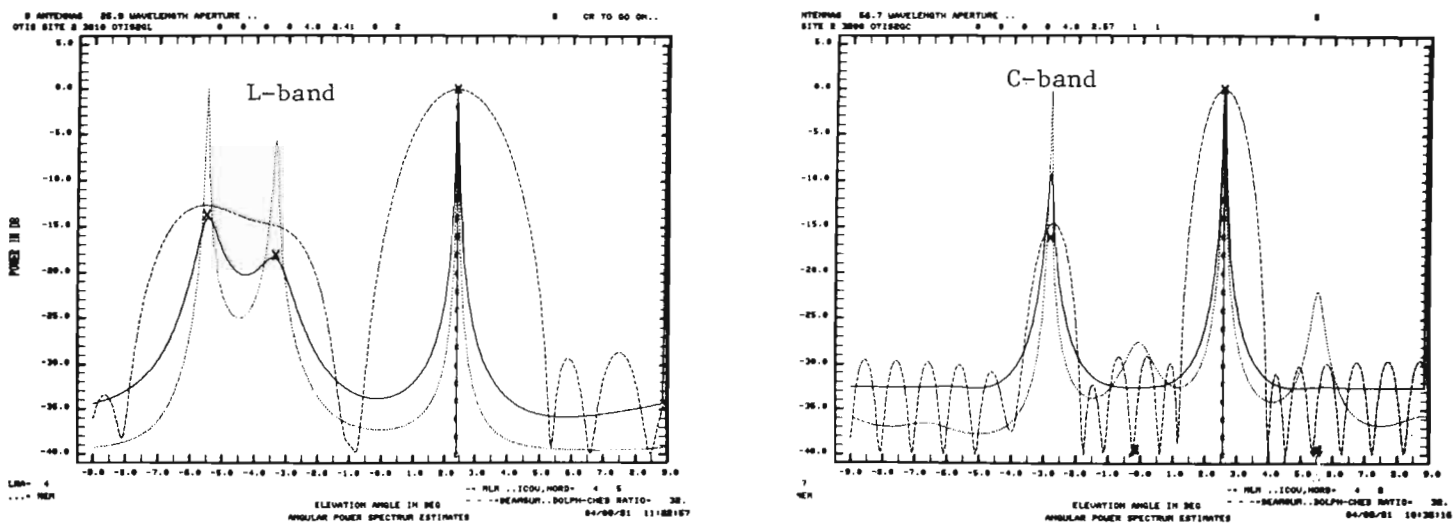

Fig. 5-65. Camp Edwards measurement: Gibbs Road E, L- and C-bands elevation arrays, $\theta_{EL} \simeq 2.5°$.

Field Measured

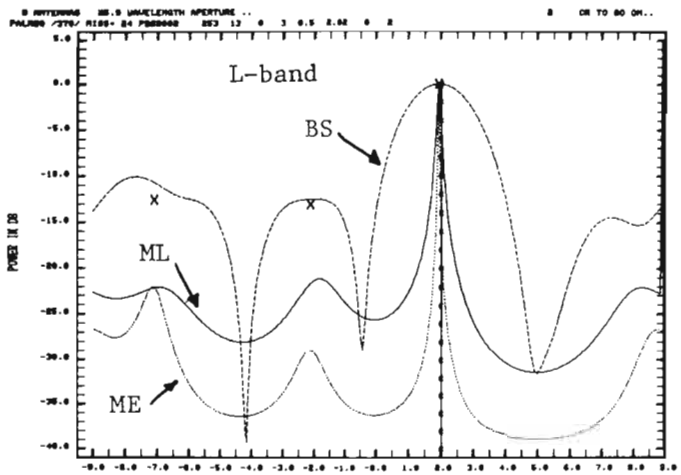

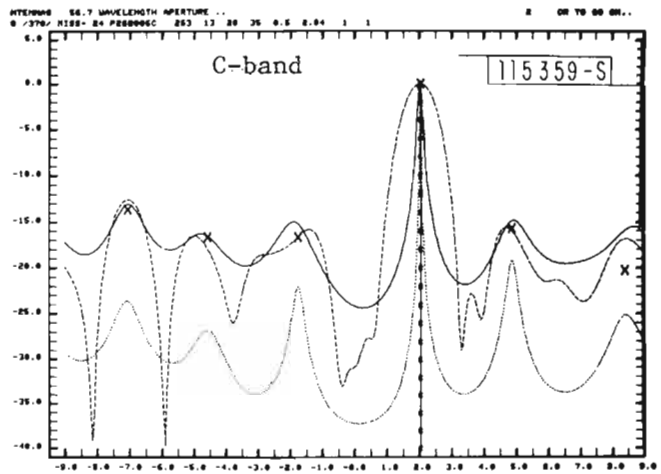

Simulation predicted (ground reflection calculation/focusing ground)

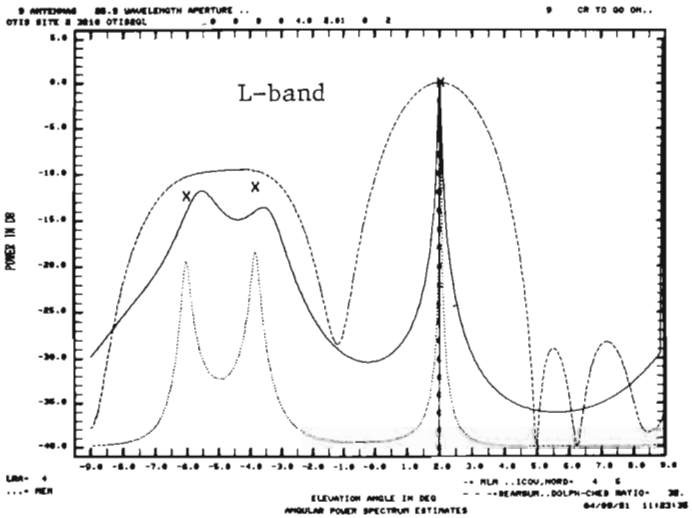

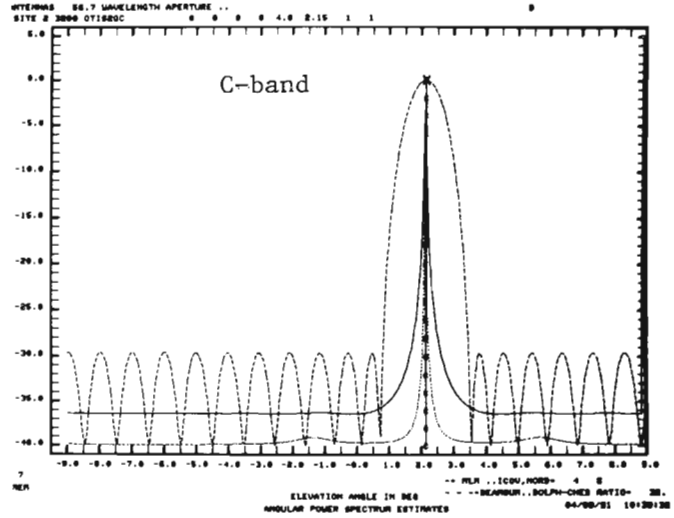

Fig. 5-66. Camp Edwards measurement: Gibbs Road E, L- and C-bands elevation arrays, $\theta_{EL} \simeq 2°$.

Field Measured

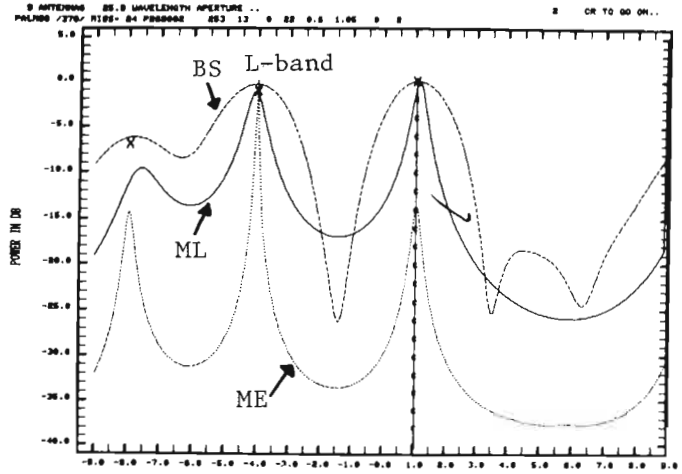

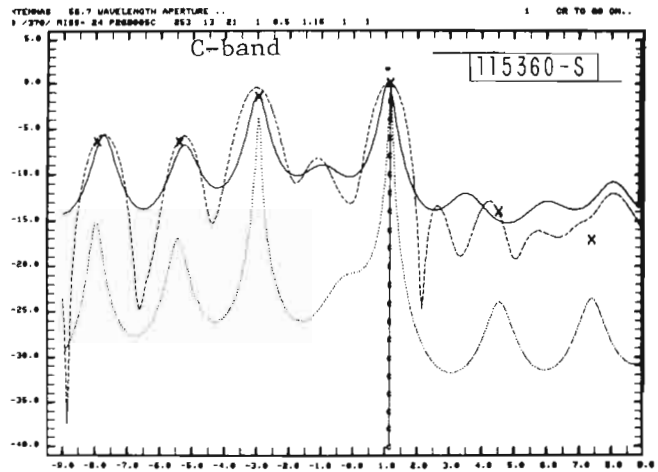

Simulation predicted (ground reflection calculation/focusing ground)

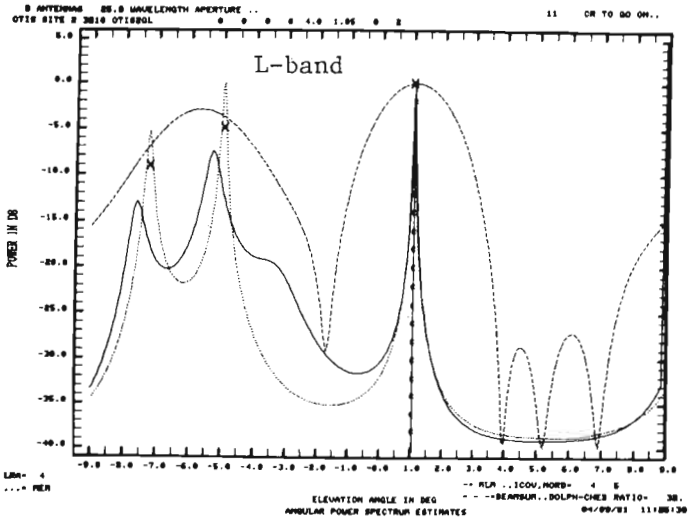

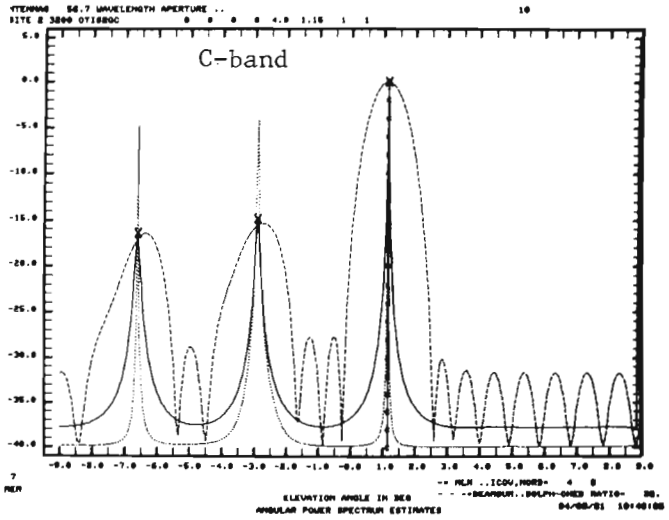

Fig. 5-67. Camp Edwards measurement: Gibbs Road E, L- and C-bands elevation arrays, $\theta_{EL} \simeq 1.2°$.

Field Measured

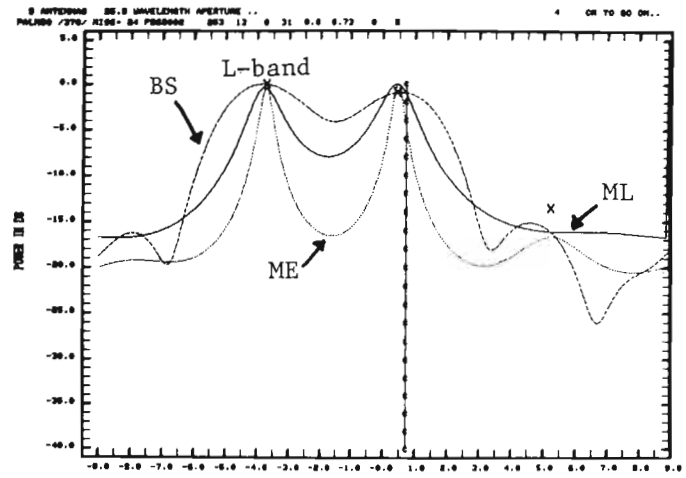

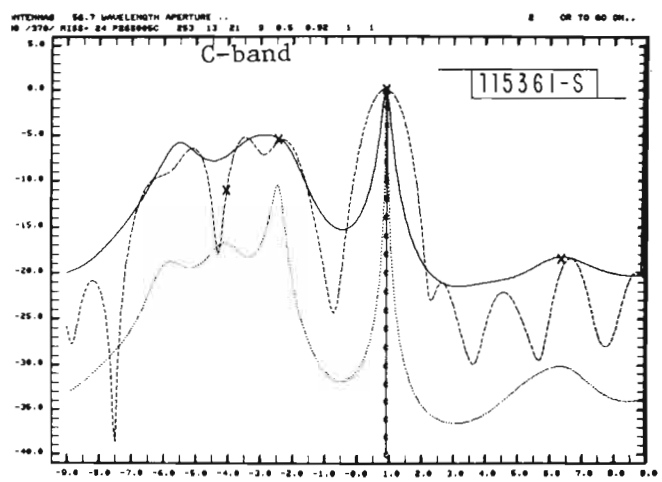

Simulation predicted (ground reflection calculation/focusing ground)

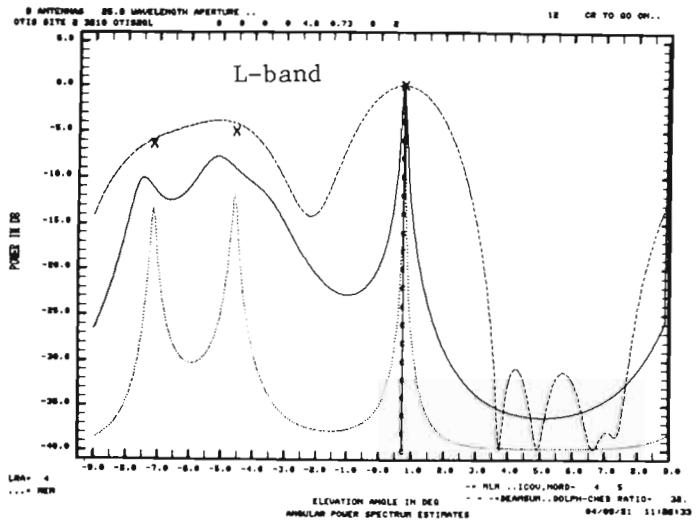

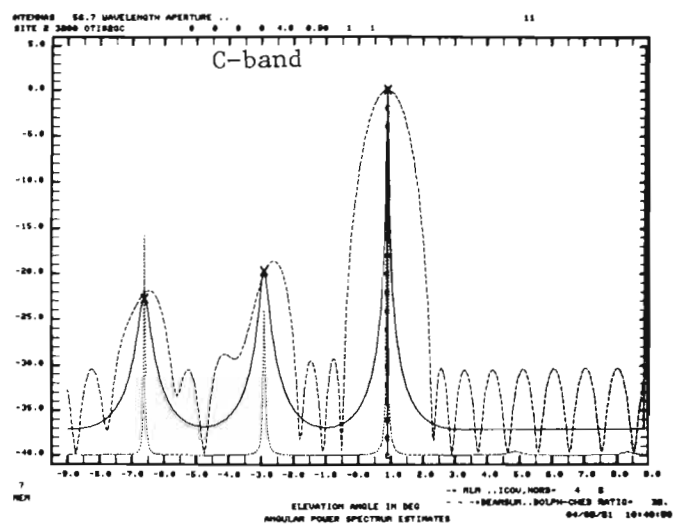

Fig. 5-68. Camp Edwards measurement: Gibbs Road E, L- and C-bands elevation arrays, $\theta_{EL} \simeq 0.9°$.

as the L band, but in much lower level. For higher elevation angles (θ_{EL} > 2°), the C-band field measured results shows relatively low multipath levels around -10 dB to -15dB. At a low elevation angle of θ_{EL} ≃1.2°, fairly high C-band multipath level (-2 dB) is observed. The focusing ground reflections, which were observed in the measurement at Fort Devens golf course where the terrain was rolling, again exist here in both the L-band the the C-band field measurement results. The multipath arrivals appear to be specular reflections, although some weak indication of diffuse reflections exist in some of the C-band results (Figs. 5-64 and 5-65).

For the L band, the comparison between the simulation predicted results and the field measured results is mixed. No good agreement is obvious for the higher elevation angles (θ_{EL} > 3°). However, for the lower elevation angles, the agreement appears to be fair, except that the simulation predicted results generally indicate much lower multipath levels. For the C band, agreement between the simulation predicted results and field measured results is very poor. For several direct signal angles (Figs. 5-58 to 5-60 and 5-66), the simulation predicted results indicate no multipath arrivals while the field measured results show several multipath arrivals. To better understand the poor agreement between the simulation predicted and the field measured results, the directions of the observed C-band and L-band ground reflections (as indicated by the field measured angular power spectra in Figs. 5-58 to 5-68) are drawn on the terrain height profile for this site, as shown in Fig. 5-69*. In this way, we can associate the observed ground reflections with terrain features and might be able to identify the specific terrain feature which causes the poor agreement. We can see that almost all ground reflections come from the ground within 200 feet of the receiving antenna array. This poor agreement, especially for the C-band results, suggests that

(1) For the complicated terrain conditions like this site, a more detailed and finer terrain survey is required for both the along-range height profile and the cross-range tilts in the region immediately in front of the array,

---

*The reflection directions were drawn only for the ground reflections with M/D ratio greater than -20 dB.

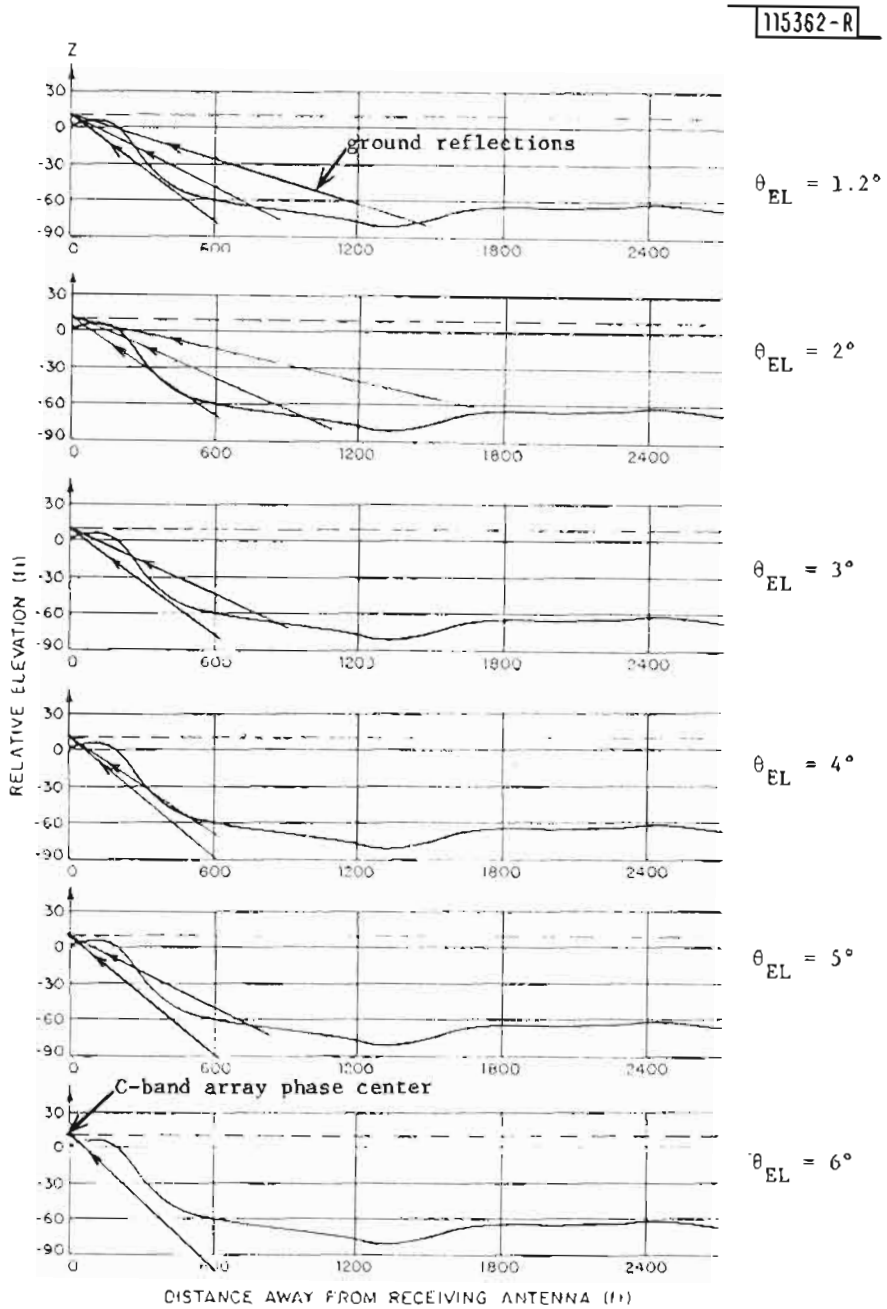

Fig. 5-69a. The observed C-band ground reflections for various helicopter elevation angles at Camp Edwards Gibbs Road entrance site.

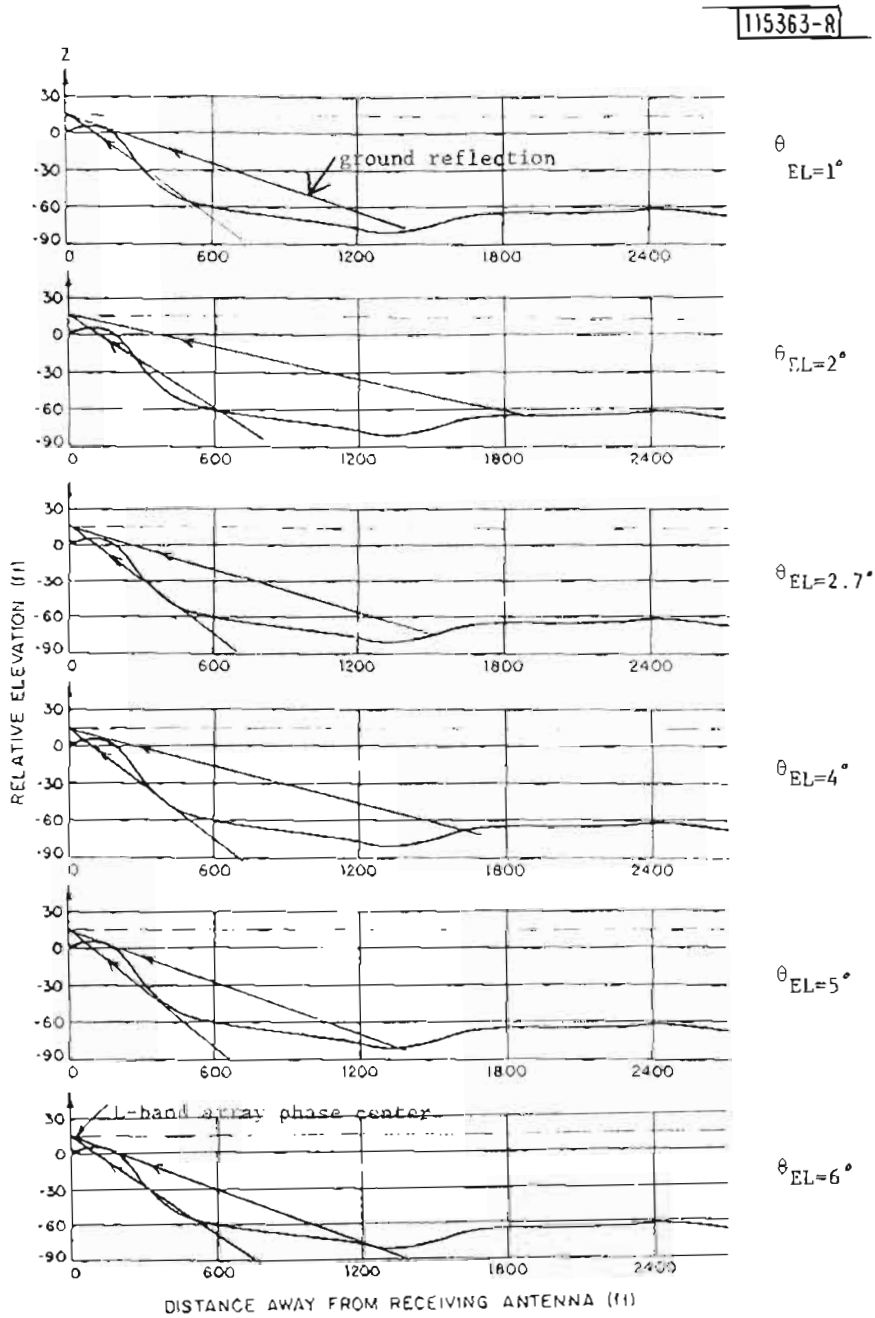

Fig. 5-69b. The observed L-band ground reflections for various helicopter elevation angeles at Camp Edwards Gibbs Road entrance site.

(2) more ground plates are needed to fit the more detailed and finer terrain survey data, especially in the cross-range direction, and

(3) the focusing ground option of the ground reflection calculation in the MLS multipath simulation needs to be augmented to handle more than just fifteen ground plates.

It should be noted that the upsloping region which starts at 3000 feet from the C-band array (Fig. 4-11) gave -15 dB to -20 dB M/D ratios. This multipath could be greater practical significance to the MLS because its elevation angle (typically -1° to +0.5°) is such as to yield

(a) smaller elevation separation angles for an elevation array and thus create inbeam multipath (see Fig. 3-4), and

(b) reduced discrimination against ground reflections by the elevation pattern of an MLS azimuth array (see Chapter I of ref. [21]).

The low levels that arose here reflect the difficulty in finding natural terrain which is flat over a sizable fraction of a Fresnal zone (approximately 26 feet crossrange and 1600 feet downrange) at the antenna to terrain distance (approximately 3500 feet). By contrast, the terrain immediately in front of the array has a much smaller Fresnel zone (e.g., 6 feet crossrange, 120 feet downrange for multipath at -3° elevation angle).

The EL multipath levels and the angle errors for the measurements at this site are summarized in Fig. 5-70.

Figures 5-71 and 5-72 show the L-band AZ angular power spectral estimates for two helicopter elevation positions. Only one spectral peak is observed in the simulation results, suggesting that the multipath arrivals indicated in the L-band EL spectral estimates had an azimuth angle close to the direct signal arrival. Although, the field measured results indicate a second spectral peak, its power level is below -15 dB. Thus, the dominant L-band multipath observed in the EL spectral estimates and the direct signal probably had similar azimuth arrival angles.

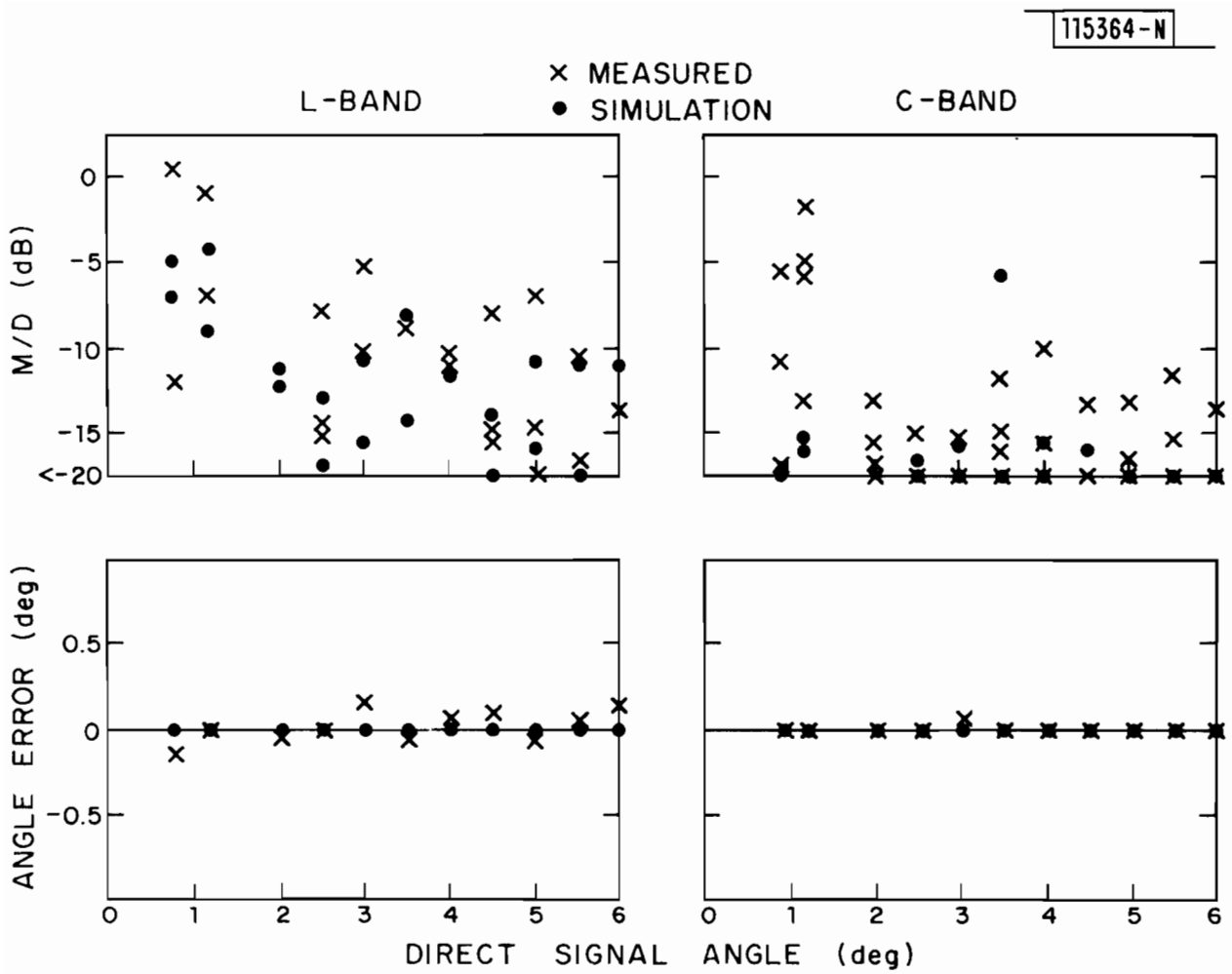

Fig. 5-70. Camp Edwards measurement: Gibbs Road E, L-band and C-band elevation arrays, M/D ratios and angle errors.

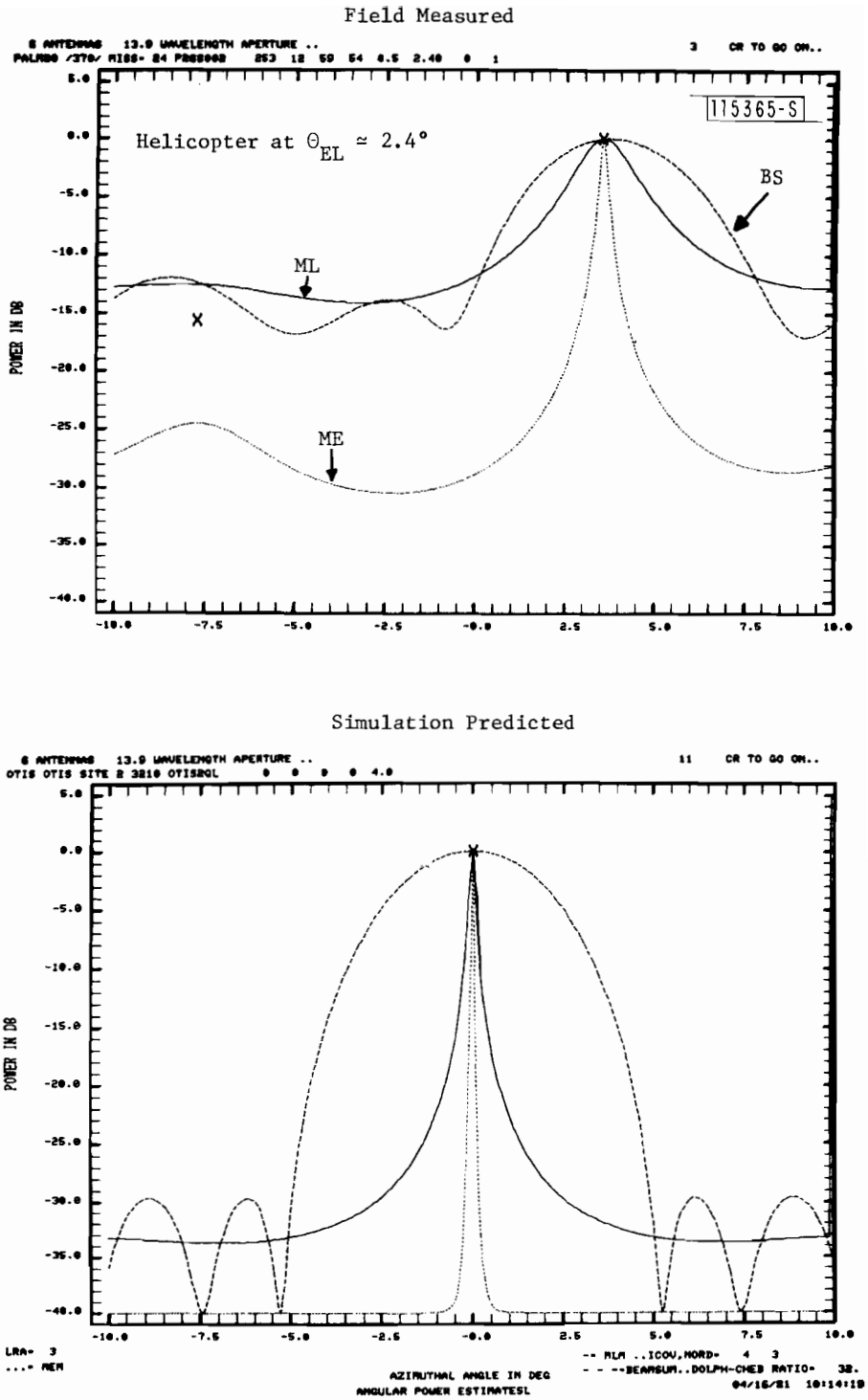

Fig. 5-71. Camp Edwards measurement: Gibbs Road E, L-band azimuth array, $\theta_{EL} \simeq 2.4°$.

Field Measured

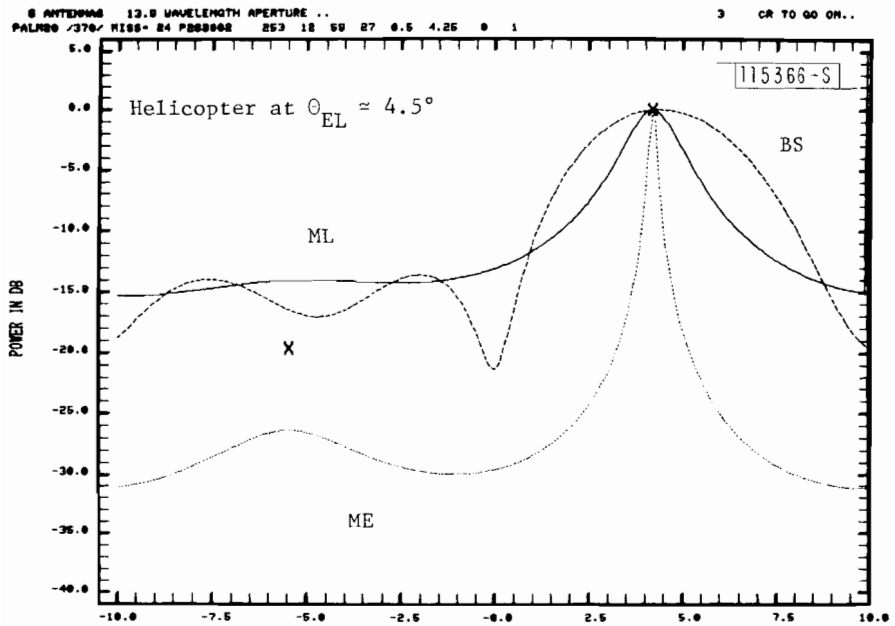

Simulation Predicted

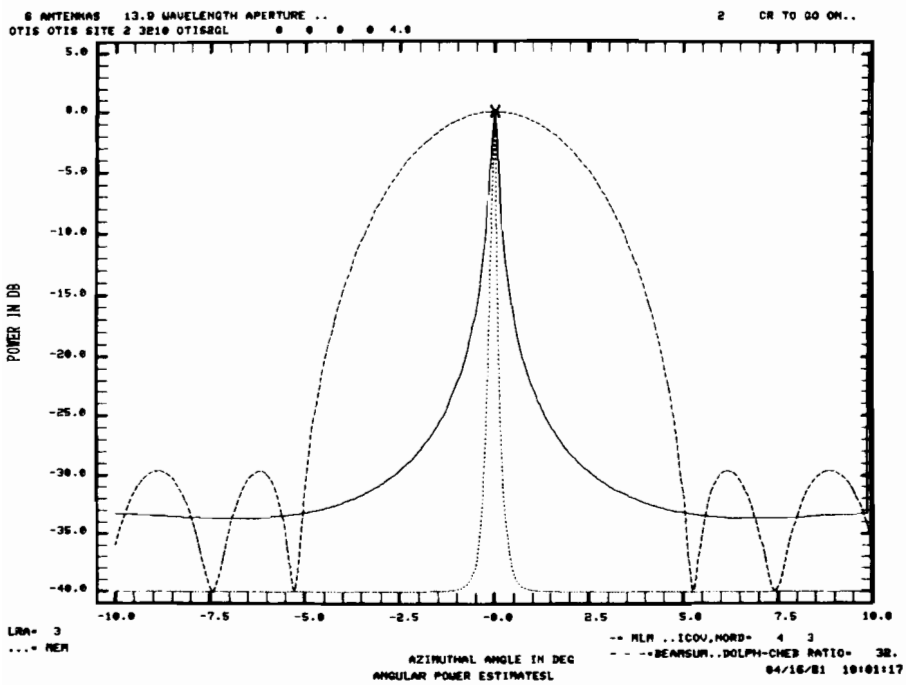

Fig. 5-72. Camp Edwards measurement: Gibbs Road E, L-band azimuth array, $\theta_{EL} \simeq 4.5°$

3. Gibbs Road N Range

As mentioned earlier, no C-band measurements were taken at this site due to the hardware failure of the C-band elevation array. Thus only the L-band results are given here. Figures 5-73 to 5-83 show examples of the L-band EL angular power spectral estimates. Although the surface condition of the terrain at this site was similar to that at the Gibbs Road entrance site, (Figs. 4-12 and 4-14), i.e., smooth along the Gibbs Road and less smooth on the off-road area, the L-band multipath levels are a bit higher here than that at the Gibbs Road entrance site. So, the ground here seems to be electrically smoother than that at Gibbs Road entrance site. The multipath levels vary from -5 dB at high elevation angles ($\theta_{EL} > 3.5°$) to -3 dB at $\theta_{EL} \simeq 2.5° \sim 3°$ and to almost 0 dB at $\theta_{EL} = 2°$. The L-band multipath arrivals appear to be specular reflections. The phenomenon of the focusing ground reflections, which appear to be typical for the rolling terrain, is again observed at this site.

The simulation predicted results generally agree well with the field measured results, in terms of number of multipath arrivals, their arrival angles and multipath levels. The simulation predicted results indicate higher multipath levels than the corresponding field measured results. This suggests that some surface roughness might exist in the terrain at this site, even at the L band. Figure 5-84 summarizes the multipath levels and the angle errors in estimating the direct signal arrival for both the field measured and simulation predicted results.

Figures 5-85 and 5-86 show the L-band AZ angular power spectral estimates for two helicopter elevation angles. The simulation predicted results show two spectral peaks. This suggests that the azimuth arrival angles of some of the multipath arrivals observed in the EL angular power spectral estimates are not the same as the direct signal azimuth arrival angle. This seems reasonable, since some cross-range tilts exist in the terrain here (Fig. 4-13). However, the field measured results only indicate one dominant spectral peak. The discrepancy between the simulation predicted results and the field measured results might be explained as follows. We notice that the angular

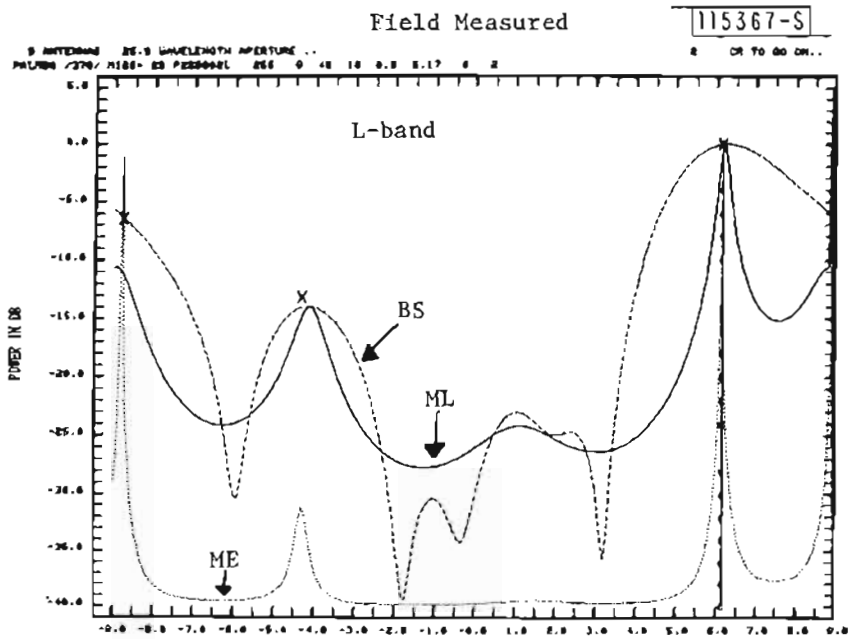

Simulation Predicted (ground reflection calculation/focusing ground)

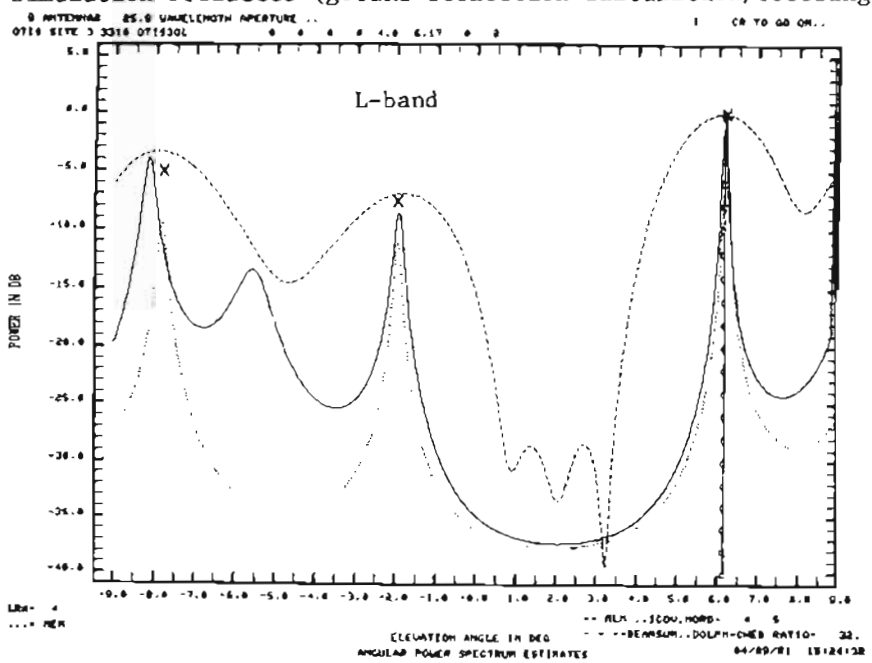

Fig. 5-73. Camp Edwards measurement: Gibbs Road N Range, L-band elevation array, $\theta_{EL} \simeq 6°$.

Field Measured

115368-S

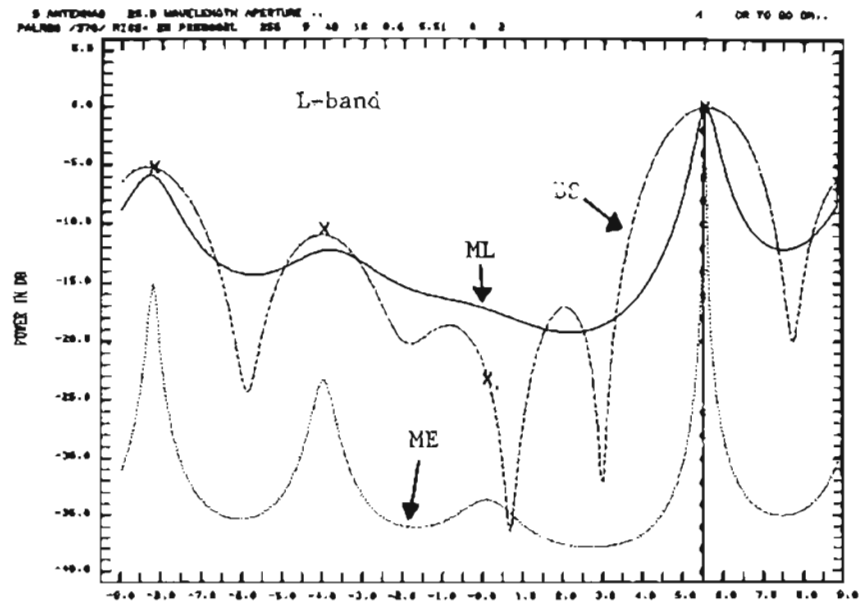

Simulation Predicted (ground reflection calculation/focusing ground)

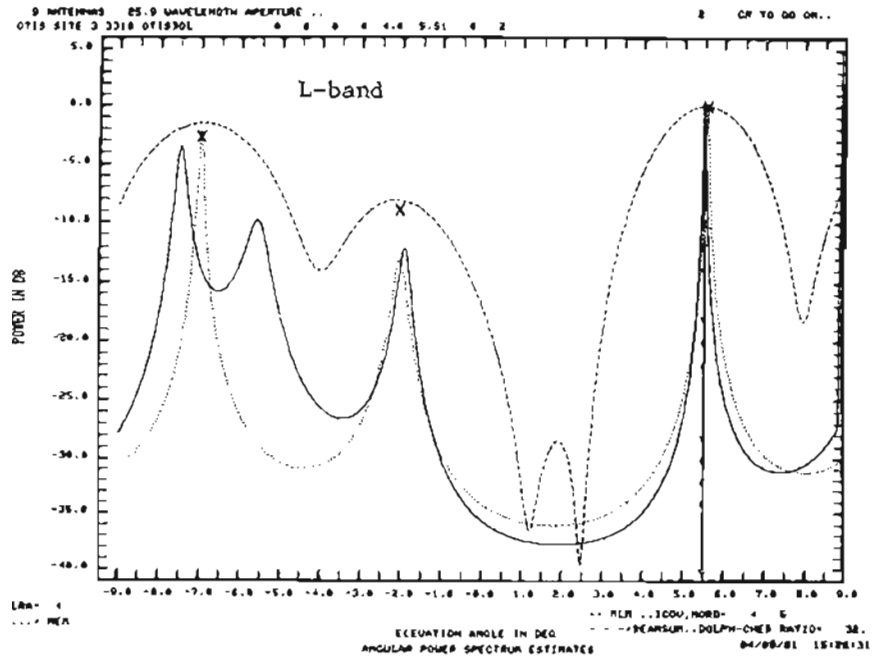

Fig. 5-74. Camp Edwards measurement: Gibbs Road N Range, L-band elevation array, $\theta_{EL} \simeq 5.5°$.

Field Measured

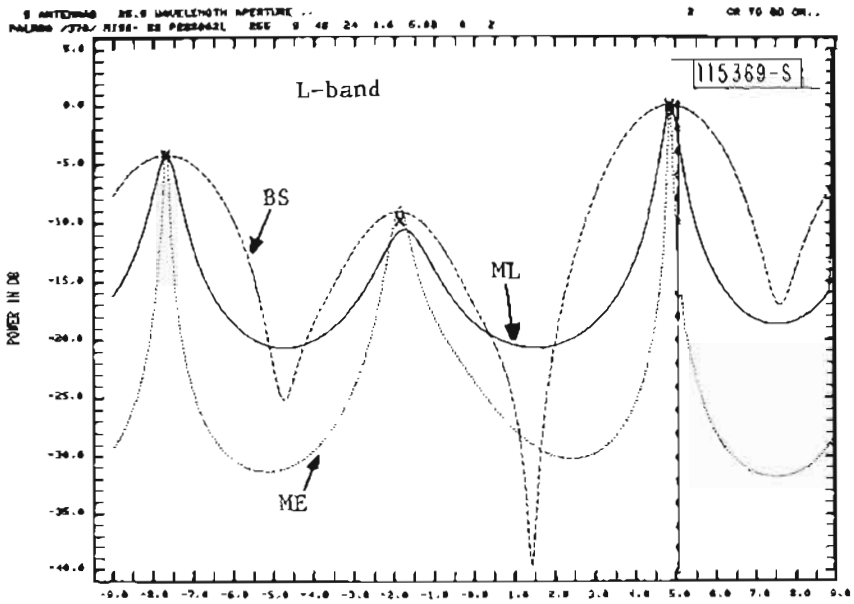

Simulation Predicted (ground reflection calculation/focusing ground)

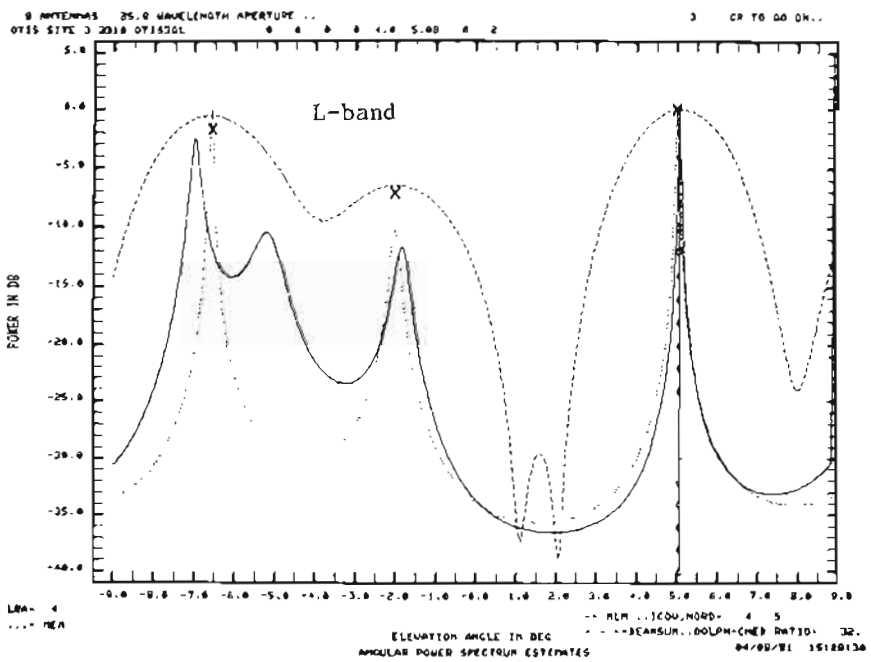

Fig. 5-75. Camp Edwards measurement: Gibbs Road N Range, L-band elevation array, $\theta_{EL} \simeq 5°$.

Field Measured

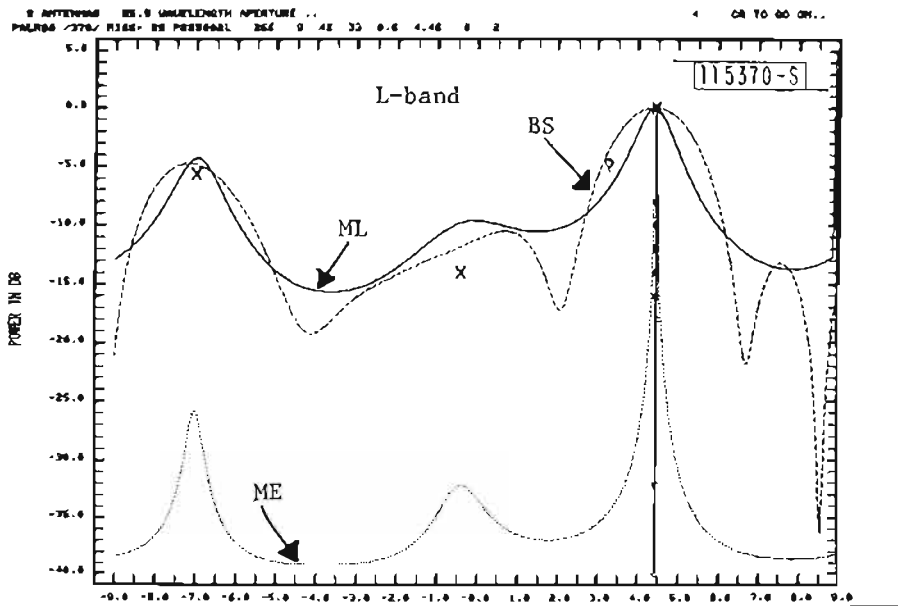

Simulation Predicted (ground reflection calculation/focusing ground)

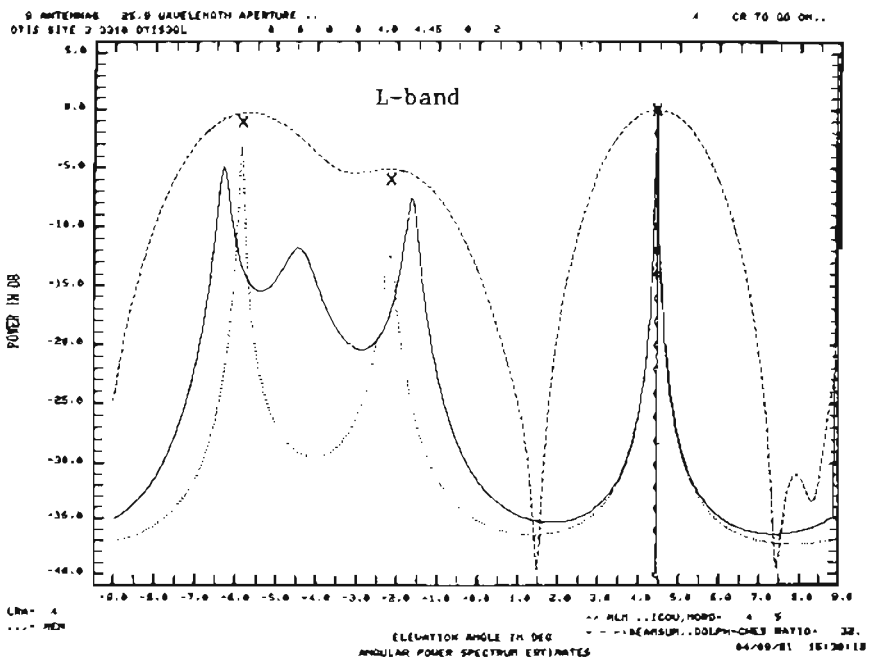

Fig. 5-76. Camp Edwards measurement: Gibbs Road N Range, L-band elevation array, $\theta_{EL} \simeq 4.5°$.

Field Measured

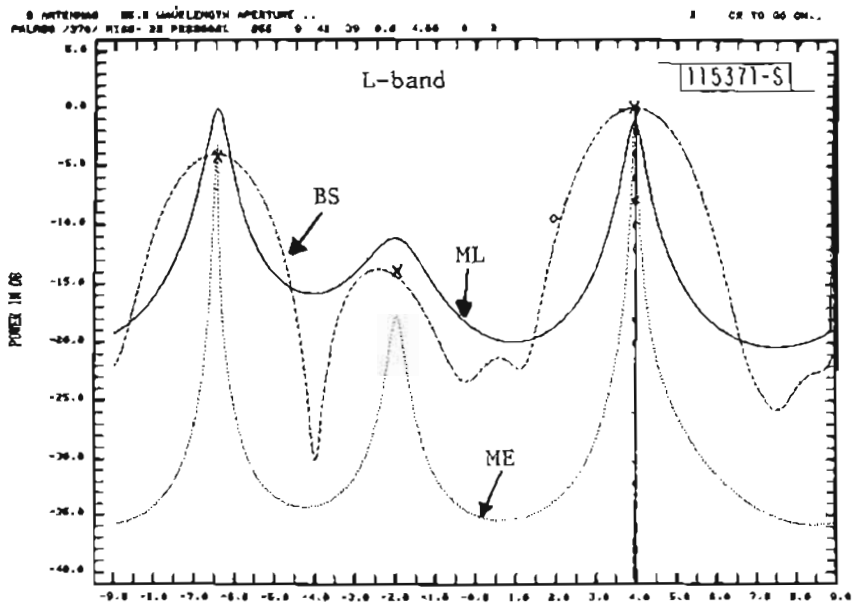

Simulation Predicted (ground reflection calculation/focusing around)

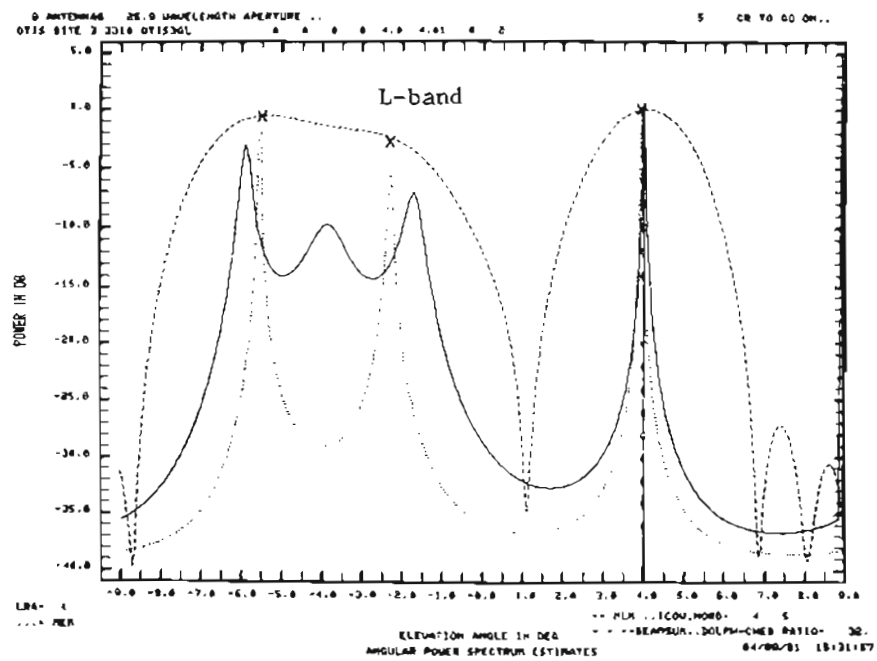

Fig. 5-77. Camp Edwards measurement: Gibbs Road N Range, L-band elevation array, $\theta_{EL} \simeq 4°$.

Field Measured

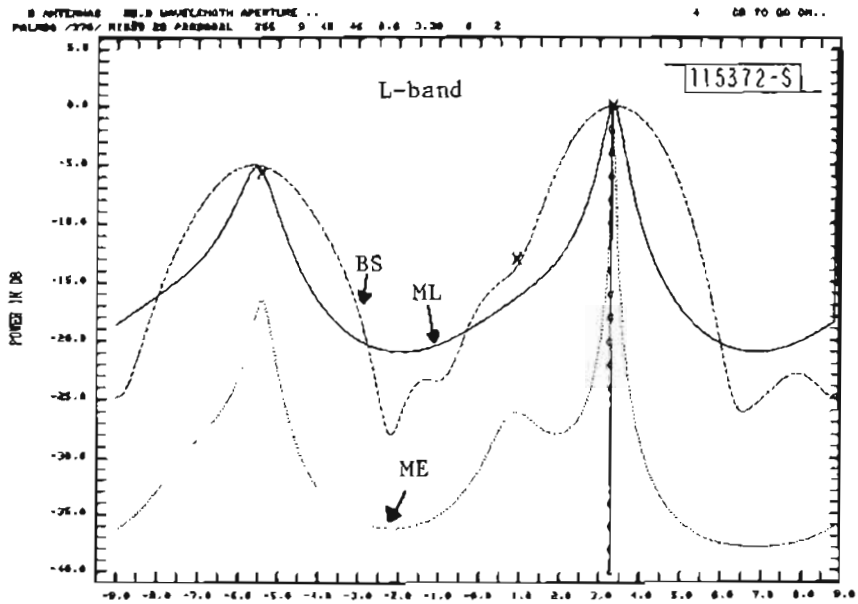

Simulation Predicted (ground reflection calculation/focusing ground)

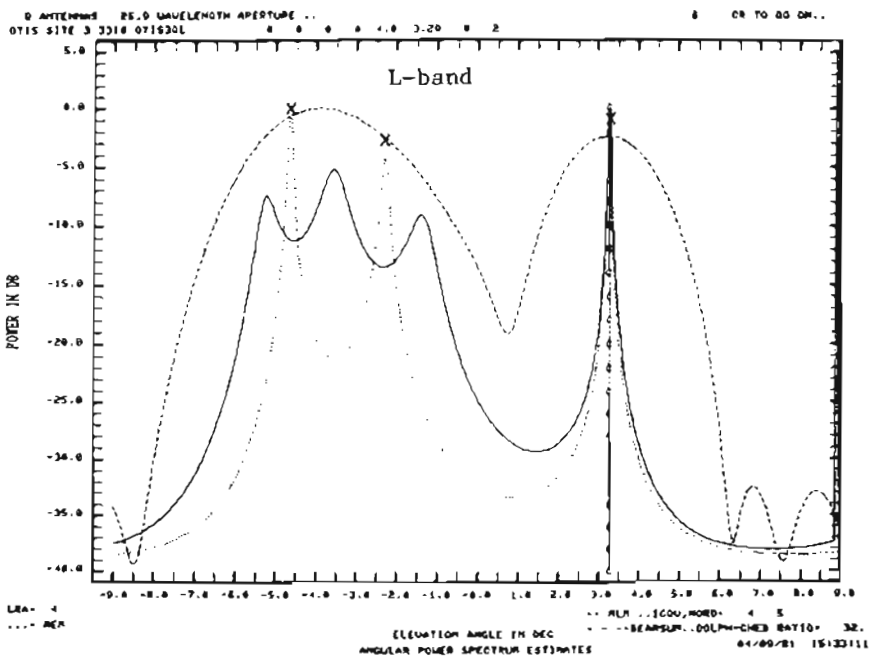

Fig. 5-78. Camp Edwards measurement: Gibbs Road N Range, L-band elevation array, $\theta_{EL} \simeq 3.5°$.

Field Measured

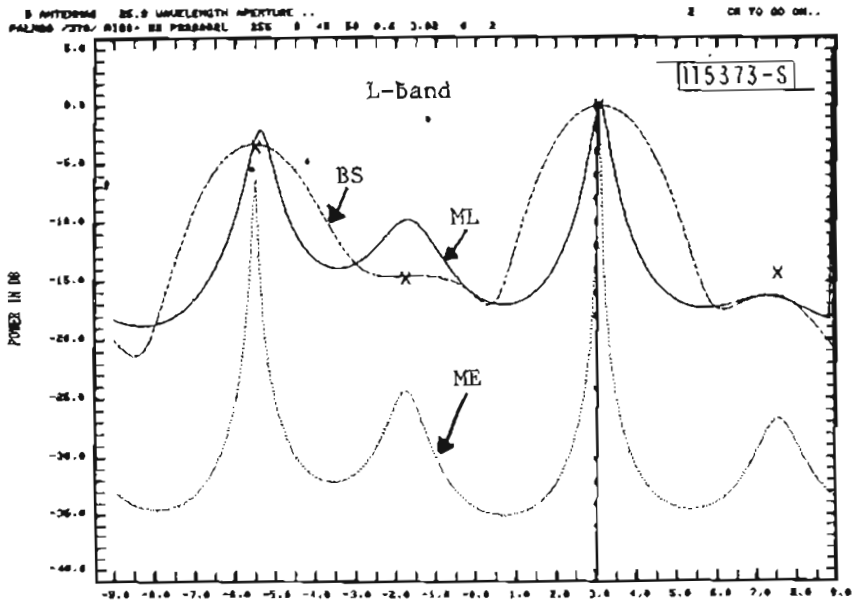

Simulation Predicted (ground reflection calculation/focusing ground)

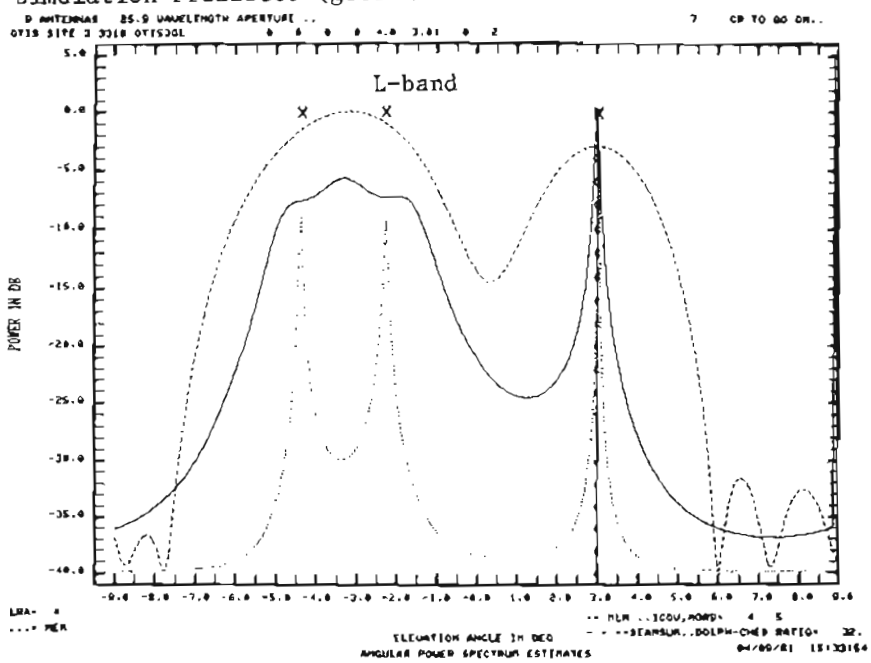

Fig. 5-79. Camp Edwards measurement: Gibbs Road N Range, L-band elevation array, $\theta_{EL} \simeq 3°$.

Field Measured

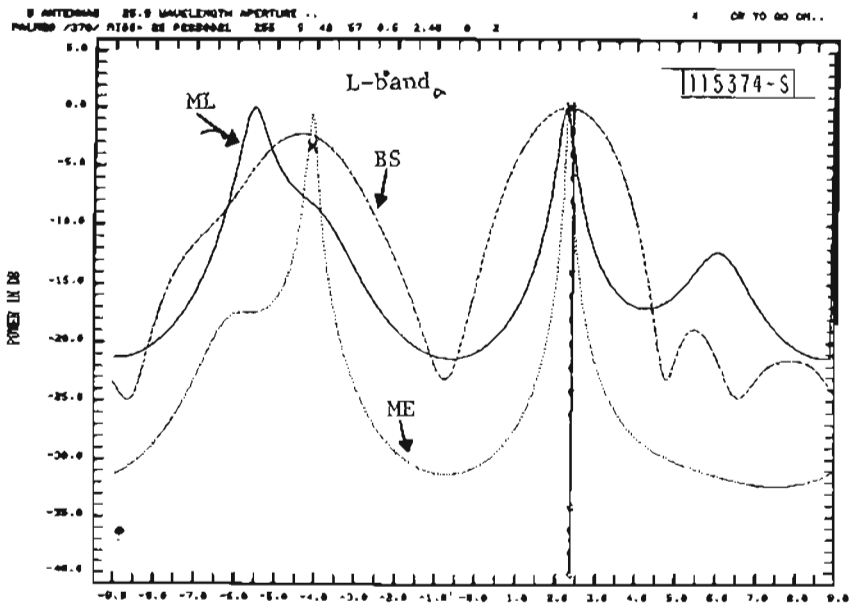

Simulated Predicted (ground reflection calculation/focusing ground)

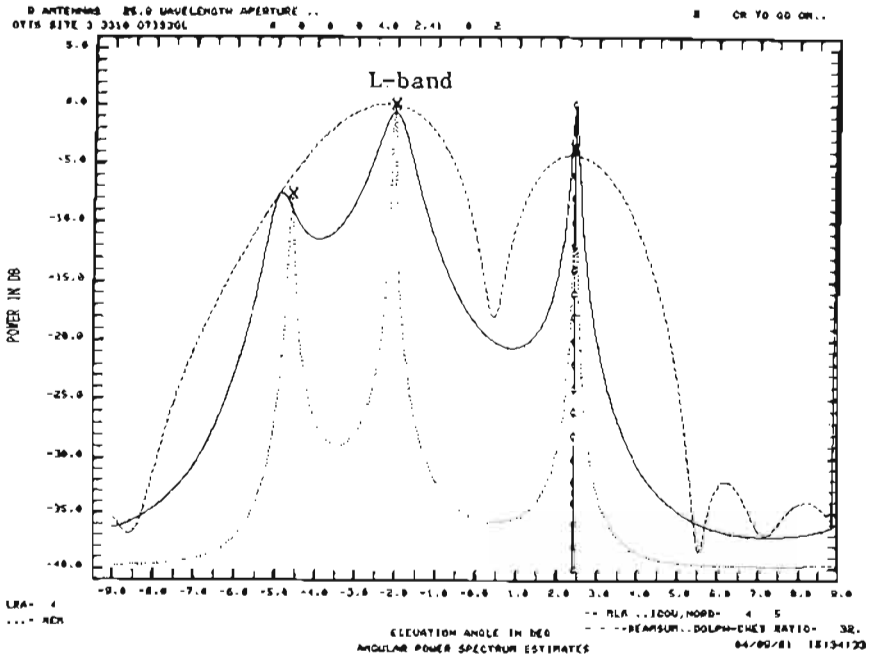

Fig. 5-80. Camp Edwards measurement: Gibbs Road N Range, L-band elevation array, $\theta_{EL} \simeq 2.5°$.

Field Measured

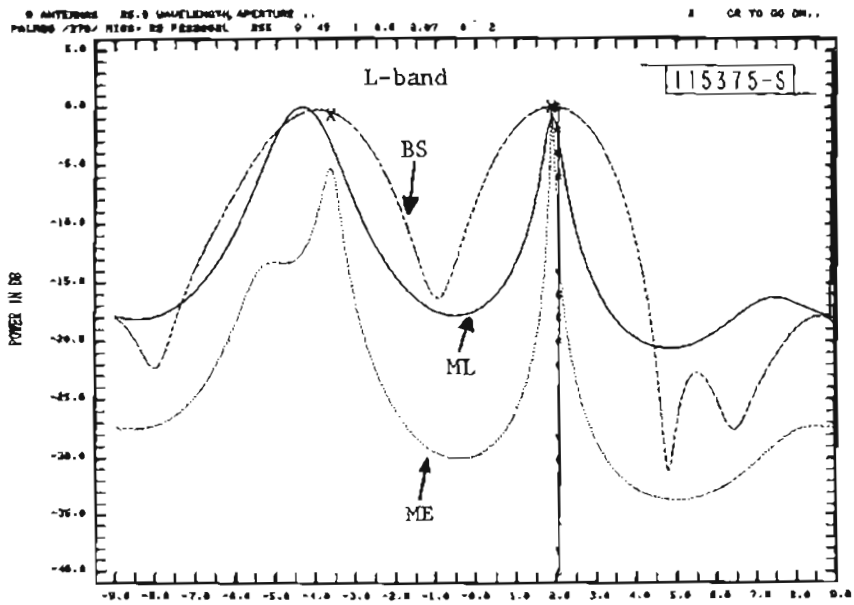

Simulation Predicted (ground reflection calculation/focusing ground)

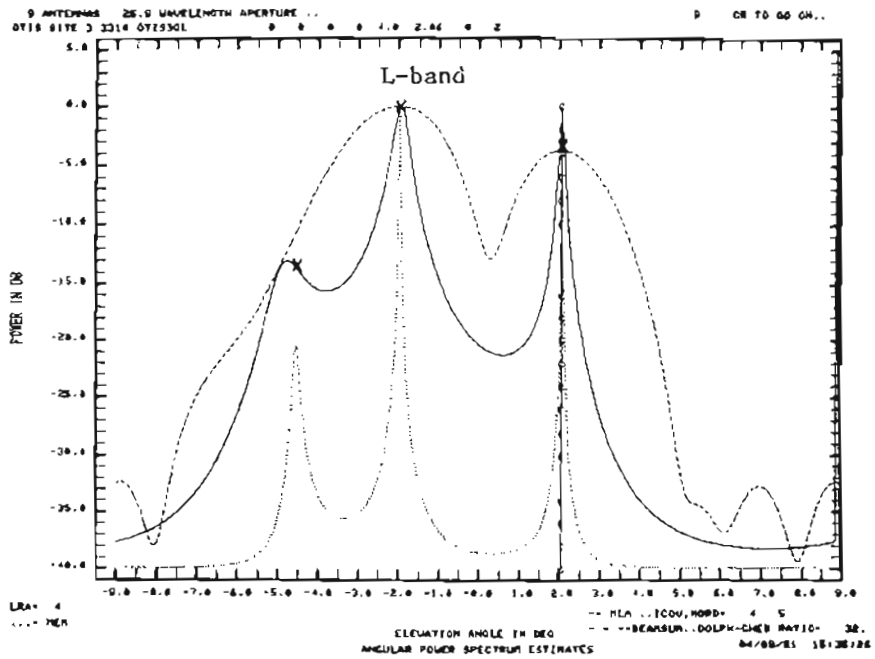

Fig. 5-81. Camp Edwards measurement: Gibbs Road N Range, L-band elevation array, $\theta_{EL} \simeq 2°$.

Field Measured

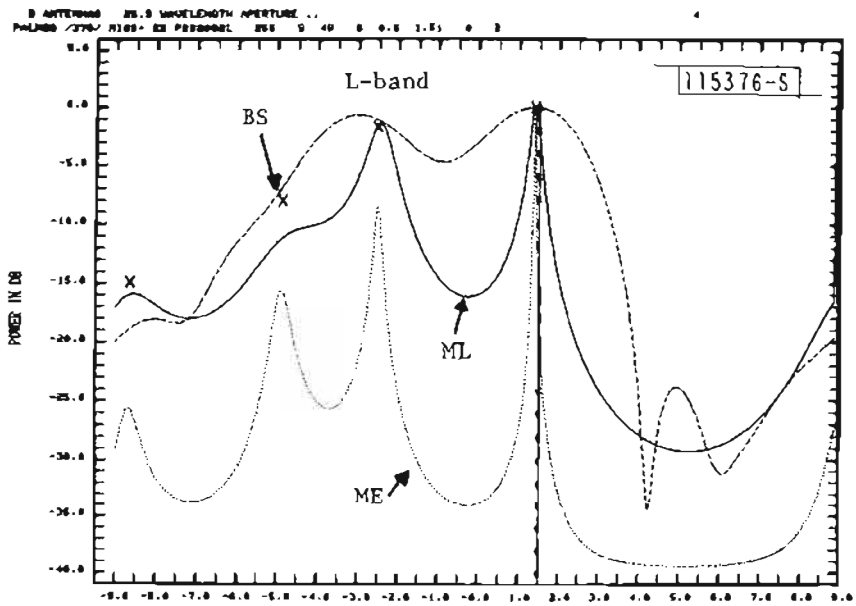

Simulation Predicted (ground reflection calculation/focusing ground)

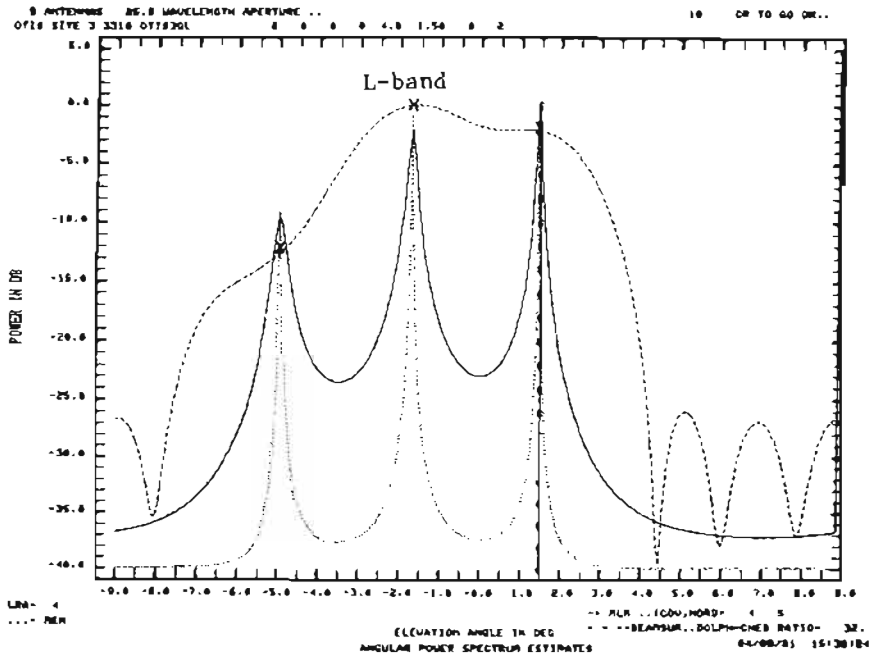

Fig. 5-82. Camp Edwards measurement: Gibbs Road N Range, L-band elevation array, $\theta_{EL} \simeq 1.5°$.

Field Measured

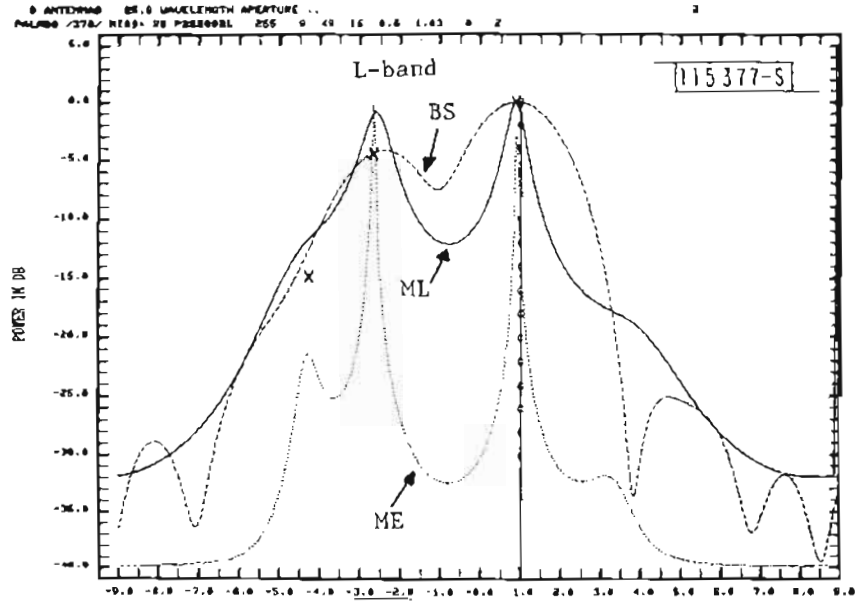

Simulation Predicted (ground reflection calculation/focusing ground)

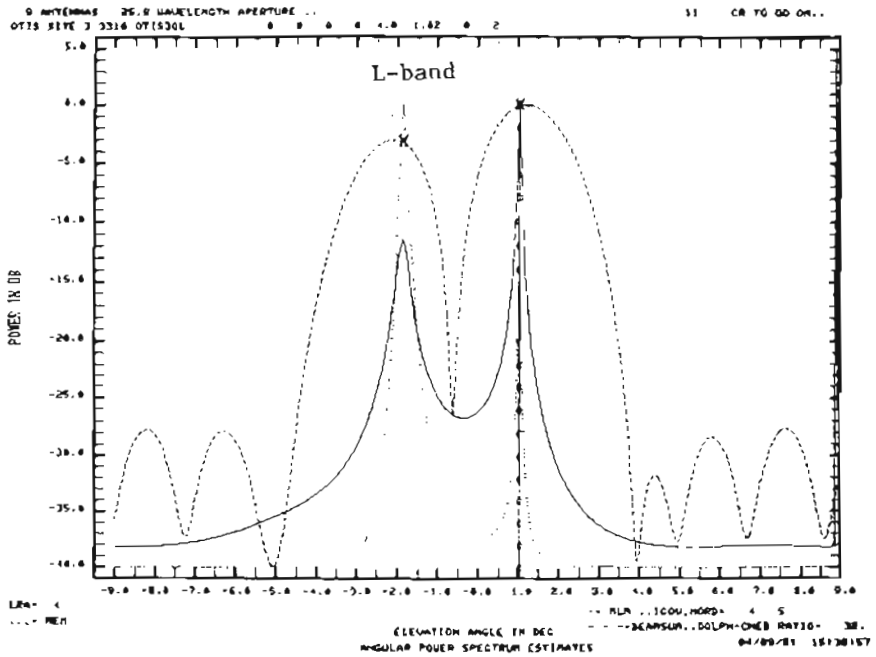

Fig. 5-83. Camp Edwards measurement: Gibbs Road N Range, L-band elevation array, $\theta_{EL} \simeq 1°$.

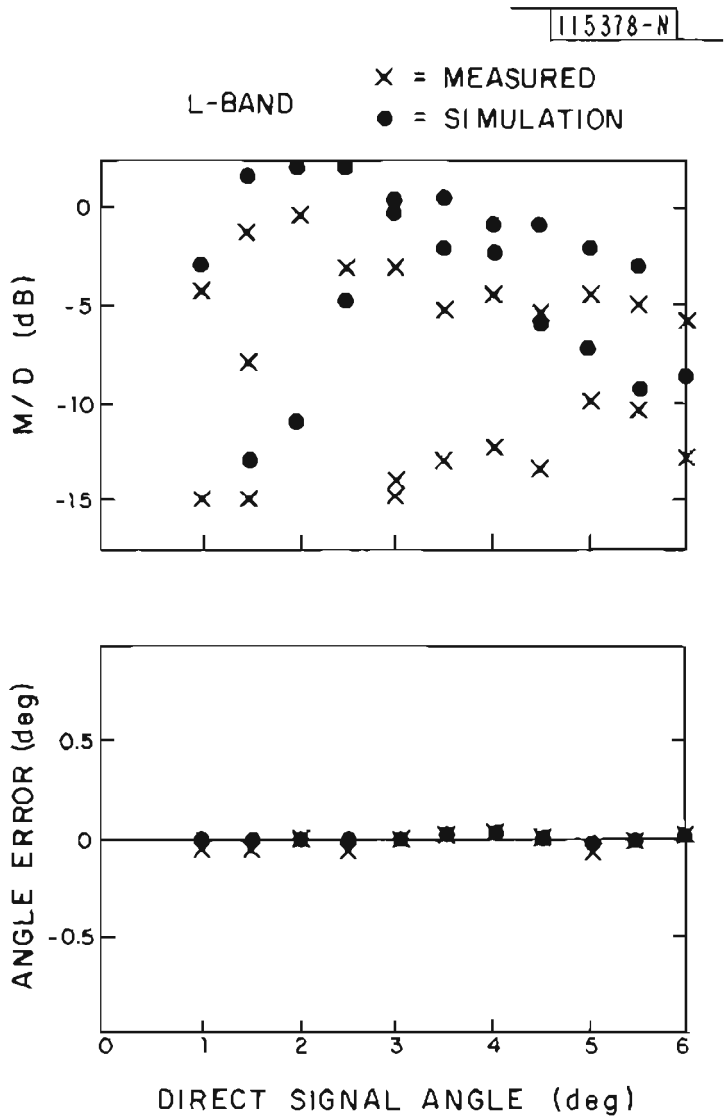

Fig. 5-84. Camp Edwards measurement: Gibbs Road N Range, L-band elevation array, M/D ratios and angle errors.

Field Measured

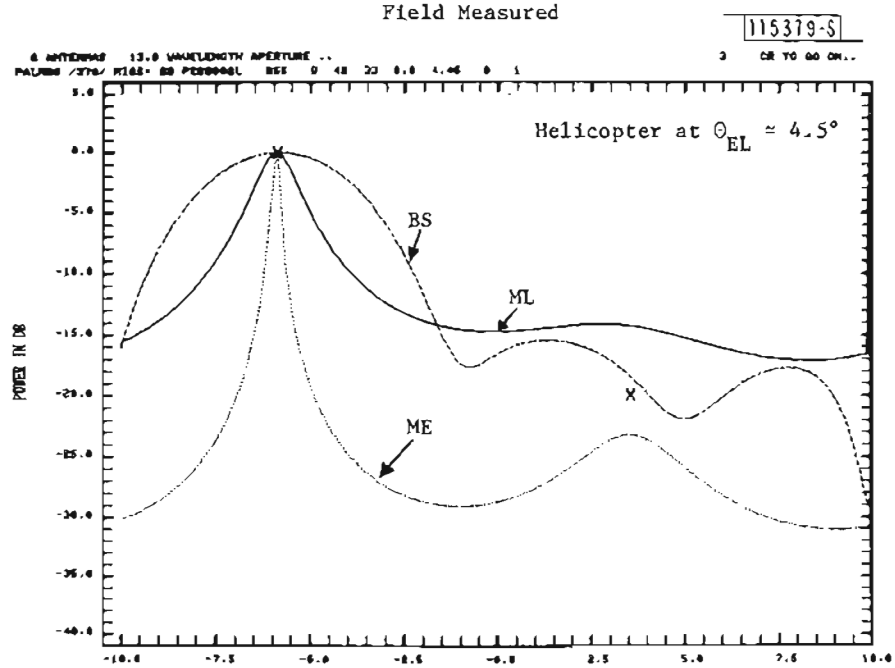

Simulation Predicted (ground reflection calculation/focusing ground)

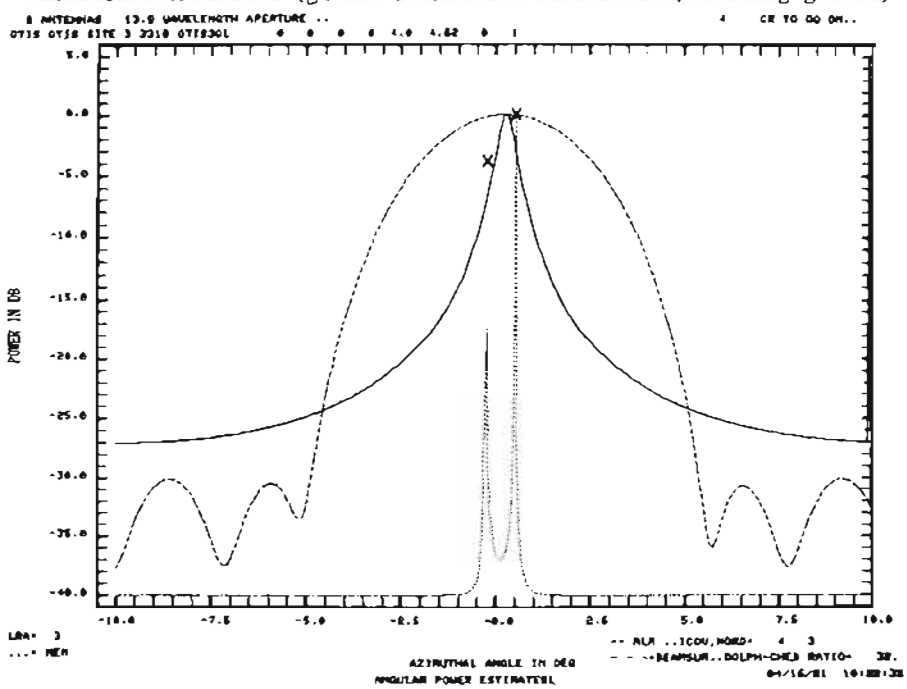

Fig. 5-85. Camp Edwards measurement: Gibbs Road N Range, L-band azimuth array, $\theta_{EL} \simeq 4.5°$.

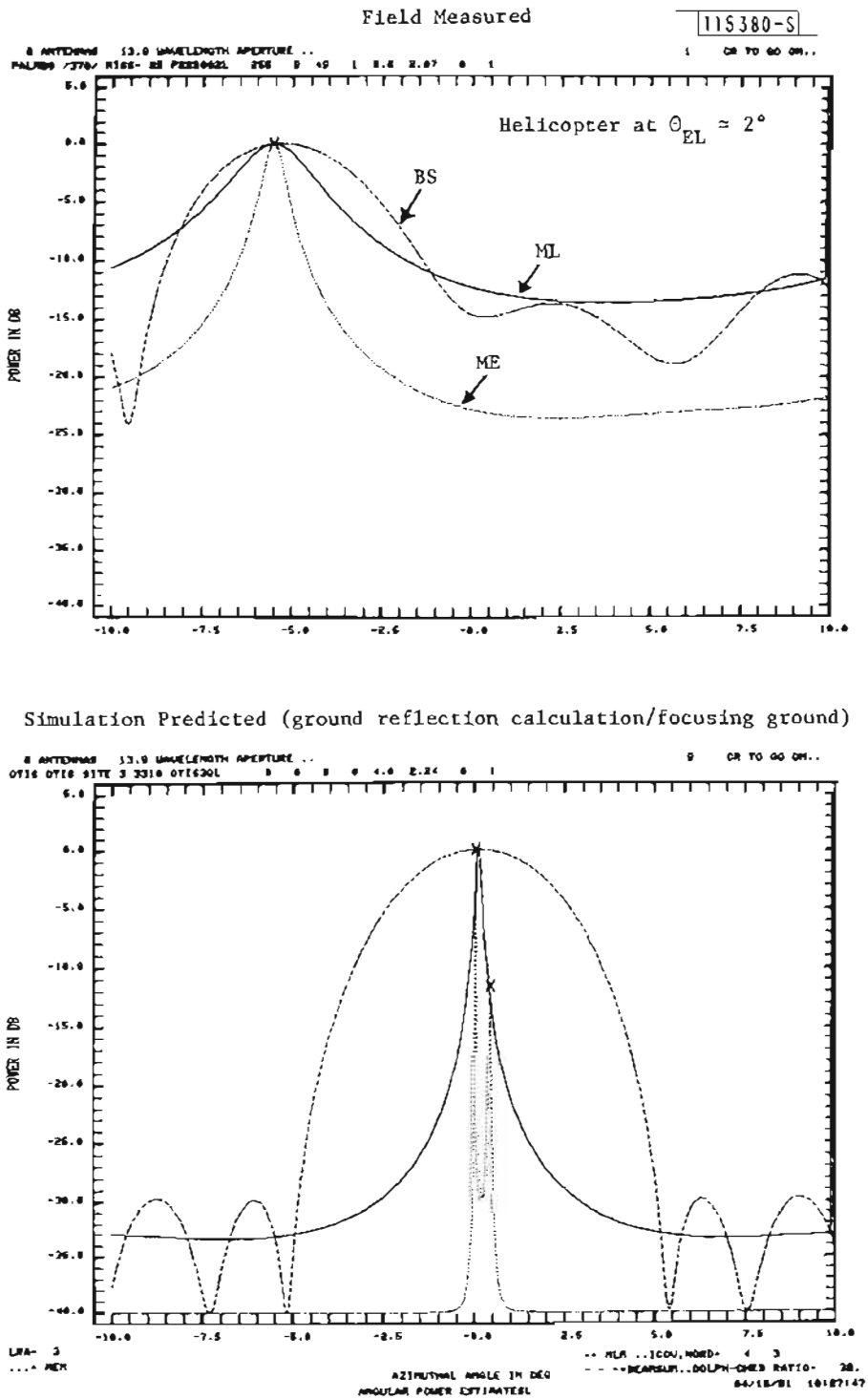

Fig. 5-86. Camp Edwards measurement: Gibbs Road N Range, L-band azimuth array, $\theta_{EL} \simeq 2°$.

separation between two spectral peaks in the simulation results is only in the order of 0.5° to 1°. This angular separation probably is too small* to be resolved in the field measured results due to inadequate signal-to-noise ratio (SNR) [6]. It should be noticed that no noise was added to the signal environment predicted by the MLS multipath simulation, as we mentioned earlier. Thus, the simulation predicted results were for noise-free cases. Even for these noise-free cases, the BS and ML spectral estimates show only one peak.

D. Summary

The observed terrain multipath environment based on the L-band and C-band field measured results obtained for various terrain conditions at Hanscom airport, Fort Devens, and Camp Edwards, MA can be summarized as follows:

(1) At L band, the terrain multipath can be explained as specular ground reflections with high multipath levels, (M/D ratios ranging from -5 dB to 1 dB). For the C band, some indication of diffuse ground reflections was evident at some measurement sites, especially at Camp Edwards J2 range site where small scale terrain roughness was fairly visible. However, these diffuse ground reflections appeared to be at fairly low levels (-15 dB to -20 dB). Also, the multipath levels of the C-band specular ground reflections were slightly lower than those of the L band, M/D ratios around -10 dB to -2 dB.

(2) The phenomenon of focusing ground reflections, i.e., more than one ground reflection present at the same time, was observed in both L band and C band. For the L band, this generally occurred in the rolling type of terrain. However, for the C band, this also happened in the physically fairly flat terrain at Hanscom airport site.

(3) The azimuth arrival angles of the observed ground reflections appeared to be the same as that of the direct signal. Apparently, the terrain cross-range tilts observed at various measurement sites were not large enough to make the azimuth arrival angles of the ground reflections deviate enough from the direct signal azimuth angle to be resolvable.

---

*The beamwidth of our azimuth array is about 4°. Thus, the angular separation of 0.5° to 1° corresponds to 0.1 to 0.25 beamwidths.

The comparison between the field measured results and the simulation predicted results indicated that the agreement between the field measured results and the simulation predicted results depended strongly on the terrain conditions. To summarize the comparison results for the validation of the terrain multipath propagation model used in the MLS multipath simulation, let us make the following grouping of the terrain conditions involved in the five measurement sites which we visited:

(1) Type A terrain: Almost no cross-range tilts and electrically smooth, such as those at Hanscom airport site (for both L band and C band), Fort Devens golf course site along the radial lines O-B (for both L band and C band) and O-C (for L band only), and Camp Edwards J2 Range site (for L band only).

(2) Type B terrain: Almost no cross-range tilts and electrically rough, such as those at Camp Edwards J2 Range site (for C band) and Fort Devens golf course site along the radial line O-C (for C band).

(3) Type C terrain: Significant cross-range tilts, such as those at Fort Devens golf course site along the radial line O-A (both L band and C band) and Camp Edwards Gibbs Road entrance site (both L band and C band).

For the type A terrain, the field measured results could be well explained with the simulation predicted results. Thus, for this terrain type, the MLS terrain multipath simulation utilizing a simple flat-plate ground model for the specular reflection calculation should be sufficient to predict the terrain multipath environment for the major features, such as the number of multipath components, their arrival angles and M/D ratios.

For the type B terrain, the agreement between the simulation predicted results and the field measured results was generally poor, especially in terms of M/D ratios. The simulation predicted results over estimate the observed multipath levels (Figs. 5-39 and 5-55). For this terrain type, the field

measured results indicated that the multipath environment was dominated by small scale roughness with low multipath levels and some additional low level diffuse multipath. Thus, if accurate predictions are required* for this terrain type, a terrain survey for the surface roughness appears to be needed and the terrain multipath propagation model has to include some mechanism to reasonably account for the surface roughness and the diffuse ground reflections.

The current MLS propogation model [1] attempts to take into account the reduction in specular reflection levels due to small scale roughness by use of a multiplicative factor

$$\rho_r = \exp\left[-\frac{1}{2}\left(4\pi\Delta h \sin \theta g/\lambda\right)^2\right] \qquad (5\text{-}1)$$

where $\Delta h/\lambda$ is the rms height variation in wavelengths and θg is the grazing angle. Several difficulties were encountered in applying eq. (5-1) to the J2 range data:

(1) it is not quite clear which terrain features (e.g., clumps of dirt, small furrows, tufts of grass, etc) should be used in estimating Δh, and

(2) the wavelengtn - grazing angle dependence suggested by (5-1) was not staisfied [e.g., the C-band specular reflections are small at 0.5° elevation angle (Fig. 5-53) whereas the L-band levels are high for all elevation angles between 5° and 2.5° (Fig. 5-44 to 5-49)].

Thus, although equation (5-1) does appear to give reasonable results over oceans [21], there is considerable question as to its applicability over terrain.

For the type C terrain, the agreement between the simulation predicted results and the field measured results was generally poor for most of three features which were used to characterize the terrain multipath environment,

---

*the observed multipath levels were low for this terrain so that it would not represent a challenge to current MLS implementations [21].

i.e., the number of multipath components, their arrival angles and M/D ratios. The factors, which we thought to be responsible for this poor agreement are:

(1) Terrain cross-range tilts which could not be realistically accounted for due to the insufficient terrain survey data and due to the limitation in the number of rectangular ground plates which were allowed to model a given terrain in our current ground model,

(2) large variations in the terrain along-range height profile which could not be modelled in detail with the maximum permissible number of rectangular ground plates in our current ground model,

(3) possible reflections from the off-azimuth hills or buildings which were not considered in the simulation, such as those observed in the measurements at Fort Devens golf course site, and

(4) the effective reflection coefficient, R_{eq}, which has been used in the current MLS multipath simulation program [1], might not be a good approximation for the significantly tilted ground plates*.

Thus, for this more complicated terrain type, improvement is needed in both the terrain survey/modelling and the current terrain multipath propagation model used in the MLS multipath simulation, as previously suggested (Chapter V Section C.2).

*Appendix A gives a detailed discussion on this subject.

VI. EXPERIMENTAL RESULTS FOR ELEVATION ANGLE ESTIMATION

Examples of elevation angle estimation results using four C-band arrays of different aperture sizes are given in this chapter for the field measurements taken at Hanscom airport, Fort Devens, and Camp Edwards, Mass. As mentioned in Chapter III Section B, the main purpose here is to compare the performances of antenna arrays with different aperture sizes in various real-world terrain multipath environments. Here the performance refers to the absolute accuracy (not the array beamwidth) of estimating the direct signal elevation angle (i.e., the helicopter elevation angle in our cases).

The angular error shown in the following figures is the difference between the estimated and the true helicopter elevation angles at that particular moment. The true helicopter elevation angle was taken to be the theodolite tracking angle with the correction for the difference in the theodolite height and the array phase center height of a given array. So, it is understood that the angular error also includes the theodolite operator tracking error, the theodolite setting error, and the helicopter range estimation error. We expect these errors to be fairly small (e.g., 0.1°).

Results were obtained with four C-band arrays with the array aperture sizes corresponding to array beamwidths of 1°, 2°, 3°, and 4°. They are shown in the symbols '1', '2', '3', and '4', respectively, in the following figures. As described in Chapter III Section B two angle estimators were used. Results from the angle estimator A (BS), which corresponds to the conventional MLS (TRSB) angle processor, are shown at the top of each figure; and those from the angle estimator B, which corresponds to the MLS "single edge" flare processor (SEP) [16,21], are given at the bottom.

A. Hanscom Airport

Figure 6-1 shows the estimated angular error versus the true helicopter elevation angle for one of the flights at the overrun area of the Hanscom airport runway 11 (Fig. 4-1). As observed in the elevation (EL) angular power spectral estimates in Chapter V Section A, the C-band terrain multipath

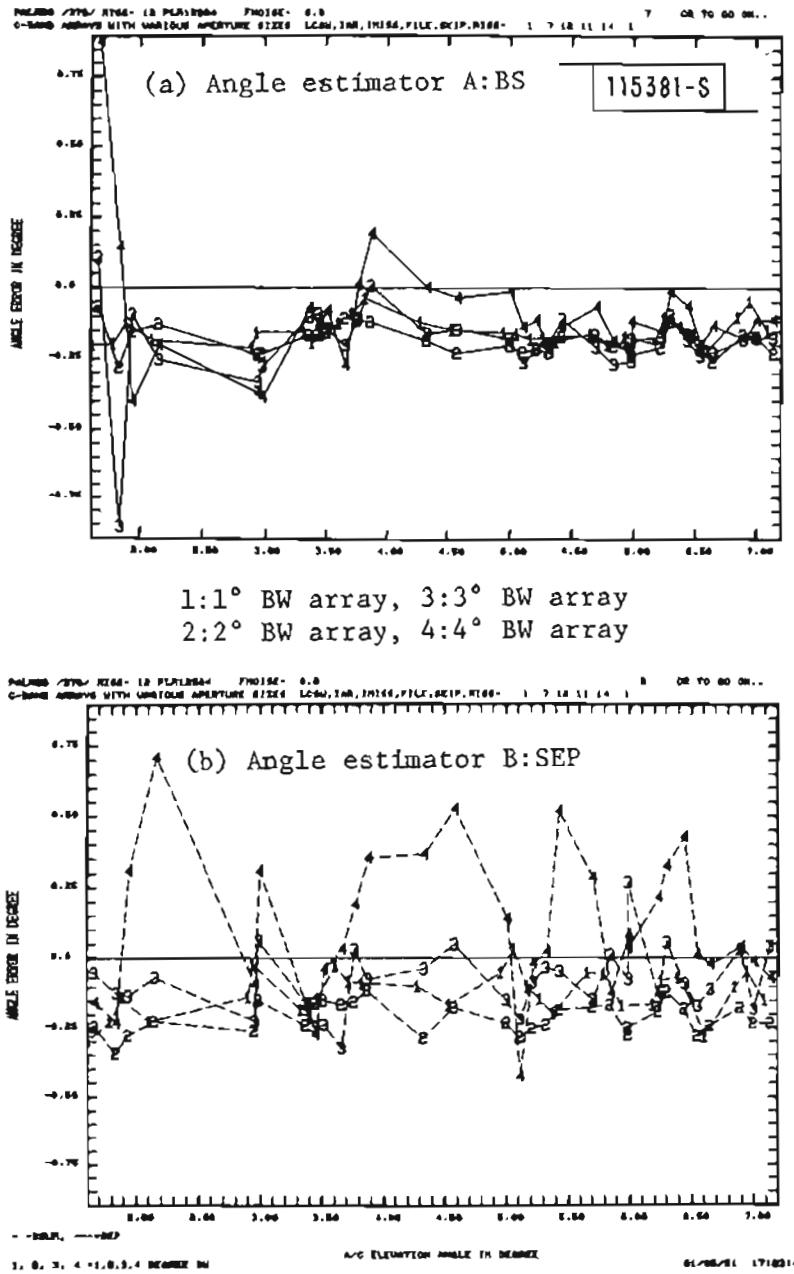

Fig. 6-1. Hanscom Airport measurement: angle estimation result.

environment here was characterized by two specular ground reflections, although the ground here was physically fairly flat. Thus, the C-band multipath environment is not as simple as that for a perfectly flat ground in the synthetic data case, shown previously in Chapter III Section B. The observed multipath separation angle (θ_{sep})* varied from > 9° at high helicopter elevation angles ($\theta_{EL} \geq 5°$) to < 2° at low elevation angles (θ_{EL} < 1.5°). The multipath was inbeam** for the 4° BW array when θ_{EL} < 5°. However, for the 1° BW array, the multipath was out-of-beam for the entire flight path.

We notice that the angular errors in Fig. 6-1 are somewhat negatively biased. This probably is due to the inaccuracy in the theodolite tracking. For the angle estimator A, the angular errors are more or less the same for four array aperture sizes, except for the elevation angle θ_{EL} < 2°. For θ_{EL} < 2°, the 1° and 2° beamwidth (BW) arrays yield a signficantly smaller error than the 3° and 4° BW arrays. This seems understandable, since for θ_{EL}< 2° the multipath would be inbeam for the 3° and 4° BW arrays. For the 1° and 2° BW arrays, the maximum angular error is in the order of 0.1° if we removed the apparent bias in the true helicopter elevation angle indicated in the figure (about 0.15°). For the angle estimator B, the angular errors are very similar for the 1° and 2° BW array, and are slightly larger for the 3° BW array. However, the 4° BW array performs much more poorly. The maximum angular error with the 1° and 2° BW arrays is around 0.15°***.

For both angle estimators, no significant reduction in the angular error was observed with decreasing the beamwidth from 2° BW to 1° BW. However,

---

*The observed multipath separation angle (θ_{sep}) is estimate from the elevation angular power spectrum of the field measured results (Figs. 5-1 to 5-6). The θ_{sep} is taken to be the angle difference between the direct signal angle (i.e., θ_{EL}) and the arrival angle of the ground reflection which is closest to the direct signal.

**Multipath is said to be inbeam when $\theta_{sep} \leq 1.5$ BW and out-of-beam when θ_{sep} > 1.5 BW.

***The error here represents a sum of ground multipath errors and SNR effects as only a single time "snapshot" was used in computing the BS spectra.

performance improvement of the 3° BW array over the 4° BW array is very clear. For a given array aperture size, say 1° BW array, both angle estimators deliver the similar performance, except for the 4° BW array, where the angle estimator A does better. This is quite contrary to what was observed in the result of synthetic data case (Fig. 3-4) where the angle estimator B showed much better performance than the angle estimator A. In fact, here the angle estimator B yields slightly greater angular errors than the angle estimator A for the 1°, 2°, and 3° BW arrays and much larger errors for the 4° BW array.

B. Fort Devens Golf Course

At this measurement site, the tree line was high, as mentioned in Chapter IV Section B. Thus, the typical helicopter flight only covered the elevation angles from 7° down to around 2.5°.

Figure 6-2 shows the elevation angle estimation results for one of the helicopter flights at the measurement point A along the radial line O-A (Fig. 4-3). The terrain along the radial line O-A was rolling with various cross-range titlts (Fig. 4-4). The observed C-band multipath environment was focusing ground reflections at moderate levels ($\sim$ -6 dB) (Fig. 5-19). Except for the 4° BW array, the observed multipath appeared to be out-of-beam for the entire flight path. For the angle estimator A, all four arrays have the similar performance, except at a couple of way-points where the 4° BW array yields significantly much larger angular errors. The maximum angular error is on the order of 0.15°. Thus, it appears that no performance improvement seems obvious with decreasing the beamwidth from 3° BW to 1° BW for the angle estimator A. For the angle estimator B, the 1° BW array gives the smallest angular errors ($\sim$ 0.1°), followed by the 2° and 3° BW arrays. The 4° BW array again yields the worst results, as observed previously in the Hanscom airport measurement. So, with the angle estimator B, noticeable error reductions are obtained with the increasing array aperture size from 4° BW to 3° BW. In general, the angle estimator A performs better than the angle estimator B for a given array, especially in the case of the 4° BW array.

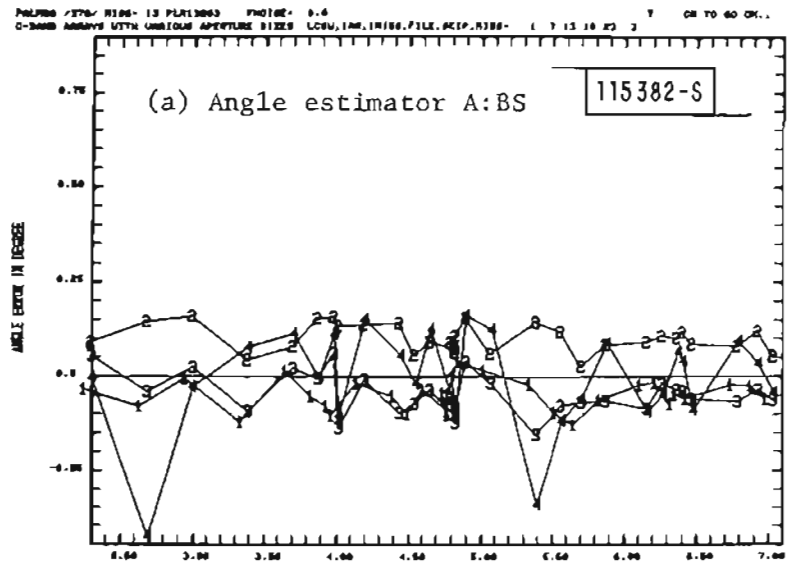

1:1° BW array, 3:3° BW array
2:2° BW array, 4:4° BW array

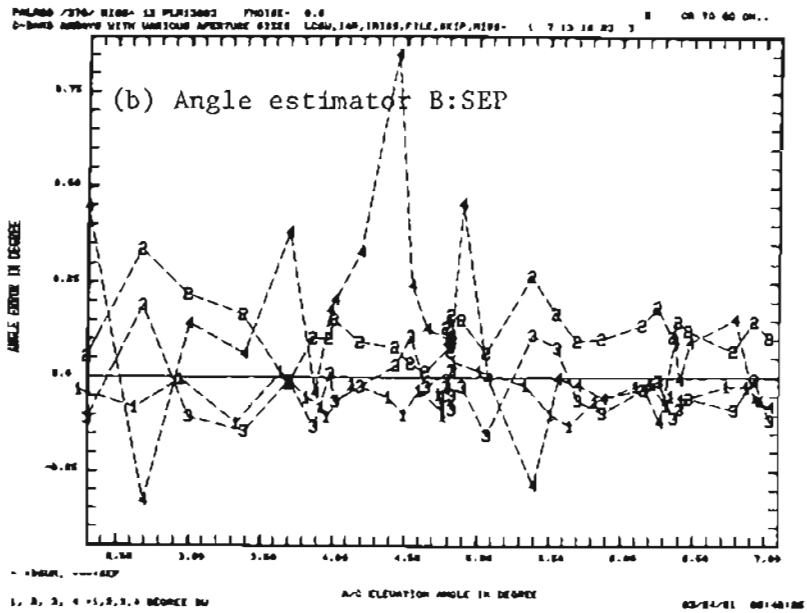

Fig. 6-2. Fort Devens golf course measurement: radial line O-A, angle estimation result.

Figure 6-3 shows the similar results at the measurement point B along the radial line O-B (Fig. 4-3). Again, as along the radial line O-A, the terrain here was rolling (Fig. 4-5) and the observed C-band multipath environment was focusing ground reflections at moderate levels (Fig. 5-30). Here, the observed multipath was inbeam for the 4° BW array for almost the entire flight path and was mostly out-of-beam for the other three arrays. For the angle estimator A, the 1° and 3° BW arrays yield similar angular errors with maximum error around 0.25°. The 2° BW array shows slightly worse performance (maximum angular error around 0.35°), and the 4° BW array gives the worst results. For the angle estimator B, the 1° and 3° BW arrays again yield similar results, except for the elevation angles around 4° where the 3° BW array gives much smaller errors. The 4° BW array again turns in the largest angular errors. For a given array aperture size, both angle estimators yield similar angular errors, except for the 4° BW array, where the angle estimator B gives much worse results. One thing to be noticed here is that the 3° BW array performs better than the 2° BW array for both angle estimators. This is somewhat surprising, since the 3° BW array has a smaller array aperture than the 2° BW array. One possible explanation is that the theodolite tracking angles might have been negatively biased. That can move the horizontal line in Fig. 6-3 (which shows zero error) upward and the 2° BW array will perform about in par with the 1° and 3° BW arrays. Also, the 2° and 3° arrays did not have the same phase center height above ground. Consequently, at some angles the relative phase between the direct signal and reflected signals may have been more unfavorable for the 2° array than the 3° array.

Figure 6-4 shows the elevation angle estimation results for one of the helicopter flights at the measurement point C along the radial line O-C (Fig. 4-3). The terrain here was rolling as along the other two radial lines (Fig. 4-6). However, due to the tall tree line, the elevation obstruction angle along this radial line was much greater than that along the radial lines O-A and O-B, 3° versus 2°. The observed C-band multipath environment was focusing ground reflections with low multipath levels (< -10 dB) mixed with the diffuse reflections at lower elevation angles (Fig. 5-39). Here again, we notice some apparent biases on the angular errors in Fig. 6-4 for both angle estimators,

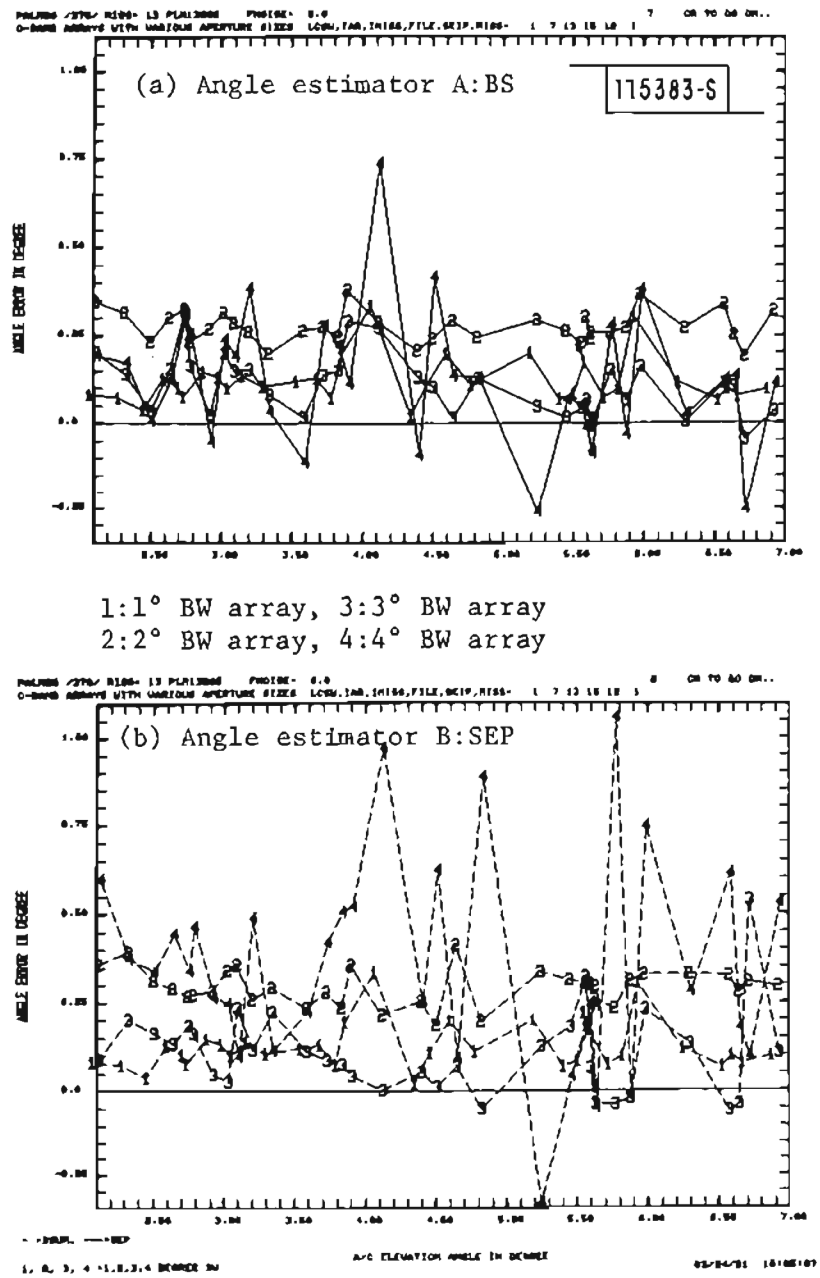

Fig. 6-3. Fort Devens golf course measurement: radial line O-B, angle estimation result.

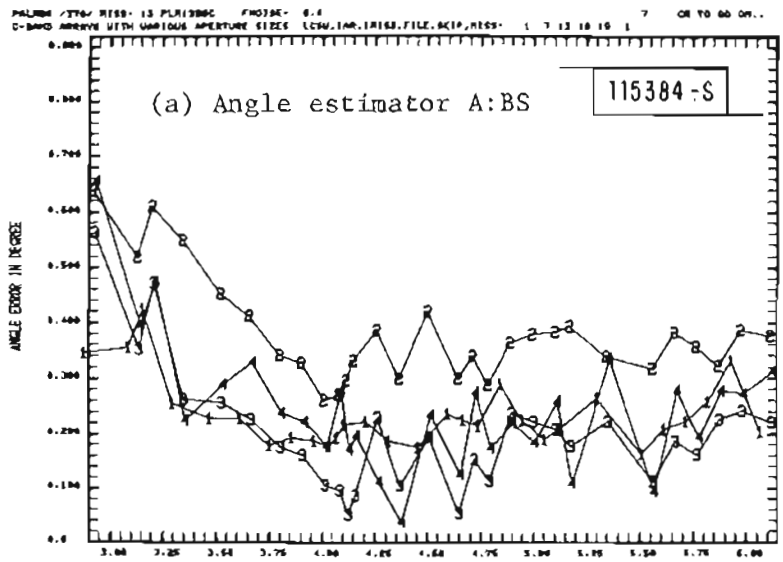

1:1° BW array, 3:3° BW array
2:2° BW array, 4:4° BW array

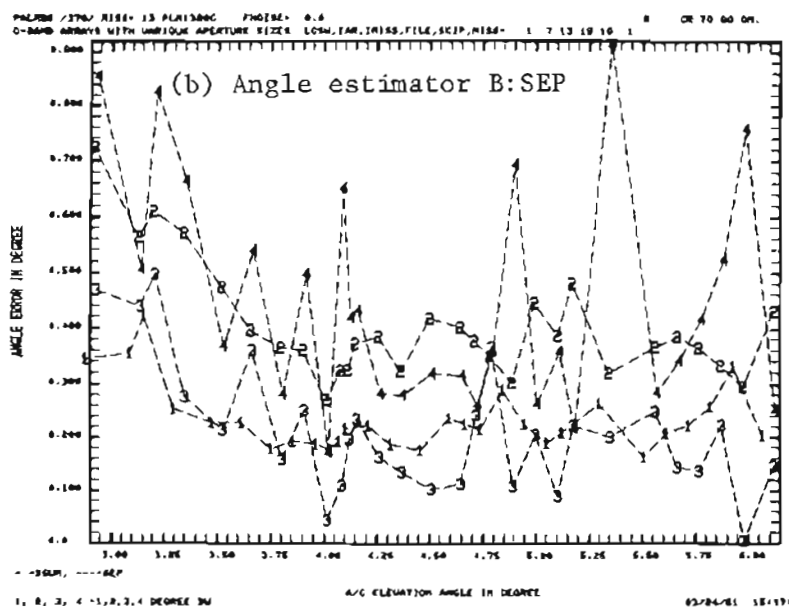

Fig. 6-4. Camp Edwards measurement: J2 Range, angle estimation result.

as observed previously in Fig. 6-3. Angular errors appear to be positively bias (about 0.2°), probably due to the theodolite tracking error. For the angle estimator A, taking into account the 0.2° bias, the 1° BW array yields the best performance (maximum angular error around 0.15°), followed by the 2°, 3°, and 4° BW arrays. It is noticed that the angular error increases drastically for helicopter elevation angle below 3.25°. For the angle estimator B, again the 1° BW array gives the smallest angular error, followed by the 2° and 3° BW arrays. However, the 4° BW array yields much larger errors. Here, in general, two angle estimators yield similar results for a given array aperture size, except that the angle estimator A performs much better for the 4° BW array.

The angle estimation results for the measurements at Fort Devens golf course, which had more complicated terrain conditions than the Hanscom airport, can be summarized as follows:

(1) no significant angular error reduction was obtained with the decreasing the array beamdwidth from 3° BW to 1° BW,

(2) the performance improvement of the 3° BW array over the 4° BW array was clear, and

(3) two angle estimators yielded similar angular errors for a given array aperture size, with the angle estimator A out performing the angle estimator B for the 4° BW array.

The first two observed results probably can be attributed to the fact that the observed multipath was inbeam for the 4° BW array for most flight paths taken at this site while it was mostly out-of-beam for the other three arrays.

C. Camp Edwards

The C-band measurements were only taken at two of three measurement sites here. Thus, elevation angle estimation results are only available for those two sites.

1. J2 Range

As previously observed in the EL angular power spectral estimates

(Chapter V Section C), the C-band multipath environment here was mainly low level (< -20 dB) diffuse ground reflections for higher target elevation angles ($\theta_{EL} > 1°$) and a single specular ground reflection for lower elevation angles with high multipath levels (-8 dB to -2 dB). For these lower helicopter elevation angles, the observed multipath was inbeam for all four antenna arrays (Fig. 5-54). Figure 6-5 shows the elevation angle estimation results for one of the flights here. This flight covered the elevation angle from 7° down to the local ground surface near 0°.

For the angle estimator A, the result here is very similar to that of the synthetic data case (Fig. 3-4), which was for the perfectly flat ground. The performances of the 1°, 2°, and 3° BW array are about the same for target elevation angles greater than 1°. The maximum angular error is around 0.06° to 0.08°. For lower elevation angles ($\theta_{EL} < 1°$), noticeable reduction in the angular error is observed by increasing the array aperture size from 4° BW to 3° BW to 2° BW, and to 1° BW. The larger angular errors are observed in the lower elevation angle region where the observed multipath environment was a single specular ground reflection with high multipath level.

For the angle estimator B, the 1° and 2° BW array yield smaller angular errors than the 3° BW array at the higher target elevation angles. And again at the low elevation angles ($\theta_{EL} < 1°$), significant performance improvement is observed with the increasing array aperture size from 4° BW, 3° BW, 2° BW, to 1° BW. For this angle estimator, the 4° BW array performs very poorly, as compared to the other three arrays.

For a given array aperture size, the angle estimator B has better performance than the estimator A, except for the 4° BW array at the high helicopter elevation angle. This improvement appears to be more pronounced for the lower elevation angle. This is very similar to what was observed in the synthetic data case where the multipath was a single specular reflection.

2. Gibbs Road Entrance

Figure 6-6 shows similar results for one of the flights at Gibbs Road entrance site (Fig. 4-8). The observed C-band multipath environment here was

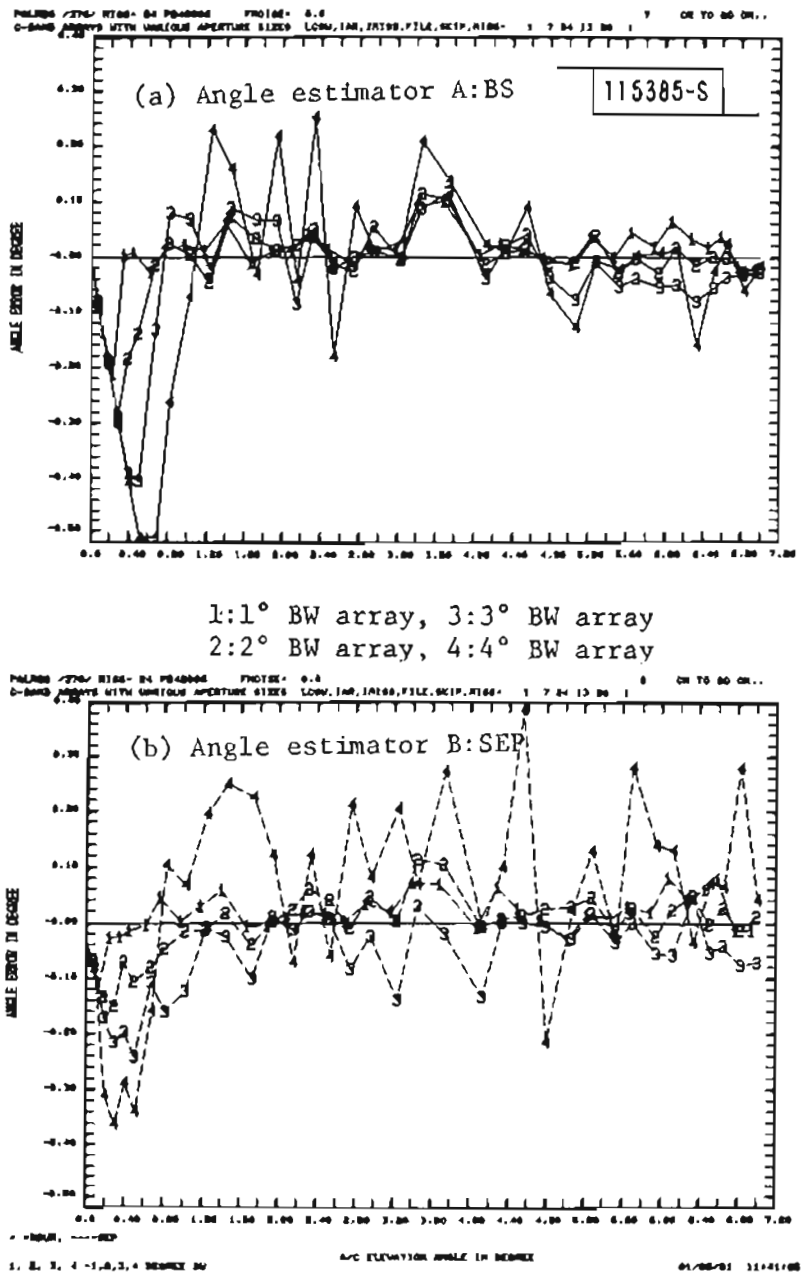

Fig. 6-5. Camp Edwards measurement: Gibbs Road E, angle estimation result.

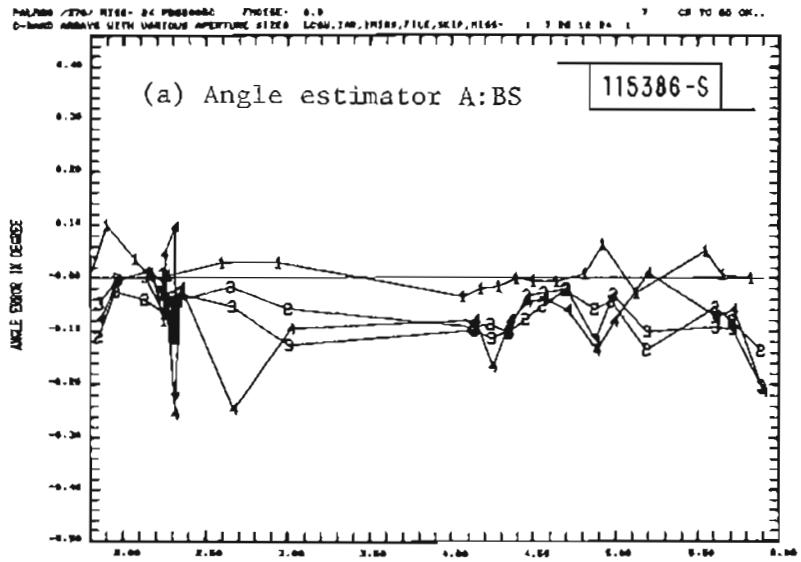

1:1°BW array, 3:3° BW array
2:2°BW array, 4:4° BW array

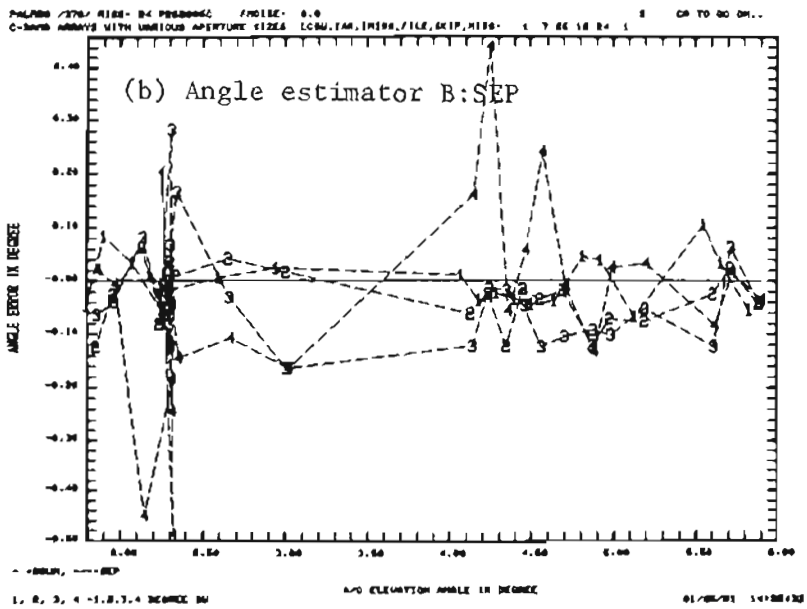

Fig. 6-6. Camp Edwards measurement: Gibbs Road E, angle estimation result.

multiple specular reflections with low multipath levels (< -10 dB) at higher elevation angles and high multipath levels (~ -2 dB) at low elevation angles (Fig. 5-70).

For the angle estimator A, the 1° BW array gives the best performance with a maximum angular error of 0.1°. The 2° and 3° BW arrays yield fairly similar results, next to the 1° BW array. The 4° BW array gives much larger errors around 0.25°. For the angle estimator B, the 1° and 2° BW arrays have similar performance (maximum angular error around 0.12°), followed by the 3° BW array. The 4° BW array yields the worst result. In general, two angle estimators have similar performance, except for the 4° BW array where the angle estimator A yields much smaller angular errors.

D. Summary

Based on the above elevation angle estimation results with four different array aperture sizes, the performance versus the array aperture size in various real-world multipath environments (C-band) can be summarized as follows:

(1) For both angle estimators, decreasing the antenna beamwidth from 4° BW to 3° BW yields a significant reduction in the angular error, especially for the SEP angle estimator. The maximum error reduction is around 0.1° to 0.2° for the angle estimator A and around 0.3° to 0.4° for the SEP angle estimator .

(2) For the angle estimator A, the 1°, 2°, and 3° BW arrays appear to have similar performances except at the Camp Edwards Gibbs Road entrance site and for the lower target elevation angles at the Hanscom airport site and the Camp Edwards J2 range site. At the Camp Edwards Gibbs Road entrance site, the 1° BW array yields smaller errors than the 2° and 3° BW arrays (0.05° veruss 0.1°). At the Hanscom airport site, the 3° BW array yields much larger errors than the 1° and 2° BW array for the target elevation angle of 1.75° (0.8° versus 0.25°). For the target elevation angles less than 0.8° at the Camp Edwards J2 range site, the maximum angular error reduces from 0.4° with 3° BW array to 0.3° with 2° BW array and to 0.2° with the 1° BW array.

(3) For the SEP angle estimator, the 1° BW array has the best performance, followed by the 2° and 3° BW arrays. However, in some cases, the 2° BW array performs about as well as the 1° BW array (Figs. 6-1 and 6-5), and in some other cases, the 3° BW array has a performance similar to that with the 1° BW array (Figs. 6-3 and 6-4).

(4) In general, except at the Camp Edwards J2 range site, the performance of the angle estimator A is equal to or better than that of the SEP angle estimator, especially for the smaller apertures (i.e., 3° and 4° BW). At the Camp Edwards J2 range site, the SEP angle estimator yields about 0.1° to 0.15° less error than the angle estimator A for the low target elevation angles ($\theta_{EL} < 0.8°$), in terms of maximum angular error in this region.

One might think that the angle estimation performance will degrade proportionally as the array aperture decreases, since the basic angular accuracy improves proportional to array aperture for the flat ground. However, this was not found to be the case at our measurement sites. For various terrain conditions at our measurement sites which are more complicated than the perfectly flat ground, the angular errors with the 3° BW array were often comparable to those with 1° BW array and no significant performance degradation was obvious with decreasing array aperture from 1° BW to 2° BW and to 3° BW. Table 6-1 shows the computed rms angular errors for the angle estimation results given in Figs. 6-1 to 6-6.

It had also been postulated that the improved performance of the SEP processor against idealized ground reflection multipath (recall Fig. 3-4) would enable one to achieve the same performance with a small array aperture that would be obtained with a larger array aperture using conventional angle estimation techniques. However, this typically was not the case at virtually all sites. For example, the SEP performance with a 4° BW was worse than that of any other processor/array combination whereas the synthetic data simulations suggested that the SEP with a 4° BW array would work nearly as well as a conventional processor with a 2° BW array. The differences here are believed due to sidelobe effects which become more pronounced as the array has fewer elements.

VII. CONCLUSIONS

Field measurements to obtain the L-band and C-band ground reflection data in various terrain conditions were made at five test sites at Hanscom airport, Fort Devens and Camp Edwards. The C-band data were collected with a 29 element elevation (EL) array, while the L-band data were collected with an 11 element EL array and a 6 element azimuth (AZ) array. For terrain multipath characterization, the angular power spectral estimates from these measurements were employed as a means to obtain the pertinent information, such as the number of multipath components, their arrival angles and M/D ratios, and specular versus diffuse reflection. Validation of terrain multipath propagation models used in the MLS computer simulation was made by comparing the field measurements with the corresponding MLS simulation predictions in terms of the angular power spectral estimates for a variety of measurements at these five sites. In addition, the C-band field data were processed with four different array aperture sizes (1°, 2°, 3°, and 4° array beamwidths) to obtain elevation angle estimation results for the assessment of angle performance degradation with reduced array apertures.

Three kinds of angular power spectral estimates, i.e., beamsum (BS), maximum likelihood (ML), and maximum entropy (ME), were computed in each case. The ML spectral estimate obtained with the modified covariance matrix showed a great deal of improvement over that obtained with the raw sample covariance matrix for resolving various signal components. However, the ME spectral estimate based on the modified covariance method still offered better resolution of various multipath arrivals than the ML spectral estimate, especially at very low elevation angles, where the multipath separation angle was small. It has been suggested [6] that the resolution and angle estimation accuracy with the ME spectral estimate for the terrain reflection type of data might be further improved by time-averaging more "data snapshots", if circumstance permits, as opposed to processing one single "snapshot" as we did here.

The L-band field measured results indicated that the principal elevation multipath was specular reflections with high multipath levels. The L-band M/D

ratios of -5 dB to 1 dB were observed for various terrain types, from fairly flat at Hanscom airport to rolling terrain at Camp Edwards Gibbs Road. These high L-band multipath levels persisted throughout any given flight path (typically from 7° elevation down to local obstruction elevation angle of 0.5° to 2.5°).

For the C band, diffuse ground reflections were evident at some measurement sites, especially at Camp Edwards J2 range site where small scale surface roughness was fairly visible. However, these diffuse ground reflections were at fairly low levels, -15 dB to -20 dB with respect to the direct signal. The multipath levels of the observed C-band specular ground reflections generally were lower than and not as consistent throughout a given flight path as those of the L-band. Except at the Hanscom airport site where the M/D ratios remained around -6 dB to -2 dB over the entire flight path, the C-band multipath levels stayed relatively low (-6 dB to -15 dB) for most of a given flight path at various test sites. For example, at Camp Edwards J2 range site where the multipath were dominantly low level diffuse reflections, the specular ground reflections (M/D ratios of -8 dB to -2 dB) were only observed at very low elevation angles (< 0.5°).

The phenomenon of "focusing" ground reflections, i.e., more than one specular ground reflection present at the same time, existed in both L band and C band. For the L band, this often occurred in the rolling type of terrain. However, for the C band this was also observed in the fairly flat terrain at Hanscom airport site. In all cases, the C-band results indicated more multipath arrivals than the L-band did.

The measurement geometry at various measurement sites which we visited, except at Hanscom airport, probably are not typical of the geometry at most of the airports in which the Microwave Landing System (MLS) will be operating. However, to some extent, some of the terrain features observed at these measurement sites, such as surface roughness and downsloping/upsloping, probably can be found near many airports, especially for the ground in the off-runway area or beyond the landing threshold [23]. So, it is thought to be appropriate to say a few words about the implication of the observed terrain

multipath environments reported here for the MLS performance.

For fairly flat and smooth terrain like that at Hanscom airport site, the terrain elevation multipath probably will have a minimal influence on the MLS performance, since the multipath generally was not very different from the classical flat earth model which has been used for MLS design. At Hanscom airport site, the rms angular error on the direct signal was about 0.04° which was obtained with an angle estimator similar to the MLS (TRSB) "dwell gate" angle processor[21] using the C-band 1° BW array for a flight path covering elevation angles from 7° down to 1.5°.

For the electrically not so smooth and/or rolling terrains like those at For Devens and Camp Edwards sites, the observed C-band multipath environments for direct signal elevation angles from 7° to 1° were typically characterized by the multiple specular ground reflections with moderate M/D ratios (-6 dB to -15 dB) and/or low level (-15 dB to -20 dB) diffuse reflections. Although these multiple reflections were at relatively moderate multipath levels as compared to those at Hascom airport site whose terrain was fairly close to the flat earth model used for MLS design, the angular errors observed for the measurement flights at Fort Devens and Camp Edwards were comparable to those at Hanscom airport, if not greater. Thus, it appears that the multiple reflections with moderate multipath levels from rolling terrain probable will produce the similar effect on the MLS performance as a high level specular reflection from a flat and smooth ground.

The L-band azimuth spectral estimates showed that the observed ground reflections and the direct signal appeared to come from the same azimuth angle. Thus, apparently, the terrain cross-range tilts in some of the measurement sites were not significant enough to make the azimuth arrival angles of various ground reflections differ from the direct signal azimuth arrival angle to be resolvable. This implies, but doesn't prove, that the angle estimation for the direct signal azimuth arrival angle should not be affected by the terrain multipath for the terrain with cross-range tilts similar to those at various test sites described here.

For the validation of the terrain propagation models, the comparison

results indicated that the agreement between the field measured results and the MLS multipath simulation results depended strongly on the terrain types, as discussed in Chapter V Section D. For the terrain which had almost no cross-range tilts and were electrically smooth and thus could be modelled in more detail with the current format of the ground model in the MLS multipath simulation program, the field measured results could be well explained with the simulation predicted results. Good agreement was obtained, in terms of number of multipath components, their arrival angles and M/D ratios.

However, for the other more complicated terrains, the comparison results were mixed, and, in general, agreement was poor, especially for those cases where the diffuse ground reflections appeared to exist in the field measured data. The experimental data multipath levels associated with poor agreement cases were typically low (e.g., less than -10 dB M/D ratio). Consequently, the poor agreement between simulation and field data would generally not result in excessive MLS errors occuring when not predicted.

Some of the discrepencies between two sets of results are expected and understandable, such as those cases with observed diffuse ground reflections and low observed multipath levels, since the diffuse scattering was not considered in the MLS multipath simulation runs and the surface of ground model was taken to be perfectly smooth. For the more complicated terrains with various cross-range tilts and along-range height variations, it is believed that part of the disagreement probably is caused by the constraint in the focusing ground option of the ground reflection calculation in the current MLS multipath simulation program. The constraint limits the maximum number of rectangular ground plates to be fifteen for modelling a given terrain. In most coses, fifteen rectangular plates are not sufficient to yield a good ground model for a complicated terrain, especially for the C-band.

Based on the comparison results on the field measured results and the multipath simulation predicted results, some suggestions for running the current MLS multipath simulation program to obtain the multipath information for various terrain types are given below:

(1) For terrain with no cross-range tilts, treat the rectangular ground plates in the ground model as the tilted building plates and use the building reflection calculation (for the reflection ray X-O-R only [1]) in the MLS multipath simulation programs with a fifty building option. This is to take the advantage of the fifty building option which can handle a maximum of fifty rectangular reflection plates. So, the terrain can be modelled in more detail.

(2) For terrain with various cross-range tilts, use the ground reflection calculation with the focusing ground option in the MLS multipath simulation run. For this case, examine the terrain survey data carefully and determine how to linearize the surveyed along-range height profile and the cross-range tilts such that the given terrain can be best fitted with fifteen rectangular plates. This terrain near the ground antenna deserves the greatest attention since smaller areas are required here to yield a sizable reflection.

(3) For terrain which appears to be not smooth, use some appropriate value* for the rms surface roughness height in the MLS multipath simulation run. This is more important for the C band than for the L band.

The details in making up a ground model from the terrain survey data are described in Appendix C.

The performance comparison among four C-band arrays with array beamwidth (BW) of 1°, 2°, 3° and 4° was based on the elevation angle estimation results obtained with two angle estimators for the measurement flights (covering helicopter elevation angles from 7° down to local elevation obstruction angles which range from 0° to about 3°) at five test sites. The angle estimator A corresponds to the MLS (TRSB) "dwell gate" angle processor and the angle estimator B corresponds to the MLS "single edge" flare processor. Significant angular error reductions (on the order of 0.1° to 0.3°) was observed when the array aperture size was increased from 4° BW to 3° BW, especially for the angle estimator B. However, in general, it is not obvious that the angle

*Ideally, this value should be that from the actual terrain survey data, if they are available. Since, a surface roughness survey is not a trivial task, the second best for this value might be from some educated guess.

estimation performance will be significantly improved with reducing the beamwidth from 3° to 2° and to 1°. In most cases, the 1°, 2° and 3° BW arrays yielded fairly similar angular error, for higher direct signal elevation angles ($\theta_{EL} > 2°$). Only at lower direct signal elevation angles ($\theta_{EL} < 2°$), where multipath became too much inbeam for the smaller aperture arrays (e.g., 3° and 4° BW array) we started to see a clear trend of decreasing angular error with increasing array aperture size.

APPENDIX A

SCATTERED FIELD FROM TILTED DIELECTRIC FACET[†]

Overview

In this appendix, the problem of scattering of arbitrarily polarized plane waves from a tilted dielectric planar facet is discussed. The scattered field in the far field is expressed as an integration over the electric and magnetic surface current densities induced on the facet surface by the incident wave. By using the tangent plane approximation, the surface fields are expressed in terms of the incident field, the Fresnel reflection coefficients, and geometrical factors depending on the normal vector to the facet and the incident and scattered field directions.

Background[*]

The MLS multipath simulation program [1] has an option whereby specular reflections can be computed for a number of arbitrarily oriented rectangular (≤ 10) and triangular (≤ 10) plates. This model has been proven useful in a number of cases for modelling actual field messurement sites [2, 15, and this report].

The formula used for computing the scattered field from an individual plate involves the use of an effective reflection coefficient, R_{eq}, which is a function only of the angle of incidence. This approximation is valid at the specular point where the reflection angle = incidence angle. However, the numerical integration used to determine the received field will include points on the plate where the reflection angle $\neq$ incidence angle. The work reported in this appendix represents a start at quantifying the error introduced by the R_{eq} approximation.

[†]This appendix contributed by N. Whitaker.

[*]This section contributed by J. Evans.

Discussion

The incident field for this problem is assumed to be a plane wave, and hence can be expressed as

$$\bar{E}_i(\bar{r}) = [E_{hi}\ \hat{h}_{oi} + E_{vi}\ \hat{v}_{oi}]\ e^{j\bar{k}_i \cdot \bar{r}} \qquad \text{(A-1)}$$

The horizontal and vertical polarization unit vectors $\hat{h}_{oi}$ and $\hat{v}_{oi}$ are defined by

$$\hat{h}_{oi} = (\hat{k}_i \times \hat{z})/|\hat{k}_i \times \hat{z}| \text{ and } \hat{v}_{oi} = \hat{h}_{oi} \times \hat{k}_i \quad .$$

We note that $\{\hat{v}_{oi}, \hat{h}_{oi}, \hat{k}_i\}$ comprise an orthogonal set. The plane wave assumption is valid when our facet is in the far field of the transmitting antenna.

As derived in Appendix B, the field scattered by the facet can be expressed as an integral over the tangential $\bar{E}$ and $\bar{H}$ fields on the surface:

$$\bar{E}(\bar{r}) = jk_o \frac{e^{jk_o r}}{4\pi r} (\bar{\bar{I}} - \hat{k}_s\ \hat{k}_s) \cdot \iint_{A_o} d^2S'\ e^{-j\bar{k}_s \cdot \bar{r}'} [\hat{k}_s \times (\hat{n} \times \bar{E}_r) + \eta(\hat{n} \times \bar{H}_x)] \qquad \text{(A-2)}$$

where $j = \sqrt{-1}$ and η is the wave impedance. All other quantities are as defined in the Appendix B and are illustrated in Fig. A-1. To evaluate the integral, we will make use of the tangent plane approximation for the surface fields. Thus, $\bar{E}_r$ and $\bar{H}_r$ are expressed in terms of the local coordinate system and the Fresnel reflection coefficients, R_v and R_h.

The local coordinate system $\{\hat{v}_i, \hat{h}_i, \hat{k}_i\}$ is defined with respect to $\hat{k}_i$ and $\hat{n}$:

$$\hat{h}_i = (\hat{k}_i \times \hat{n})/|\hat{k}_i \times \hat{n}| \quad , \quad \hat{v}_i = \hat{h}_i \times \hat{k}_i$$

We now compose the incident field along the horizontal and vertical polarization vectors. To do this, we write

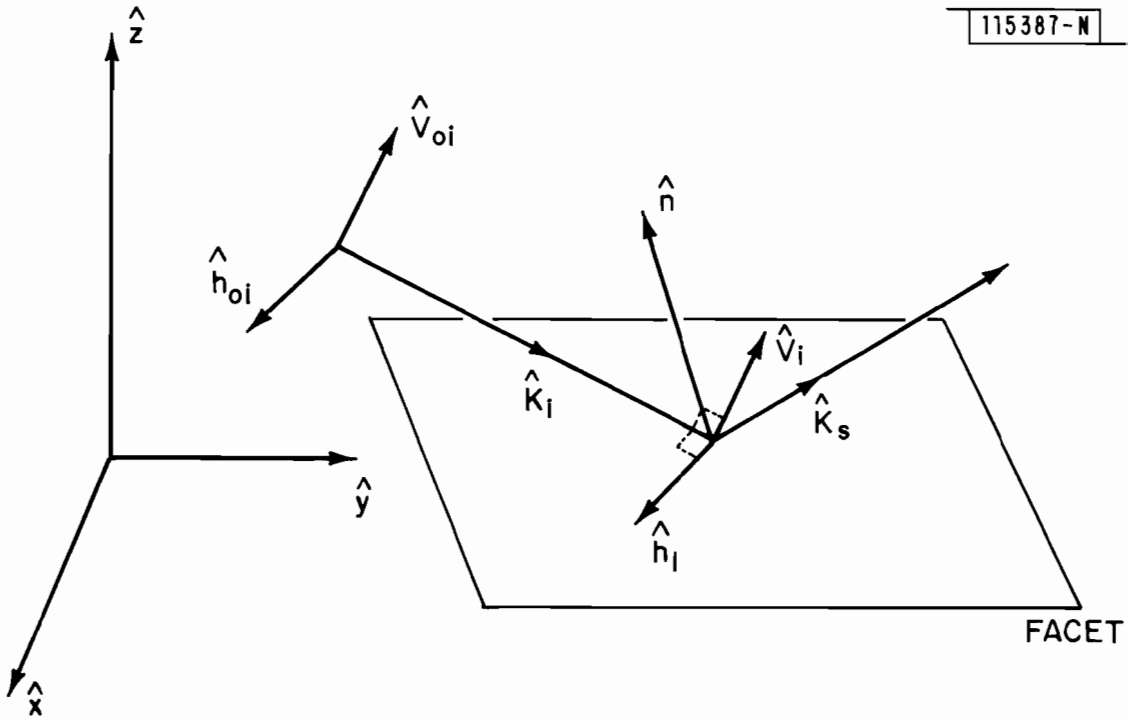

Fig. A-1. Coordinate system.

$$\bar{E}_i = E_o(\bar{r})\,\hat{e}_i \qquad \text{(A-3)}$$

This allows us to compute the incident $\bar{H}$ field from Faraday's law

$$\eta\bar{H}_i = E_o(\bar{r})\,(\hat{k}_i \times \hat{e}_i) \qquad \text{(A-4)}$$

and, in local coordinates, we see that

$$\hat{e}_i = \hat{v}_i(\hat{v}_i \cdot \hat{e}_i) + \hat{h}_i(\hat{h}_i \cdot \hat{e}_i)$$

$$(\hat{k}_i \times \hat{e}_i) = \hat{h}_i(\hat{e}_i \cdot \hat{v}_i) - \hat{v}_i(\hat{e}_i \cdot \hat{h}_i)$$

It is an easy matter, then, to compute the tangential components of the reflected field on the surface

$$\hat{n} \times \bar{E}_r\Big|_{z = h(x,\,y)} = \left[-R_v'(\hat{n} \times \hat{v}_i) + R_h'(\hat{n} \times \hat{h}_i)\right]E_o(\bar{r})\Big|_{z=h(x,y)} \qquad \text{(A-5)}$$

$$\hat{n} \times \bar{H}_r\Big|_{z = h(x,\,y)} = \left[R_v'(\hat{n} \times \hat{h}_i) + R_h'(\hat{n} \times \hat{v}_i)\right]E_o(\bar{r})/\eta\Big|_{z = h(x,y)}$$

where

$$R_v' = (\hat{e}_i \cdot \hat{v}_i)\,R_v$$

$$R_h' = (\hat{e}_i \cdot \hat{h}_i)\,R_h$$

and R_v and R_h are the Fresnel reflection coefficients evaluated at the local incidence angle.

$$R = (Z_i - Z_o)/(Z_i + Z_o) \qquad \text{(A-6)}$$

where for vertically polarized waves $Z_i = \varepsilon_i(\varepsilon_i - \sin^2\theta_t)^{-1/2}$ and

for horizontally polarized waves $\quad Z_i = (\varepsilon_i - \sin^2\theta_t)^{-1/2}$

θ_t is the local incidence angle and is defined by the relation

$$\cos\theta_t = -\hat{n} \cdot \hat{k}_i \tag{A-7}$$

In order to make use of equation (A-2), we identify another local coordinate system for the scattered field $\{\hat{v}_s, \hat{h}_s, \hat{k}_s\}$ where

$$\hat{h}_s = (\hat{k}_s \times \hat{n})/|\hat{k}_s \times \hat{n}| \text{ and } \hat{v}_s = \hat{h}_s \times \hat{k}_s$$

In equation (A-2), we identify $(\bar{\bar{I}} - \hat{k}_s \hat{k}_s) = \hat{v}_s \hat{v}_s + \hat{h}_s \hat{h}_s$ and note the following useful vector identity for any vector $\bar{A}$:

$$(\hat{v}_s \hat{v}_s + \hat{h}_s \hat{h}_s) \cdot (\hat{k}_s \times \bar{A}) = -\hat{v}_s(\hat{h}_s \cdot \bar{A}) + \hat{h}_s(\hat{v}_s \cdot \bar{A}) \tag{A-8}$$

Substituting the tangential fields (A-5) into (A-2), and making use of the above vector identities, we can write the scattered field as

$$\bar{E}(\bar{r}) = jk_o \frac{e^{jk_o R}}{4\pi r} \bar{F} \iint_{A_o} d^2S' \, e^{-j\bar{k}_s \cdot \bar{r}'} E_o(\bar{r}') \tag{A-9}$$

where

$$\bar{F} = (\hat{v}_s R_v' + \hat{h}_s R_h')(\hat{v}_s \cdot (\hat{n} \times \hat{h}_i) + \hat{h}_s \cdot (\hat{n} \times \hat{v}_i))$$

$$+ (\hat{v}_s R_h' - \hat{h}_s R_v')(\hat{v}_s \cdot (\hat{n} \times \hat{v}_i) - \hat{h}_s \cdot (\hat{n} \times \hat{h}_i))$$

We are primarily interested in the scattering of vertically polarized waves into vertically polarized waves. We therefore define a fourth orthogonal system at the receiver $\{\hat{v}_{os}, \hat{h}_{os}, \hat{k}_s\}$ where

$$\hat{h}_{os} = (\hat{k}_s \times \hat{z})/|\hat{k}_s \times \hat{z}| \text{ and } \hat{v}_{os} = \hat{h}_{os} \times \hat{k}_s$$

We next define

$$F_{vv} = \hat{v}_{os} \cdot \overline{F} \Big|_{\substack{\hat{e}_i = \hat{v}_{oi}}}$$

As shown in Appendix B, we can simplify the vector dot and cross products in equation (A-9) to find

$$\begin{aligned} F_{vv} = &-[R_v \cos\alpha_1 \cos\alpha_2 + R_h \sin\alpha_1 \sin\alpha_2] (\hat{h}_s \cdot \hat{h}_i) (\cos\theta_r + \cos\theta_t) \\ &-[R_v \sin\alpha_1 \cos\alpha_2 - R_h \cos\alpha_1 \sin\alpha_2] [(\hat{v}_s \cdot \hat{h}_i) (\cos\theta_r + \cos\theta_t) \\ &+ (\hat{n} \cdot \hat{v}_s) (\hat{k}_s \cdot \hat{h}_i)] \end{aligned} \qquad \text{(A-10)}$$

where we have used the following definitions from [5]

$$\cos\alpha_1 = \hat{v}_{oi} \cdot \hat{v}_i = \hat{h}_{oi} \cdot \hat{h}_i$$

$$\cos\alpha_2 = \hat{v}_{os} \cdot \hat{v}_s = \hat{h}_{os} \cdot \hat{h}_s$$

$$\sin\alpha_1 = \hat{v}_{oi} \cdot \hat{h}_i \sim \hat{h}_{oi} \cdot \hat{v}_i$$

$$\sin\alpha_2 = \hat{v}_{os} \cdot \hat{h}_s \sim \hat{h}_{os} \cdot \hat{v}_s$$

Note also that θ_r is defined by

$$\cos\theta_r = \hat{n} \cdot \hat{k}_s \qquad \text{(A-11)}$$

Equation (A-10) is the full and exact expression for the surface field amplitude on a tilted dielectric which radiates vertically polarized waves from incident waves which are vertically polarized.

The following special cases are of interest.

a. Specular Scatter

In the specular direction, $\hat{h}_s \cdot \hat{h}_i = 1$, $\hat{v}_s \cdot \hat{h}_i = 0$ and $\hat{k}_s \cdot \hat{h}_i = 0$. Thus,

$$F_{vv} = R_{eq}(\cos\theta_r + \cos\theta_t) \tag{A-12}$$

where $R_{eq} = R_v \cos\alpha_1 \cos\alpha_2 + R_h \sin\alpha_1 \sin\alpha_2$. Except for the sign, this is in exact agreement with the result in [5].

b. Flat Plane

For a flat plane $\hat{n} = \hat{z}$ and

$$F_{vv} = -R_v(\hat{h}_s \cdot \hat{h}_i)(\cos\theta_r + \cos\theta_t) \tag{A-13}$$

The result in [5] reduces to this except for the $-(\hat{h}_s \cdot \hat{h}_i)$ term.

Conclusions

This analysis snows that the result in [1] for the surface field on a titled dielectric facet is by and large correct. The result is exactly true in the specular direction, and therefore a good approximation provided the radiation pattern of the aperture provided by the facet is sharply peaked. This is true by assumption, since diffraction effects at the facet edges are ignored which implies the facet dimension is many wavelengths in extent.

A more exact result has been derived here from first principles which is valid for arbitrary incident and scattered directions and surface slope. The only approximations are in the tangent plane approximation itself. This result should be used when a more accurate result for the scattered field is needed, particularly if there is significant scattering in the non-specular direction.

APPENDIX B

DERIVATION OF INTEGRAL EQUATION FOR SCATTERED FIELD

In this appendix, we consider computation of the field scattered from a terrain surface in terms of the induced current on the terrain surface. The geometry is depicted in Fig. B-1.

I. For Equation (A-2)

We consider the terrain surface as dividing the space into two regions: the upper halfspace $z \geq h(x, y)$ ("region of interest") and the lower halfspace $z < h(x, y)$. The region of interest is comprised of a volume V bounded by the surface $S_I + S_{II}$.

In the region of interest, we introduce the free space dyadic Green's function $\bar{\bar{G}}(\bar{r}, \bar{r}')$ which satisfies the radiation condition and the vector Helmholtz equation

$$\nabla \times \nabla \times \bar{\bar{G}}(r, \bar{r}') - k_o^2 \bar{\bar{G}}(\bar{r}, \bar{r}') = \bar{\bar{I}} \delta(\bar{r} - \bar{r}') \qquad \text{(B-1)}$$

where $\bar{\bar{I}}$ is the idenfactor, i.e., a unit dyadic, k_o is the wavenumber in the region of interest, and $\bar{r}$ and $\bar{r}'$ are the field and source points, respectively. In addition, the $\bar{E}$ field in the region of interest satisfies the source free vector Helmholtz equation.

$$\nabla \times \nabla \times E(\bar{r}) - k_o^2 \bar{E}(\bar{r}) = 0 \qquad \text{(B-2)}$$

$\bar{E}(\bar{r})$ will be expressed in terms of surface sources on the boundary of our region of interest.

To derive the desired integral, we integrate the vector identity

$$\bar{P} \cdot \nabla \times \nabla \times \bar{Q} - \bar{Q} \cdot \nabla \times \nabla \times \bar{P} = \nabla \cdot \{\bar{Q} \cdot \nabla \times \bar{P} - \bar{P} \cdot \nabla \times \bar{Q}\}$$

(B-3)

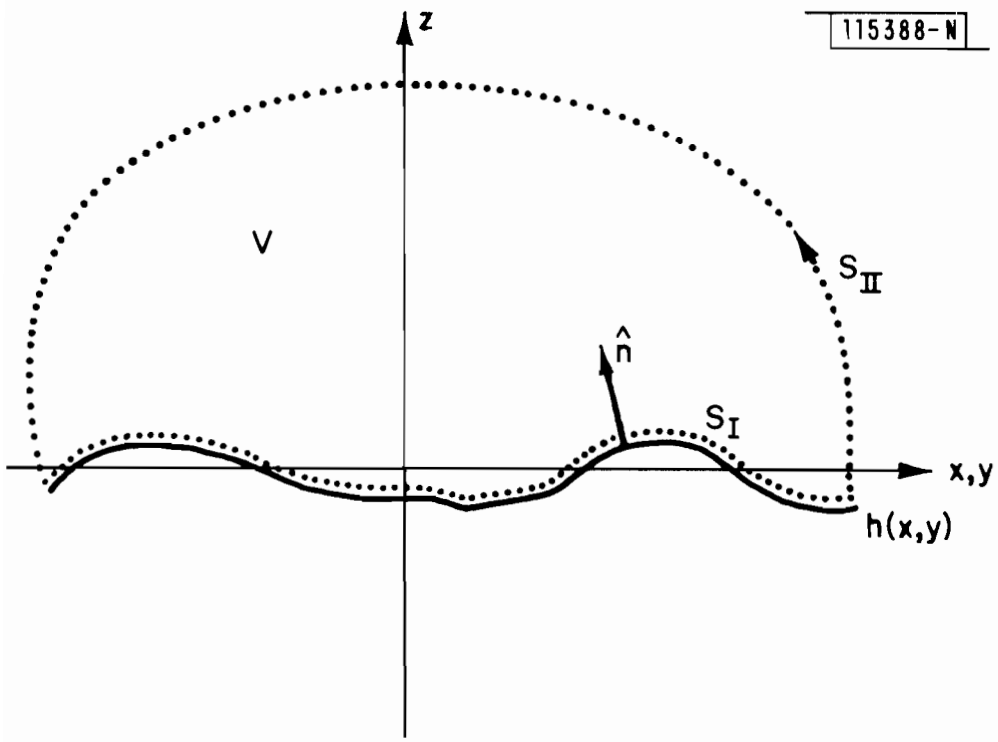

Fig. B-1. Integration region.

by letting $\overline{P} = \overline{E}$ and $\overline{Q} = \overline{\overline{G}} \cdot \overline{a}$, $\overline{a}$ is an arbitrary constant vector. By substituting (B-1) and (B-2) into (B-3), and using the above identifications, we find that:

$$\nabla \cdot \{\overline{\overline{G}} \cdot a \cdot \nabla \times \overline{E} - \overline{E} \cdot \nabla \times \overline{\overline{G}} \cdot \overline{a}\} = \overline{E} \cdot \overline{a}\, \delta(\overline{r} - \overline{r}') \qquad \text{(B-4)}$$

Note that by reciprocity $\overline{\overline{G}}(\overline{r}, r') = \overline{\overline{G}}^{T}(\overline{r}', r)$ where $\overline{\overline{G}}^{T}$ is the transposed dyadic. Furthermore, $\overline{\overline{G}}(\overline{r}, \overline{r}') = \overline{\overline{G}}(\overline{r} - r')$. By integrating (B-4) over the volume V, we can use Green's theorem to change our volume integral to a surface integral over $S_I + S_{II}$

$$\overline{a} \cdot \overline{E}(\overline{r}') = \int_{S_I+S_{II}} \int d^2S' \{-\hat{n} \cdot [\overline{\overline{G}}(\overline{r},\overline{r}') \cdot \overline{a} \times (\overline{\nabla} \times \overline{E}(\overline{r})) - \overline{E}(\overline{r}) \times \nabla \times \overline{\overline{G}}(\overline{r}, \overline{r}') \cdot \overline{a}]\} \qquad \text{(B-5)}$$

By rearranging terms, we find that (as $R \to \infty$)

$$E(r) = \int_{S_I} d^2S' \, [\overline{\overline{G}}(\overline{r}, \overline{r}') \cdot (\hat{n} \times \nabla \times \overline{E}(\overline{r}')) + \nabla \times \overline{\overline{G}}(\overline{r}, \overline{r}') \cdot \hat{n} \times \overline{E}(\overline{r}')] \qquad \text{(B-6)}$$

We neglect the integral over the surface at infinity, since $\overline{E}$ $(\overline{r})$ satisfies the radiation condition.

Note that since $\nabla \times \overline{E} = j\omega\mu\overline{H}$, our integral is over the electric and magnetic surface current densities on the surface ($\hat{n} \times \overline{H}$ and $\hat{n} \times \overline{E}$)

$$\overline{E}(\overline{r}) = \int_{S_I} d^2S' \, [j\omega\mu \, \overline{\overline{G}} \cdot \hat{n} \times \overline{H} + \nabla \times \overline{\overline{G}} \cdot \hat{n} \times \overline{E}] \qquad \text{(B-7)}$$

The free space dyadic Green's function from (B-1) can be written as

$$\overline{\overline{G}}(r, r') = (\overline{\overline{I}} + \frac{\nabla\nabla}{k_o^2}) \frac{e^{jk_o|\overline{r} - \overline{r}'|}}{4\pi|\overline{r} - \overline{r}'|} \qquad \text{(B-8)}$$

If the surface of interest is sufficiently flat on length scales larger than a wavelength, we can compute the field scattered from the whole surface as that scattered by individual facets. If $\frac{kr'^2}{r}$ is << 1 where r' is the facet dimension, we see that

$$|\bar{r} - \bar{r}'| = ((\bar{r} - \bar{r}') \cdot (\bar{r} - \bar{r}'))^{1/2} = |\bar{r}|\left(1 - \frac{2\bar{r} \cdot \bar{r}'}{|r|^2} + \bar{r}' \cdot \bar{r}'\right)^{1/2}$$

$$\cong |\bar{r}| - \hat{r} \cdot \bar{r}' \qquad \text{(B-9)}$$

If we let $\bar{k}_s = k_o \hat{r}$, we can rewrite (B-8) in the far-field form

$$\bar{\bar{G}}(\bar{r}, \bar{r}') = \frac{e^{jk_o r}}{4\pi r} (\bar{\bar{I}} - \hat{k}_s \hat{k}_s) e^{-j\bar{k}_s \cdot \bar{r}'} \qquad \text{(B-10)}$$

Note that $\hat{k}_s = \hat{r}$.

In addition, we find that in the far field

$$\nabla \times \bar{\bar{G}}(r, \bar{r}') = -j\bar{k}_s \times \bar{\bar{I}} \frac{e^{jk_o r}}{4\pi r} e^{-i\bar{k}_s \cdot \bar{r}'} \qquad \text{(B-11)}$$

By substituting (B-10) and (B-11) into (B-7), we obtain equation (A-2) directly.

II. DERIVATION OF EQUATION (A-10)

We start with the two vector identities, for any vector $\bar{A}$

$$\hat{v}_s \cdot \bar{A} = \hat{h}_s \cdot (\hat{k}_s \times \bar{A}) \qquad \text{(B-12)}$$

$$-\hat{h}_s \cdot \bar{A} = \hat{v}_s \cdot (\hat{k}_s \times \bar{A})$$

We use these to find the following

$$\hat{v}_s \cdot (\hat{n} \times \hat{h}_i) = -(\hat{h}_s \cdot \hat{h}_i)\,(\hat{n} \cdot \hat{k}_s) \tag{B-13}$$

$$\hat{h}_s \cdot (\hat{n} \times \hat{v}_i) = (\hat{h}_s \cdot \hat{h}_i)\,(\hat{n} \cdot \hat{k}_i)$$

$$\hat{h}_s \cdot (\hat{n} \times \hat{h}_i) = (\hat{v}_s \cdot \hat{h}_i)\,(\hat{n} \cdot \hat{k}_s) - (\hat{n} \cdot \hat{v}_s)\,(\hat{h}_i \cdot \hat{k}_s)$$

$$\hat{v}_s \cdot (\hat{n} \times \hat{v}_i) = (\hat{h}_i \cdot \hat{v}_s)\,(\hat{n} \cdot \hat{k}_i)$$

Making use of (B-13), (A-9), (A-7), and (A-11), we find (A-10).

APPENDIX C

CONSTRUCTION OF GROUND MODEL TO BE USED IN THE MLS MULTIPATH SIMULATION RUN

In this appendix, the step-by-step procedure to make up the ground model from the surveyed terrain data will be described. To best utilize the reflection calculation options in the current MLS multipath simulation program [1], ground models will be given for two specific terrain types, i.e., terrain with no cross-range tilts and terrain with various cross-range tilts, as suggested in Chapter VII. Since, at best, the ground model can only be as good as the terrain described by its terrain survey data, a few words will be given first about the terrain survey.

I. TERRAIN SURVEY

The needed terrain survey data include (1) the along-range height profile, (2) the cross-range tilts, (3) the surface roughness profiles, and (4) the ground surface composition, such as the type of soil, vegetation cover. The along-range direction refers to the direction along the line connecting the surface coordinates of the transmitter and the receiver, as sketched in Fig. C-1. The cross-range direction is transverse to the along-range direction. Normally, the first two terrain features can be surveyed with fairly reasonable effort and accuracy. However, the terrain survey for the surface roughness profiles can be complicated and tedious.

The surveyed distances for the along-range and cross-range directions have to be, respectively, no less than the lengths of the major and minor axes of the first Fresnel ellipse for the lowest transmitter or receiver elevation position anticipated in the field measurements. The survey can be done on the uniform grids over the terrain to be surveyed, or it can be done non-uniformly according to the changes in the ground slopes on the along-range heights and the cross-range tilts, as we did in our survey data shown in Fig. C-2.

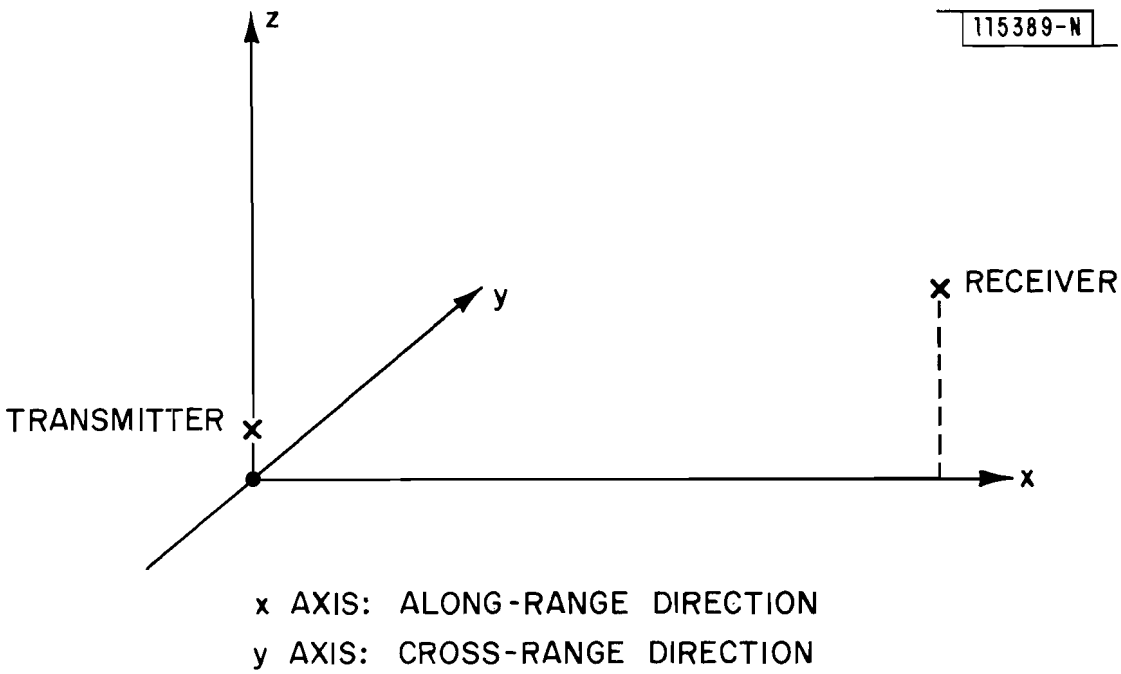

Fig. C-1. Coordinate system.

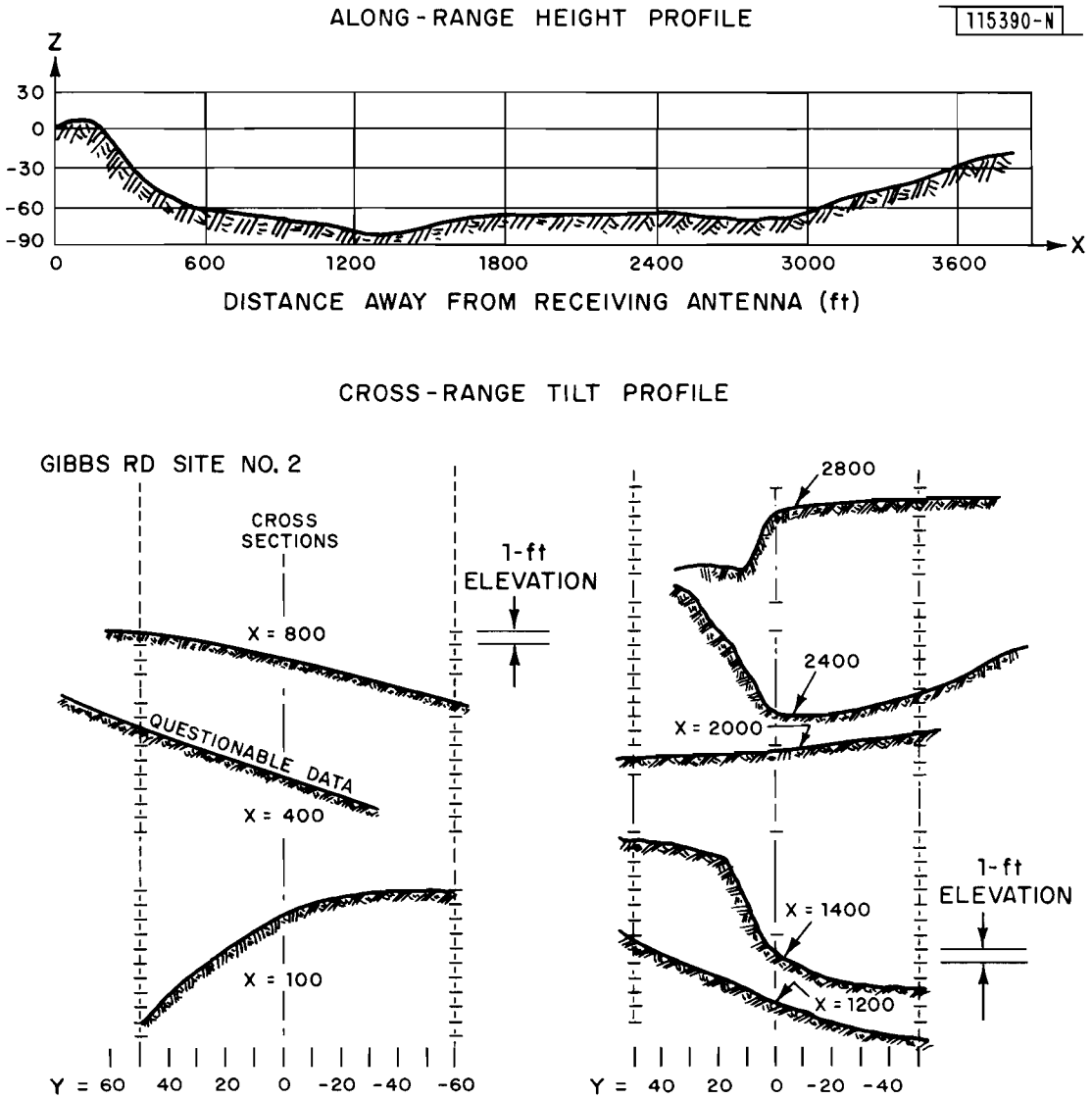

Fig. C-2. Terrain survey data.

II. GROUND MODEL

The ground model consists of a limited number of rectangular plates.* To use the ground reflection calculation with focusing ground option, the maximum number permissible rectangular plates is fifteen (15)** and these plates can be arbitrarily oriented (i.e., both along-range slope and cross-range tilt can be modelled). To treat the ground plates as tilted building plates in order to use the building reflection calculation, the maximum number of permissible rectangular plates is fifty (50), however, these plates can only be sloping in one direction (i.e., either along-range slope or cross-range tilt can be modelled, but not both).

A. Terrain With no Cross-Range Tilts

For this terrain type, treat the ground plates as the tilted bulding plates and use the building reflection calculation (with reflection ray X-O-R only) in the MLS multipath simulation run, since here only the terrain along-range slopes have to be modelled. The procedure to form the ground model is as follows:

Step 1: Linearization of the surveyed terrain height profile

As shown in Fig. C-3, use straight line segments to fit the surveyed terrain height profile as detailed as possible, but keep the total number of line segments to be no greater than fifty.+ Determine the angle between the z-axis and each line segment. This angle should be measured from the positive z-axis to a given line segment in counter-clockwise direction, as indicated in Fig. C-3.

---

*In the MLS multipath simulation program, the reflection plates for the ground reflection calculation with focusing ground option can actually be both rectangular and triangular, however, those for the building reflection calculation can only be rectangular. So, to be uniform for both reflection calculations, our ground models will only consist of rectangular plates.

**The actual number is 10 for the rectangular plates and 10 for the triangular plates. Since one rectangular plate can be divided into two triangular plates, the limiting number for ground model consisting entirely of rectangular plates would be 15.

+If the terrain height profile can be fitted with a small number of line segments, it is suggested [1] that finer divisions are given to those line segments corresponding to the ground closer to the receiver/transmitter, as is done in Fig. C-3.

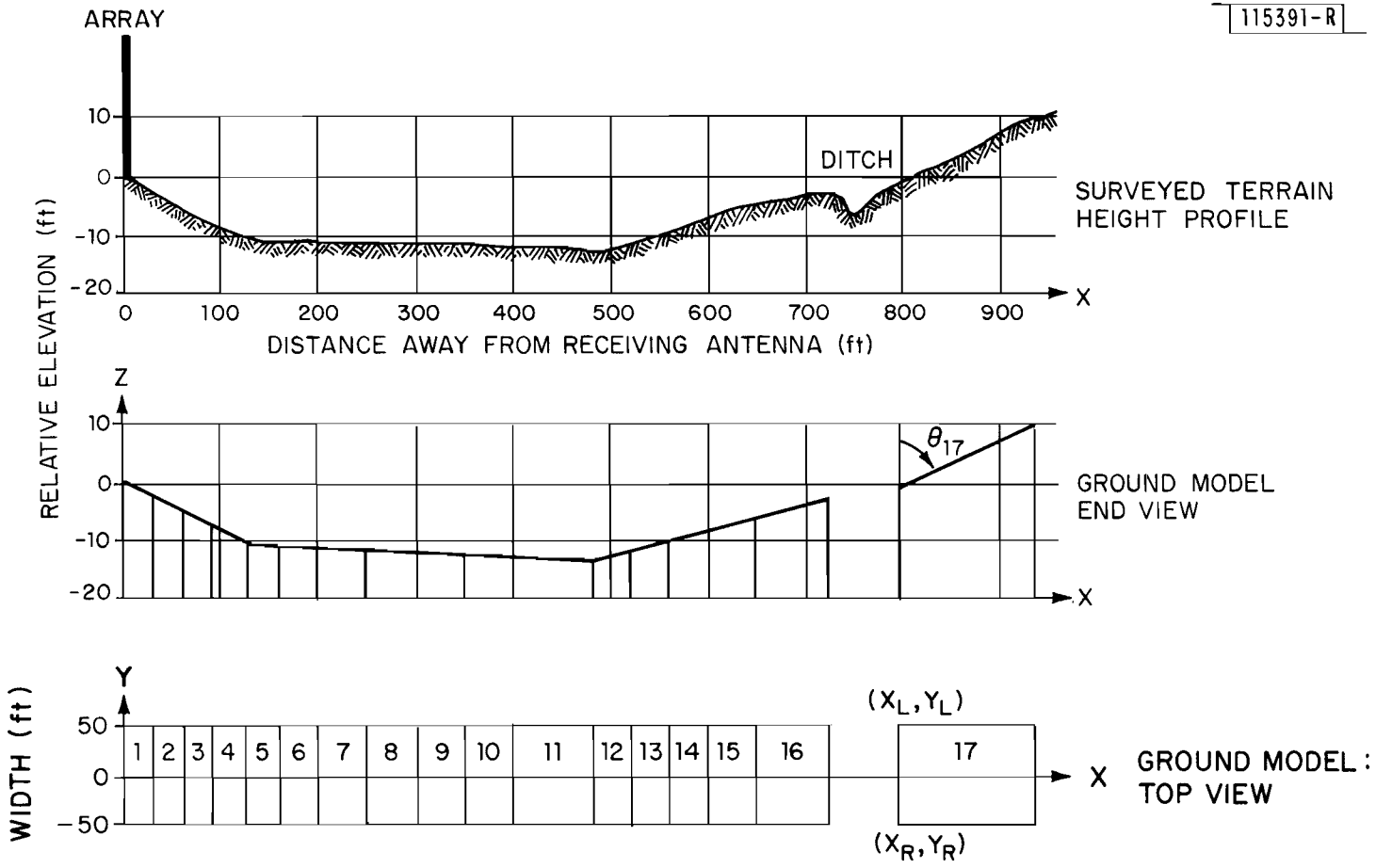

Fig. C-3. Linearization of surveyed terrain height profile: terrain with no cross-range tilts.

Step 2: Formation of a rectangular ground plate

Each line segment represents the X-Z projection of a rectangular ground plate. The length of the rectangular plate is equal to the length of the line segments. The width of the rectangular plate can be set either equal to the actual surveyed cross-range dimension of the ground, or equal to a value no less than the minor axis of the first Fresnel ellipse for the lowest transmitter or reciever elevation position anticipated in the field measurements. The X-Y projection of the rectangular ground plate, which is also a rectangle, shows the total number of the rectangular ground plates forming the ground model in Fig. C-3.

Step 3: Parameter specification for a ground plate treated as a tilted building plate.

The rectangular ground plate is then treated as the tilted building plate according to the following rules:

(1) The edge of the rectangular ground plate with smaller X coordinate is taken to be the bottom edge of the building plate, specified by the X and Y coordinates of the two ends of the edge, say (X_R, Y_R) and (X_L, Y_L). The height of this bottom edge, HBOT, is the Z coordinate of the edge.*

(2) The height of the building plate, HB, is equal to the length of the rectangular ground plate.

(3) The tilt angle of the building plate, TILT, is equal to the angle described in Step 1.

(4) The complex dielectric constant $(\varepsilon_R, -\varepsilon_I)$** and surface roughness heights (σ_h) of the building plate is equal to those of the ground plate.

---

*The Z coordinate of the ground surface at the transmitter is always taken to be 0.

**The complex dielectric constants for various materials can be found in a variety of references. Table C-1 gives some values for the often encountered ground surface material.

TABLE C-1

DIELECTRIC CONSTANT AND CONDUCTIVITY

GROUND SURFACE	$\varepsilon/\varepsilon_0$	σ
Fresh water (lake)[a]	80	0.01 0.001
Wet turf-short grass[b]	6	0.1
Dry turf-short grass[b]	3	0.05
Short grass-city area[b]	5	0.001
Wet sandy loam[a]	24	0.6
Dry sandy loam[a]	2	0.03
Fresh snow[b]	1.2	0.07
Packed snow[b]	1.5	0.6
Sea[a]	80	4
Dry earth[a]	2-5	10^{-3} - 10^{-5}
Wet earth[a]	5-30	10^{-1} - 10^{-3}

$\varepsilon/\varepsilon_0$ = relative dielectric constant

σ = conductivity in mho/meter

$\varepsilon_R = \varepsilon/\varepsilon_0$, $\varepsilon_I = \frac{\sigma}{\omega\varepsilon_0} \approx 6\phi\lambda\sigma$

[a] These values are from reference [19].

[b] These values are from reference [20].

Take plate 17 in Fig. C-3 for example, the above rules yield the building plate with the following parameter values:

(1) HBOT = -1.5', HB = 148'

(2) TILT = 85°

(3) (X_R, Y_R) = (800', -50'), (X_L, Y_L) = (800', +50')

Repeat this step and obtain the parameter values for all rectangular ground plates. Table C-2 gives the full description of these parameter values for the ground model shown in Fig. C-3 which is treated as a series of building plates.

B. Terrain with Cross-Range Tilts

For this terrain type, treat the ground plates as the ground plates and use the ground reflection calculation with focusing ground option in the MLS multipath simulation run, since here both the terrain along-range and cross-range slopes have to be modelled. The procedure to form the ground model is as follows:

Step 1: Linearization of the surveyed terrain height profile and cross-range tilts

As shown in Fig. C-4, use straight line segments to fit the surveyed terrain height profile first. Then, for a given line segment, find the surveyed terrain cross-range tilts for the ground whose along-range slope is represented by this line segment. Again use straight line segments to fit this cross-range tilt profile, as shown in the Y-Z projection of Fig. C-4. In so doing, remember that the total rectangular plates represented by these various along-range and cross-range line segments have to be no more than fifteen. Determine the X, Y, and Z coordinates of two end points of each line segment.

Step 2: Formation of a rectangular ground plate

Each along-range line segment and the corresponding cross-range line segment represent, respectively, the X-Z and Y-Z projections of a rectangular ground plate. The length and width of the rectangular plate are the length of the along-range line segment and the length of the cross-range line segment, respectively. Total number of the rectangular ground plates which form the ground model in Fig. C-4 is indicated in the X-Y projection.

TABLE C-2

PARAMETER VALUES FOR A GIVEN GROUND MODEL TREATED AS TILTED BUILDING PLATES

PLATE NO.	X_L	Y_L	X_R	Y_R	HB	HBOT	TILT
1	0	50	0	-50	30.1	0	94.5°
2	30	50	30	-50	30.1	-2.4	94.5°
3	60	50	60	-50	30.1	-4.8	94.5°
4	90	50	90	-50	36.1	-7.1	94.5°
5	126	50	126	-50	37	-10	90.5°
6	163	50	163	-50	37	-10.3	90.5°
7	200	50	200	-50	50	-10.6	90.5°
8	250	50	250	-50	50	-11.1	90.5°
9	300	50	300	-50	50	-11.5	90.5°
10	350	50	350	-50	50	-11.9	90.5°
11	400	50	400	-50	82	-12.3	90.5°
12	482	50	482	-50	38	-13	87.6°
13	520	50	520	-50	40	-11.4	87.6°
14	560	50	560	-50	11	-9.8	87.6°
15	600	50	600	-50	50	-8.1	87.6°
16	650	50	650	-50	74.1	-6.1	87.6°
17	792	50	792	-50	148.5	-1.5	85.2°

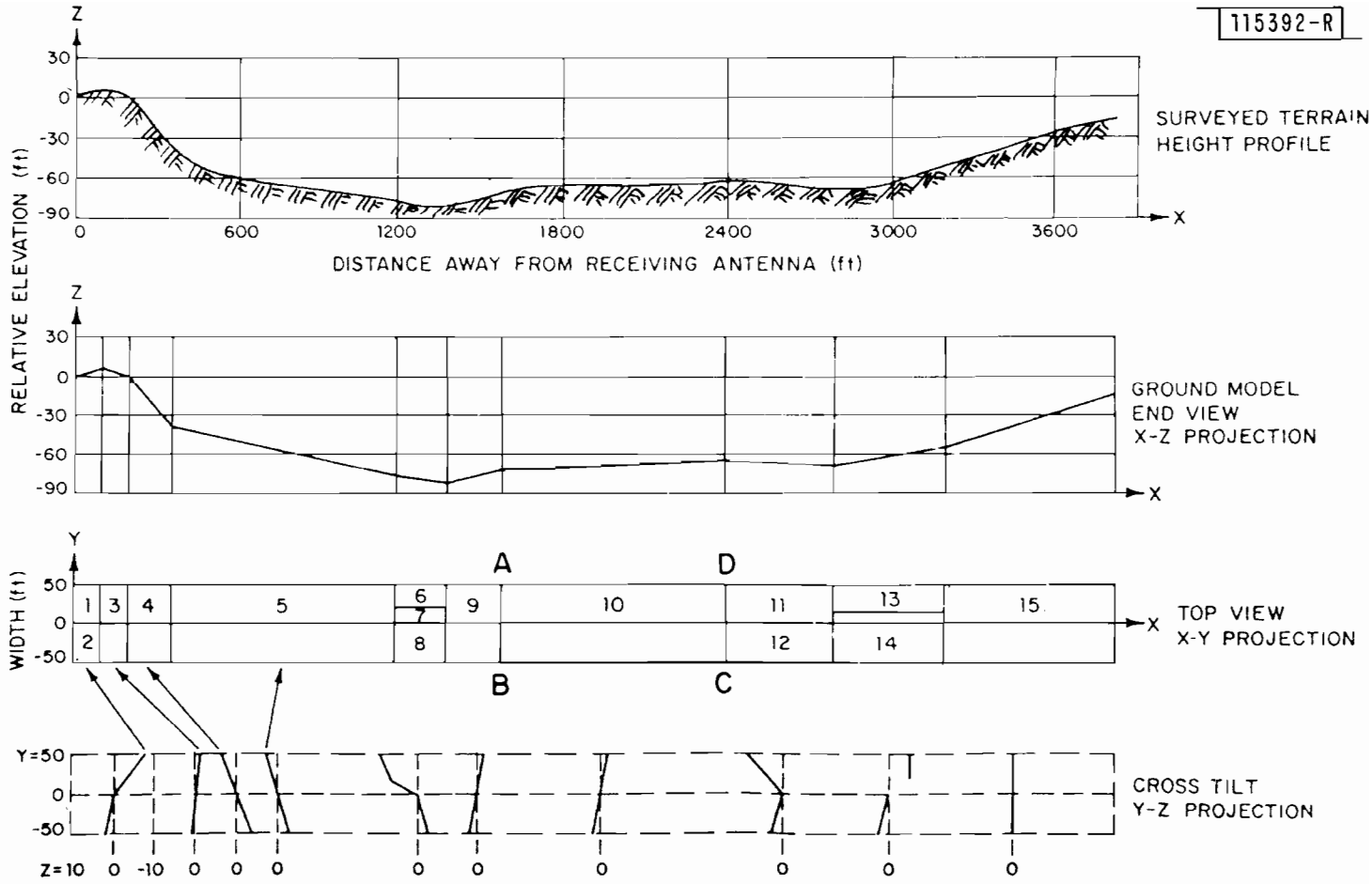

Fig. C-4. Linearization of surveyed terrain height and profiles: terrain with cross-range tilts.

Step 3: Parameter specification for a ground plate treated as a ground plate

A rectangular ground plate is specified by the X, Y and Z coordinates of its three corners, (X_i, Y_i, Z_i), $i = 1,3$. These coordinate values are easily obtained from those determined in Step 1. Take plate 10 in Fig. C-4 for example, its three corners, say A, B, and C, are described by

$$A(X_1, Y_1, Z_1) = (1600', 50', -74')$$
$$B(X_2, Y_2, Z_2) = (1600', -50', -72')$$
$$C(X_3, Y_3, Z_3) = (2400', -50', -65')$$

In addition to these coordinate values, the complex dielectric constant $(\varepsilon_R, -\varepsilon_I)$ and the surface roughness height (σ_h) have to be specified for each ground plate.

Repeat this step and obtain the parameter values for all rectangular ground plates. Table C-3 gives the full description of the parameter values for the ground model shown in Fig. C-4. As mentioned earlier, the maximum numbers of permissible ground plates for the ground reflection calculation with focusing ground option are ten for the rectangular plates and 10 for the triangular plates. Thus, in actual parameter input to the MLS multipath simulation program, some of the rectangular plates have to be divided into two triangular plates if the total number of the rectangular ground plates forming a ground model exceeds ten. For example, for the ground model described in Fig. C-4 and Table C-3, we can conveniently treat the rectangular plates 11 to 15 as total of 10 triangular plates in the actual parameter input.

TABLE C-3

PARAMETER VALUES FOR A GIVEN GROUND MODEL TREATED AS GROUND PLATES

PLATE NO.	$A(X_1, Y_1, Z_1)$	$B(X_2, Y_2, Z_2)$	$C(X_3, Y_3, Z_3)$
1	0, 50, -7.8	0, 0, 0	100, 0, 5.7
2	0, 0, 0	0, -50, 1.5	100, -50, 4.2
3	100, 50, 5.2	100, -50, 6.2	200, -50, 0.5
4	200, 50, 3.5	200, -50, -3.5	400, -50, -42.3
5	400, 50, -36.8	400, -50, -40.8	1200, -50, -77.1
6	1200, 50, -66.6	1200, 50, -68.1	1400, 20, -74.5
7	1200, 20, -68.1	1200, 0, -75.1	1400, 0, -81.5
8	1200, 0, -75.1	1200, -50, -76.5	1400, -50, -83.2
9	1400, 50, -82.5	1400, -50, -80.5	1600, -50, -72.1
10	1600, 50, -74.1	1600, -50, -72.1	2400, -50, -64.6
11	2400, 50, -54.2	2400, 0, -65.6	2800, 0, -68.4
12	2400, 0, -65.6	2400, -50, -63.6	2800, -50, -66.4
13	2800, 50, -72.7	2800, 12, -72.4	3200, 12, -61.7
14	2800, 0, -68.4	2800, -50, -66.6	3200, -50, -55.9
15	3200, 50, -57.7	3200, -50, -57.7	3800, -50, -18.8

REFERENCES

1. J. Capon, "Multipath Parameter Computations for the MLS Simulation Computer Program," Project Report ATC-68, Lincoln Laboratory, M.I.T. (8 April 1976), FAA-RD-76-55, DDC AD-A024350/1.

2. J. E. Evans, D. F. Sun, S. J. Dolinar, and D. A. Shnidman, "MLS Multipath Studies, Phase 3, Final Report, Volume I: Overview and Propagation Model Validation/Refinement Studies," Project Report ATC-88, Lincoln Laboratory, M.I.T. (25 April 1979) FAA-RD-79-21, DTIC AD-087827/2.

3. J. E. Evans, D. Karp, R. R. LaFrey, R. J. McAulay, and I. G. Stiglitz, "Experimental Validation of PALM - A System for Precise Aircraft Location," Technical Note 1975-29, Lincoln Laboratory, M.I.T. (29 April 1975) DDC AD-A010112/1.

4. S. W. Lang, "Performance of Maximum Entropy Spectral Estimators," Master Thesis, Department of Electrical Engineering and Computer Science, M.I.T. (May 1979).

5. S.W. Lang, "Near Optimal Frequency/Angle of Arrival Estimates Based on Maximum Entropy Spectral Techniques," Proc. 1980 Intl. Conf. on Acoustics, Speech, and Signal Processing (ICASSP), Denver, Colorado, 9-11 April 1980, pp. 829-832.

6. J. E. Evans, J. R. Johnson, and D. F. Sun, "Application of Advanced Array Processing Techniques for Improved Angle of Arrival Determination in ATC Systems," Technical Report 582, Lincoln Laboratory, M.I.T. (to be published).

7. J. E. Evans, R. C. Burchsted, J. Capon, R. S. Orr, D. A. Shnidman, and S. M. Sussman, "MLS Multipath Studies, Volume I: Mathematical Models and Validation," "Volume II: Application of Multipath Model to Key MLS Performance Issues," Project Report ATC-63, Lincoln Laboratory, M.I.T., (25 Feb. 1976) FAA-RD-76-3, DDC AD-A023040/9, and AD-A025108/2.

8. T. E. Bernard, "Analytical Studies of Techniques for the Computation of High-Resolution Wavenumber Spectra," Special Report No. 9, Texas Instruments Inc., Dallas, Texas (14 May 1969), Project No. VELA/7701.

9. J. Capon, "High Resolution Frequency Wave Number Spectrum Analysis," Proc. IEEE 57, 1408 (1969).

10. J. Makhoul, "Linear Prediction; A Tutorial Review," Proc. IEEE, 63, 561 (1975).

11. J. P. Burg, "Maximum Entropy Spectral Analysis," in Proc. 37th Mtg. Soc. in Exploration Geophysics, Oklahoma City, Oklahoma, 31 October 1967.

12. T. E. Bernard, "The Maximum Entropy Spectrum and the Burg Technique," Advanced Signal Processing Technical Report No. 1, Texas Instruments Inc., Dallas, Texas, (25 June 1975), ALEX (03)-TR-75-01.

13. P. F. Fougere, "A Solution to the Problem of Spontaneous Line Splitting in Maximum Entropy Power Spectrum Analysis of Complex Signals," Proc. RADC Spectrum Estimation Workshop, Rome, New York, 24-26 May 1978, pp. 77-84.

14. J. E. Evans and D. F. Sun, "Experimental Measurement of the Low Angle Terrain Scattering Interference Environment," Proc. Natl. Telecommunications Conf., Houston, Texas, 30 November - 4 December 1980, Vol. 1, pp. 11.3.1 - 11.3.5.

15. D. F. Sun, "Experimental Measurements of Ground Reflection Elevation Multipath Characteristics and Its Effects on a Small Aperture Elevation Tracking Radar," Technical Note 1979-21, Lincoln Laboratory, M.I.T. (5 March 1979), DDC-AD-A077915/7.

16. J. Beneke, D. Wightman, A. Offt, and C. Vallone, "TRSB Multimode Digital Processor," Final Report, Calspan Corp., FAA-RD-78-84 (April 1978).

17. H. Akaike, "Statistical Predictor Identification," Ann. Inst. Statist. Math., 22, 205 (1970).

18. D. Barton, "Low Angle Radar Tracking," Proc. IEEE, 57 (1974).

19. D. E. Kerr, Propagation of Short Radio Waves (McGraw-Hill, New York, 1951).

20. G. F. Spingler, "Experiment and Analysis of Siting Criteria", NAFEC, FAA Report RD-69-43 (1969).

21. J. E Evans, S. J. Dolinar, D. A. Shnidman and R. C. Burchsted, "MLS Multipath Studies, Phase 3, Final Report, Volume II: Development and Validation of Model for MLS Techniques," Project Report ATC-88, Lincoln Laboratory, M.I.T. (7 February 1980), DTIC AD-A088001/3.

22. H. Berger and J. E. Evans, "Diversity Techniques for Airborne Communications in the Presence of Ground Reflection Multipath," Technical Note 1972-27, Lincoln Laboratory, M.I.T. (8 September 1972), DDC AD-752249.

23. "Siting Criteria for Instrument Landing System," Dept. of Transportation, Federal Aviation Administration, FAA Order 6750.16A (14 August 1973).